VILNIUS UNIVERSITY
CENTER FOR PHYSICAL SCIENCES AND TECHNOLOGY

Kazimieras
NOMEIKA

Novel ways of improving quantum efficiency of InGaN LED active layers by controlling carrier diffusivity

DOCTORAL DISSERTATION

Technological sciences,
Materials Engineering T 008

VILNIUS 2019

This dissertation was written between 2014 – 2018 at the Institute of Photonics and Nanotechnology, Vilnius University.
The research was supported by the Research Council of Lithuania (scholarships for academical accomplishments DOK-16421 and DOK-17351).

Academic supervisor:
Assoc. Prof. Dr. Ramūnas Aleksiejūnas (Vilnius University, Technological Sciences, Materials Engineering – T 008),

Dissertation Defense Panel:
Chairman – **Assoc. Prof. Dr. Renata Butkutė (**Vilnius University, Technological Sciences, Materials Engineering – T 008**);**
Members:
Prof. Dr. Vincas Tamošiūnas (Vilnius University, Technological Sciences, Materials Engineering – T 008),
Prof. Habil. Dr. Sigitas Tamulevičius (Kaunas University of Technology, Technological Sciences, Materials Engineering – T 008),
Prof. Habil. Dr. Gintaras Valušis (Center for Physical Sciences and Technology, Technological Sciences, Materials Engineering – T 008),
Dr. Pranciškus Vitta (Vilnius University, Technological Sciences, Materials Engineering – T 008).

The dissertation shall be defended at a public meeting of the Dissertation Defense Panel at 2 pm on October 24th, 2019, in the D401 auditorium of the Center for Physical Sciences and Technology. Address: Saulėtekio av. 3, Vilnius, Lithuania, tel. +37052648884; e-mail: office@ftmc.lt.

The text of this dissertation can be accessed at the libraries of Vilnius University and the Center for Physical Sciences and Technology, as well as on the website of Vilnius University: www.vu.lt/lt/naujienos/ivykiu-kalendorius.

VILNIAUS UNIVERSITETAS
FIZINIŲ IR TECHNOLOGIJOS MOKSLŲ CENTRAS

Kazimieras
NOMEIKA

Nauji būdai kvantinio našumo pagerinimui InGaN šviestukų aktyviojoje srityje valdant krūvininkų difuziją

DAKTARO DISERTACIJA

Technologijos mokslai,
Medžiagų inžinerija T 008

VILNIUS 2019

Disertacija rengta 2014 – 2018 metais Vilniaus universiteto Fotonikos ir nanotechnologijų institute.
Mokslinius tyrimus rėmė Lietuvos mokslo taryba (stipendijos už akademinius pasiekimus DOK-16421 ir DOK-17351).

Mokslinis vadovas:
doc. dr. Ramūnas Aleksiejūnas (Vilniaus universitetas, technologijos mokslai, medžiagų inžinerija – T 008).

Gynimo taryba:
Pirmininkė – **doc. dr. Renata Butkutė** (Vilniaus universitetas, technologijos mokslai, medžiagų inžinerija – T 008).
Nariai:
prof. dr. Vincas Tamošiūnas (Vilniaus universitetas, technologijos mokslai, medžiagų inžinerija – T 008),
prof. habil. dr. Sigitas Tamulevičius (Kauno technologijos universitetas, technologijos mokslai, medžiagų inžinerija – T 008),
prof. habil. dr. Gintaras Valušis (Fizinių ir technologijos mokslų centras, technologijos mokslai, medžiagų inžinerija – T 008),
dr. Pranciškus Vitta (Vilniaus universitetas, technologijos mokslai, medžiagų inžinerija – T 008).

Disertacija ginama viešame Gynimo tarybos posėdyje 2019 m. spalio mėn. 24 d. 14 val. Nacionalinio fizinių ir technologijos mokslų centro D401 auditorijoje. Adresas: Saulėtekio al. 3, Vilnius, Lietuva, tel. +37052648884; el. paštas office@ftmc.lt.

Disertaciją galima peržiūrėti Vilniaus universiteto ir Fizinių ir technologijos mokslų centro bibliotekose ir Vilniaus universiteto interneto svetainėje adresu: https://www.vu.lt/naujienos/ivykiu-kalendorius

ACKNOWLEDGEMENT

I would like to sincerely thank the following people:

My academic supervisor Dr. Ramūnas Aleksiejūnas for supervising my work and sharing his knowledge with me;

My dear colleagues Žydrūnas Podlipskas and Dr. Saulius Nargelas for helping me with the experimental work;

Prof. Kęstutis Jarašiūnas for fruitful discussions and efforts to introduce me to the scientific community;

Justė Kudzytė for helping out with the formal part of doctoral studies;

My teachers by whom I was educated by, especially my physics teacher Algimantas Adomėnas and my English teacher Rima Simonaitienė;

My colleagues Paulius Baronas for some of the TRPL measurements with a streak camera, and Dr. Ignas Reklaitis for etching of the samples;

Dr. Andrius Petrulis, Dr. Akvilė Zabiliūtė, and Dr. Roland Tomašiūnas for the help with spectrometer calibration;

My beloved wife Aistė for her endless patience and support;

My mother Rasa, brother Algirdas, sister Augustė, and grandmother Darija for encouragement and support;

All the other people that one way or another contributed to the writing of this thesis.

In loving memory of my dear father Algirdas, who inspired me to take up doctoral studies.

LIST OF ABBREVIATIONS / SANTRUMPŲ SĄRAŠAS

AFM	atomic force microscope
AlGaInN	aluminum gallium indium nitride
AlGaInP	aluminum gallium indium phosphide
AlGaN	aluminum gallium nitride
CB	conduction band
CCD	charge coupled device
DAP	donor-acceptor pair
DOS	density of states
DT	differential transmission
EBL	electron blocking layer
EL	electroluminescence
ELO	epitaxial lateral overgrowth
FCA	free carrier absorption
FWHM	full width at half maximum
GaAsP	gallium arsenide phosphide
GaN	gallium nitride
GaP	gallium phosphide
HEMT	high electron mobility transistor
InGaN	indium gallium nitride
InN	indium nitride
IQE	internal quantum efficiency
LD	laser diode
LED	light emitting diode
LITG	light induced transient gratings
LO	longitudinal optical
MBE	molecular beam epitaxy
MOCVD	metalorganic chemical vapor deposition
MQW	multiple quantum wells
NH_3	ammonia
NRC	non-radiative recombination center
OPA	optical parametric amplifier
PL	photoluminescence
QB	quantum barrier
QCSE	quantum-confined Stark effect
QW	quantum well
RIE	reactive ion etching

RT	room temperature
SEI	staircase electron injector
SHGC	second harmonic generation crystal
SRH	Shockley-Read-Hall
STEM	scanning transmission electron microscope
TD	threading dislocation
TEM	transmission electron microscope
TIPL	time-integrated photoluminescence
TMAl	trimethylaluminum
TMGa	trimethylgallium
TMIn	trimethylindium
TRPL	time-resolved photoluminescence
u-GaN	undoped gallium nitride
UV	ultraviolet
VB	valence band
XRD	x-ray diffraction
YAG:Ce^{3+}	cerium-doped yttrium aluminum garnet

AlGaN	aliuminio galio nitridas
FL	fotoliuminescencija
GaAsP	galio arsenido fosfidas
GaN	galio nitridas
GaP	galio fosfidas
InGaN	indžio galio nitridas
InN	indžio nitridas
YAG:Ce^{3+}	ceriu legiruotas itrio aliuminio granatas
KB	kvantinis barjeras
KD	kvantinė duobė
LD	lazerinis diodas
LIFL	laike integruota fotoliuminescencija
LSFL	laikinės skyros fotoliuminescencija
NRC	nespindulinės rekombinacijos centras
SG	supergardelė
ŠIDDG	šviesa indukuotos dinaminės difrakcinės gardelės
SLK	sugertis laisvaisiais krūvininkais
SP	skirtuminis pralaidumas
TMGa	trimetilgalis
TMIn	trimetilindis
VKN	vidinis kvantinis našumas

CONTENTS / TURINYS

INTRODUCTION

Light technologies play a very important role in our everyday life: general lighting, indicators on various electronic devices, remote controls, blue, red, and infrared lasers in the corresponding BLU-RAY, DVD, and CD drives, various sensors, displays, automotive lighting and so on. Most of these technologies are well developed, however it took more than a hundred years and several technological breakthroughs to get to the current state. Not surprisingly, to this day the researchers and developers are still pushing the limits to pursue better efficiency and quality in light technologies, which is particularly driven by environmental and power usage concerns.

Since the application of the Thomas Edison's patent in 1879, incandescent light bulbs were one of the main lighting sources, which although are cheap, but very inefficient, with less than 5% of electrical power being converted to light and only up to 19 lm/W luminous efficacy. Nowadays the market share for incandescent light bulbs (including halogen lamps) has dropped drastically, with many countries already prohibiting their use in general lighting (a.k.a. phase-out of incandescent light bulbs [1]). This is perfectly understandable with much better alternatives present.

One of them is fluorescent light sources, developed in 1938. With wall-plug efficiencies reaching 40% (and more) and typically having 60 lm/W, they come as very attractive, especially when used in commercial areas, such as shopping malls and offices. However certain limitations apply, with one of the main being the fact that an ultraviolet light conversion in the fluorescent coating has to take place, where photons with ~5.5 eV energies are converted to ~2.5 eV photons that correspond to visible light. This Stokes shift means that only up to 45% of UV energy can be used with the rest being dissipated as heat [2]. Further losses in modern lamps are introduced via a smaller than 90% quantum efficiency of conversion in the fluorescent coating. In addition to this, the higher initial cost if compared to incandescent lamps (higher complexity and more electrical components are needed), faster aging due to frequent switching, warm up time, health and safety concerns due to mercury gas, disposal and dimming issues, prevent this technology from standing out as superb.

In terms of luminous efficacy, sodium-vapor lamps (developed in 1965) surpass the above mentioned light sources by having up to 200 lm/W. Although they are among the most efficient light sources, the emitted narrow

spectrum which is near the peak sensitivity to human eye (555 nm [3]) gives poor color rendering indexes (CRI), meaning that colors of objects appear different from those when illuminated by natural light. Therefore this lighting technology is mainly used for outdoors (e.g. street lighting), where the best visibility at the lowest cost is the main priority.

This is where the solid state lighting technology steps in, with the first red light emitting diode (LED) developed in 1962 by Nick Holonyak. With no strict theoretical limitations to reach nearly 100% internal quantum efficiency, ease of exceeding 100 lm/W [4] (LED maker Cree has even managed to reach 303 lm/W at room temperature in 2014 [5]) and far less issues if compared to other lighting sources, LEDs possess a high potential to take over the market. With red, yellow and green LEDs made from semiconductor materials such as GaAsP, AlGaInP, and blue, green, and yellow LEDs from InGaN, the entire visible spectrum can be covered, providing broad possibilities: general or automotive lighting, color displays for TVs and smart phones, projectors, light sources with adaptive spectra for optimal color rendition [6] or plant growth, etc. The global LED lighting market was estimated to be worth nearly 30 billion USD in 2016, with forecasts to double by the year 2022 [7,8].

The main material for blue light emission – InGaN – is currently under intensive studies conducted by many researchers from all over the world. Not only it is efficient and widely used for blue, green and white (by using light conversion in phosphors, such as yellow YAG:Ce^{3+}) LEDs, with bandgap engineering it can theoretically cover the whole visible spectrum all by itself. The latter can be achieved with varying the ratio between InN and GaN in the compound. However, compounds with high InN molar fractions for green emitters possess low structural quality due to defect formation and have high internal electric fields, which together result in relatively poor internal quantum efficiencies (IQEs, ~30% if compared to up to ~90% in blue emitters [9]), which are even worse when going further into the red spectral part. In the meantime, in AlGaInP system the increase in the defect density is accompanied with a transition from a direct bandgap to indirect when aluminum content increases and peak wavelengths change from red to green and beyond [10,11]. Combination of these efficiency declines results in the emission wavelength range (~550-600 nm) where IQEs of LEDs are so low that it is hard to compete even with incandescent light bulbs, which is the effect known as the “green gap”.

It is apparent that filling of the “green gap” is essential, and not only in terms of power saving. It could unlock a full potential of solid state lighting,

which can only be exploited by color mixing approaches without phosphor-based conversion [12]. Furthermore, it would allow manufacturing of LED displays, just like in the OLED (organic LED) display technology, where much higher contrast ratio and color saturation are achieved if compared to the now market-dominating LCD (liquid crystal display) technology, where such limitations arise from the back-light filtering nature. Meanwhile, OLED displays are expensive and their organic-based pixels decay over time – here LED-pixel displays could be very competitive. Costs and complexity could be cut down if formation of red, green and blue emitters could be achieved by using a single material system, overcoming the difficulties related to the integration of different materials together. So far, InGaN seems to be the best candidate for overcoming the "green gap", and a lot of effort is put into the search for the ways to improve the material quality.

Unfortunately, there is another issue with InGaN based devices, the so called droop effect – decrease of efficiency at high current densities. It becomes very important when talking about high-power light sources – either the efficiency has to be sacrificed while driving them at high currents, or multiple chips, operating at lower currents, have to be used to achieve high photon fluxes, drastically increasing the complexity and the cost of the device. Mitigating the droop effect is a serious concern, however only multiple theories exist regarding the cause for it, with Auger recombination currently leading the way [13], but there are still no clear solutions on how to overcome it.

It is obvious that finding the ways to deal with the "green gap" and efficiency droop is necessary to exploit the full potential of solid state lighting and advance the light technologies further. This process is currently facing a sort of stagnation, with the occurrence of mainly slight improvements throughout the last decade. Thus the search for other innovative approaches to increase the efficiency may be worth the consideration. Either way, the full knowledge of the processes that occur in InGaN LEDs during the light emission is needed.

Main goal

The main goal of this work is to get a better understanding of radiative and non-radiative recombination processes in InGaN quantum structures and to define the structural and/or material properties that influence them the most by using the complementary non-destructive optical pump-probe techniques.

The gathered results are intended to be used for the optimization of an LED active region for the maximum quantum efficiency and for a better understanding of the droop effect nature.

Objectives

- To evaluate the values of the absolute internal quantum efficiency and the absorption coefficient in the active layers of InGaN QW (quantum well) structures. These values are necessary for distinguishing the most efficient samples and for properly comparing carrier density-dependent processes between them and the least efficient samples.
- To optically investigate the evolution of carrier dynamics in a large set of $In_xGa_{1-x}N$ structures under excitations below and above the onset of the efficiency droop.
- To search for correlations between the structural parameters, material properties, and IQE in the $In_xGa_{1-x}N$ structures.
- To model the carrier density dependent recombination processes in order to gain insights into the possible efficiency droop causes.
- To generalize the obtained results and to suggest the guidelines for the optimization of the active layers of InGaN LEDs.

Scientific novelty and importance

In this work, a lot of attention is given to careful calibration of carrier density in each sample with its own distinct absorption coefficient. This allows a more precise comparison of density-dependent processes in InGaN QWs when compared to the same procedures but with carrier densities calculated by using the average absorption coefficient values from the literature. The latter do not account for the individual properties of the samples.

Room temperature IQEs in QW structures are directly evaluated by measuring absorption and emission in an integrating sphere, with additionally considering the absorption in thick underlying layers. Contrary to the temperature-dependent IQE evaluation, this is a relatively easy technique that does not rely on assumption that at low temperatures the non-radiative channel is fully suppressed.

Finding the optimal InGaN LED active layer design is burdened by a large amount of variables in device fabrication and characterization. A single

parameter that could be used as a guide to perfecting the LED design would ease the process. This concept may be possible with the negative correlation between carrier diffusivity and the quantum efficiency revealed in this work. Because this tendency is seen among a large number of diverse samples, diffusivity is suggested as a universal efficiency limiting parameter. The possibility to reduce the diffusion coefficient by adjusting the well thickness and modifying the growth procedures looks promising for further improvements in InGaN LEDs.

Difficulties in defining the unequivocal cause of the droop effect may lie in the simultaneous occurrence of several mechanisms. Diffusion-driven defect recombination and Auger recombination are both evidenced by measurement and modelling results. However, it is suggested that whichever prevails is determined by localization conditions and the quality of the material, with Auger having the main role in highly efficient samples. This may be the answer for why the standard ABC model does not work for poor quality samples.

Statements presented for defense

- Higher carrier diffusivity in InGaN quantum structures leads to lower peak IQE. This fundamental limitation arises due to the promoted non-radiative recombination of delocalized carriers at the defects, evidenced by a linear decrease of the carrier lifetime with the increasing diffusion coefficient.
- Carrier diffusivity decreases in narrower InGaN quantum wells due to increased potential fluctuations originating from well-width fluctuations. Increased carrier localization reduces the droop onset carrier density and leads to higher peak IQE by limiting carrier ability to reach the non-radiative recombination centers.
- Peak IQE of InGaN quantum structures can be enhanced by limiting carrier diffusivity through an introduction of (i) a superlattice interlayer that reduces carrier delocalization, (ii) an interrupted growth MOCVD regime that improves localization conditions through a better atom distribution, and (iii) temperature ramping right after the QW growth that creates barriers to carrier diffusion.
- The dominant cause of the efficiency droop depends on the structure quality, revealed by the magnitude of the peak IQE value: Auger recombination was found to be the main non-radiative loss mechanism in

higher quality InGaN quantum structures, while carrier delocalization and transport to non-radiative recombination centers was a more important mechanism in lower quality structures. The approximate boundary distinguishing these structures can be drawn at peak IQE ≈ 20%.

Layout of the thesis

This thesis consists of an introduction, a literature review section, an experimental section, a results and discussion section, and conclusions.

Literature review section consists of a review of III-nitride compounds and their associated features, a brief introduction to carrier generation/recombination processes in semiconductors, and an overview of specifics of layered quantum structures.

Experimental section consists of a description of measurement techniques, equipment, samples under study, and procedures of the quantum efficiency and the absorption coefficient evaluation.

In the results and discussion section, Chapters 3.1 and 3.2 reveal the connection between carrier diffusivity and the quantum efficiency, as well as the benefits of the insertion of a superlattice (SL) interlayer in the MQW structure. In Chapter 3.3, diffusivity is presented as the main peak IQE limiting factor which depends on the QW width. In Chapter 3.4, the Stokes shift is discussed in terms of the carrier localization degree and internal electric fields. Chapter 3.5 shows how timing in the interrupted growth metal-organic chemical vapor deposition (MOCVD) regime alters the quality and localization conditions in the active layers of the structures. Chapter 3.6 reveals the reduction of diffusivity in QWs through the introduction of gross well-width fluctuations. The limits of the standard ABC model are discussed in Chapter 3.7, along with peculiarities of the efficiency evolution with increasing carrier density. Chapter 3.8 describes the general guidelines obtained in this thesis to achieve the highest peak IQEs in InGaN QWs.

Author's contribution

Most of the work presented in this thesis was done by the author: measurements, calculations, data analysis, and graphing.

Approbation of the research results

A part of the results presented in this thesis was published in several peer-reviewed scientific journals and presented in national and international scientific conferences.

List of publications directly related to this thesis:

[P1] A. Kadys, T. Malinauskas, M. Dmukauskas, I. Reklaitis, **K. Nomeika**, V. Gudelis, R. Aleksiejūnas, P. Ščajev, S. Nargelas, S. Miasojedovas, K. Jarašiūnas, Photoluminescence features and carrier dynamics in InGaN heterostructures with wide staircase interlayers and differently shaped quantum wells, Lith. J. Phys. 54 (2014) 187–198. doi:10.3952/physics.v54i3.2959.

[P2] R. Aleksiejūnas, **K. Nomeika**, S. Miasojedovas, S. Nargelas, T. Malinauskas, K. Jarašiūnas, Ö. Tuna, M. Heuken, Carrier dynamics in blue and green emitting InGaN MQWs, Phys. Status Solidi. 252 (2015) 977–982. doi:10.1002/pssb.201451583.

[P3] **K. Nomeika**, M. Dmukauskas, R. Aleksiejūnas, P. Ščajev, S. Miasojedovas, A. Kadys, S. Nargelas, K. Jarašiūnas, Enhancement of quantum efficiency in InGaN quantum wells by using superlattice interlayers and pulsed growth, Lith. J. Phys. 55 (2016) 255–263. doi:10.3952/physics.v55i4.3221.

[P4] J. Mickevičius, D. Dobrovolskas, R. Aleksiejūnas, **K. Nomeika**, T. Grinys, A. Kadys, G. Tamulaitis, Influence of growth temperature on carrier localization in InGaN/GaN MQWs with strongly redshifted emission band, J. Cryst. Growth. 459 (2017) 173–177. doi:10.1016/j.jcrysgro.2016.12.008.

[P5] **K. Nomeika**, R. Aleksiejūnas, S. Miasojedovas, R. Tomašiūnas, K. Jarašiūnas, I. Pietzonka, M. Strassburg, H.-J. Lugauer, Impact of carrier localization and diffusion on photoluminescence in highly excited cyan and green InGaN LED structures, J. Lumin. 188 (2017) 301–306. doi:10.1016/j.jlumin.2017.04.055.

Publications not directly related to this thesis:

[N1] R. Aleksiejūnas, Ž. Podlipskas, S. Nargelas, A. Kadys, M. Kolenda, **K. Nomeika**, J. Mickevičius, G. Tamulaitis, Direct Auger recombination and density-dependent hole diffusion in InN, Sci. Rep. 8 (2018) 4621. doi:10.1038/s41598-018-22832-6.

List of conference presentations related to this thesis:

1. **K. Nomeika**, "Spectral characteristics of (In,Ga)N quantum structures with different design and growth parameters", Open Readings 2015, Saulėtekio av. 9, Vilnius, March 24-27, 2015 (**oral session**).
2. **K. Nomeika**, R. Aleksiejūnas, P. Ščajev, S. Miasojedovas, S. Nargelas, M. Dmukauskas, A. Kadys, K. Jarašiūnas, "Impact of pulsed growth and superlattice interlayer to LED quantum efficiency", 41-oji Lietuvos Nacionalinė Fizikos Konferencija (LNFK 41), Konstitucijos av. 14, Vilnius, June 17-19, 2015 (**poster session**).
3. **K. Nomeika**, S. Miasojedovas, S. Nargelas, R. Aleksiejūnas, P. Ščajev, D. Dargis, V. Avrutin, H. Morkoç, Ü. Özgür, K. Jarašiūnas, "Excitation-dependent carrier dynamics in active regions of multiple InGaN double heterostructures", 11th International Conference on Nitride Semiconductors (ICNS-11), Beijing, China, August 30 - September 4, 2015 (oral session).
4. R. Aleksiejūnas, **K. Nomeika**, P. Ščajev, S. Miasojedovas, S. Nargelas, M. Dmukauskas, A. Kadys, K. Jarašiūnas, "Optical study of quantum efficiency in InGaN LED structures with and without short period superlattice", 11th International Conference on Nitride Semiconductors (ICNS-11), Beijing, China, August 30 - September 4, 2015 (poster session).
5. S. Nargelas, A. Kadys, **K. Nomeika**, S. Miasojedovas, P. Ščajev, D. Dmukauskas, R. Aleksiejūnas, K. Jarašiūnas, "Carrier dynamics in InGaN/GaN LED structures grown by pulsed metalorganic chemical vapor deposition", 11th International Conference on Nitride Semiconductors (ICNS-11), Beijing, China, August 30 - September 4, 2015 (poster session).
6. **K. Nomeika**, R. Aleksiejūnas, "Carrier diffusivity as the key parameter behind the quantum efficiency droop in (In,Ga)N quantum structures", Open Readings 2016, Saulėtekio av. 9, Vilnius, March 15-18, 2016 (**oral session**).
7. **K. Nomeika**, Ž. Podlipskas, R. Aleksiejūnas, D. Dargis, P. Ščajev, S. Nargelas, K. Jarašiūnas, „Carrier diffusivity as the key parameter behind the peak quantum efficiency in (In,Ga)N quantum structures", International Workshop on Nitride Semiconductors 2016 (IWN 2016), Orlando, Florida, USA, October 2-7, 2016 (**poster session**).
8. J. Mickevičius, D. Dobrovolskas, R. Aleksiejūnas, **K. Nomeika**, S. Stanionytė, M. Skapas, T. Grinys, A. Kadys, G. Tamulaitis, "Influence of growth temperature on emission properties of InGaN/GaN MQWs deposited on strain-relieving buffer", International Workshop on Nitride

Semiconductors 2016 (IWN 2016), Orlando, Florida, USA, October 2-7, 2016 (poster session).

9. M. Budreckaitė, **K. Nomeika**, R. Aleksiejūnas, "Analysis of InGaN structures using time–resolved spectroscopic techniques", Open Readings 2017, Vilnius, Lithuania, March 14-17, 2017 2016 (poster session).

10. J. Mickevičius, D. Dobrovolskas, M. Kolenda, M. Dmukauskas, T. Grinys, A. Kadys, T. Malinauskas, **K. Nomeika**, R. Aleksiejūnas, G. Tamulaitis, "Krūvininkus lokalizuojančio potencialo InGaN kvantinių duobių dariniuose modifikavimas", 42-oji Lietuvos Nacionalinė Fizikos Konferencija (LNFK 42), Saulėtekio av. 3, Vilnius, Lithuania, October 4-6, 2017 (oral session).

11. K. Gelžinytė, R. Aleksiejūnas, **K. Nomeika**, S. Nargelas, S. Miasojedovas, A. Alkauskas, K. M. Kelchner, L. Kuritzky, S. Nakamura, J. S. Speck, "Study of excess carrier dynamics in homoepitaxial m-plane InGaN quantum well", 42-oji Lietuvos Nacionalinė Fizikos Konferencija (LNFK 42), Saulėtekio av. 3, Vilnius, Lithuania, October 4-6, 2017 (oral session).

12. **K. Nomeika**, M. Budreckaitė, S. Nargelas, A. Kadys, R. Aleksiejūnas, "Impulsiniu MOCVD būdu užaugintų InGaN darinių tyrimas laikinės spektroskopijos metodais", 42-oji Lietuvos Nacionalinė Fizikos Konferencija (LNFK 42), Saulėtekio av. 3, Vilnius, Lithuania, October 4-6, 2017 (**poster session**).

13. **K. Nomeika**, R. Aleksiejūnas, S. Nargelas, K. Jarašiūnas, "Carrier diffusivity-limited peak internal quantum efficiency in InGaN QWs with different widths", 34th International Conference on the Physics of Semiconductors (ICPS-2018), Montpellier, France, July 29 - August 4, 2018 (**poster session**).

14. **K. Nomeika**, S. Nargelas, J. Mickevičius, M. Dmukauskas, A. Kadys, R. Aleksiejūnas, "Influence of metalorganics flow interruption on deposited atom migration in InGaN LED structures", 34th International Conference on the Physics of Semiconductors (ICPS-2018), Montpellier, France, July 29 - August 4, 2018 (**poster session**).

1. LITERATURE REVIEW

1.1. Group III nitrides

1.1.1. III-nitrides and their emergence

The general name III-nitrides stands for the family of direct bandgap compounds, composed of a group V element nitrogen (N) and at least one of the elements of the group III: aluminum (Al), gallium (Ga) or indium (In). Hence the base binary compounds are GaN, InN and AlN, which can form ternary alloys InGaN, AlGaN, InAlN or quaternary alloy InGaAlN. More exotic compounds formed with boron (B) are also possible [14], however they are not very common due to the lack of researches and are not used in the nitride-based LEDs.

Research period of III-nitrides spans to as early as 1971, when the first green LED prototypes based on a metal-insulator-semiconductor junction were demonstrated [15]. Nonetheless only two decades after the real breakthrough of III-nitrides took place. In 1989, I. Akasaki and H. Amano successfully developed p-type doping of the inherently n-type GaN by using Mg as an acceptor impurity and treating the grown layers with low-energy electron beam irradiation (LEEBI) [16]. In 1991, S. Nakamura from Nichia lab demonstrated a significant improvement in GaN quality by introducing an initial low-temperature GaN nucleation (buffer) layer on the substrate, with growth performed in a novel two-flow MOCVD reactor [17]. In 1992, he and others showed an improvement of p-type doping by thermal annealing and explained the mechanism of Mg acceptor passivation [18]. In 1994, blue emitting InGaN/GaN double heterostructures were fabricated [19]. These technological advancements paved the way for the era of the extensive research of III-nitrides, continuing up until now. Their significance is evidenced by the Nobel Prize in physics, given in 2014 to I. Akasaki, H. Amano, and S. Nakamura “for the invention of efficient blue light-emitting diodes, which has enabled bright and energy-saving white light sources” [20].

1.1.2. Crystal structure and main properties

III-nitrides are mainly grown in hexagonal (wurtzite) (Fig. 1.1(a)) or cubic (zinc-blende) (Fig. 1.1(b)) structures. The former are more

thermodynamically stable [21], hence most of the nitride-based devices are in a such form (all the properties presented later will be related to the materials in a wurtzite form). Two lattice constants are used to describe wurtzites: *c*, which is parallel to the [0001] direction and defines its height, and *a*, which is the edge length of a hexagon. A wurtzite crystal can be imagined as two separate interlocking structures of closely-packed cations and anions, shifted along the *c*-axis in the length of $u \approx 3/8c$ [22]. Such a lattice has a tetrahedral geometry with sp3 covalent bonding – each atom is bonded to four atoms of other type, which are located at the vertices of a tetrahedron. This tetrahedron is asymmetrical, with the -N-Ga- bond along the *c*-axis being slightly shorter than the other three, whose bonding angles are smaller than the value of 109.5° for the ideal tetrahedron [23] (Fig. 1.1(a)). Depending on the arrangement of atoms, wurtzites can either be cation-faced ([0001] direction) or anion-faced ([000$\bar{1}$] direction), though the former are more common due do difficulties in growing high-quality MOCVD N-faced GaN base layers. The type of the face defines chemical and mechanical properties of the grown layer [24]. For instance, nitrogen-faced structures have increased stability of InN at higher temperatures, meaning that more In can be incorporated in the InGaN alloy [25]. Meanwhile, a zinc-blende structure is defined by a single lattice constant *a*, which is the edge of a cube (Fig. 1.1(b)). Its lattice is also tetrahedrally coordinated, with atoms symmetrically distributed in the same way as in a diamond, only with alteration of atoms.

GaN is a wide band-gap (3.4 eV), hard material with high heat capacity and thermal conductivity. At room temperature its electron mobility can reach ~440 $cm^2/(V \cdot s)$. The size of a GaN lattice is defined by the following room temperature parameters – a = 3.189 Å and c = 5.185 Å [26]. AlN has a wider bandgap of 6.2 eV, its room temperature lattice parameters are a = 3.112 Å and c = 4.982 Å [26], electron mobility reaches ~300 $cm^2/(V \cdot s)$. InN is a narrow bandgap semiconductor, with a bandgap of 0.7 eV and lattice parameters a = 3.545 Å and c = 5.703 Å. Due to the smallest effective electron mass among the III-nitrides, InN has the highest electron mobility that can exceed 3000 $cm^2/(V \cdot s)$ at room temperature [27].

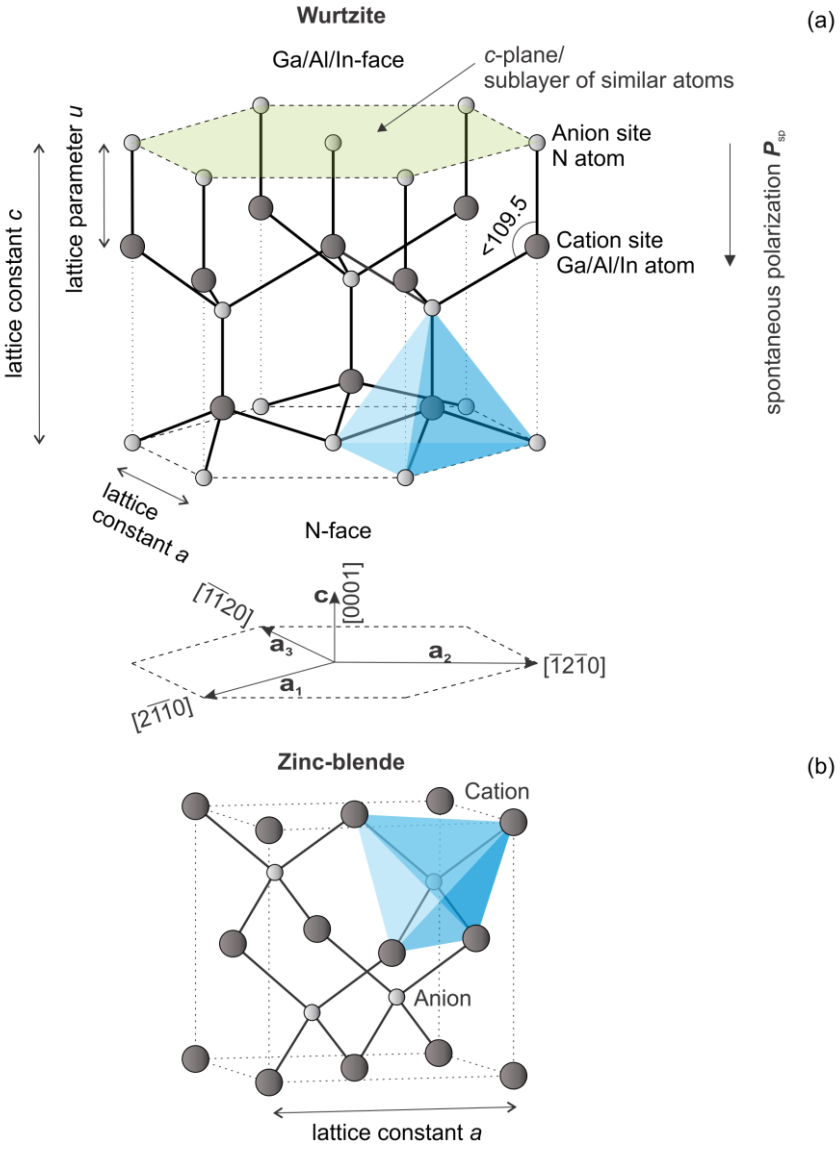

Fig. 1.1. Wurtzite (a) and zinc-blende (b) structures.

The band structure of III-nitrides mainly consists of a single lowest conduction band and three valence bands: light hole (LH), heavy hole (HH) and a split-off (CH) band. The latter forms due to a crystal field inside the semiconductor, while the former two arise from different effective masses of the corresponding holes. Since a larger effective mass also means the higher

density of states (DOS), the properties of III-nitrides are dominated by heavy holes. The band structure of GaN is shown in Fig. 1.2. The parabolic dispersion of energy is only present in the vicinity of the Γ point where the wave vector $k = 0$. Band structures of AlN and InN have many similarities with that of GaN, however there are certain distinctions as well.

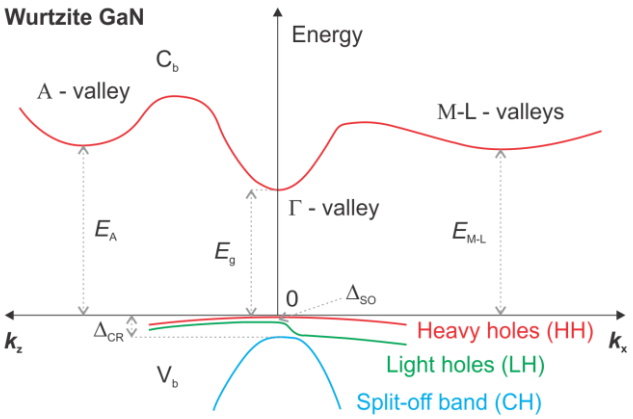

Fig. 1.2. Wurtzite GaN band diagram [28]. The origin of the Δ_{so} energy split is the spin-orbit interaction, while Δ_{cr} originates from the hexagonal crystal field [29].

The combination of III-nitrides opens up a theoretical possibility to synthesize ternary (InGaN, AlGaN, AlnN) or quaternary (AlInGaN) alloys with emission wavelengths continuously changing from 1800 nm (short-wavelength infrared) to 200 nm (deep UV). This can be done by changing the molar ratios between the binary (or ternary) constituents (Fig. 1.3). Since they have different lattice sizes, lattice parameters of the resulting alloys depend on the molar ratio too. The full coverage of the visible spectrum (400-700 nm) makes the III-nitrides very suitable for general lighting and other technologies that encompass the light interaction with the human eye. Other uses of these materials include UV emitters (like laser diodes (LDs)) and solar cells (tandem solar cells especially, where utilization of the infrared solar spectrum part is very important). Beyond the light technologies, wide bandgap III-nitride alloys are suitable for high power devices such as high-electron mobility transistors (HEMTs) due to the advantages associated with a large band gap that include higher breakdown voltages, ability to sustain larger electric fields, lower noise generation, and higher operating temperatures.

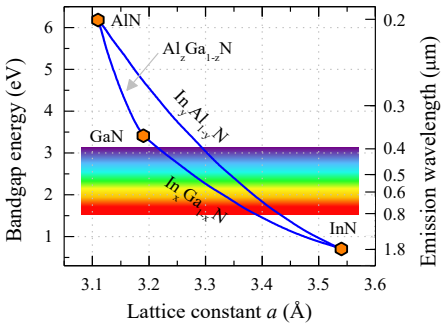

Fig. 1.3. Lattice constants and bandgap energies of the main alloys of the III–nitride family: InN, GaN and AlN. The connecting lines correspond to ternary alloys with different compositions. The curvature can be described by the bowing parameter in Vegard's law.

1.1.3. Growth, doping, and associated challenges

III-nitrides are mainly grown by two techniques: molecular beam epitaxy (MBE) and metal-organic chemical vapor deposition (MOCVD). The former is known to provide better structural quality and is more precise, however growth times in MBE reactors are considerably longer along with the higher cost of the process. Therefore it is mainly used for synthesizing materials for laboratory experiments where outstanding quality and very precise layer thicknesses are needed, while MOCVD reactors lead the field in both laboratory and commercial use.

The common substrates with a hexagonal structure used for growth of nitride-based devices are sapphire (α-Al_2O_3, a = 4.759 Å, c = 12.991 Å, [30]), 6H-SiC (a = 3.08 Å, c = 15.12 Å), ZnO (a = 3.252 Å, c = 5.213 Å), or GaN itself. The latter is the best option in terms of lattice parameters, however its high price and relatively small available wafer sizes prevent it from being the mostly used one. Sapphire, on the contrary, has the largest mismatch (with respect to GaN) of lattice (+33%) and thermal expansion coefficient (-34%) [31,32]. Despite these drawbacks and its poor thermal conductivity, sapphire's lowest price, larger wafer diameters (two inches standard with several times larger sizes available), and high availability make it the mostly used substrate in fabricating the nitride-based devices. Furthermore, the extremely large lattice mismatch is reduced (to ~14%) when the grown layer cell rotates 30° around the c-axis with respect to the sapphire cell [33]. In an attempt to reduce costs, Si substrates have also been used to grow GaN [34] – they are cheap, with large diameters exceeding 150 mm, and are compatible with existing process lines commonly used in the electronics industry. Unfortunately, this method has issues with high dislocation densities and Si wafer cracking due

to mismatches of lattice parameters (17%) and thermal expansion coefficients (+100%). Researches in this field regarding the stress control are being carried out [35].

For n-type conductivity, the main dopant of III-nitrides is silicon (Si), which creates an energy level ~20 meV below the conduction band. Oxygen (O) with ~35 meV level [36] can also be used, however it can be an undesirable and uncontrollable dopant, if present in growth reactors as a background material or if it diffuses out of a sapphire substrate. Thermal energy k_BT (k_B – the Boltzmann constant) at room temperature is around 25 meV, therefore most of the donors are generally activated in the n-type material. For p-type doping magnesium (Mg) is used, which in GaN creates a deep energy level, ~170 meV above the valence band [37]. At room temperature, only ~2% of acceptors are thermally activated, therefore high concentrations of Mg atoms for sufficient p-type conductivity are needed (~10^{20} cm^{-3} acceptor concentration for ~10^{18} cm^{-3} hole concentration), for which the quality of the alloy significantly deteriorates. This is the main reason why in InGaN LED structures p-type contact layers are grown last – this way structural quality of other layers is maintained. Another issue with Mg is that it can form complexes with hydrogen (H) atoms, produced by NH_3 (ammonia) dissociation during growth by MOCVD, making acceptors electrically inactive. Luckily, this can be overcome with thermal annealing at the N_2 ambient atmosphere, which breaks these complexes apart [18].

One of the most important parameters in growing III-nitride layers is the growth temperature, as the structural quality and bandgap heavily depend on it. For GaN layers, the growth temperature is usually higher than 1000 °C [38,39], with around 1050 °C being the optimal one [40], whereas for InGaN layers it is usually around 800 °C or lower provided that higher In content is intended [P4]. This is because the maximum growth temperature for In-polarity InN should be about 500 °C [27] as the growth rate falls at higher temperatures due to the low InN dissociation temperature (550 °C) and desorption of In atoms from the surface. For the same reason GaN barriers in QW structures have to be grown at lower than optimal temperatures to maintain high indium content in the wells [41]. On the other hand, the dissociation rate of NH_3 is reduced at lower temperatures [42,43], resulting in the formation of nitrogen vacancies due to deficiency of its atomic species when growing GaN or InGaN [44,45]. Therefore growth temperatures have to be carefully selected to obtain high quality layers with a designated In content.

In MOCVD, the main precursors used for the growth of III-nitrides are trimethylindium (TMIn), trimethylgallium (TMGa), trimethylaluminum (TMAl), and ammonia, while doping is performed with bis(cyclopentadienyl)magnesium (Cp_2Mg), silane (SiH_4), or nitrogen oxide (N_2O). The ratio between ammonia and precursors constituting group III elements (V/III ratio) in the growth chamber is usually kept much higher than the stoichiometric one due to limited decomposition of NH_3 and the nitrogen's tendency to desorb from the surface. It was shown that higher V/III ratio can reduce the formation of crystalline donor-type defects that are related to nitrogen vacancies [46,47]. As for the ratios between the group III elements, they are chosen according to the designated In content in the layers – an increased partial pressure of TMIn allows higher incorporation of the indium content [48], however at the same time the process heavily depends on the growth temperature.

A huge challenge in growing $In_xGa_{1-x}N$ layers with a uniformly distributed high indium content is its limited miscibility in GaN. It can be induced by spinodal decomposition, a mechanism due to which compounds with In contents $x > 10\%$ may experience the phase separation, leading to the coexistence of two phases – indium rich and indium poor [49,50]. For a given growth temperature, $In_xGa_{1-x}N$ has a region of solid immiscibility, and for alloys having compositions in this region, there is no energy barrier for the phase separation to occur. Another cause can be the "compositional pulling" effect – strain decreases the incorporation of a larger diameter In atoms into the GaN matrix to reduce the deformation potential that arises from the lattice mismatch between the grown and the underlying layer [51,52]. In other words, the composition (x) of the grown layer is pulled towards the one that gives the lattice matching between the two layers, hence the name [53]. Therefore, as the layer gets thicker and strain relaxes, more In can be incorporated, which might result in a compositional gradient along the growth direction [25,50,54]. According to a theoretical study conducted by Inatomi et al., a compressive biaxial strain hinders the incorporation of In atoms, while a tensile biaxial strain promotes it [51]. This is because the In-N bond, which is longer than the Ga-N bond, relaxes the tensile strain, which is energetically favorable. This suggests that a substrate with a larger lattice constant might enable the growth of a layer with a higher In concentration, provided that the mismatch is not too high and the formation of dislocations is not induced. Another natural process that hinders the uniform incorporation of In is its segregation, which can be both vertical and lateral. Vertical segregation takes place due to

different energies required for occupation of surface sites with more favorable conditions being for Ga atoms [55]. Lateral segregation of In atoms can be attributed to the more stable In–In bonds rather than the In–Ga bonds.

Growth of III-nitrides is associated with the abundance of defects. The most elementary are point defects such as vacancies, when anions or cations are missing from their designated sites and dangling bonds form [56], interstitial and antisite atoms, which occupy the lattice sites not designated for them, or unintended impurities (C, O). For vacancies, a missing nitrogen atom creates a shallow level below the conduction band, while gallium creates a deep level above the valence band [46,47]. Another type of defects is planar, such as crystal surfaces and boundaries between the layers. However, nearly the most important type is the linear defects – threading dislocations (TDs), which are practically unavoidable when the lattice unmatched substrates are used. They originate at the interface of the substrate and the grown layer and thread through the latter (usually parallel to the *c*-axis) to the surface, where they often end up in V-pits having the hexahedron cone morphology [50,57]. Threading dislocations fall into three categories: edge, screw, and mixed type (having both screw and edge components). Their typical densities are in the range from 10^7 to 10^9 cm^{-2} [58–60], which significantly degrades the electronic properties of the layers. One of the ways to reduce them is the epitaxial lateral overgrowth (ELOG) technique. In it, parts masked with SiO_2 block the propagation of TDs that originate from the underlying GaN/sapphire interface [59,61,62] into the regrown layer. Growth of the new layer above the SiO_2 mask takes place both vertically and laterally, hence the name ELOG. The ELOG technique can also be realized without masking the templates but by simply etching them, however this may provide smaller improvements [63]. Another way to reduce TDs is to use the patterned sapphire substrates (PSS) [64–67]. In it, the lateral growth takes place too, however, this is achieved with only one MOCVD growth, if compared to two growths necessary for the ELOG technique. Usage of PSS can also improve light extraction [68].

III-nitrides are usually grown along the [0001] direction, which results in their surface being the *c*-plane. However, strong internal electric fields form in this direction, with typical values of 0.5-2 MV/cm in InGaN with In contents in the range of 10-20% [58,69]. To reduce their impact another growth directions can be exploited. The resulting planes are called non-polar or semi-polar. The examples of the former are the m-plane, grown along the $[1\bar{1}00]$ direction, and a-plane, grown along the $[\bar{1}2\bar{1}0]$ direction (Fig. 1.4).

Vectors of internal electric fields are parallel to the *c*-axis, which is perpendicular to the growth direction in non-polar layers, hence electrons and holes are not pushed to the different sides of the QWs (Chapter 1.3.2). An example of a semi-polar plane is the r-plane, grown along the $[10\bar{1}2]$ direction. This arrangement results in the partial reduction of internal electric fields perpendicular to QW layers. However, quality non- or semi-polar plane structures are difficult to grow, with one of the reasons being the lack of suitable high quality substrates. Therefore although they look promising, they are still far from reaching the IQEs of polar structures.

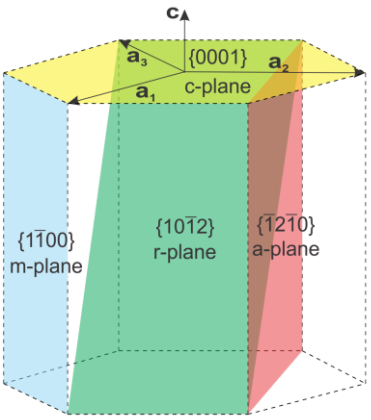

Fig. 1.4. Crystal planes in a wurtzite crystal. $\{0001\}$ is a polar c-plane, $\{1\bar{1}00\}$ – non-polar m-plane, $\{\bar{1}2\bar{1}0\}$ – non-polar a-plane, $\{10\bar{1}2\}$ – semi-polar r-plane.

1.1.4. Spontaneous and piezoelectric polarizations

The lack of inversion symmetry in a wurtzite crystal along with different cation and anion electronegativities (tendencies of atoms to attract the bonding pairs of electrons) results in the internal electric field, which is an effect known as the spontaneous polarization. In the case of GaN, electronegativity of nitrogen (3.0) is significantly higher than that of gallium (1.6), meaning that the bond between these two atoms is partially ionic, with electrons shifted more towards nitrogen, resulting in a dipole moment pointing from nitrogen to gallium. Because the tetrahedral coordination of a wurtzite is not ideal, electrical dipoles are not cancelled out along the *c*-axis due to unequal projections of nearby -N-Ga- and -Ga-N- bonds on it, with the center of a negative charge shifted more towards the $[0001]$ direction in the tetrahedron than the center of a positive charge [23] (Fig. 1.1(a)). In the meantime, perpendicular to the *c*-axis lie sublayers of the same type evenly distributed

atoms, and on a macroscopic scale, the projections of -N-Ga- bonds on these sublayers are compensated, which results in a zero net dipole moment.

In the presence of a wurtzite crystal deformation, an internal electric field can be generated by another type of polarization, which is piezoelectric. During the tensile stress along the *c*-axis (compressive along *a*-axis), the three bonds which are not parallel to it are tilted away from the parallel bond, increasing their projections on the *c*-axis. This results in higher compensation (or even overcompensation) of a net dipole moment, hence in this case the piezoelectric polarization has an opposite direction to the spontaneous polarization. The most common origin of such deformation is a mismatch of lattice constants, when the underlying layer has smaller lattice constants than a grown layer (for example InGaN on GaN). If a compressive stress along the *c*-axis (tensile along the *a*-axis) is applied, the three bonds that are not parallel to it are tilted towards the parallel bond. This gives lower compensation of a net dipole moment and the piezoelectric polarization has the same direction as the spontaneous polarization. This can happen when the underlying layer has larger lattice constants than a grown layer (for example AlGaN on GaN, or GaN on a sapphire substrate).

The total polarization field (P) from spontaneous and piezoelectric polarizations induces the electrostatic charge density, the sign of which depends on the polarization direction (pointing from the negative charge to the positive charge, as opposed to the electric field vector). It causes the rearrangement of surface charges in a bulk material, where it is assumed that they screen the spatially uniform polarization field. In heterostructures, however, variations in composition create non-vanishing internal spontaneous (P_{sp}) and piezoelectric polarization (P_{pe}) fields. The associated charge densities form at the abrupt heterojunction interfaces due to the differences in spontaneous polarization between the two heterojunction constituents and an abrupt change in the strain that gives rise to discontinuity in piezoelectric polarization [70]. The sheet charge density at the interface of a top and a bottom layer can be defined by [71]:

$$\sigma = P_{top} - P_{bottom} = \left(P_{sp\_top} + P_{pe\_top}\right) - \left(P_{sp\_bottom} + P_{pe\_bottom}\right). \quad (1.1)$$

If the polarization induced sheet charge density is positive ($\sigma > 0$), free electrons will tend to compensate it by accumulating at the interface. The negative sheet charge density ($\sigma < 0$) will cause the accumulation of free holes at the interface.

1.1.5. Carrier localization

Localization plays a very important role in nitride-based devices. It prohibits the charger carriers from reaching a vast amount of dislocations and defects which act as non-radiative recombination centers (NRCs) [59,72] (Fig. 1.5). Typical dislocation densities of 10^7 – 10^9 cm^{-2} are considered way too extreme for other material based devices. For example, the limit for operation of AlGaInP-based LEDs is exceeded by more than 4 orders of magnitude [59]. There are several localization origins in InGaN QWs which can be divided into two sections: compositional and structural variations.

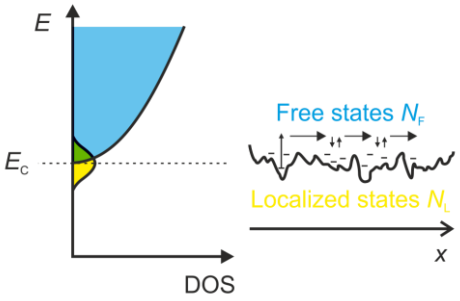

Fig. 1.5. Density of localized states at the bottom of the conduction band of a bulk semiconductor. Electrons have to hop between the localized states, which significantly limits their movement and prevents them from reaching the defect states.

In the case of compositional variations, the smallest of them is a random alloy disorder, where In, Ga, or Al atoms occupy cation sites randomly (Fig. 1.1(a)). It occurs on the scale of a unit cell and is unavoidable. Density functional theory (DFT) calculations in InGaN showed that two indium atoms sharing the same nitrogen atom decrease the band gap energy by 8 meV, while three and four atoms that share the same nitrogen atom decrease the band gap energy by 18 meV and 29 meV, correspondingly [57,73]. Typically, density of localized states due to the random alloy disorder decreases with their depth with exponential or Gaussian distribution [74] (Fig. 1.5). Random alloy fluctuations are of a bigger scale (> 1nm), and they stand for average local composition variations, which stem from the large difference in the bandgaps of the InGaN alloy constituents (InN and GaN) – even the slight variations in the average composition can lead to potential fluctuations of tens of meV in the valence band [75]. Another cause of localization might be the cation segregation, which can basically be seen as the formation of In clusters or even quantum dots [76,77]. It was believed to be one of the main causes of strong localization in the early days of researches. However the picture changed after

finding out that the strain contrast seen in TEM (transmission electron microscope) images increased with longer exposure to the electron beam. The observed artifacts that were initially ascribed to In clusters were then attributed the electron beam damage [78,79]. Randomly distributed dopants also lead to unavoidable fluctuations of the doping concentration on a macroscopic scale, which act as potential fluctuations [38].

Speaking of structural variations, localization can be a consequence of well width fluctuations. Due to the quantum confinement (more details in Chapter 1.3.1), both electron and hole energies are shifted up in QWs with respect to the bulk material. The magnitude of this shift depends on the width of the well – a narrower well means a higher energy. Hence width variations along the planes of the QWs give different potential energies. In addition to this, the influence of large piezoelectric fields also changes with the well width due to variations in local strain. Taking everything into account, Graham et al. calculated that the smallest possible variation of one monolayer (~0.26 nm) in a 3.3 nm well with 25% In content can result in the difference of 58 meV [80], which significantly exceeds the room temperature $k_B T$ energy. The fact that monoatomic variations in the quantum well thickness can result in carrier localization even at room temperature was also shown in [81].

The potential landscape can also be shaped by the crystal lattice defects. For example, a threading dislocation that ends up in a V-pit at the surface of a multilayered quantum structure can create a potential barrier around itself [60]. This is because the QWs that grow on the inclined walls of V-pits (that coincide with the semipolar $\{1\bar{1}01\}$ plane) have narrower widths than the QWs that grow on the c-plane due to a slower growth rate [82,83]. Again, thinner QWs result in a higher local potential, which acts as a barrier that prevents the charge carriers from reaching the dislocation core. Inclined planes also have lower In incorporation rate, increasing the potential barrier further [84]. Even more, In tends to accumulate in the region surrounding V-pits [25]. It should be noted that dislocations also cause distortion to the crystal lattice that leads to variations in the local strain and internal electric fields, which also shape the potential landscape. Lattice distortion can also be induced by point defects, for example if a substitutional atom has a larger radius than the intended one. As for the Coulomb interaction, a negatively (positively) charged defect site will repel electrons (holes), creating a potential barrier. This applies to both point defects and extended defects.

Localization mechanisms are believed to have different impacts on different carriers – while holes are mainly localized in In-N chains, electron movement is mainly restricted due to the potential minima caused by QW width fluctuations [73,80,85–87]. Along with much stronger localization for holes due to their larger effective mass [88–90], this translates into separate localization lengths being 1-3 nm for holes and 5-10 nm for electrons [86,91,92]. Furthermore, in QWs carriers are separated by the internal electric fields, meaning that localization takes place in different atomic planes, where random distributions of In atoms are likely to differ [93]. Therefore, strong independence of hole and electron localization in quantum structures is expected.

1.1.6. Green gap

Tuning of the bandgap of InGaN quantum structures is a very appealing ability, enabling fabrication of LEDs in the green or even in the red spectral part. This so called bandgap engineering is mainly performed in two ways: by changing the amount of indium in the compound [P2], or by changing the width of the QWs. However, longer peak emission wavelengths generally result in lower peak IQEs. On one hand, increasing the In content results in the formation of more structural defects, such as strain-relieving misfit dislocations [94], indium or, particularly, nitrogen vacancies, leading to higher non-radiative losses. Furthermore, larger lattice mismatch increases strain and stronger piezoelectric fields that separate the charge carriers build up. On the other hand – widening the QWs increases the separation distance between holes and electrons due to internal electric fields, which decreases the oscillator strength and diminishes the radiative recombination probability [95]. It has been shown that the radiative rate of carriers is proportional to the wave-function overlap squared [96], making it a very sensitive dependence. Stronger uncorrelated lateral localization of electrons and holes in QWs when In content is higher [93] decreases the overlap even more. Therefore, green InGaN emitters have relatively poor IQEs. In this work they do not exceed more than 20% in samples with longer than 500 nm peak emission wavelengths, and drop to less than 1% in the 560-580 nm range (Fig. 1.6(a)).

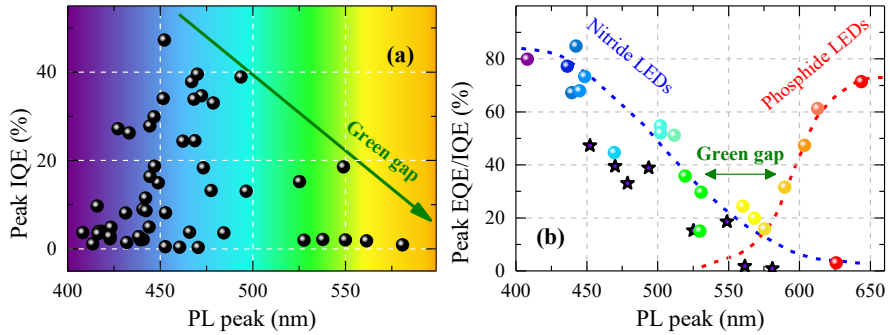

Fig. 1.6. Peak IQE vs the PL peak position in samples from this work (a). Maximum external quantum efficiency (EQE) of different commercial nitride and phosphide LEDs, illustrating the "green gap" problem (colored spheres, with data taken from [97,98]) (b). Stars represent the peak IQE values of several samples from this work. The lines are guides to the eye. Image adapted from [93].

Phosphide-based LEDs also show poor IQEs in the green spectral region. For GaAsP, its constituent GaP is an indirect bandgap (2.26 eV – 549 nm) semiconductor, which makes the ternary alloy indirect too when the composition is changed to shift the emission wavelength from the red spectral part to green [99]. A similar situation is observed in AlGaInP system when the Al content is high [10]. The transition from a direct to an indirect bandgap greatly decreases the radiative recombination probability, which can be additionally quenched by an increase in the density of defects.

Combining the nitride- and phosphide-based emission wavelength dependencies of IQE results in its overall severe drop in the 500-600 nm spectral range, which is known as the "green gap" [93,95,100] (Fig. 1.6(a) and (b)). Closing this gap is of great importance in order to achieve the full potential of solid state lighting. In the case of InGaN, one of the main tasks is to tackle the low quality issue in high In concentration alloys used in LEDs. This could be done by a better lattice matching of different layers, for example, by using a quaternary AlGaInN alloy, with growth of the entire structure performed on a lattice-matched GaN substrate. Such substrates, however, are too expensive at this time to offer a final device at a competitive price. The other way around is to exploit the localization effect – even in a highly defective material, strong carrier localization may provide sufficiently high potential barriers to prevent carrier diffusion to defects. As for the reduction of the impact of internal electric fields, no options have yet proven to be very promising: structures grown along the non-polar directions have

low IQEs, if compared to the polar one, and any attempts to compensate the internal electric fields in QWs by high dopant concentrations [101] usually end up in very high defect densities.

1.1.7. Efficiency droop

The efficiency droop is a detrimental effect, observed as a decline of efficiency at high non-equilibrium charge carrier densities, and is common to all alloys in the family of III-nitrides [102–105]. A typical efficiency curve consists of an initial rise, a droop onset corresponding the peak IQE value, and a following decline with increasing the carrier density (Fig. 1.7(a)). In an ideal case, the efficiency of an LED should rise and reach a constant value (Fig. 1.7(b)). This phenomenon is the main obstacle hindering the usage of LEDs in high-power light sources, therefore it has a considerable interest among the scientists working in the field of nitrides. However to this day there are multiple theories as to the cause of the droop effect, with none of them being definite.

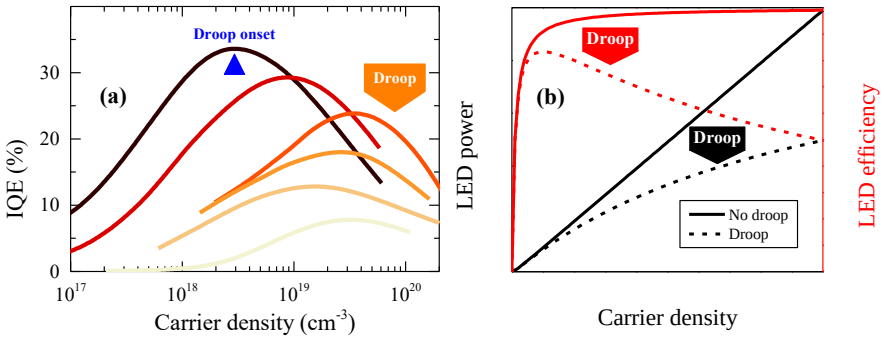

Fig. 1.7. (a) Measured IQE vs carrier density curves of several InGaN MQW samples from this work. (b) Illustration of LED power and efficiency curves without (solid lines) and with (dashed lines) the efficiency droop (adapted from [102]). Note that (a) has a semi log scale, while in (b) the scale is linear.

Auger recombination is by far the most debated droop mechanism. It was first mentioned in the work by Shen et al. in 2007 [106], and was first claimed to have been identified as the main cause by an experimental study in 2013 [107] via observation of high energy electron emission from the sample surface [108]. Due to the threshold energy implied by the energy and momentum conservation, the process is believed to be mainly indirect [109]

(read more in Chapter 1.2.2) with an exception for certain In concentrations where a resonance between the lowest and the adjacent conduction bands may take place [110,111]. This is supported by calculations that show bulk InGaN direct Auger recombination coefficient C values lower than 10^{-32} cm^6/s [111], while for the indirect process they are higher, exceeding 10^{-31} cm^6/s [109]. It is suggested that in QWs, Auger recombination rates can be significantly enhanced due to the lack of momentum conservation along the confining direction [112–115]. Carrier confinement in real space is expected to spread the carrier wave function in the reciprocal space, which should favor direct Auger recombination in particular. On the other hand, it is argued that spatial carrier separation due to internal electric fields should reduce the probability of Auger recombination [96,116]. It is also suggested that even small Auger coefficients can cause the droop due to the reduced effective volume in QWs, as the carrier density distribution is strongly non-uniform due to localization, polarization fields, and an unequal carrier distribution among the different wells [117]. Either way, C values as high as 10^{-30} cm^6/s were reported in QWs [118,119].

Another plausible cause of the droop can be the diffusion-driven defect recombination, also known as the density-activated defect recombination (DADR) [120]. It stems from the increasing carrier mobility with their delocalization [121,122]. The increased mobility enhances the probability to reach the distant defects and to overcome the potential barriers that may surround them. This non-radiative process becomes critical after all the localized states get filled and all additional non-equilibrium charge carriers populate the states above the mobility edge. The DADR rate is expected to be proportional to the 2^{nd} power of carrier density [120].

While the previous droop causes are associated with the losses inside the active region, electron leakage encompasses the non-radiative losses taking place outside of it. There are different reasons for the process to occur, one of them being the band bending due to the polarization charges at the interfaces of the layers that constitute the active region and its vicinity, which makes it energetically convenient for electrons to escape into the p-region [104]. The electron escape can be diminished by using the AlGaN electron blocking layer (EBL) that creates a high potential barrier between the active region and a p-contact [123,124]. However, this makes the another issue – poor hole injection, which is already burdened by their high effective mass, polarization charges, and ineffective p-doping – worse, as EBL creates an additional potential barrier to holes. The net outcome is an asymmetrical hole distribution

in the active region. Usually, only one [125,126] or two QWs closest to the p-side get filled with holes, meaning that mainly there radiative recombination occurs. This unbalance between different carriers further enhances the electron escape [126]. On the other hand, it was shown that electron confinement can be enhanced with minimum sacrifices in hole injection by using a specially designed superlattice EBL with graded composition [123].

Electrons injected into the active region may not thermalize to lose their kinetic energy and thus exit into the p-contact without being captured in QWs. This can happen without any scattering (ballistic transport), or with a few scattering events (quasiballistic transport). To prevent the overflow of these "hot electrons", the aforementioned EBL can be used, or alternatively – a staircase electron injector (SEI). In the latter, a step-like increase in the In content helps to effectively "cool" the electrons so as to eliminate the overflow current [127] [P1]. The advantage of using the SEI is that it does not impede the hole injection.

Among other possible droop causes related to the electron leakage, there is defect-assisted tunneling, in which electrons tunnel through the deep states in barriers and other layers into p-GaN [128], thermionic emission from QWs [129], current crowding [130] (which can also favor Auger recombination), and saturation of radiative recombination [66] [P3]. It should be noted that Auger recombination can enhance the electron escape as well because of the gained kinetic energy that exceeds the conduction band edge of the barrier layers [107,111,131].

Stimulated recombination has also been identified as a possible cause of the droop in GaN epilayers, where its onset was observed simultaneously with the droop onset [14,132]. The stabilization of carrier density by stimulated emission at high excitations was held responsible for the decreased efficiency of spontaneous recombination. Meanwhile, the total efficiency of stimulated and spontaneous recombination did not suffer any droop. The same effect has not yet been presented in InGaN LED structures, where the droop occurs significantly earlier than stimulated recombination.

Both Auger recombination and diffusion-driven defect recombination appear to be feasible to explain the droop that is observed in both electroluminescence (EL) and PL experiments. Meanwhile, droop causes associated with electron leakage have certain contradictions to them. The optical pumping of samples creates a symmetrical distribution of holes and electrons in QWs, while the carrier overflow should not be induced in the absence of the external electric field. As for the polarizations charges, they

should be screened at high excitation energy densities. Furthermore, the droop is observed even at low temperatures, as well as at pulsed carrier injection regimes with small duty cycles, diminishing the role of thermionic emission.

1.2. Charge carriers in semiconductors

1.2.1. Charge carrier generation

When an incident photon reaches the boundary between the two mediums, it can be reflected or enter the second medium. In the latter case, a photon can be transmitted through the second medium and exit it, or it can be absorbed by generating a pair of non-equilibrium charge carriers (this can happen after the reflection from the second boundary as well). In the case of the absorption in semiconductors, there are several mechanisms by which this can happen.

If the energy of an incident photon $h\nu$ is equal to or exceeds the bandgap E_g of the semiconductor, an absorbed photon transfers an electron from the valence band E_v to the conduction band E_c, creating a free electron-hole pair, which is a process called an interband absorption. (Fig. 1.8(a)). In a direct bandgap semiconductor, where the minimum of the conduction band energy has the same wave vector (k-vector) as the maximum of the valence band, the momentum ($p = \hbar k$) remains the same after this transition. Meanwhile in an indirect bandgap semiconductor, where the minimum of the conduction band energy and the maximum of the valence band have different momentums, the transition requires the change of $\hbar k$, for which the participation of phonons is necessary. This is why the indirect absorption coefficient is generally smaller than the direct one. In addition to this, it changes with temperature, as phonon density is lattice-temperature dependent.

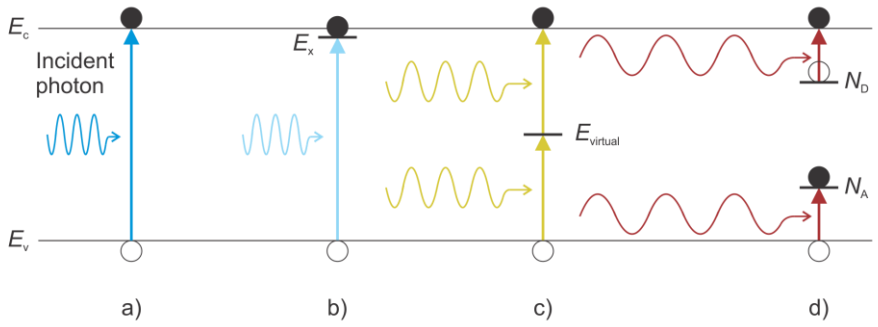

Fig. 1.8. Non-equilibrium charge carrier generation scheme: interband transition (a), exciton absorption (b), two-photon absorption (c), and absorption through impurities or defects (d).

If the energy of an incident photon is lower than the bandgap by a small amount, exciton generation is possible (Fig. 1.8(b)). An exciton is a bound state of an electron and a hole which are attracted to each other by an electrostatic Coulomb force. If a hole is heavier than an electron, the system can be imagined like a hydrogen atom, with a negative electron orbiting a positive hole. The absorption by excitons is generally observed at low temperatures, with the transition energy smaller than bandgap of the material by the exciton binding energy. However, at room temperature the excitons typically dissociate into free electrons and holes and such transitions are not observed.

For photons that have a substantially smaller energy than the bandgap of the material, multi-photon absorption processes can take place. The simplest of them is a two-photon absorption, where the sum of the energy of two photons exceeds the bandgap energy (Fig. 1.8(c)) [133]. This process involves a virtual energy level and is proportional to the 2^{nd} power of the excitation intensity, whereas a single-photon absorption rate is linearly proportional. For a higher order n multi-photon absorption the rate is proportional to the n^{th} power of the excitation intensity, and the absorption coefficient is proportional to the $(n-1)^{th}$ power. This implies that such absorption rates can only become dominant at very high excitations intensities, particularly with highly focused laser pulses [134].

Another case of carrier generation with a smaller energy photon than the bandgap is the absorption through impurity and defect states. Electrons are generated by the ionization of neutral donors, and holes – by the ionization of neutral acceptors (Fig. 1.8(d)). Shallow impurities absorb light in the far-infrared range, while deep impurities – in the infrared range. The absorption coefficient for this mechanism is a few orders of magnitude smaller than the one for the interband transition, and depends on the density of impurities and the absorption cross-section, which depends on the photon energy. Furthermore, the generated electron and hole densities are usually different. In the case of high excitation intensities, multi-photon processes can occur – one photon ionizes a deep impurity, and another transfers the electron (hole) to the conduction (valence) band, thus creating a free electron-hole pair. This is similar to the multi-photon absorption, with the main difference being a real energy level within the bandgap instead of a virtual.

An important thing to keep in mind is that that all transitions require the conservation of energy and momentum. Furthermore, they depend on the

occupation of the participating energy states. This applies to recombination processes as well, which will be discussed in the next chapter.

1.2.2. Charger carrier recombination

The generated free carriers exist only temporarily, as immediately after the excitation recombination processes occur, and the absorbed energy is dissipated as photons and/or phonons. Recombination processes can be divided into two groups: radiative, which is the photon emission that can be accompanied with phonons, and non-radiative, which is basically emission of phonons. A phonon is a quantum mechanical description of an elementary vibrational motion in which a lattice of atoms or molecules uniformly oscillates at a single frequency [135]. Phonon emission may occur due to carrier scattering mechanisms, such as electron-phonon coupling, alloy scattering (due to atomic disorder in an alloy), defect scattering, etc.

Bimolecular recombination is a process, which involves two particles – an electron in a conduction band and a hole in a valence band. When these particles meet at the same point in space (or, in this case, in a crystal lattice), an electron shifts to the valence band instead of a hole, and a hole shifts to the conduction band instead of an electron, with both transitions happening simultaneously (Fig. 1.9(a)). Since the particles have to meet each other for this process to initiate, its rate can generally be described by

$$R = BNP, \tag{1.2}$$

where B is the bimolecular recombination coefficient, which is a material-dependent parameter, N and P – non-equilibrium electron and hole densities, respectively. When $N = P$, for example when free carriers are generated via interband transitions –

$$R = BN^2. \tag{1.3}$$

Bimolecular recombination has a much higher probability in direct bandgap semiconductors, as it can happen without the initial phonon transition, unlike in indirect bandgap semiconductors, where phonons are required to change the momentum. The process is generally radiative, however bimolecular recombination can be non-radiative as well [P3]. The origin of the latter can be recombination via trap sites which accept both electrons and holes.

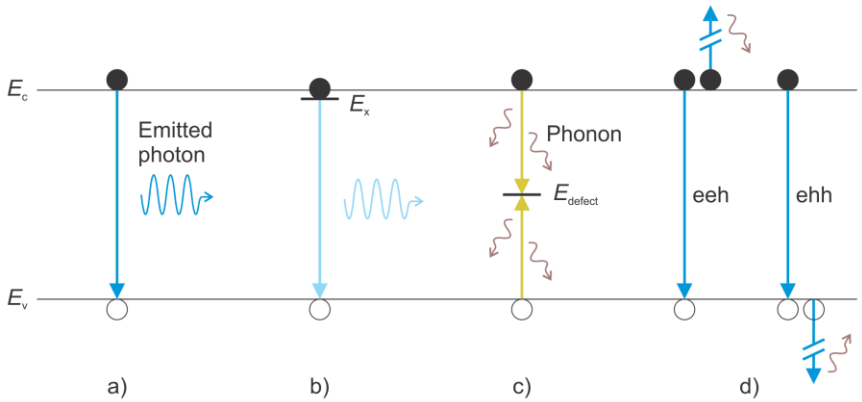

Fig. 1.9. Recombination processes in semiconductors: bimolecular recombination (a), exciton recombination (b), SRH recombination (c), and Auger recombination (d).

Radiative bimolecular recombination is a form of a spontaneous emission process. When population inversion at increased carrier densities occurs, the spontaneously emitted photon can stimulate a recombination event, resulting in a generated photon with similar properties to the one responsible for the event. This is exploited in UV, blue, and green III-nitride laser diodes [62,136]. In GaN, stimulated emission is evidenced by the appearance of a sharp peak in luminescence spectra, which has a lower energy than the spontaneous emission. This is in contrast to AlGaN alloys with high Al content [14] and to InGaN alloys [137], where the stimulated emission peak has a higher energy.

The radiative transition can happen with the participation of one or more phonons, with some of the energy transmitted to the lattice vibrations. In nitrides this is usually evidenced by the main emission peak replicas, shifted to lower energies with multiples of ~90 meV, which corresponds to the energy of the longitudinal optical phonon (LO) [138,139]. Phonon-related peaks are generally observed at low temperatures, where it is easier to distinguish them from other components.

If an exciton can be formed in the material, for example, at low temperatures, exciton recombination may occur (Fig. 1.9(b)). In InGaN alloys, this process can be observed even at room temperature due to sufficiently high binding energies of localized excitons that may exceed the k_BT energy [86]. Exciton recombination rate that can be observed at relatively low carrier densities has a linear dependence on the density of correlated electron-hole pairs [P1]. Excitonic phase in a highly excited QW becomes unstable as the

two dimensional electron-hole density exceeds $N_C = 1/\pi a_b^2$, with a_b being the Bohr radius [140].

Shockley-Reed-Hall (SRH), also called the trap-assisted recombination (Fig.1.9(c)), is generally a non-radiative process. During it, an energy state created within the bandgap by an impurity or an imperfection in the crystal lattice traps a carrier of one sign, which is then followed by a capture of another sign carrier, and the two subsequently recombine, with the energy dissipated mainly as phonons [141]. It can also be imagined as a two-step transition of an electron from the conduction band to the valence band through that energy state. If the latter is positioned energetically closer to the conduction band edge, electrons get trapped more quickly than holes, and the recombination rate mainly depends on how long it takes for holes to be captured. Thus, assuming that the capture probability is the same for all holes, the total recombination rate is simply a product between a one hole capture rate and the number of holes. The same analogy can be applied for the defect state which is closer to the valence band edge. This is why SRH usually has a linear dependence on carrier density [142]. Its rate can be described by

$$R_{SRH} = \frac{PN - N_i^2}{\tau_{h0}(N+N_1)+\tau_{e0}(P+P_1)}, \tag{1.4}$$

where $N_i^2 = N_1 N_2$ is the intrinsic carrier concentration, τ_{h0} and τ_{e0} are lifetime parameters for holes and electrons, respectively, whose values depend on the type of the traps and their volume density [143]. The quantities N_1 and P_1 are parameters that introduce the dependency of the recombination rate on the trapping energy level E_t as follows:

$$N_1 = N_C \cdot \exp\left(\frac{E_t - E_C}{k_B T}\right), \tag{1.5}$$

$$P_1 = N_V \cdot \exp\left(\frac{E_V - E_t}{k_B T}\right). \tag{1.6}$$

Here N_C and N_V are the effective densities of states in the conduction and the valence band, respectively. These expressions are of the same form as the charge carrier concentration in terms of the Fermi energy level.

According to (1.4), (1.5) and (1.6), the most efficient are the deep energy traps, positioned in the middle of the bandgap, provided that τ_{h0} and τ_{e0} are of the same order. This is because once trapped, carriers cannot escape these deep traps, which is otherwise possible in the case of shallow defect states, where the carriers can be freed with the help of phonons. Important things to note are that defect states can absorb differences in momentum between the carriers so that the conservation is easily satisfied, and in direct bandgap

semiconductors SRH is the dominant recombination process at low carrier densities.

The surface of a crystal is a defect itself, abundant with electrically active dangling bonds, as well as with other defects. Grain boundaries and layer interfaces can also contain these crystal lattice imperfections, which are responsible for the surface recombination [144]. The process is very similar to SRH recombination, with the main difference in that the surface recombination depends on a two-dimensional density of traps, not a volume density.

Direct Auger recombination is a three particle non-radiative process. Its initial stage is similar to bimolecular recombination, however afterwards the energy of the interband transition is passed to a third particle, rather than emitted as a photon. The third particle, which can be an electron in the conduction band (eeh Auger recombination, corresponding to two electrons and a hole) or a hole in a valence band (ehh), is then moved to the extended states in the corresponding band (Fig. 1.9(d)). After the interaction, the particle loses its excess kinetic energy to thermal vibrations via the emission of phonons and returns to the bottom of the energy band. The total rate of such a process is generally described by

$$R_{Auger} = C_1 N^2 P + C_2 P^2 N. \quad (1.7)$$

Here C_1 and C_2 are the Auger recombination coefficients for eeh and ehh processes correspondingly. For equal hole and electron densities, (1.7) becomes

$$R_{Auger} = C_1 N^3 + C_2 N^3 = C N^3. \quad (1.8)$$

The energy and momentum conservation is required in this process as in all transitions. For the simplest case of eeh Auger recombination, the momentum conservation can be represented as

$$k_1 + k_2 + k_h = k_f, \quad (1.9)$$

where k_1, k_2 and k_h are the initial momenta of electrons and a hole, k_f is the final momentum of the electron that gains the energy and is lifted in the parabolic conduction band (Fig. 1.10(a)). Considering a hole that is much heavier than an electron (a case in III-nitrides) so that it carries all the initial momentum,

$$k_h \approx k_f, \quad (1.10)$$

which means that a hole must have a non-zero kinetic energy which exceeds a certain threshold for the direct Auger process to occur, thus limiting the number of available states that participate in the transition [145]. Furthermore,

in large bandgap semiconductors, the direct eeh Auger recombination is quite improbable, because the conservation of momentum and energy is unlikely to be fulfilled for a high energy portion transfer resulting from the interband transition. This is because at high energies the conduction band dispersion curve differs essentially from a parabolic one, an approximation which is only true near the band edge [146]. The situation is quite similar for the direct ehh Auger recombination, however it can be more probable due to the presence of a complex valence band (Fig. 1.2), where a heavy hole can be rebounded to the light hole subband.

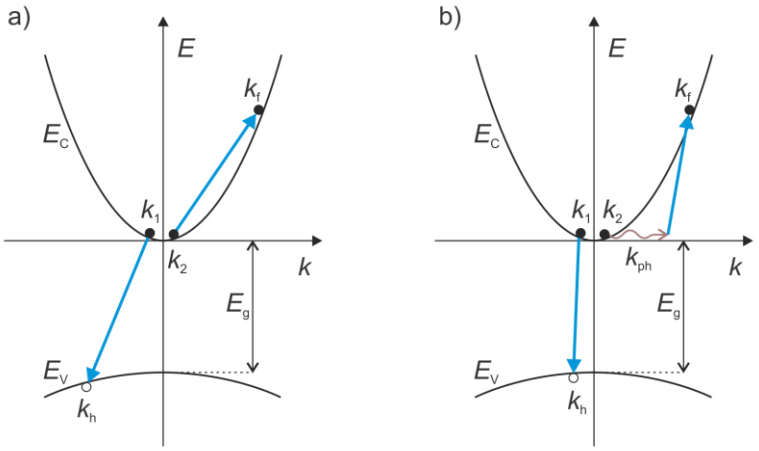

Fig. 1.10. Direct (a) and indirect eeh Auger (b) schematic diagrams in the vicinity of band edges.

Auger recombination becomes indirect, when an additional momentum k_{ph} is provided to the process via an electron-phonon interaction, alloy scattering, or Coulomb scattering by a charged defect [109] (Fig. 1.10(b)). This eases the conservation of momentum and energy and allows a broader range of final states, thus increasing the transition probability. This is very significant where the band parabolicity ceases. Such a non-threshold Auger process rate has a non-exponential dependence on temperature [147]. In InGaN alloys, the indirect Auger recombination coefficient is typically higher for the ehh process [109,148]. In addition to this, phonon scattering has a greater influence than alloy scattering, with scattering by charged defects being negligible [109].

The trap-assisted Auger recombination is a variation of the standard process, where the initial interband transition is replaced with recombination of an electron or a hole through a trap, just like in SRH recombination. The energy of this transition is not transferred to the crystal lattice through phonons, but to a particle in a band which is shifted to higher energy [149]. The rate of the process can be described by [150]:

$$R_{TAA} = C_{TAA} N_T NP = C_{TAA} N_T N^2, \quad (1.11)$$

where C_{TAA} is the trap-assisted Auger recombination coefficient, N_T is the density of participating traps. Because the latter is generally constant, the process depends only on carrier concentration –

$$R_{TAA} = B_{TAA} N^2, \quad (1.12)$$

where B_{TAA} is the product of the trap-assisted Auger recombination coefficient and the trap density.

1.2.3. Charge carrier diffusivity

In general, a charge carrier current is driven by two physical processes: carrier flow induced by the external electric field and diffusivity caused by the carrier concentration gradient. In the absence of the external electric field, carriers are transported due to the diffusive flux, which is quantitatively described by the diffusion coefficient *D*. In the non-degenerate semiconductor, *D* is related to carrier mobility μ with the generalized Einstein relation [151]

$$D = \frac{k_B T}{e} \mu \chi, \quad (1.13)$$

where e is the elementary charge and χ is called the thermodynamic factor, which contains the effect of the interactions among the carriers (when $\chi > 1$). If χ equals to 1, then (1.13) becomes the classical Einstein relation. Carrier mobility itself is the proportionality factor between the drift velocity v_d and the driving electric field E –

$$v_d = \mu E. \quad (1.14)$$

In other words, electron (hole) mobility characterizes how quickly an electron (or a hole) can move through a metal or a semiconductor, when pulled by the electric field. It can also be described by the equation

$$\mu = \frac{e}{m^*} \langle \tau \rangle, \quad (1.15)$$

where m^* is the effective particle mass and $\langle \tau \rangle$ is the average momentum relaxation time of non-equilibrium carriers. The latter depends on the

scattering mechanisms, of which the main in semiconductors are: phonon scattering (most relevant at high temperatures), scattering by other carriers (at high concentrations), and scattering by defects and crystal surfaces (dominant at low temperatures).

In the case when both holes and electrons are generated in the semiconductor simultaneously, for example with an interband transition, diffusivity is ambipolar. The generated electron-hole pairs will diffuse along the concentration gradient towards the lower concentration, however, the more mobile carriers (usually electrons due to their lower effective mass) will do so at a faster speed. The increasing spatial separation between electrons and holes will induce the electric Dember field, which will prevent the further separation between the carriers. Therefore, the diffusive flux will mainly be determined by diffusivity of the less mobile carriers. The ambipolar diffusion coefficient D_a is described by:

$$D_a = \frac{N+P}{\frac{N}{D_h}+\frac{P}{D_e}}. \quad (1.16)$$

Here D_e and D_h are monopolar diffusion coefficients of electrons and holes, correspondingly. When $N = P$ (equal generation rates of electrons and holes),

$$D_a = \frac{2D_eD_h}{D_e+D_h}. \quad (1.17)$$

Because in most semiconductors $D_e \gg D_h$, therefore $D_a \approx 2D_h$. For the cases where densities of carriers of a different sign are significantly unequal, $D_a \approx D_e$ when $N \ll P$, and $D_a \approx D_h$ when $N \gg P$.

Knowing the carrier lifetime τ_R and D, one can calculate the average distance that the carriers travel before recombining (in the absence of the external electric field) – the diffusion length:

$$L_D = \sqrt{D\tau_R}. \quad (1.18)$$

1.3. Quantum structures

1.3.1. Properties of quantum wells

Quantum structures are inherent components of LEDs. Their emergence can be traced back to the formulation of the concept of double heterostructure lasers in 1963 [152,153]. Non-equilibrium charge carriers are effectively confined when injected into the semiconductor with a smaller bandgap sandwiched between semiconductors with wider bandgaps (which act as barriers). The current cannot pass through the barriers at the interfaces, which increases the carrier density in the confinement region and enhances the probability of radiative recombination. These heterostructures are very important to p-n junction lasers, where they allow lasing at room temperatures with considerably lower currents [154]. For LEDs, double heterostructures are usually narrowed to the size where they become quantum wells. In such a case, not only the carriers are confined in space – their discreet energy levels also form. This happens when a QW width becomes comparable to a characteristic dimension. In the case of thermalized electrons, it is the de Broglie wavelength (also called the thermal wavelength)

$$\lambda_{dB} = \frac{h}{p} = \frac{h}{m^* v} = \sqrt{\frac{h^2}{2m^* \xi}}, \tag{1.19}$$

where h is Planck's constant, p is the momentum, m^* – the effective electron mass, v – electron velocity, ξ – thermal kinetic energy. The de Broglie wavelength for room temperature electrons (with ξ = 26 meV) for GaN is about 20 nm and for AlN it is about 14 nm [155]. For excitons, the characteristic dimension is the Bohr radius, which is ~3 nm for GaN [156].

The formation of discrete energy levels in QWs is called the quantum confinement. It stems from the fact that electrons and holes are both waves that need to be squeezed in along the confinement direction. This results in standing waves positioned perpendicularly to the interfaces of the layers. For a standing wave to occur, its half wavelength (or multiples of it) have to match the distance between the barriers. Only particular waves meet this requirement, hence quantization arises. The easiest way to understand this is by taking the "particle in a box" model [157]. In it the Schrödinger's equation in one dimension for the particle (an electron or a hole) is

$$\frac{-\hbar^2}{2m^*}\frac{d^2\phi_n}{dz^2} + V(z)\phi_n = E_n\phi_n, \tag{1.20}$$

where $V(z)$ is the potential (the barrier height) that a particle sees along the direction of the confinement (z), m^* is the effective mass of the particle, E_n and ϕ_n are the eigenenergy and the eigenfunction, associated with the n^{th} solution of the equation, correspondingly. The equation can be simplified if the barriers are considered to be infinitely high. Then the wave function must be zero at the walls of a quantum well. In such a case, the solutions are

$$E_n = \frac{-\hbar^2}{2m^*}\left[\frac{n\pi}{L_z}\right]^2, \tag{1.21}$$

$$\phi_n = A\sin\left(\frac{n\pi z}{L_z}\right). \tag{1.22}$$

Here n = 1, 2, 3… is an energy level, L_z is the width of the well, A – the normalization constant. The energy levels are quadratically spaced and the wave functions are sine waves (Fig. 1.11, top left). The spacing between the energy levels becomes more prominent with the narrower wells and smaller effective masses m^*. Note that the energies of each level are referred to the bottom of the well. To determine the total shift of the transition energy with respect to the bulk semiconductor, one has to take into account the shifts for both electrons and holes.

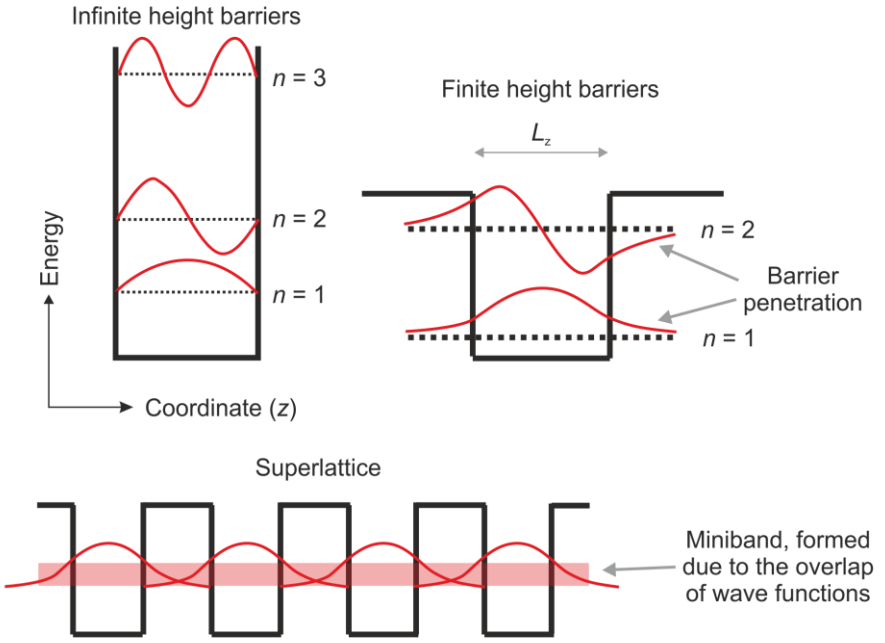

Fig. 1.11. Depiction of a quantum well and its energy levels with an infinite height barriers (top left) and with a finite height barriers (top right). At the bottom, a superlattice is shown. Adapted from [157].

An infinite well is an idealized case. In real-world conditions, finite height barriers exist, which means that at the walls of the wells the wave function is not zero, and because it has to be continuous, it penetrates the barriers. The result is a sine wave inside the QW, which exponentially decays in the barriers (Fig. 1.11, top right). If there are two or more QWs, separated by barriers sufficiently thin that the exponentially decaying neighboring wave functions overlap, a superlattice is formed. In such a structure, a carrier has the probability to tunnel through a barrier. Furthermore, when the overlapping of the wave functions of separate energy levels is significant, superlattice minibands arise (Fig. 1.11, bottom).

In a QW, the movement of carriers in directions parallel to the planes of the layers is not restricted. Thus carriers can gain kinetic energies from the in-plane motion

$$E_k = \frac{p_x^2}{2m^*} + \frac{p_y^2}{2m^*} = \frac{h^2 k_x^2}{2m^*} + \frac{h^2 k_y^2}{2m^*}. \quad (1.23)$$

Due to this, there are subbands instead of discreet energy levels in QWs. These subbands begin at the energy levels calculated for the confined states (where $E_k = 0$). This results in a step-like DOS function, with the steps emerging from the fact that for the in-plane motion DOS remains constant (Fig. 1.12). If the width of the well increased constantly, the steps would continuously shrink, with a smooth transition at some point to a bulk material DOS curve.

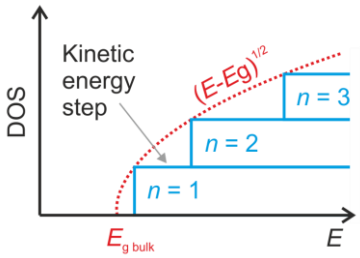

Fig. 1.12. Comparison of DOS functions in a bulk material (red dotted line) and in a quantum well (blue steps). Adapted from [157].

Transitions with photons (absorption or recombination) in a QW take place only between the same energy levels of electrons and holes (Δn=0), and the conservation of the momentum has to be fulfilled. They are known as "vertical" transitions, and their essence is that momentum in the conduction band has to be the same as the one in the valence band. In an ideal QW, these transitions would follow the DOS function.

An important parameter of QWs is a band offset ratio. Its value represents how the conduction and valence bands of different semiconductors align in a

heterojunction. For example, in a GaN/InGaN system the band offset ratio is generally considered to be 70/30 [114], meaning that 70% of bandgap energy difference between GaN and InGaN goes to the offset of the conduction bands, while 30% of it goes to the offset of the valence bands.

1.3.2. Quantum-confined Stark effect

The quantum-confined Stark effect (QCSE) is a phenomenon inherent to quantum wells where electric fields are present (internal or external). In the case of polar nitride-based structures, the effect arises due to the internal polarization fields (Chapter 1.1.4), which bend the conduction and valence bands, thus spatially separating electrons and holes in the direction perpendicular to the QW plane. The negatively charged electrons accumulate on one side of the QW, while the positively charged holes accumulate on the other side (Fig. 1.13(a) and (b)). This reduces the overlap of carrier wave functions, the probability of the radiative interband transition and its energy, as the energy levels shift down. These unwanted effects can be diminished by designing narrower QWs (Fig. 1.13(c)). In them, a shorter separation distance gives a better overlap of the wave functions (which in the meantime overcome a smaller distortion) as the quantum confinement energy levels are raised higher and do not fall into triangular potential minima that originate from the tilted energy potentials.

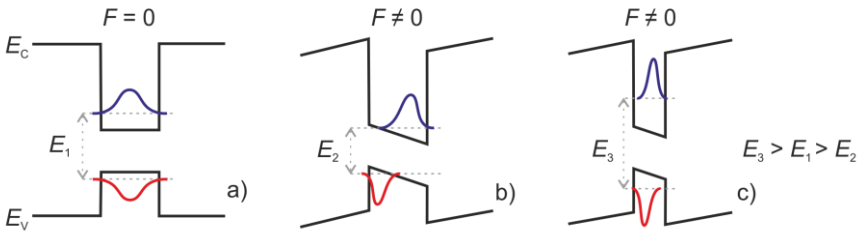

Fig. 1.13. First energy levels of electrons and holes and their wave functions: in a wide QW without internal fields (a), in a wide QW with internal fields (b), and in a narrow QW with internal fields (c). Adapted from [157].

Internal polarization fields can be screened at high carrier densities, which cancels the bending of the potential in a QW. This can be observed as a blueshift of the radiative emission spectra with increasing the excess carrier density, either by photoexcitation or by the electrical driving current.

2. EXPERIMENTAL

2.1. Measurement techniques and equipment

A few complementary nondestructive measurement techniques were used to thoroughly investigate the absorption/emission properties and non-equilibrium carrier dynamics in samples.

The main laser system used in the experiments was PHAROS, with 1030 nm (~1.2 eV), a 30 kHz repetition rate, and 250 fs pulses. To set the desired excitation wavelength, these pulses were passed through the ORPHEUS optical parametric amplifier (OPA), capable of changing the wavelengths in the range from 600 to 2600 nm, then frequency-doubled with the second harmonic generation crystal (SHGC). The resonant excitation of the active layers was performed with ~390-392 nm (~3.18-3.16 eV) pump pulses, which were chosen considering that they exceed the energy of the QW states that participate in the absorption, but do not reach the energy required for the direct absorption in other layers.

For the delay in time resolved pump-probe experiments a fast AEROTECH PRO165LM linear motor stage was used, having the ability to move with a 1 μm accuracy and reach movement speeds of up to 2 m/s.

All measurements were performed at the Institute of Photonics and Nanotechnology, Vilnius University, Lithuania.

2.1.1. Time-integrated photoluminescence and IQE measurement

Time-integrated photoluminescence (TIPL) is one of the basic material characterization techniques, in which emission from an excited sample is registered. Throughout the entire set exposure time, a spectrometer constantly collects light, emitted after each incident laser pulse, therefore a time-integrated spectrum is recorded. This relatively easy and quick technique provides valuable information about the spectral distribution of emission.

The TIPL setup used in this work is presented in Fig. 2.1. The tuned laser pulse is passed through a gradient filter, with which the excitation energy density throughout the experiment is changed, then through a shutter, which can be closed to measure the background, then it is focused with a lens on a front side of the sample. For calibration of the internal quantum efficiency, a sample is positioned inside an integrating sphere (SphereOptics, 6 inch

diameter) and emission is collected through a small aperture on the side of it, where an optical fiber that guides light to the spectrometer (AvaSpec ULS 2048, with a 300 lines/mm grating) is placed. In other measurements, light emitted from the sample (placed outside the integrating sphere) is collected with a lens in front of the sample (front-face configuration), and then focused onto the fiber, which guides light to the spectrometer. The front-face configuration allows the collection of PL spectra in a wider range of excitations, since the spectrometer is not saturated by the scattered relatively intensive laser line at lowest (where long exposures are needed to collect the weak PL signal) and highest excitations.

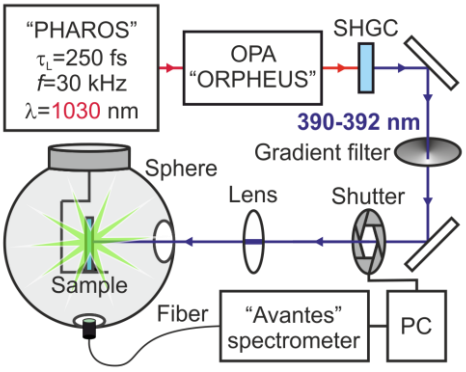

Fig. 2.1. Schematic of a TIPL setup with an integrating sphere.

The most direct way to evaluate IQE of a sample is to calculate the exact ratio between the emitted and absorbed photons. This is done with the help of the integrating sphere – all light that enters it and is scattered and/or emitted by the sample is reflected from the inner surface, coated by barium sulphate ($BaSO_4$, reflectance >95% in the visible range). After multiple reflections, a homogeneous light distribution throughout the entire sphere is reached. A small part of this light is reflected from a baffle into a small aperture located beneath it. A fiber, positioned at this aperture, collects reflected light and guides it to the spectrometer, which measures the spectral intensity distribution.

In the simplest case, one can evaluate IQE by measuring two spectra: one with an empty integrating sphere and on with a sample placed inside. However, it is more accurate to use the three-measurement approach presented by Leyre et al. [158] which additionally takes into account the sample's indirect absorption of the scattered/reflected excitation pulse. In this method,

three spectra are measured: one without a sample in the sphere (I), one with a sample in the sphere but out of the way of the incident laser beam (II), and one with a sample in the sphere and in the path of the laser beam (III). The spectra are divided into two components: L is the region of incident radiation and P is the region of luminescence. In the former component, the quantities are: L_a is the number of photons in the incident radiation region detected in spectrum I (total intensity of a laser beam), L_b is the number of photons in the incident radiation region in spectrum II (intensity of a laser beam after the indirect absorption in the sample), and L_c is the number of photons in the incident radiation region in spectrum III (intensity of a laser beam after the direct and the indirect absorption in the sample). In the second component, P_b is the number of photons in the luminescence region in spectrum II (intensity of luminescence from the indirect absorption) and P_c is the number of photons in the luminescence region in spectrum III (intensity of luminescence from the indirect and the direct absorption). A schematic overview of these quantities is shown in Fig. 2.2.

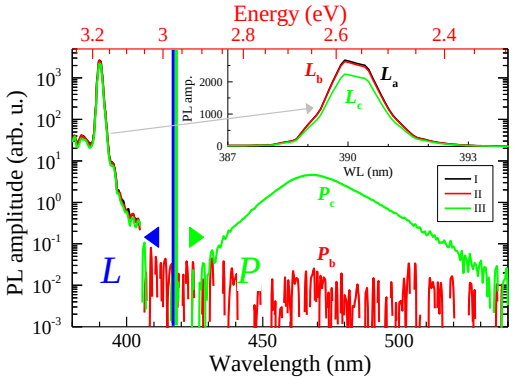

Fig. 2.2. PL spectra of the MQWs sample from this work, used in the three-measurement approach calculations. Sample T815 from Table 1.

The value of IQE in the three-measurement approach is calculated by using the following equation:

$$IQE = \frac{P_c - (1 - A_{dir})P_b}{L_a A_{dir}}. \quad (2.1)$$

The A_{dir} term here stands for the amount of directly absorbed light,

$$A_{dir} = 1 - \frac{L_c}{L_b}. \quad (2.2)$$

2.1.2. Time-resolved photoluminescence

Time-resolved photoluminescence (TRPL) expands the limitations of TIPL by providing additional information about carrier dynamics and the ability to monitor how the emission spectra evolve with time. In this work, a Hamamatsu C10627 streak camera along with an Acton SP2300 monochromator were used for the measurements of TRPL spectra and kinetics.

The principle of a streak camera is presented in the figure below (Fig. 2.3). A monochromator, mounted on the front of the camera module disperses the incoming light, which is then passed through a narrow horizontal slit. Afterwards, with the help of the optics, the dispersed light is projected onto the surface of a photocathode placed in a vacuum streak tube. The incident light on the photocathode is converted into a number of electrons proportional to the intensity of the light flux. Emitted electrons are accelerated towards a pair of horizontally mounted sweep electrodes, where a high voltage is applied at a timing synchronized to the incident light. This initiates a high-speed sweep of electrons from the top to the bottom. Electrons, which arrive at slightly different times, are deflected at slightly different angles in the vertical direction and then enter the micro-channel plate (MCP). There their number is multiplied several thousands of times, after which they impact against the phosphor screen and are converted into light again. A CCD camera registers the resulting image. Its vertical axis gives the time resolution, with the earliest portion of the optical pulse under study placed in the uppermost position, horizontal axis gives the spectral resolution, and brightness of each point is proportional to the studied optical pulse intensity.

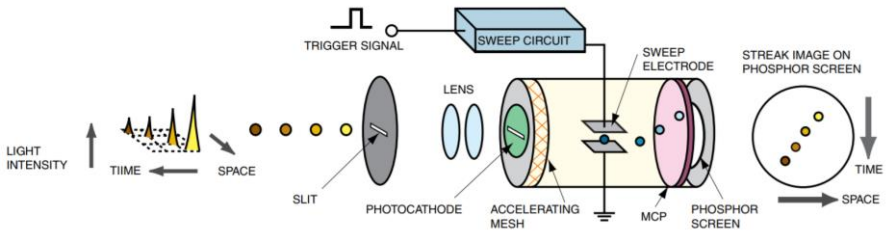

Fig. 2.3. Principle scheme of the Streak Tube. Image taken from [159].

2.1.3. Differential transmission spectroscopy

Time-resolved differential transmission (DT) spectroscopy is a complementary technique to PL, which allows monitoring of the changes in the occupancy of the electronic states that contribute to PL signal as well as of the ones that do not. Thanks to this, interesting features such as carrier redistribution between these states can be observed, giving a deeper insight into the overall recombination process.

When a probe, composed of different energy photons (the white probe) passes through an unexcited sample, some of the photons that have enough energy to complete the transitions between the valence band (E_v) and the conduction band (E_c) are absorbed (Fig. 2.4 left). Absorption may also occur between the localized states, which are present in the III-nitride materials, or other energy levels. This alters the initial spectral distribution of the probe, with the changes resembling the DOS function. The picture changes when prior to the contact with the probe beam, the sample is excited by the incident laser pulse. Absorption of the latter lifts the electrons from the valence band to the conduction band, leaving behind holes. The energy difference between the bandgap and photons determines how high the carriers are lifted in the corresponding bands. Shortly after the excitation (typically on the order of several picoseconds), the non-equilibrium carriers thermalize and populate the lowest possible energy states, which are determined by a product of a DOS function and a Boltzmann distribution (or a Fermi-Dirac distribution if carrier density is high). The occupation of these states prohibits further absorption within them. Hence if a white probe passes through the sample after its excitation, the photons that otherwise would be absorbed in an unexcited sample, pass through unabsorbed (Fig. 2.4 right). The principle of the DT technique lies in recording of these changes in the transmission of the probe beam (Fig. 2.4 bottom). The use of the white probe in the experiment provides the spectral resolution, while the temporal resolution is achieved by varying the delay between the pump and the probe beams. The time resolution is mainly limited by the duration of a laser pulse, meaning that in the used system observation of sub-picosecond processes is possible.

The DT signal (measured in OD – optical density – units) is given as a logarithm of the ratio between the intensities of a probe beam, transmitted through an unexcited sample ($T_0(\lambda)$), and a delayed probe beam, transmitted

through an excited sample ($T_p(\lambda, t)$), at a given wavelength λ and a delay time t:

$$T(\lambda, t) = \log\left(\frac{T_0(\lambda)}{T_p(\lambda,t)}\right). \quad (2.3)$$

A negative signal sign indicates the absorption bleaching, i.e. absorption of a probe decreases, while a positive stands for the opposite process – induced absorption.

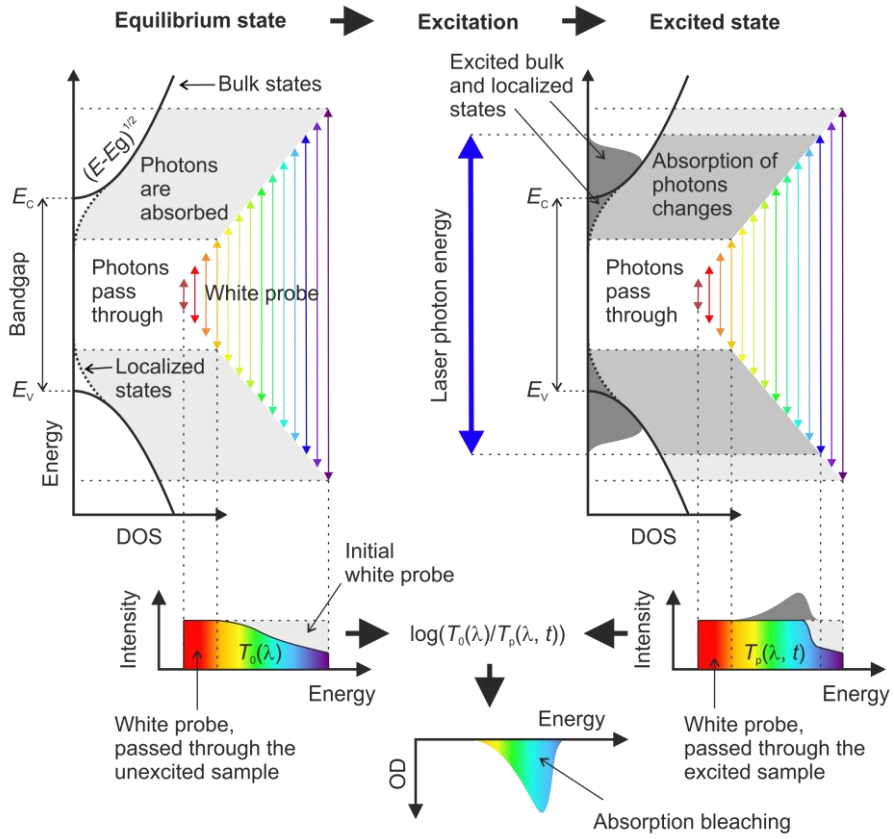

Fig. 2.4. DT principle scheme. For the sake of simplicity, it is assumed that the initial white probe spectral distribution has a rectangular shape.

In the DT setup used in this work (Fig. 2.5), the laser output beam is split into two, with one of them serving as a pump beam and another as a probe. The former is tuned and then passed through a chopper so that it can be periodically closed to measure the transmittance of a probe with excitation and without it; afterwards, the pump is focused onto a sample. The probe beam is

passed through a shutter, which can be closed for the measurement of the background, then frequency doubled, reflected on the retroreflectors on a mechanical delay line, and then passed through a sapphire crystal, where a white light continuum is generated (with spectral range from ~360 to ~530 nm, corresponding to ~3.44 and ~2.34 eV). The latter is directed with parabolic mirrors onto the sample, after which transmitted light enters a spectrograph (Andor Shamrock) through a narrow slit. Collected light is then dispersed with a 300 lines/mm grating and projected onto a CCD camera. A Harpia system (Light Conversion) is used to acquire data.

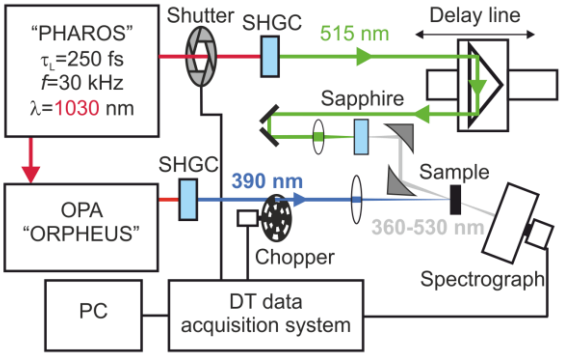

Fig. 2.5. DT setup scheme.

2.1.4. Free carrier absorption

Free carrier absorption (FCA) experiment relies on the differences of the probe beam absorption like in the DT experiment, but in a distinct way. When electrons and holes are excited to conduction and valence bands, respectively, they can absorb light that is of much lower energy than the bandgap of the material under study. That is, free carriers can be excited within their respective bands. The longer the wavelength of light, the more probable this process is as the conservation of the momentum eases. The absorption coefficient of free carriers depends on their density

$$\Delta\alpha_{FCA}(t) = \sigma_{eh}\Delta N(t), \tag{2.4}$$

where $\sigma_{eh} = \sigma_e + \sigma_h$ is the cross-section of absorption by a single free electron-hole pair. Because of this, the intensity of the transmitted probe beam is directly related to the non-equilibrium carrier density. Thus, by delaying the probe beam with respect to the pump beam, free carrier decay can be monitored. The transients are plotted as

$$T(t) = \ln\left(\frac{T_0}{T_p(t)}\right), \quad (2.5)$$

where T_0 is the intensity of the transmitted probe when no excitation is present, $T_p(t)$ is the intensity of the transmitted probe after the excitation at a given delay time.

The experimental scheme for FCA is basically similar to the DT scheme shown in Fig. 4.5. The main differences are that for a probe beam, instead of a SHGC, an OPA is used, which tunes the wavelength to 1.65 μm (0.75 eV), and there is no sapphire crystal in its further path. Since the experiment does not provide the spectral resolution, an InGaAs detector is used instead of a spectrograph to measure the intensity of the transmitted probe beam. During the measurements, samples were aligned at the Brewster's angle with respect to the probe beam to lessen the latter's interference effects.

2.1.5. Light-induced transient gratings

Light-induced transient gratings (LITG) is a unique measurement technique, which provides means to observe non-equilibrium carrier recombination and diffusion simultaneously. The principle lies on the excitation of the sample by an interference field of two short coherent pump pulses, creating a transient spatially modulated free carrier pattern. This pattern modulates the refractive index, acting as a decaying diffraction grating, and diffracts the incident probe, for which the material is transparent. The decay of the intensity of the diffracted beam is then registered.

Two coherent beams that meet at the same point in space create a periodic light intensity field with the distribution, defined as

$$I(x) = I_0\left(1 + m\cos\left(\frac{2\pi}{\Lambda}x\right)\right), \quad (2.6)$$

where $I_0 = I_1 + I_2$ is the total intensity of the incident beams, $m = \frac{2\sqrt{I_1 I_2}}{I_1 + I_2}$ – modulation depth of the interference field, Λ – its period. The latter depends on the wavelength λ of interfering beams and an angle Θ between them (Fig. 2.6):

$$\Lambda = \frac{\lambda}{2\sin\left(\frac{\Theta}{2}\right)}. \quad (2.7)$$

Placing a semiconductor sample in this interference field results in the generation of non-equilibrium carriers with their density distribution following the light intensity pattern:

$$N(x,z) = N_0\left[1 + m\cos\left(\frac{2\pi x}{\Lambda}\right)\right]\cdot\exp(-\alpha z). \quad (2.8)$$

Here α is the light absorption coefficient, x – the coordinate along the light intensity pattern, z – the coordinate perpendicular to the surface of the sample, N_0 – average density of photogenerated carriers. The last part of the equation shows how carrier density decreases with the depth of the sample.

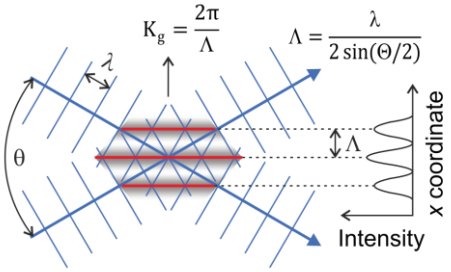

Fig. 2.6. The scheme for the interference of two coherent beams.

The periodic distribution of non-equilibrium carriers modulates the refractive index, creating a diffraction grating. This can be described by the semi-classical Drude model, in which an electron (hole) in the conduction (valence) band is a quasi-free particle with an effective mass m_e^* (m_h^*), oscillating in the electromagnetic field of light [160]. According to this model, changes in the refractive index Δn and free-carrier absorption coefficient $\Delta\alpha$ are expressed as:

$$\Delta n = -\frac{e^2}{2n_0\omega^2\varepsilon_0}\left(\frac{\Delta N_e}{m_e^*} + \frac{\Delta N_h}{m_h^*}\right) = \Delta N n_{eh}, \quad (2.9)$$

$$\Delta\alpha = \frac{e^2}{n_0\omega^2 c\tau_d\varepsilon_0}\left(\frac{\Delta N_e}{m_e^*} + \frac{\Delta N_h}{m_h^*}\right) = \Delta N\sigma_{eh}, \quad (2.10)$$

where n_0 is the refractive index of the material, ω – the circular frequency of light (in this case – the probe beam) and of the resulting carrier oscillation, τ_d – the electron momentum relaxation time (the mean time between any two scattering events), ΔN – photoexcited carrier density, n_{eh} – the refractive index change caused by a single electron-hole pair, σ_{eh} – the absorption cross-section of a single electron-hole pair, e – an elementary charge, ε_0 – the vacuum permittivity. According to these equations, every created free electron-hole pair reduces the refractive index and increases the free-carrier absorption coefficient. The effects are stronger when the frequency of light is further away from the resonant frequency of the material, i.e. in its transparency region.

The diffraction grating in a material can also be induced by a periodic temperature modulation (called the thermal grating). The crystal lattice can

heat up locally with the same pattern as the previously mentioned interference field. The energy to the lattice can be transferred via the thermalization of hot carriers, which are created when the energy of the excitation pulse greatly exceeds the bandgap or due to the free-carrier absorption in a material, or via the non-radiative recombination including phonons. This results in the opposite effect, when compared to the non-equilibrium carrier pattern induced changes, with the increase in the refractive index:

$$\Delta n = \frac{\partial n}{\partial T}\Delta T. \tag{2.11}$$

Thermal gratings are more common at low temperatures, though they can be seen at room temperature as well [161].

Right after the excitation of the sample with the pump interference field, the induced grating starts to decay over time (hence the name transient) due to two processes – carrier recombination and carrier density gradient caused diffusion. The former decreases the carrier density, while the latter reduces the modulation depth *m* of the transient grating. The diffracted probe beam intensity follows the decay of the transient grating. Since the probe only partially diffracts, its decay is presented as the intensity ratio η between the diffracted I_{diff} and the transmitted I_{trans} parts of a probe beam (diffraction efficiency). For a thin grating [150], it can generally be described with a first-order Bessel function

$$\eta = \frac{I_{diff}}{I_{trans}} = |J_1(\phi)|^2 = \left|J_1\left(\frac{2\pi\Delta\tilde{n}d}{\lambda}\right)\right|^2, \tag{2.12}$$

where $\tilde{n} = n + ik$ is a complex refractive index, *d* is the grating thickness, λ is the probe wavelength. The use of a complex refractive index shows that diffraction gratings can be created either due to the changes in the real part of the refractive index (*n*), or due to the changes in the absorption coefficient (*ik*). If the function argument $\phi \ll 1$ (for very small diffraction efficiencies, which is the case in this work), then the Bessel function can be approximated as

$$J_1(\phi) \approx \frac{\phi}{2}. \tag{2.13}$$

This simplifies the diffraction efficiency equation:

$$\eta = [J_1(\phi)]^2 \approx \left|\frac{\pi\Delta\tilde{n}d}{\lambda}\right|^2 = \left(\frac{\pi\Delta nd}{\lambda}\right)^2 + \left(\frac{\Delta\alpha d}{4}\right)^2. \tag{2.14}$$

If free-carrier absorption in the material is negligible ($\alpha d \ll 1$), the second term in (2.14) can be omitted, further simplifying the equation to

$$\eta = \left(\frac{\pi\Delta nd}{\lambda}\right)^2. \tag{2.15}$$

Combining (2.15) with (2.9) results in

$$\eta(t) \propto \Delta N^2(t). \quad (2.16)$$

As mentioned before, carrier density profile decays due to recombination processes and diffusion along the grating vector $\boldsymbol{K}_g = \frac{2\pi}{\lambda}$ (Fig. 2.6), which can be described by the following equation [162]:

$$\frac{\partial N(x,t)}{\partial t} = D\frac{\partial^2 N(\mathrm{x,t})}{\partial \mathrm{x}^2} - \frac{N(x,t)}{\tau_{SRH}} - BN^2(x,t) - CN^3(x,t) + G(x,t), \quad (2.17)$$

where D is the diffusion coefficient, $G(x, t)$ – the carrier generation term. If the latter has the Dirac delta function profile, the analytical solution for (2.17) is:

$$N(x,t) = N_0\left[1 + exp\left(-\frac{t}{\tau_D}\right)cos\left(\frac{2\pi x}{\Lambda}\right)\right]\exp\left(-\frac{t}{\tau_R}\right), \quad (2.18)$$

where τ_D is the grating decay time due to carrier diffusion and τ_R is the recombination time that takes all recombination mechanisms into account.

It can be seen, that density of non-equilibrium carriers in a transient grating decays exponentially with a characteristic time τ_G:

$$\frac{1}{\tau_G} = \frac{1}{\tau_R} + \frac{1}{\tau_D} = \frac{1}{\tau_R} + \frac{4\pi^2 D}{\Lambda^2}. \quad (2.19)$$

Because the diffraction efficiency has a quadratic relation to carrier density (2.16), τ_G can be extracted from

$$\eta(t) \propto exp\left(-\frac{2t}{\tau_G}\right). \quad (2.20)$$

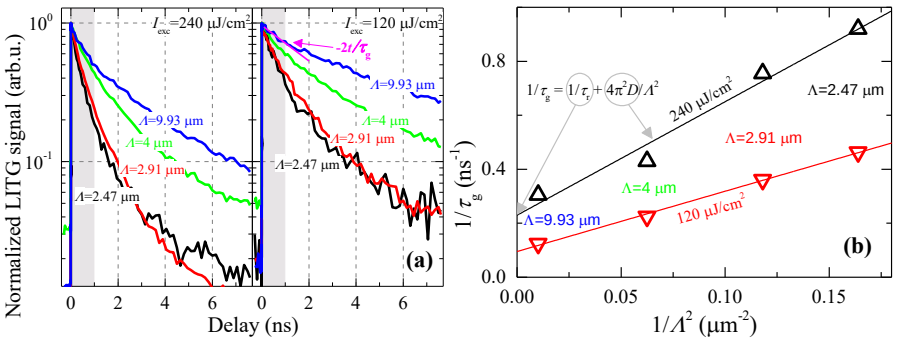

Fig. 2.7. LITG decays, measured with 4 different induced grating periods Λ (9.93 μm, 4 μm, 2.91 μm, and 2.47 μm) at two excitation energy densities in an InGaN MQWs sample (tp12 from Table 1) (a), and reciprocal decay times, calculated from the initial parts of these decays (fitting range marked by grey bands), presented as functions of $1/\Lambda^2$ (b). The black fitting line (I_{exc} = 240 μJ/cm²) corresponds to D = 1.1 cm²/s, τ_R = 4.4 ns, the red one (I_{exc} = 120 μJ/cm²) corresponds to D = 0.6 cm²/s, τ_R = 10.5 ns.

The equation (2.19) shows, that τ_D can be varied by changing the induced grating period. By doing so, one can separate the influence from recombination and diffusion processes. By measuring LITG transients (kinetics) at different induced grating periods Λ (Fig. 2.7(a)) and calculating τ_G from them, a $\frac{1}{\tau_G} = f\left(\frac{1}{\Lambda^2}\right)$ graph can be plotted (Fig. 2.7(b)). Fitting its data with a linear function gives two quantities: an intercept, corresponding to $1/\tau_R$, and a slope, corresponding to $4\pi^2/D$. It can be seen that τ_G decreases with smaller Λ, which is due to a higher carrier density gradient along the grating vector $\boldsymbol{K}_\mathbf{g}$, and, subsequently, a faster diffusive decay.

In a LITG setup (Fig. 2.8) the laser output beam is split into two (a pump and a probe), just like in a DT setup. A pump beam is modulated with a chopper (for signal synchronization) prior to the frequency doubling, then passed through a holographic beam splitter (HBS), where it is diffracted. In this work, Λ_{HBS} ranged from 10 μm to 40 μm. A lens with a focal length f_1 collects the diffracted beams, which are then filtered with a spatial filter so that only -1 and 1 maxima are further allowed. Another lens (f_2) directs these beams onto a sample, where their interference field creates a transient grating. A probe beam is passed through a shutter, which can be closed for background measurements, then it is reflected from retroreflectors on a delay line and then focused on a sample. The diffracted and transmitted parts of the probe beam are recorded with the corresponding detectors. A single measurement is performed at two HBS positions, corresponding to 0 and $0 + 1\frac{1}{4}\Lambda_{HBS}$, changed by a stepper motor so as to eliminate the influence of the interference of a diffracted probe with a coherent background on the detector [161].

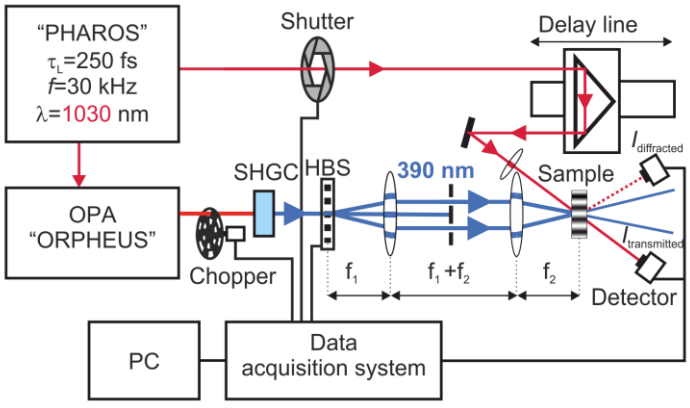

Fig. 2.8. LITG setup scheme.

A few samples were measured in another analogous LITG setup. In it the YAG:Nd^{3+} laser with a 25 ps pulse duration and a 10 Hz repetition rate was used. The third harmonic of the laser (355 nm – 3.49 eV) was shifted to 405 nm (3.06 eV) for the selective excitation of QWs by exploiting the Raman shift in distilled water [163]. The first harmonic was used to probe the samples (1064 nm – 1.17 eV).

2.2. Consistency between the measurement techniques

Consistency between the measurement techniques was ensured by carefully measuring the diameters of the excitation beams with the Thorlabs CCD Camera Beam Profiler. The diameter of each beam was calculated as the width of the Gaussian beam at its height of I_{peak}/e. Throughout the experimental setups, the excitation spot diameters were kept between 300-400 μm, whereas for probing spots with ~3 times smaller diameters were used. Excitation powers were measured by the OPHIR Nova 2 laser power meter placed right before the samples.

2.3. Samples under study

In this thesis the investigated samples mainly consist of different sets of multilayered GaN/InGaN LED-like structures. They were grown in different MOCVD (metalorganic chemical vapor deposition) reactors by several separate growers in Virginia Commonwealth University (VCU, USA), University of Cambridge (CU, United Kingdom), Aixtron SE (Germany), OSRAM Opto Semiconductors GMBH (Germany), Vilnius University Institute of Photonics and Nanotechnology (VU IPN, Lithuania), and University of California, Santa Barbara (UCSB, USA). The full list of samples is presented in Table 1 along with their most relevant parameters. The sets include samples: with pulsed or constant growth modes (Chapter 3.5), with and without intentionally made gross QW width fluctuations [164] (Chapter 3.6), with different types of interlayers (Chapter 3.1), with varying In content in the active region, with different QW, QB, or cap layer thicknesses, with varying growth temperatures. One set consists of non-polar m-plane samples grown on GaN templates (m1-m7), whereas all other samples were grown along the *c*-axis on sapphire. Additionally, samples differ in buffer thicknesses, doping concentrations, presence of EBL, etc., making them truly

diverse in parameters. More information will be presented in the corresponding chapters and/or can be found in the given references in Table 1.

The widths of the quantum wells/barriers and indium contents were obtained by TEM (transmission electron microscope) or XRD (X-ray diffraction) measurements, or were evaluated from growth procedures.

Table 1. Samples measured in this work with their most relevant parameters. Where available, sources are indicated with the corresponding references to learn more about the samples. Colors roughly match the PL emission.
* – values for the most intense PL peak only.

Sample name	**QW width** nm	**QW periods** count	**QB width** nm	**QW In content** %	**PL peak** eV at peak IQE	**FWHM** eV	**Source/ Ref.**
V1	2	6	3	23	3.00	0.14	VCU
V2	2	6	3	20	2.96	0.13	VCU
V3	2	6	12	20	2.93	0.14	VCU[125]
V4	3	6	3	17	2.93	0.13	VCU
Green	3	5		30	2.36	0.12	OSRAM [P5]
Cyan	3	5		26	2.50	0.14	OSRAM [P5]
SQW	4	1		22	2.76	0.14	OSRAM
Blue	3	5			2.79	0.11	OSRAM[165]
Sample A	3.5	5	6	8	2.68	0.16	IPN [P3]
Sample B	3.5	5	6	8	2.81	0.20	IPN [P3]
Sample 1	3.5	5	6	8	2.79	0.12	IPN [P3]
Sample 2	3.5	5	6	8	2.80	0.14	IPN [P3]
Sample 3	3.5	5	6	8	2.80	0.16	IPN [P3]
In1	4.7	5	18	5.1	2.98	0.18	AIXTRON [P2]
In2	4.2	5	18	8.4	2.77	0.22	AIXTRON [P2]
In3	6	5	18	11.3	2.82	0.17	AIXTRON [P2]
In4	5.8	5	18	13.2	2.74	0.17	AIXTRON [P2]
In5	5	5	18	23	2.63	0.20	AIXTRON [P2]
Quad	3.5	4	4.5	15	2.87	0.12	VCU[166]
Hexa	3.5	6	4.5	15	2.81	0.17	VCU[166]
1T	2.6	10	7.1	18.9	2.79	0.10	CU[164]

Q2T	2.6	10	7.1	17.4	2.78	0.11	CU[164]
2T	2.6	10	7.1	18	2.74	0.12	CU[164]
T-bounce	2.6	10	7.1	18	2.74	0.13	CU[164]
S1	3.1	5	7.1	12	2.74	0.15	IPN [P4]
S2	3.7	5	6.6	12	2.66	0.20	IPN [P4]
S3	3.1	5	7.8	12	2.56	0.27	IPN [P4]
S4	3.9	5	7.8	12	2.35	0.29	IPN [P4]
S5	4.2	5	8.7	12	2.31	0.27	IPN [P4]
S6	4.5	5	7.7	12	2.25	0.29	IPN [P4]
S8	4.5	5		12	2.21	0.39	IPN [P4]
S7	4.8	5	9	12	2.13	0.44	IPN [P4]
tp3	4.1	5	6.7	10.5	2.62	0.16	IPN
tp6	4.1	5	6.7	10	2.60	0.17	IPN
tp9	3.8	5	7.2	9.5	2.66	0.15	IPN
tp12	4.1	5	6.7	10	2.65	0.17	IPN
tp15	4.1	5	6.8	9	2.64	0.15	IPN
tp0	3.8	5	6.6	10.5	2.59	0.14	IPN
T810	3.8	5	6.6	10	2.63	0.13	IPN
T815	3.8	5	6.6	10	2.65	0.13	IPN
W1	1	8	12	25	2.90	0.14	UCSB
W2	1	8	12	25	2.86	0.14	UCSB
W3	2	8	12	25	2.51	0.14	UCSB
W4	2.7	8	12	25	2.26	0.13	UCSB
W5	4	8	12	25	2.69*	0.15*	UCSB
m1	8.2	3	8.8	13.3	2.93	0.27	UCSB
m2	8.2	3	8.8	9.2	3.04	0.10	UCSB
m3	6.8	3	8.8	13.1	2.98	0.15	UCSB
m4	7.8	3	8.8	10.4	2.98	0.23	UCSB
m5	8.2	3	14.8	13.2	2.93	0.21	UCSB
m6	4.5	3	14.8	13.5	2.83	0.29	UCSB
m7	4.5	3	14.8	13.5	2.87	0.25	UCSB

A typical LED structure grown on a sapphire substrate (Fig. 2.9) consists of a low temperature GaN buffer layer, followed by a few microns thick high-temperature GaN buffer layer, with its top part n-doped to serve as a contact

for a negative terminal in a full device (a cladding layer). Subsequently, an interlayer is usually grown, which can be a staircase electron injector (SEI) [P1] [127] to cool the electrically injected hot carriers, a superlattice [P3] or a bulk prestrain layer [167] for strain modification in the QWs, or another type of layer. A periodic structure of quantum wells and quantum barriers is then deposited, which is usually followed by an AlGaN EBL. On top, a protective p-GaN cap layer is formed, serving as a positive terminal contact. Based on other intents, LED structures can differ in the design with the incorporation of additional layers. Note that in the picture below, buffer and cap layers are not indicated as n- or p-, because not all structures were intentionally doped. The sequence of layers in non-polar structures are similar, except for different substrates used.

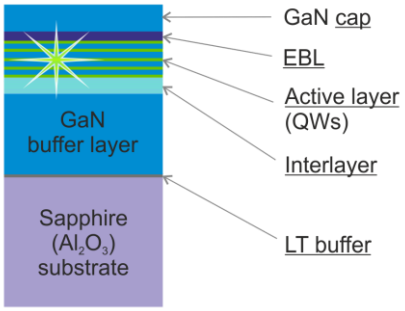

Fig. 2.9. Typical structure of samples presented in this work.

2.4. Absorption of the excitation pulse in a u-GaN buffer and active layers of the structures

Many authors evaluate PL IQE in nitride-based quantum structures by assuming that at near 0 K temperatures non-radiative recombination, which is supposedly thermally activated, vanishes, and that IQEs peak at 100% [66]. Then a room temperature IQE is simply the ratio of the PL intensity at RT and the PL intensity at low temperature. However, there are no straightforward proofs verifying that non-radiative recombination channels can be fully suspended at 0 K [168]. What is more, this assumption can be fundamentally wrong, because the absorption can happen with the involvement of the defect levels – it is then likely that the excited carrier is already trapped in the defect state, which will eventually be freed by a non-radiative recombination process.

The most direct way of evaluating the IQE is the three measurement approach (Chapter 2.1.1). However, it works well for individual layers, where

absorption is uniform throughout the entire thickness. In the case of multilayered heterostructures like LEDs, the situation gets more complicated, since absorption of incident light may take place in layers other than the active one, where the IQE is supposed to be measured. Not only the latter procedure is burdened by the unwanted light emission from other layers, it becomes difficult to correctly estimate the amount of directly absorbed light A_{dir}, which leads to an underestimation of IQE. Tuning the pump wavelength for the selective excitation of QWs partially resolves this problem, as the interband absorption in other layers can be prevented, however absorption through defects remains active. Transitions can occur between the valence band or a shallow/deep acceptor and a deep/shallow donor, or between a shallow/deep acceptor and the conduction band. The presence of such energy states within the bandgap can be evidenced by characteristic yellow or blue luminescence bands [39,169] [P1].

The interband transitions are generally much more frequent than the defect-assisted transitions, and the latter are relatively negligible in thin layers, such as the selectively excited QWs. However, in a thick layer, such as an unintentionally doped GaN buffer, the amount of light absorbed with the assistance of defects can be quite high. Therefore, to evaluate this amount, several selected structures from this work were etched by the reactive ion etching (RIE) with Cl_2 plasma to remove the top-most layers, including the cap, the active layer and the interlayer, leaving only the u-GaN buffer on sapphire. What is important is that knowing the correct amount of light that the active layer absorbs not only allows the correct estimation of IQE, but it also enables the evaluation of the absorption coefficient, which can be used for calculation of distinct carrier densities in samples without solely relying on literature values. This way, carrier density-dependent processes can be directly compared.

Prior to the etching, samples were split in half so that one part could be etched and another part would be left unmodified in order to compare them later. The etching rate of ~6 nm/s was estimated from a reference sample, where 75 s of etching resulted in a removal of ~450 nm of the topmost material. The other samples were then etched for 20 s resulting in a total thickness of the removed material to be ~120 nm, just enough to expose the GaN buffer. It is assumed that the quality of the surface did not change after the etching since light scattering did not increase.

The light absorption measurements were carried out in an integrating sphere, following the steps of a three-measurement approach. Samples were

tested for any residual photoluminescence from the QWs to make sure they were completely removed. After that, total collected intensities of the excitation pulses were compared. In Fig. 2.10 it can be seen that after the incident 392 nm pulse passes through an etched sample, its intensity is higher (black dashed line) when compared to the case where light is passed through an unetched sample (black solid line) by an amount that the top layers (mostly QWs) absorb. However, the direct absorption still takes place in the remaining structure, which is evidenced by the increase of the laser line intensity when the etched sample is moved out of the way of the incident light (dashed blue line). Note that during the experiment it was ensured that light reflected from the sample surface remains inside the integrating sphere, therefore the reflection is included in the collected excitation pulse intensity in all cases.

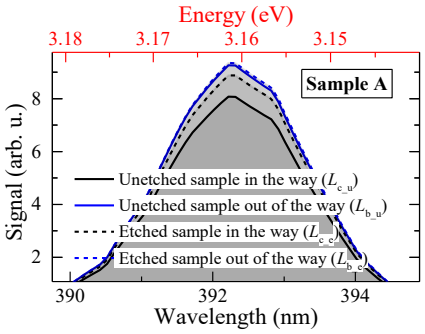

Fig. 2.10. Excitation pulse spectra with the unetched (solid lines) and etched (dashed lines) parts of the sample (Sample A from Table 1) present in the integrating sphere. Black lines correspond to spectra when the sample is in the way of the excitation pulse, blue lines correspond to the spectra when the sample is out of the way.

The calculations in four etched structures show that ~5% of the incident 392 nm laser pulse intensity is in a 3 μm thick u-GaN buffer layer (Fig. 2.11). This becomes very important when evaluating IQEs in thin or weakly absorbing active layers. An example of this is a single QW structure (SQW in Table 1), which absorbs only 8% of the total light trapped inside the integrating sphere. This leads to the modification of Eq. (2.1) and Eq. (2.2) by subtracting the amount of directly absorbed light in a buffer layer $A_{dir_{GaN}}$ [P5]:

$$A_{dir_{eff}} = A_{dir} - A_{dir_{GaN}} = \frac{L_{c_u}}{L_{b_u}} - \frac{L_{c_e}}{L_{b_e}}, \tag{2.21}$$

$$IQE = \frac{P_c - (1 - A_{dir_{eff}})P_b}{L_a(A_{dir_{eff}})}. \tag{2.22}$$

The quantities in these equations are as follows: L_{c_u} is the intensity of the excitation pulse when the unetched sample is in its way, L_{b_u} is the intensity of

the excitation pulse when the unetched sample is out of its way, L_{c_e} is the intensity of the excitation pulse when the etched sample is in its way, and L_{b_e} is the intensity of the excitation pulse when the etched sample is out of its way (Fig. 2.10). This modification increases the evaluated efficiency in the said SQW structure by ~2.7 times.

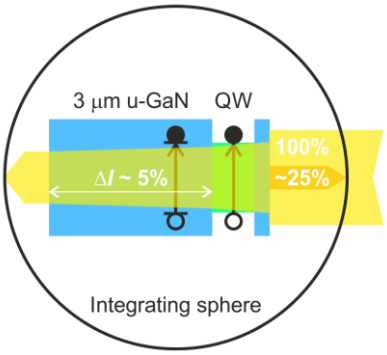

Fig. 2.11. Scheme of a 392 nm excitation pulse attenuation in a multilayered GaN/InGaN structure. ~25% of the incident pulse is reflected back into the integrating sphere, with ~5% lost in the u-GaN buffer layer.

The absorption coefficient α for u-GaN can be calculated using the exponential absorption law

$$I = 0.75I_0 - \Delta I = 0.75I_0\exp(-\alpha d), \quad (2.23)$$

where d is the thickness of the layer, I_0 – intensity of the incident laser pulse, ΔI – loss of the laser pulse in the layer, equal to $A_{dir_{GaN}}$. The 0.75 multiplier in the equation is due to the reflectance of the incident laser pulse, which was measured to be ~25%. A rough estimation in a GaN-sapphire heterostructure with refractive indices n = 1, n = 2.6, and n = 1.8 for air, GaN, and sapphire, respectively, yields ~26.8% reflectance when light attenuation is not included. The reflectance from GaN alone is estimated to be ~19.8%. Therefore the measured reflectance is probably not only from the surface, but from other boundaries within the sample as well. Since these different values only negligibly alter the results, the measured value was used. The estimated absorption coefficient for the 392 nm laser pulse in 3 μm u-GaN is 225 cm^{-1}, which is in good agreement with the 200 cm^{-1} value for the 400 nm laser pulse, obtained in [170]. A similar value was estimated from the measurements in the as-grown 2 μm thick u-GaN layer (Fig. 2.12). For u-GaN layers with thicknesses ranging from 4.8 to 25.5 μm, the absorption coefficient appears to be smaller, probably due to a better crystalline quality and a lower density of defects in overgrown GaN [171]. Therefore, in the case of a

relatively thick underlying u-GaN layer, smaller absorption coefficients may need to be used. As for the n-GaN underlying layers, the absorption coefficient should not differ much, since u-GaN layers themselves are usually n-type, with the density of impurities on the order of ~10^{17} cm^{-3}. Furthermore, the defect-assisted transitions related to yellow luminescence should be mostly influenced by the acceptor type impurities, which create deep levels in the bandgap [39].

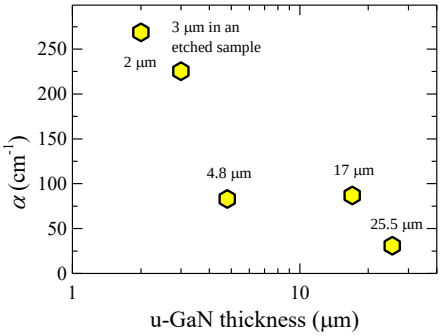

Fig. 2.12. Absorption coefficient in different thickness u-GaN layers, including one from an etched sample.

One of the etched samples had only some of the p-GaN cap layer removed (~120 nm) as evidenced by the unchanged luminescence intensity from QWs, which resulted in a ~1.34% drop of the direct absorption of the laser pulse in this sample. It allowed a rough estimation of the absorption coefficient in p-GaN of ~1.5×10^{3} cm^{-1}. It meets the idea that p-GaN should absorb more light than u-GaN due to a higher density of acceptors. However, more measurements should be performed for clarification, and with the assumption that p-GaN layers are sufficiently thin, absorption in p-GaN was not taken into account in this work in IQE calculations.

The absorption coefficients of the active layers of the samples were calculated in the same way as in u-GaN by taking the sum of all QW widths in the structures as d (Fig. 2.13). The essence of absorption coefficient evaluation is that carrier densities can be calculated individually for different samples, which allows a direct comparison of carrier density-dependent processes. The complex nature of absorption in InGaN QWs, where localization, excitonic effects, and energy levels due to the quantum confinement have to be taken into account, results in the scattering of α in the range of the order of the magnitude, with values of 2.6×10^{4} cm^{-1} and 4.1×10^{5} cm^{-1} obtained in samples with the smallest and largest absorption coefficients, respectively. This means that for the same excitation energy density, carrier

density can vary nearly as much in different samples, even though they can have the same PL emission wavelength.

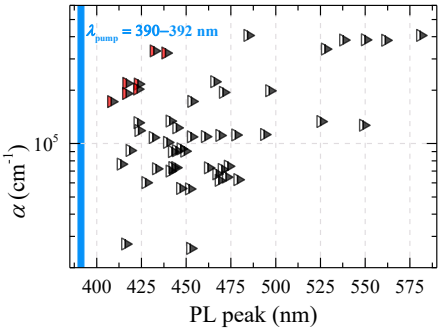

Fig. 2.13. Calculated absorption coefficients α for 390-392 nm excitation pulses (indicated by a blue line) in the samples from this work vs PL peak wavelengths at the corresponding droop onsets (carrier densities where IQEs peak). Red interior marks m-plane samples.

Knowing the individual absorption coefficients it is possible to calculate the actual non-equilibrium charge carrier concentrations at different excitation energy densities. This was done by using the expression

$$N = \frac{I\alpha}{h\nu_{pump}} \cdot \exp(-\alpha d), \tag{2.24}$$

where I is the excitation energy density that reaches the active region of the structure (without the 25% reflection from the surface and other boundaries within the sample), ν_{pump} – the frequency of incident photons, d – the overall thickness of QWs in the active layer. It should be noted that charge carrier density should be the same in all the QWs that constitute the active layer, as the exponential decrease of intensity changes negligibly after passing through it.

To sum up, the absorption in u-GaN takes place even if the pump wavelength does not exceed the bandgap, due to absorption in defect states. A 3 μm thick u-GaN buffer layer in the structures from this work absorbs ~5% of the incident 390-392 nm laser pulse trapped in an integrating sphere, resulting in a 225 cm^{-1} absorption coefficient. This has to be taken into account when calculating IQEs in multilayered QW structures by using the three-measurement approach. Knowing the correct amount of light that the active layers absorb, the absorption coefficients can be evaluated, which allows a precise calculation of carrier densities for individual samples, thus allowing a direct comparison of carrier density-dependent processes.

3. RESULTS AND DISCUSSION

3.1. Enhancement of quantum efficiency in InGaN quantum wells by using a superlattice interlayer

GaN-based structures for LEDs are predominantly grown on sapphire substrates, as they are much cheaper and more abundant than GaN substrates. However, there is a large mismatch between the lattice constant and thermal expansion coefficient of GaN and sapphire, which results in a considerable strain and, consequently, a large amount of dislocations and high internal electric fields that quench the IQE. Several technological modifications have been developed for strain management and dislocation density reduction, such as use of low temperature buffer layers [17,171], SiO_2 masks with the openings for overgrowth [172,173], interlayers of varying In content [P1], or short period superlattices (SL) [174]. It has been demonstrated that the latter increase IQE [175,176] and reduce PL peak shifting with increasing the carrier injection [174] due to supposedly smaller defect density and lower internal electric fields.

This chapter presents the effects of a SL insertion through analysis of carrier dynamics in two similar MQW structures on 3 μm sapphire substrates, grown with (Fig. 3.1) and without a SL (Sample A and Sample B correspondingly, see Table 1). The superlattice consists of 8 periods of $In_{0.06}Ga_{0.94}N$/GaN heterostructures of ~32 nm total thickness; such a structure was an optimized result obtained from several growths. The active regions comprise five 3-4 nm wide $In_{0.1}Ga_{0.9}N$ wells, separated by 6 nm GaN barriers. As expected, increase in IQE is achieved in the structure with a SL, which is explained by the reduction of the internal electric fields and carrier delocalization.

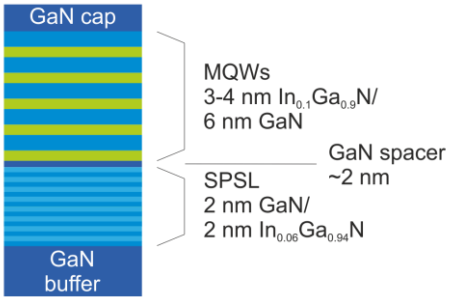

Fig. 3.1. Schematic of Sample A (with a short period superlattice).

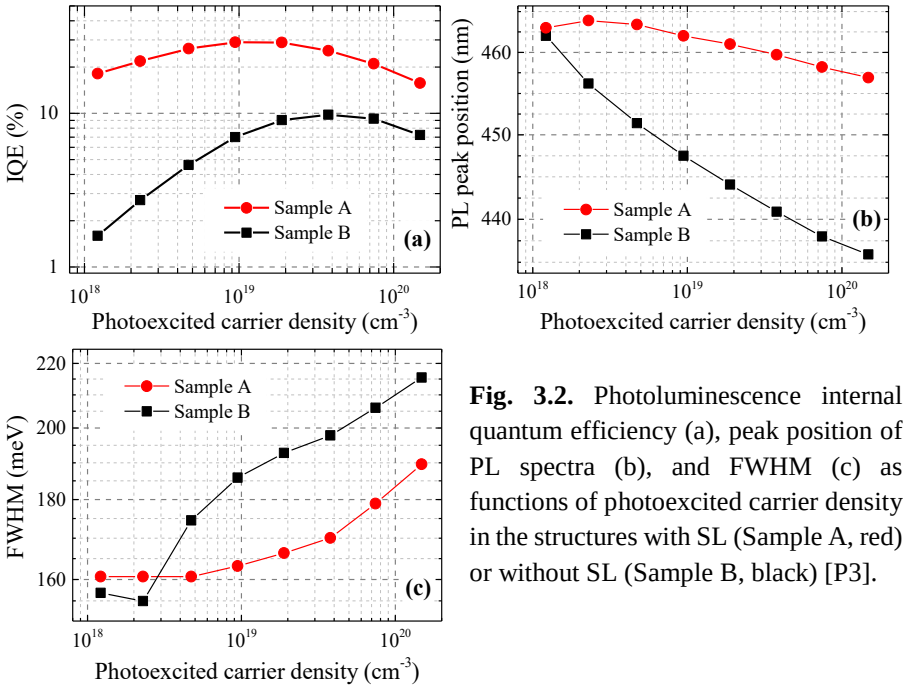

Fig. 3.2. Photoluminescence internal quantum efficiency (a), peak position of PL spectra (b), and FWHM (c) as functions of photoexcited carrier density in the structures with SL (Sample A, red) or without SL (Sample B, black) [P3].

Fig. 3.2(a) shows the IQE as a function of photoexcited carrier density. Both IQE curves reveal the typical features of "efficiency droop" in InGaN QWs: IQE value increases up to carrier densities of (1-3)×10^{19} cm^{-3} and starts to decline at higher excitations. The insertion of a SL results in a threefold increase of the peak IQE value (30% in Sample A versus 10% in Sample B) and a much "flatter" IQE vs excitation curve. Meanwhile, a rather large blueshift of PL peak position with excitation is observed in Sample B (170 meV), compared to the shift by 40 meV in Sample A (Fig. 3.2(b)). Consequently, the full width at half maximum (FWHM) of PL spectrum in Sample B is considerably broader at high excitations, while at low ones the FWHM values are similar in both structures (Fig. 3.2(c)). Different blueshift and emission wavelengths can be attributed to the effects of the internal electrical field. A larger blueshift with excitation indicates a stronger internal piezo electrical field in Sample B due to a larger strain, while the much shorter emission wavelengths at high carrier densities point out to a smaller indium amount in this structure. Reported strain relaxation due to the SL [174] and slower indium incorporation in the compressively strained QWs [177] support the latter assumption. In addition, TEM and XRD data (not shown here)

suggest that QW growth rate is larger in the more strained structures. As a result, thinner QWs with a higher In content can be expected in Sample A, which is favorable for higher IQE [178,179] and a smaller efficiency droop. The impact of the internal electrical field, however, cannot fully account for the differences in IQE, especially at high carrier densities. Also, a large PL peak shift can be caused by saturation of localized states at the low energy side of the PL spectrum [180–182] [P2].

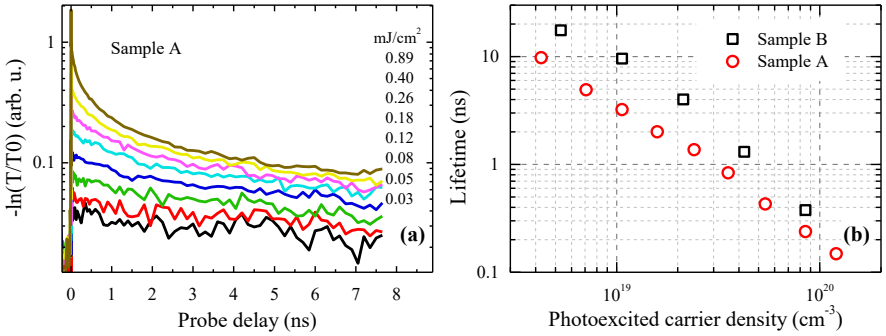

Fig. 3.3. (a) FCA kinetics in Sample A at various excitations. (b) Instantaneous carrier lifetime at 90-200 ps delay as a function of photoexcited carrier density [P3].

Time-resolved FCA, PL, and DT measurements were carried out for a direct observation of carrier dynamics and discrimination between the radiative and non-radiative recombination pathways. FCA technique allowed determination of the average lifetime of the net carrier population, while DT provided complementary information on temporal changes in the occupancy of particular states. Fig. 3.3(a) shows the FCA kinetics recorded in Sample A for various excitation energy densities within 30÷890 μJ/cm^2 range. The peak amplitude of the transients increases linearly with carrier density within the entire excitation range, thus confirming linear increase of photoexcited carrier density and the absence of absorption bleaching. Precise calibration of carrier density N and density-dependent recombination constants of "ABC" model [102] (standard ABC model is presented in Chapter 3.7) are feasible under these conditions. For the sake of estimation simplicity, instantaneous decay times at the very initial part of the kinetics (within 90-200 ps after the pump) were calculated as functions of N (Fig. 3.3(b)). These dependencies revealed close-to-linear decrease of the lifetime with excitation, which may be attributed either to the increase of the radiative recombination rate ($1/\tau_{rad} \sim B_{rad}N$, with B_{rad} being the radiative recombination coefficient) or

to the diffusion-driven non-radiative recombination after carriers escape from the potential minima and are captured by traps [120], which can be expressed by a non-radiative recombination rate $A(N) = B_{nr}N$. If both processes take place simultaneously, only a part of total density-dependent recombination rate can contribute to the radiative decay, i.e. $B^* = B_{rad} + B_{nr}$, in agreement with previous observations [122,183].

The described model was applied for the analysis of the excitation-dependent carrier lifetime. Following the standard ABC model, the constant non-radiative recombination coefficient *A* (or the excitation-independent non-radiative lifetime $\tau_{NR} = 1/A$) and the effective recombination coefficient $B^* \sim 1/N$ can be obtained from the fitting of the decay time $\tau = (A + B^*N + CN^2)^{-1}$; here, *C* is the Auger recombination term. However, in this study it was chosen not to use the Auger term, which should be important only at carrier densities well above 10^{19} cm^{-3}. For both samples $\tau_{NR} = 1/A \approx 35$ ns was estimated from TRPL transients at long delay times (>30 ns); this term is dominant at carrier densities below 10^{18} cm^{-3}. The values of recombination coefficient *B** were estimated from Fig. 3.3(b) as 0.8×10^{-11} cm^3/s and 2.4×10^{-11} cm^3/s for samples B and A, correspondingly. The ratio of three between the *B** as well the IQE values agree quite well for these samples, suggesting that competition between the radiative and non-radiative processes varies with excitation and depends on each sample's structural quality. On the other hand, different IQE values may be a consequence of different density of carriers contributing to the radiative recombination. The measured IQE curves were fitted with the modified AB*C model:

$$IQE = \frac{B_{rad}N}{A+(B_{rad}+B_{nr})N} \quad (3.1)$$

To better account for the IQE droop, saturation of B_{rad} with excitation due to the phase-state filing was included [184]:

$$B_{rad} = \frac{B_0}{1+\frac{N}{N^*}} \quad (3.2)$$

Here, B_0 is the unsaturated recombination coefficient and N^* is the threshold carrier density of saturation. $B^* = B_{rad} + B_{nr} = const$ was also assumed since FCA measurements showed no saturation of the net B^* term. A good fit of IQE curves was obtained under these assumptions, without adding the Auger term (Fig. 3.4). Eq. 3.1 allowed obtaining exact absolute IQE values, while the standard ABC model with *C* term of 2×10^{-31} cm^6/s yields an overestimated IQE. Fitting parameters were as follows: $1/A$=26 ns, B^*=2.4×10^{-11} cm^3/s, N^*=9.4×10^{19} cm^{-3}, B_0=0.9×10^{-11} cm^3/s (Sample A);

$1/A$=15 ns, B^*=0.8×10^{-11} cm^3/s, N^*=20×10^{19} cm^{-3}, B_0=0.11×10^{-11} cm^3/s (Sample B). Net B^* values were taken from the fit in Fig. 3.3(b). Analysis of Eq. 3.1 shows that the peak IQE value is governed by the ratio of B_{rad}/B_{nr}: this ratio is 0.6 and 0.16 in samples A and B, which correlates with IQE peak values of 30% and 10%. The efficiency droop, according to the modelling results, occurs due to the expected saturation of B_{rad} [185] and predominantly due to the increase of B_{nr} [121,122]. The initially constant A term, being relatively small in the samples, has impact only at lower excitations. Different values of radiative recombination term B_{rad} in samples can be attributed to the quantum confined Stark effect: stronger electrical field results in a larger separation of the electron-hole wave functions and a smaller radiative recombination rate in Sample B. It should be noted that N^* values can also be affected by the electrical field, since it is not accounted for in the simplistic model (Eq. 3.1).

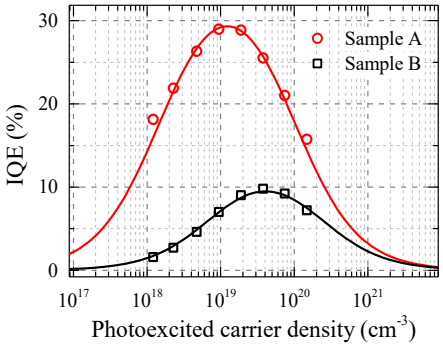

Fig. 3.4. Fitted IQE curves using the modified AB*C model (Eq. 3.1) [P3].

To assess the physical reasons behind the lower radiative recombination rate in Sample B, PL and DT spectra at various excitations and delay time instants were compared (Fig. 3.5). DT signal has a negative sign indicating the bleaching of absorption in the bandgap vicinity. A shift between the spectral positions of DT and PL spectra indicates that absorption takes place in the higher energy states (presumably – in the extended states of QWs), then carriers relax to the low energy localized states, where the radiative recombination occurs. An overlap between DT and PL spectra pointed out to the most efficient spectral range of carrier transfer from high to low energy states. This process may influence the PL efficiency, since the PL efficiency from the high energy states is low if compared to that from the localized low energy states [60]. At 46 μJ/cm^2 excitation (corresponding to 6.2×10^{18} cm^{-3} carrier density), the shift between PL and DT spectra is 25 nm (150 meV) and

31 nm (200 meV) in samples A and B, correspondingly. Larger separation between the absorption and PL peaks results in smaller IQE in Sample B, especially at lower excess carrier densities. With increasing the excitation, PL spectra broaden as the localized states get saturated and the fast PL transients point to emission from the higher energy states. This broadening is larger in Sample B (Fig. 3.2(c)), pointing out to the lower density of localized states in it with respect to Sample A.

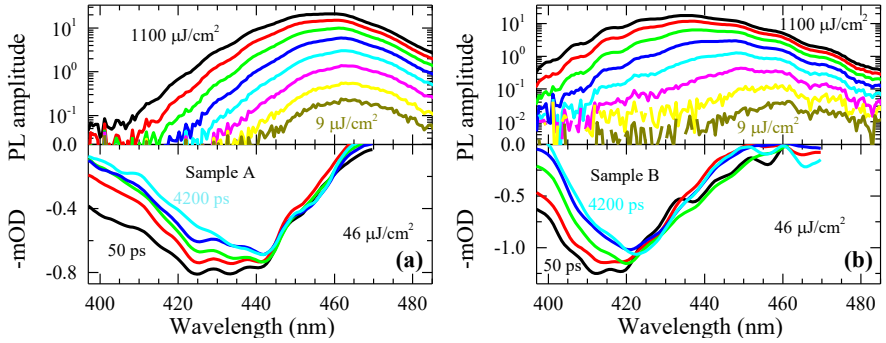

Fig. 3.5. Time-integrated PL spectra at various excitations (top figures, excitation range is indicated on the plot) and DT spectra at 46 μJ/cm^2 excitation and various delay times (bottom figures) in samples with SL (a) and without SL (b) [P3].

Stronger carrier localization in Sample A is further evidenced by the dependence of the diffusion coefficient D on carrier density (Fig. 3.6). D is equal to 0.5 cm^2/s and 1 cm^2/s at carrier density of 1×10^{19} cm^{-3} in samples A and B, correspondingly. It increases with excitation in both samples, but the increase is more pronounced in Sample B. LITG gives the ambipolar diffusion coefficient, which under the used experimental conditions is proportional to the hole mobility [144]. Higher mobility of free carriers (holes) in Sample B are explained by a larger part of free carriers occupying the extended states in QWs, as compared to Sample A. With increasing the excitation, a relatively larger part of carriers are being transferred to the extended states, and this is reflected in the asymmetrical broadening of DT and PL spectra towards the higher energies. A similar effect has been reported previously [122]. Therefore, it can be suggested that larger increase in D value is also a signature of faster non-radiative recombination and, thus, lower IQE at high excitations. Delocalization of presumably holes and a subsequent increase of non-radiative recombination of carriers with increasing density is the physical origin of the term B_{nr} and a possible reason for the efficiency droop.

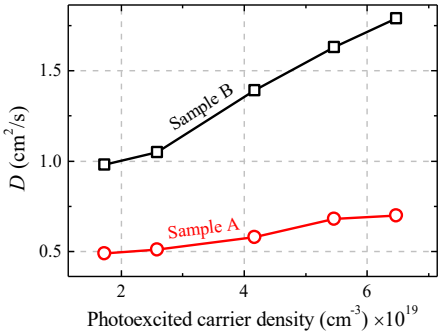

Fig. 3.6. Diffusion coefficient as a function of the photoexcited carrier density [P3].

In summary, a detailed investigation by all-optical techniques with time resolution was employed to analyze the physical origin of the droop and the improvements that the use of a short-period superlattice interlayer provides. It was found that the insertion of the SL results in a lower strain and smaller internal electric fields in the above grown MQWs. Furthermore, weaker delocalization was achieved, and as an inverse correlation between the IQE values and the carrier diffusion coefficient has shown, it has a crucial influence on the IQE and its droop. The combination of these improvements yielded a threefold increase in the peak IQE. A simple model based on the modified AB*C rate equation with the excitation dependent non-radiative recombination at the defects term was used to account for the increasing rate of non-radiative recombination with excitation. With the addition of the saturation of the radiative recombination coefficient due to the phase-space filling, it successfully described the IQE droop.

3.2. Impact of carrier localization and diffusion on photoluminescence in highly excited InGaN structures for cyan and green LEDs

Localization of charge carriers is of crucial importance to InGaN light emitting devices since it governs carrier transport and ensures high radiative efficiency, a fact clearly evident from the previous chapter. Role of carrier localization becomes stronger with the increasing indium content since it is accompanied by a larger disorder in the distribution of indium atoms [93]. On the other hand, higher indium content also results in higher strain, stronger internal electric fields, and larger defect densities. Stronger carrier localization can further separate the carriers from the defect states, but it may also result in the decrease of the radiative recombination coefficient [93,186] due to non-correlated potential fluctuations of valence and conduction bands and a smaller overlap of electron and hole wave functions [74,156]. Carrier localization can also alter non-radiative recombination (SRH and Auger) rates [186,187]. An opposite process of carrier delocalization takes place at high temperatures and/or carrier densities, which increases carrier mobility and non-radiative recombination rate leading to the onset of efficiency droop at carrier densities that are lower than those required for Auger recombination [120,122,188].

In this chapter, the impact of localization to carrier dynamics is studied by analyzing the time and excitation-dependent spectra of photoluminescence and absorption, as well as diffusion coefficient, provided by TIPL, TRPL, DT, and LITG techniques. Concerted application of PL and DT enables monitoring the electronic transitions in both the localized and extended states, while LITG allows overcoming a certain limitation of SNOM (scanning near-field optical microscopy) and confocal microscopy, were only a product of the carrier diffusion coefficient and the carrier lifetime – carrier diffusion length – can be measured [189–191]. An untypical redshift in PL peak position is revealed, which increases with time and carrier density and cannot be related neither to band gap renormalization nor to the electric field dynamics. Based on the analysis of DT and PL data, the shift is attributed to a slow relocalization of carriers from shallower to deeper potential minima. It is shown that carrier diffusivity increases with density due to delocalization and that there is a correlation between the growth of diffusivity and the onset of the efficiency droop.

The studied samples are two InGaN/GaN multiple quantum well (MQW) LED structures that emit light in the cyan and green spectral ranges with

characteristic peak wavelengths of 500 nm and 530 nm (hereafter, the structures are referred to as ‘‘cyan’’ and ‘‘green’’, respectively; for more information see Table 1). The samples consist of a standard sequence of LED epilayers: a buffer layer (unintentionally doped GaN), a moderately n-doped GaN:Si current spreading layer followed by a highly n-doped GaN:Si contact layer, an active layer consisting of a stack of five InGaN QWs with 3 nm wide wells (with an indium content of ~26% for cyan and ~30% for green emission), separated by GaN barriers, and a p-doped AlGaN:Mg EBL as well as a p-type GaN:Mg contact layer on top. Since the growth processes and layer structures of both samples are basically identical, the In distributions are estimated to be fairly similar, although the amplitude of variations might be a bit larger in the sample with a higher In content [192].

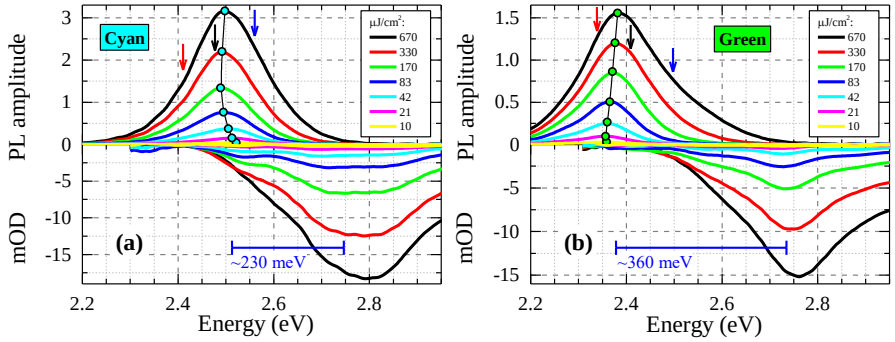

Fig. 3.7. Time integrated PL (top) and instantaneous (at 120 ps delay) DT (bottom) spectra in the cyan (a) and green (b) QW structures at various excitations. The arrows indicate the spectral positions where PL decay times shown in Fig. 3.9 were assessed [P5].

Fig. 3.7 shows the TIPL (top pictures) and DT (bottom pictures) spectra in the cyan (a) and green (b) QW samples recorded at various excitation levels. At low excitation (10 μJ/cm^2), the PL lines are centered at 2.53 eV (490 nm, cyan) and 2.36 eV (525 nm, green) and have FWHMs of around 140 meV for both samples. The IQE curves (see Fig. 3.10(b)) are typical for the optically pumped InGaN QWs, with the onset of efficiency droop at ~60-70 μJ/cm^2 (this corresponds to the carrier density of ~10^{19} cm^{-3}). The measured peak IQE values reach 13±3% in the cyan and 15±3% in the green structures; it should be noted that light extraction was not optimized in the structures, however it is assumed to be the same in both samples due to their identical structures. Since the PL linewidth is determined by the fluctuations of hole localization

energy due to the random alloy disorder [92] and a direct link was shown to exist between the disorder and luminosity of polar InGaN layers [193], similar FWHMs and IQEs of PL emission indicate similar structural quality of investigated structures, despite higher indium content in the green QWs. DT signal has a negative sign (bottom pictures in Fig. 3.7) indicating the absorption bleaching due to the state filling effect [194]. DT spectra are shifted towards the higher photon energies with respect to the PL peak by ~230 meV (cyan) and ~360 meV (green). Stokes shift is considerably larger in the green sample, which points out to stronger carrier localization in this structure [195].

Two trends are visible in TIPL spectra with increasing excitation: (i) the width of PL spectra increases and (ii) a redshift in PL peak position at low excitations is followed by a blueshift at high excitations; this is especially noticeable in the cyan sample (indicated by open circles in Fig. 3.7). The PL line broadening with increasing carrier density has been attributed to the gradual saturation of shallow localized states and the consequent population of both higher and lower energy states [181,196]. The behavior of PL line position, however, is untypical: in polar QWs, one expects a PL blueshift with excitation due to the screening of the internal electrical field and state filling [197]. Only at very high carrier densities, a redshift of PL band due to band gap renormalization has been observed [180].

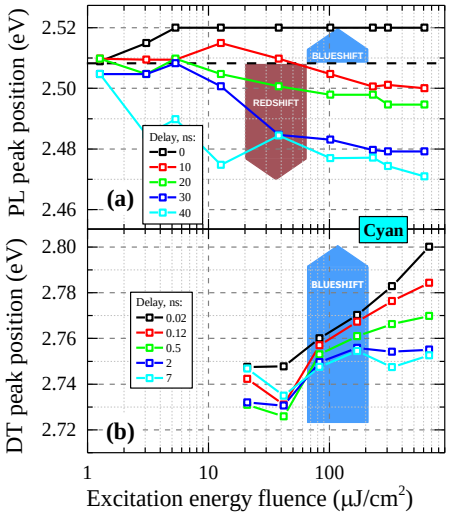

Fig. 3.8. Peak positions at various time delays as functions of excitation energy density obtained from (a) PL and (b) DT spectra [P5].

To investigate the temporal evolution of PL peak position, TRPL and DT spectra were recorded at various excitations. Fig. 3.8 displays the PL and DT peak positions for several delay times as functions of excitation in the cyan sample. It is seen from Fig. 3.8(a) that the PL redshift at high excitations evolves in time span of tens of nanoseconds. Thus, within first 5 ns only a blueshift in PL peak position is seen. A closer look into the early stage of spectral dynamics is provided by DT measurements with a better time resolution (Fig. 3.8(b)). Only the blueshift of DT spectra is seen within 7 ns delay; but the difference between the DT peak position at high and low excitations constantly decreases with increasing delay (from ~50 meV at 20 ps delay to ~20 meV at 7 ns delay). By comparing the DT and PL spectra, it is estimated that the redshift becomes dominant between 7 ns and 10 ns. At 40 ns, the PL peak in the cyan sample redshifts by 30±4 meV from 2.5 eV to 2.47 eV. In the green sample the picture is qualitatively similar, but the shift is smaller reaching 20±4 meV after 40 ns at the highest excitation (not shown).

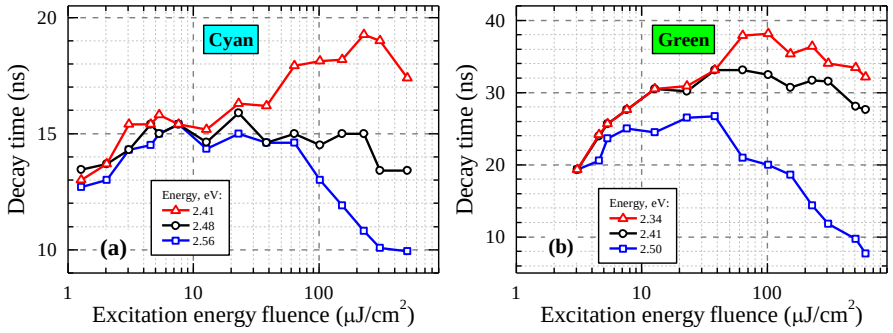

Fig. 3.9. PL decay time at different spectral positions (the blue wing, the central part, and the red wing of a corresponding PL spectrum; the exact spectral positions are indicated by arrows in Fig. 3.7) as a function of excitation in cyan (a) and green (b) QW structures [P5].

In Fig. 3.9, the PL decay times at three different spectral positions are shown as functions of excitation. Two excitation regions can be distinguished: low excitations below 10 – 20 μJ/cm^2, where the PL decay rate remains roughly the same at all wavelengths within the PL band, and high excitations, where the blue PL wing decays faster than the red one. In the low excitation range, the PL decay time in the cyan and green samples falls within 12 – 15 ns and 20 – 30 ns, correspondingly. It is interesting to note, however, that almost twofold difference in the carrier lifetime does not result in substantial

differences in peak IQE values. This fact suggests that the PL lifetime by itself is not a decisive indicator of the LED emission efficiency, as it reveals the carrier dynamics in a rather narrow spectral window with respect to DT [198].

Next, the possible origins of the PL redshift are discussed. The band gap renormalization (BGR), screening of the electrical field, and carrier redistribution between the localized states will be considered as the possible causes of this redshift. BGR is a fast process appearing instantly after generation of free carriers. Its origin is the interaction between electrons (holes) when their density becomes high enough, as they start to repel each other due to Coulomb forces, with the addition of particles with the same spin avoiding each other due to statistical reasons (Pauli exclusion principle) [199]. The net result is the screening of carriers that leads to a decrease in the energy of the conduction band minimum (an increase in the energy of the valence band maximum). A shift of PL emission band due to BGR is usually presented as

$$E_G(N) = E_{G0} - \beta N^{1/3}; \quad (3.3)$$

here, N stands for carrier concentration and β is a fitting coefficient with the reported values in the range $(1.66 – 2) \times 10^{-8}$ eV cm [180,197]. BGR should appear instantly after the excitation even at small delay times; redshift of PL position due to BGR must increase with excitation, as it was observed in $In_{0.2}Ga_{0.8}N$ QW by G. Sun et al.[180]. In contrast, the PL peak is blue shifted at small delays (see black curve in Fig. 3.8(a)) making BGR an unlikely reason behind the PL redshift at later times.

Similarly, a redshift of PL emission due to the QCSE in a QW with an internal electric field can be expressed as

$$h\nu(N) = E_G(0) - edF(N); \quad (3.4)$$

here d is the QW thickness, e is elementary charge and $F(N)$ is the internal electric field strength

$$F(N) \approx F_0 - \frac{Ned}{\varepsilon\varepsilon_0} \quad (3.5)$$

with the maximum electric field strength F_0, the electric constant ε_0, and the static relative dielectric constant ε [197]. QCSE results in a rapid PL blueshift due to the screening of the electrical field by free carriers and a subsequent field recovery when carriers recombine; the spectral shift is proportional to free carrier density N. While this situation resembles that depicted in Fig. 3.8, one has also to bear in mind that the redshift due to recovery of internal field cannot exceed the initial blueshift, i.e. the PL peak position with increasing delay should approach that at small excitations. In the samples under study,

the redshift at long delays and high excitations exceeds the initial blue shift considerably, thus indicating that screening and a subsequent recovery of the internal electrical field cannot single handedly explain the PL spectral dynamics.

Hence, the observed redshift of PL emission at long delays is attributed to the redistribution of carriers from the initially occupied shallower localized states to deeper ones. This is feasible in a system with large potential inhomogeneities and many local potential minima that are considerably deeper than the thermal energy k_BT [200,201]. After the excitation, non-equilibrium carriers are randomly distributed between these minima. At low densities, the quasi-Fermi energies of electrons and holes are low, thus carriers can get trapped in the shallower potential minima. Increasing excitation raises the quasi-Fermi levels increasing probability for carriers to escape the shallower minima and reach the deeper ones. It was proposed that localization of carriers into deeper states is slower than that into the shallower ones [181]. This model agrees with a larger PL redshift at higher excitations and longer delay times, presented in Fig. 3.8. Similar arguments were used in explaining a tendency of the small redshift of PL spectra (few meV) with increasing excitation power observed by near-field photoluminescence in semipolar QWs [190]. Also, it is in line with the fact that at low excitations the PL decay time is the same for all states within the PL bands (Fig. 3.9). Usually, the PL decay time is constant in the red part of PL band for the localized states and then exponentially decreases with photon energy for the extended states [198,202]. In the case of samples from this work, the distribution of localized states must be very broad and emission from these states seems to govern the entire PL line at low excitations. It can be concluded that the deep localized states become saturated with increasing excitation resulting in the transfer of carriers into the extended mobile states, which is reflected in the appearance of a fast recombination component within the blue PL wing with the recombination rate increasing with excitation (Fig. 3.9). Within this model, a smaller PL redshift and a longer PL decay time (up to the excitation where the extended states come into play) in the green sample indicates relatively small disorder and smooth indium distribution.

To investigate the dependence of carrier mobility on excitation, the ambipolar diffusion coefficient D (diffusivity) was measured using LITG technique; the obtained values are shown in Fig. 3.10(a) as functions of excitation. It should be noted that D values were extracted within the first nanosecond after the photoexcitation when the carrier density is close to the

initial one. It is seen that (i) diffusivity non-monotonously increases with excitation and (ii) D values in the samples under study differ below 40 μJ/cm^2 but become very similar at higher excitations. Increase in D with excitation was observed previously in a blue LED structure and was explained by the increasing ratio of carriers in the mobile extended states with respect to those in the localized states; a change in the occupancy was proposed as a reason for the increasing rate of non-radiative recombination with excitation [122]. The different recombination rates in cyan and green samples at low excitations can be therefore attributed to different diffusivity, which in highly excited nitrides is mainly governed by the mobility of holes [203]. Indeed, at 10 μJ/cm^2 D is 0.44±0.02 cm^2/s and 0.26±0.07 cm^2/s in cyan and green structures and correlates well with the values of τ_{PL} 15±0.3 ns and 25±0.3 ns, correspondingly; i.e. an increase by 1.7 times in diffusivity results in the same drop in the lifetime. With increasing excitation, the extended mobile states become increasingly more populated, causing faster non-radiative recombination from these states. As it was discussed, this is also expressed as the increase in the recombination rate of the blue PL wing (Fig. 3.9). Interestingly, the droop threshold (60-70 μJ/cm^2) is very close to that when D becomes equal in both structures. To illustrate the possible role of carrier transport in the efficiency droop, in Fig. 3.10(b) quantum efficiency (PL normalized to excitation, open symbols) and PL signal normalized to the corresponding diffusion coefficient (filled symbols) as functions of excitation are plotted. It can be seen that both types of curves behave similarly above the droop threshold. This similarity suggests that the onset of efficiency droop in the given samples is related to the increasing mobility of holes with excitation due to their delocalization. This result agrees well with the numerical study by P. Dawson et al. [89] showing that while electrons are mostly delocalized at all densities, the holes remain localized both in-plane and cross-plane even at room temperature. With increasing excitation, a relative part of delocalized holes increases, which gives rise to a higher rate of non-radiative recombination and efficiency losses. The delocalization is expected to be of significance up to densities of ~10^{19} cm^{-3} when the majority of carriers should become delocalized. At higher densities, the e-e-h Auger recombination process was suggested to dominate the efficiency droop [204].

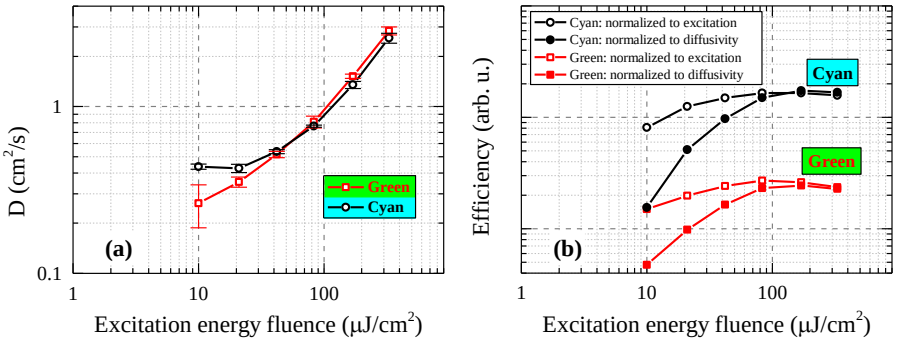

Fig. 3.10. (a) Diffusion coefficients in the cyan and green QW samples as functions of excitation energy fluence. (b) PL signal normalized either to the excitation energy fluence (open symbols) or the diffusion coefficient (filled symbols) in the cyan (black color) and green (red color) structures. The efficiency curves of cyan and green samples are arbitrarily shifted in respect to each other for the sake of visibility [P5].

In summary, two complete LED structures emitting in cyan (500 nm) and green (530 nm) spectral ranges were investigated using several optical techniques. Both structures are shown to be of similar optical and structural quality, in spite of higher indium content in the green structure. The dynamics of carrier redistribution between the localized states of various depths are observed as an untypical redshift of PL peak emerging at long delays and increasing with excitation. Considerably different PL decay time did not result in different IQEs at higher carrier densities; therefore, it cannot be used as a reliable criteria for LED luminosity prognosis. The increase in carrier density resulted in faster carrier recombination in the high energy states and higher diffusivity, which in turn correlated with the onset of efficiency droop. This fact supports the claim that increasing diffusivity plays an important role in efficiency droop since probability for carriers to reach non-radiative recombination centers increases with carrier mobility.

3.3. Carrier diffusivity-limited peak internal quantum efficiency in InGaN QWs with different widths

In previous chapters it was shown that carrier localization has a huge impact on emission properties of InGaN QWs. It is generally agreed that carrier localization is the main reason enabling the inherently defective material to efficiently emit light by prohibiting the carriers from reaching the non-radiative recombination centers [59]. However, localization is a rather complex and not yet completely understood mechanism. It is mainly explored by studying how localization-governed parameters, such as PL peak position or intensity, change with temperature [138,180] or carrier density [182,205]. This is usually done in small sets of relatively similar samples, thus the knowledge of the impact of structural and/or material properties on localization remains limited. On the other hand, carrier diffusivity and the lifetime are closely related to localization, as carriers that need to overcome the higher energy landscape potentials have more movement restrictions and tend to live longer, which was shown in a number of works [121,122] [P2, P5]. In this chapter, a deeper insight into localization mechanism is gained through the connections of the diverse structural and material properties with data of carrier diffusivity and lifetime obtained in a large array of samples (all samples from Table 1). It appears that regardless of the vast differences in the samples, diffusivity comes out as one of the key peak efficiency-limiting factors in the nitride-based light emitting devices. Moreover, the width of QW is considered to be one of the main parameters that influences diffusivity, as well as the droop onset carrier density.

The mitigation of droop effect is still an unresolved task, as to this day there are only barely working solutions, none of which truly eliminate the issue [125,178,206]. Therefore the main focus of this study is the peak IQE, observed at the specific droop onset (i.e. carrier density where IQE peaks) of each sample, and the corresponding state of carrier dynamics (Fig. 3.11). The further emerging efficiency droop and its magnitude are disregarded, and the key objective is to find the structural/material parameters that correlate with the highest peak efficiency, which can be held as the quality revealing factor. Such a strategy can be particularly useful for efficient low power devices, or their arrays that could make up high output power devices [11].

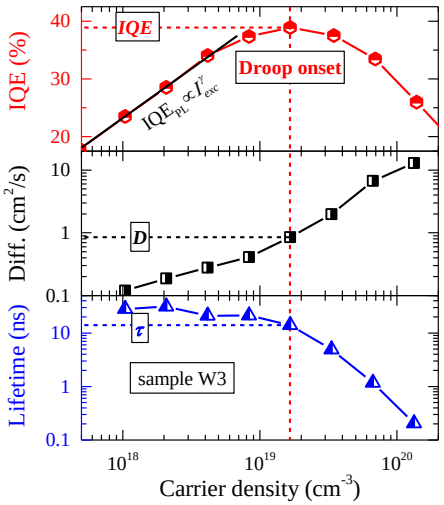

Fig. 3.11. TIPL IQE (top), carrier diffusivity (middle), and the lifetime (bottom) as functions of carrier density in sample W3 from Table 1. Drop lines indicate values that resemble the state of carrier dynamics at the droop onset carrier density. Diffusivity and carrier lifetime values were calculated from LITG kinetics within the first nanosecond after the excitation. Note that no indications of stimulated recombination were observed in PL spectra or LITG kinetics even at the highest carrier densities.

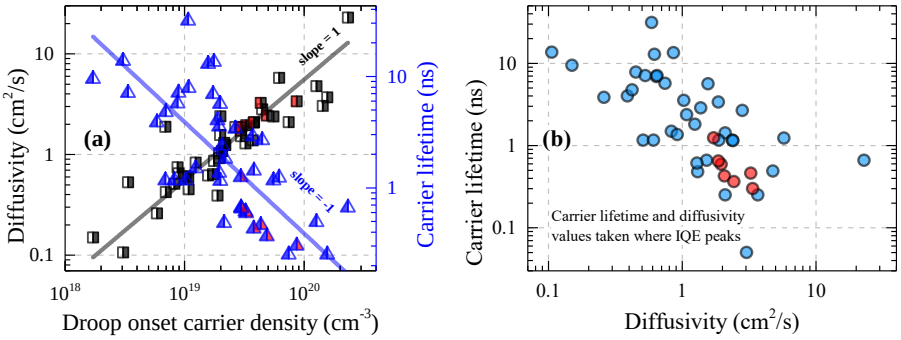

Fig. 3.12. Droop onset carrier density dependencies of the corresponding diffusivity (black squares) and carrier lifetime (blue triangles) values with their linear fit functions (a). Carrier lifetime as a function of diffusivity (b). Each data point represents values of an individual sample, taken at the specific carrier density where IQE peaks (i.e. the droop onset). Red interior marks the m-plane samples, in which the transient gratings were induced perpendicular to the *c*-axis, meaning that measured values are related to carrier diffusion along the *a*-axis.

Droop onset carrier density dependencies of the corresponding ambipolar diffusivity and carrier lifetime values in each sample are presented in Fig. 3.12(a). Note that in LITG experiment carrier densities are averaged over the period of a transient grating [N1]. Linear decrease of the carrier lifetime (blue triangles) shows that there are no indications of a fast non-linear recombination process such as Auger recombination [207], at least up to the droop onset, even though in some samples its carrier density exceeds 1×10^{20}

cm^{-3}. According to the ABC model, the slope should be -2 for direct Auger recombination [207] [N1]. In the meantime, linear diffusivity increase indicates the constantly growing delocalization of carriers, which is likely the cause of the decreasing lifetime. Indeed, as the Fig. 3.12(b) shows, although the data points are fairly scattered, a clear correlation between the carrier lifetime and diffusivity is observed, which suggests that carriers with higher mobility decay faster. Therefore it can be said that the state of carrier dynamics at the droop onset of samples in this work is largely governed by the diffusivity-driven process. This process linearly depends on carrier concentration and appears to be universal due to its observation among different samples.

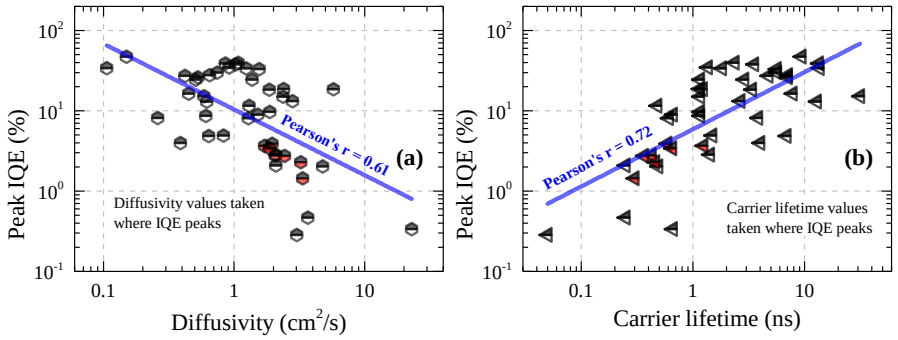

Fig. 3.13. Correlation between the peak IQE and carrier diffusivity (a) and the peak IQE and the carrier lifetime (b). Each data point represents values of an individual sample, taken at specific carrier densities where IQE peaks. Red interior marks the m-plane samples.

The origin of a faster decay can either be non-radiative or radiative. This is because carriers can not only diffuse to the defect states, but to the other localized states as well [P5]. Since the carriers of the opposite signs can be localized in an uncorrelated manner [74,196], this might promote probability for them to meet and recombine radiatively, therefore increasing the rate of bimolecular recombination and reducing the carrier lifetime. However, everything gets clear when looking at Fig. 3.13(a), where the relation between the peak IQE and the corresponding diffusivity is presented – IQE peaks with lower value (falling from ~47% to less than 1%) when carrier diffusion coefficient at the droop onset increases (from ~0.1 cm^2/s to more than 6 cm^2/s). Meanwhile, an opposite trend with the carrier lifetime is seen, with values extending from hundreds of picoseconds to more than 10 ns (Fig. 3.13(b)).

Here only the samples with lifetimes longer than 1 ns achieve IQEs higher than 30%. All this suggests that a faster decay is mainly caused by the increased rate of non-radiative recombination: the more delocalized carriers are able to reach the point or extended defects easier, which in turn leads to the decrease of the peak IQE. Simply put, IQE is limited by carrier diffusivity. Interestingly, a similar trend has been recently observed in perovskites as well [208]. Diffusivity grows with carrier density in all the samples from this work, suggesting that the shift of the droop onset to higher carrier concentrations is detrimental, and will result in lower peak IQE, as in fact will be shown in Chapter 3.7. There are indeed works where a shift of the droop onset to higher carrier densities by introduction of changes to the growth or structural parameters of the analogous samples went together with a reduction of the peak IQE [166,209,210] [P3]. On the other hand, some works show a reduced rate of efficiency decline after the droop onset [206], but this is out of the scope of this study.

The diffusion-driven limitation of the peak IQE implies that suppression of diffusivity should give a positive effect on the emission output at the droop onset. One of the obvious ways, of course, is to lower the droop onset itself. The search of correlations between various structural parameters and the droop onset carrier density revealed, that the latter is lowest in the samples with the thinnest wells (Fig. 3.14(a)). In the meantime, it was found that diffusivity values at equal carrier densities of 5×10^{18} cm^{-3} also decrease in narrower QWs (Fig. 3.14(b)), a tendency which is valid for other equal carrier densities as well. This proposes a connection between the three parameters.

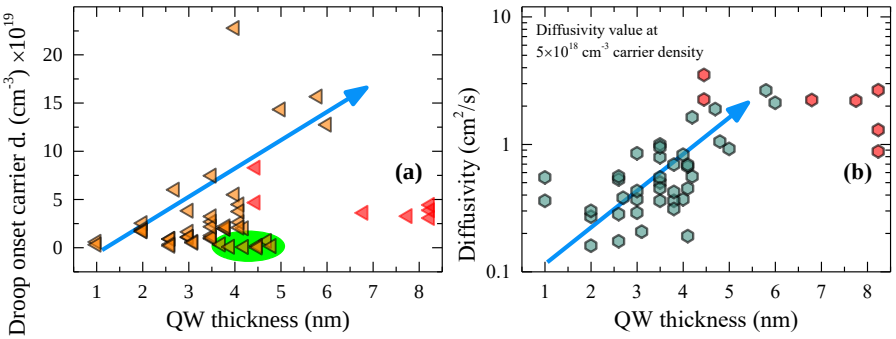

Fig. 3.14. Correlation between the droop onset carrier density and the well width (a). Carrier diffusivity dependence on the QW thickness, with values taken at similar carrier densities of 5×10^{18} cm^{-3} (b). Red interior marks the m-plane samples; the green ellipse marks samples from [P4].

In the case of the well width and diffusivity, the most plausible reason behind their correlation is the well thickness fluctuations that cause the potential fluctuations [85], with the latter expected to have a higher magnitude when the wells are narrow [211]. This can be explained with an inverse square relation of quantum confinement energy levels with the QW width, using a simple particle in a box with infinitely high barriers model [157] (Chapter 1.3.1), where the energy levels are:

$$E_n = \frac{h^2 n^2}{8m^* L^2}. \tag{3.6}$$

The equation above gives a considerably larger quantum confinement energy E_n when the QW width L is smaller. Consequently, the energy fluctuations ΔE caused by the width fluctuations ΔL are also larger in a narrower QW, which implies greater differences in the potential energy landscape, leading to deeper localization. Deeper localization was observed earlier in the narrower InGaN QWs in [207,212], as well as in AlGaN QWs, as evidenced by an increased localization parameter σ in [14]. Simply adding or subtracting from the nominal well width L the smallest possible ΔL value, which is a 0.259 nm atomic monolayer [80,91], changes the first energy level ($n = 1$) of holes E_{h1} with 6-8 meV and 1-2 meV for the 3 and 5 nm thick quantum wells, correspondingly, when the effective hole mass m^* is $1.1m_0$ [29]. Applying the same for electrons with an effective mass of $0.18m_0$ [29], changes E_{n1} by 35-46 meV and 12-15 meV, for the 3 and 5 nm thick quantum wells, correspondingly. The results of these calculations are presented in Fig. 3.15, where it can be rougly estimated that that the effect comes into play below ~6 nm. Note that in Fig. 3.14(b) the decrease of diffusivity is observed when the QW width is below the same value. Although these oversimplified calculations do not take into account the variations in strain and internal electric fields, not to mention the finite barrier height, they still quantitatively show that in the narrower wells the width fluctuation-induced energy fluctuations are noticeably higher. Their values for electrons are comparable to the ~25 meV room temperature thermal energy, not to mention that they would be higher for two or more monolayer fluctuations, which means that electron movement by hoping through the states could indeed be effectively constrained. A similar effect is expected for the already strongly localized holes. However, the magnitude of the effect to different carriers may be different.

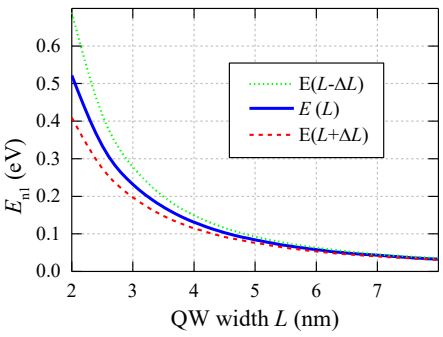

Fig. 3.15. Calculated first energy level of electrons $E(L)$ in a square quantum well with infinite barriers. The red dashed curve $E(L+\Delta L)$ depicts the decreased confinement energy when a monolayer (0.259 nm) is added to the nominal thickness L, the green dotted curve $E(L-\Delta L)$ depicts the increased confinement energy when a monolayer is subtracted.

The effective mass of holes is significantly higher, therefore, their diffusivity is also significantly lower than the one of electrons. In such a case, according to the equation

$$D_a = \frac{2D_nD_p}{D_n+D_p}, \tag{3.7}$$

the ambipolar diffusivity values, obtained from the LITG technique, should mainly reflect the diffusivity of holes [213]. Therefore it is easy to assume that the reduction of the diffusion coefficient in the thinner wells arises due to the limitations in hole movement. However, it is commonly accepted that holes are localized by the -In-N- chains, while the QW width fluctuations localize mainly electrons [80,85–87]. Furthermore, the earlier evaluated potential fluctuations due to well width fluctuations are considerably smaller to holes. These contradictions can mean a couple of things. One is that the value of diffusion coefficient of electrons in a QW due to the well width fluctuations becomes so low, that the changes it encounters are reflected in the ambipolar diffusion coefficient (Eq. 3.7). Another thing is that the well width fluctuations can in fact further restrict the movement of holes that should already be mostly localized by random alloy fluctuations [86]. At this point it is hard to tell which is more probable, therefore both will be held as feasible.

The scattering at the interfaces of a QW may also be considered as a possible mechanism behind the carrier mobility restriction. As the well narrows, less volume for the carrier movement is left. This reduces the probability to find the paths with the same potential energy, i.e. the percolation paths [214], without being scattered by the rough QW/QB interfaces and the defects that are created there. Less volume for transport should restrict the movement of both types of carriers. However the magnitude of this effect is unclear, therefore at this time it will be considered as minor.

Knowing that localization of carriers is stronger in narrower wells, it is now possible to explain earlier droop onsets in them (Fig. 3.14(a)). One way to picture this is that the stronger the localization, the lower the probability to reach the NRCs, thus the localized states get filled easier. Carrier density in these states is locally increased if compared to other parts of the medium, and such non-uniformity of carrier density distribution reduces the effective, optically active volume [104]. This in turn gives rise to an earlier droop onset resulting from a fast non-radiative process such as Auger recombination (or other) that heavily depends on the carrier density. Another way is that greater potential fluctuations can ease the momentum conservation in the Auger recombination process [112,115] allowing it to appear at lower carrier densities. These ideas can be supported by the increasing droop onset with weaker localization that was observed earlier in AlGaN QWs and epilayers [215]. They also provide an explanation for anomalously low droop onsets in samples marked by the green ellipse in Fig. 3.14(a) (S1-S8 in Table 1). A large redshift of PL spectra in these samples was shown to be a consequence of strong carrier localization [P4] despite relatively wide wells.

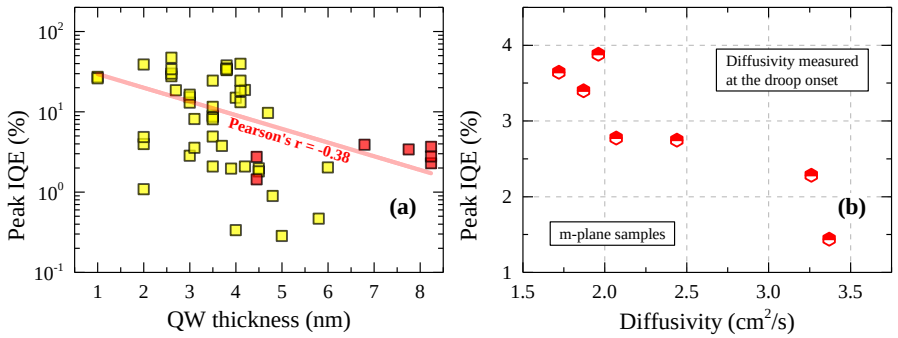

Fig. 3.16. Peak IQE vs the QW thickness (a). Correlation between the peak IQE and carrier diffusivity in m-plane samples (b). Red interior marks m-plane samples.

Since an earlier droop onset is a subject to lower diffusion-driven non-radiative losses, an increased peak IQE can be expected in the narrower wells. This is seen Fig. 3.16(a) and is in agreement with the results presented in the works [212,216]. However, in these works the QCSE is held as the responsible mechanism for the reduction of the radiative recombination intensity in wider wells, whereas in this work it is the increased carrier mobility. The major role of diffusivity can be supported by its negative correlation with the peak IQE in non-polar samples (Fig. 3.16(b)), where reduced carrier wave function

overlap due to carrier separation should not be present. Nevertheless, QCSE is not ruled out as an additional efficiency quenching mechanism in polar structures. In fact, it should be taken into account when designing an LED active layer – QW thickness should be picked with regard to the enhancement of localization and a sufficient overlap of wave functions, as well as leaving enough optically active volume to prevent too high carrier densities in the case of current injection. According to Fig. 3.16(a), the optimal QW thickness lies between 2-3 nm.

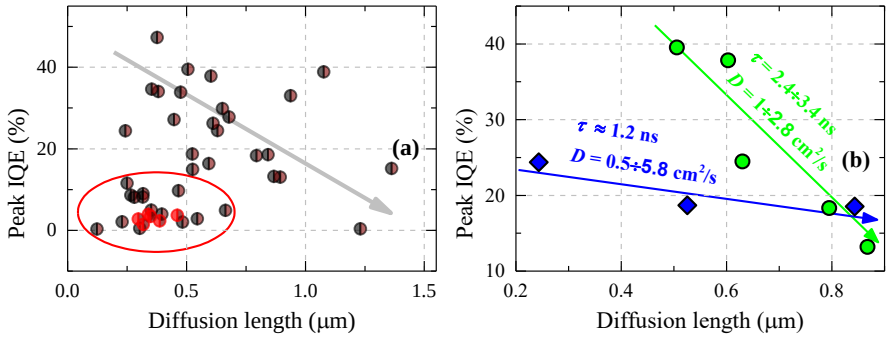

Fig. 3.17. Peak IQE vs the diffusion length at the droop onset carrier density (a). The same is shown in (b), but here only two groups of samples with similar carrier lifetimes are left. Red interior marks the m-plane samples.

In Fig. 3.17(a), the peak IQE vs the calculated diffusion length ($L_D = \sqrt{D\tau}$) at the droop onset is shown. Two main cases are seen here: there are samples that show the drop of IQE with the increasing diffusion length at the droop onset (grey arrow), and then there are samples where the diffusion length is short (less than 0.5 μm), but the peak IQE also remains poor (encircled in red). In the first case, the limitation of the diffusion length is clearly a factor that improves the peak IQE, which is mostly related to stronger localization of carriers. In the second group, the diffusion length is limited by the short carrier lifetime rather than a small diffusion coefficient, due to fast recombination at abundant defect states. The values of diffusion lengths vary in the 0.1-1.4 μm range, which is comparable to the distance between the neighboring dislocations in InGaN grown on sapphire [57,60]. This suggests that the extended defects are closely related to the peak IQE. In fact, a clear inverse correlation between the peak IQE and the threading dislocation density was presented in [66]. Romanov et al. [69] also showed that an increase of quality by reducing the dislocation density increases the peak IQE, and according to

Sugahara et al. [217] the efficiency of light emission should be high as long as the carrier diffusion length is shorter than the dislocation spacing. Therefore one can assume that IQE can be enhanced by ensuring that localization-limited diffusion length of carriers is shorter than the average distance between the threading dislocations [218]. This is depicted in Fig. 3.17(b), where two groups of samples with similar carrier lifetimes show shorter diffusion lengths and higher peak IQEs when carrier diffusivity is smaller. Hence the localization degree can determine whether carrier recombination is mostly influenced by the radiative recombination rate at the localized states or by the non-radiative recombination rate at the defects.

To illustrate that the peak IQE can be enhanced despite the quality of the active layer, in Fig. 3.18 the peak IQE dependence on diffusivity is shown in the samples from the same set (W1-W5 in Table 1). The equal nominal In content of 25% in them and the same growth procedures allow the assumption that quality is comparable, with the only difference being the well width, which apparently changes the diffusivity. It can be seen, that an increase in the diffusion coefficient from 0.3 cm^2/s to 0.83 cm^2/s at 5×10^{18} cm^{-3} carrier density results in the peak IQE falling from 39% to nearly zero. The latter value implies that the defect density is quite high in these structures. This approves that if the localization conditions are sufficient, the non-radiative recombination can indeed be suppressed despite the high density of defects coming from the high In content.

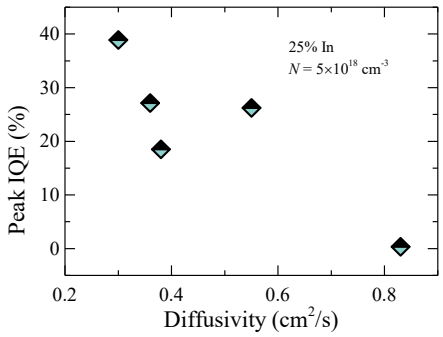

Fig. 3.18. Peak IQE vs diffusivity at 5×10^{18} cm^{-3} carrier density in the same set of samples with 25% In content but with different well widths.

To summarize, in this chapter it was shown that in InGaN QWs the peak IQE inversely correlates with the ambipolar diffusion coefficient. As a fundamental limitation, it arises due to the promotion of non-radiative recombination at the defects. Diffusivity decreases in the narrower QWs pointing out to stronger localization, which is mainly due to higher well width

fluctuation-induced potential energy fluctuations that enhance the scattering of the charge carriers. Increased potential energy fluctuations can prohibit the diffusion of carriers to the extended defects so the localized states get filled earlier, as well as enhance the Auger scattering rate, thus giving rise to an earlier droop onset. Lower droop onset carrier density is advantageous to the peak IQE, since smaller diffusion-driven non-radiative losses are expected. The combined results suggest that the diffusion length must be shorter than the distances between the neighboring threading dislocations to improve IQE, which can be achieved by the reduction of diffusivity even if the material is highly defective.

3.4. Stokes shift in InGaN quantum structures

Photon energy difference between the absorption and emission spectra, known as the Stokes shift, has been observed in a number of InGaN-based structures, including epitaxial layers, LEDs, and LDs [59,122,195,198,219,220]. In the presence of this shift, only the low energy tail of the absorption edge overlaps with the emission spectrum. The same is found in InGaN quantum structures, studied in this work, which exhibit redshifted TIPL spectra with respect to instantaneous DT spectra [P2-P5]. The energy difference between DT and PL spectra peaks (ΔE) linearly decreases with higher PL peak emission energy (from ΔE = 0.54 eV at 2.2 eV in this work) and appears to be converging to zero at GaN bandgap value (black half-filled diamonds in Fig. 3.19), a trend previously observed in other works. This phenomenon is important to LEDs or LDs, because it makes reabsorption of light emitted in QWs close to negligible by the interband transitions, thus enhancing the light extraction [221]. A larger Stokes shift may even lower the probability of reabsorption further, thus implying the positive impact of this effect. On the other hand, in the work [P3], lower IQE was related to a smaller overlap of PL and DT spectra, stating the opposite. Either way, to this day the phenomenon still lacks the complete understanding, with last major studies completed in the early 2000s. In this chapter, a deeper insight into the Stokes shift is gained by comparing its values in a large number of c-plane QW structures (Table 1) and several InGaN epilayers. The results suggest that variation in QW width changes the diffusion coefficient as well as the magnitude of the QCSE induced redshift, which together may be responsible for the large Stokes shift values in QWs.

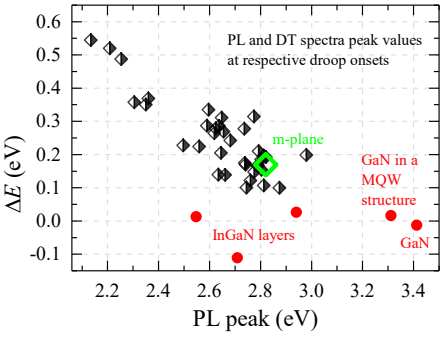

Fig. 3.19. Energy difference between the peaks of TIPL and DT spectra (the Stokes shift) as a function of PL peak emission energy. Each data point represents values of individual samples at their specific droop onset carrier densities. The black diamonds correspond to QW structures, the red circles correspond to epitaxial layers, and the green empty diamond corresponds to the non-polar sample with a 10 nm thick SQW from the work by K. Gelžinytė [222].

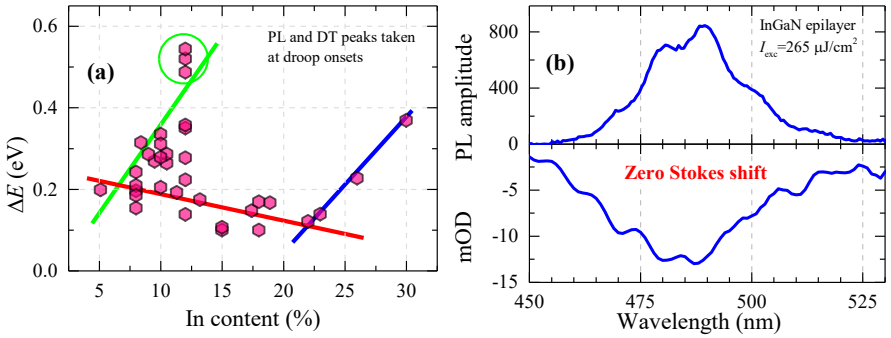

Fig. 3.20. The Stokes shift dependence on the In content in QW structures (a). PL and DT spectra of an InGaN epilayer with no Stokes shift present (b).

The Stokes shift in III-nitrides has been generally ascribed to localization effects in the way that absorption takes place in the higher energy states, from which the carriers relax to the localized states and recombine there radiatively [59] [P3]. Localization strength generally increases with higher magnitude of In fluctuations [44,76], so it is natural to expect a larger Stokes shift in the samples with higher In content [44]. However, a unified correlation is not observed in QW structures from this work (Fig. 3.20(a)); instead it looks like there are several ranges of In content where different types of correlations are seen. Up to ~12% of In content, at which phase-separation supposedly occurs, there is a rise in ΔE (indicated by a green line). It was shown in the work [P4] that the encircled samples that peak this dependence (S1-S8 in Table 1) have very deep localized states, therefore it can be related to the increasing depth of localization. In the meantime, a decrease in ΔE is also observed, spanning up to ~22% In (red line), which then changes to an increase (blue line). In the work by Schenk et al. [219], a non-monotonous dependence of ΔE on In content was observed in InGaN epilayers as well. Furthermore, a few epilayers with different In contents (including GaN) and with peak emission wavelengths of up to 490 nm (2.53 eV) were measured additionally in this work, and they appear to be experiencing a close to zero redshift of PL spectra with respect to DT spectra or even a small blueshift (Fig. 3.19 red circles and Fig. 3.20(b)). A small Stokes shift (<80 meV) has also been observed previously in thick and homogeneous InGaN layers with In content up to 17% and with the peak emission wavelength up to 448 nm (2.7 eV) [223]. According to [38], the absence of the Stokes shift demonstrates the dominance of band-to-band or excitonic recombination pathways. Regarding the localization effects, this is either due to a relatively smooth In distribution

[223] or a mechanism that prevents the occupation of the deeply localized states. Considering all these things, localization due to random alloy fluctuations cannot be the sole mechanism causing the Stokes shift, especially in QWs where the Stokes shift appears to be a universal linear function of emission energy.

The emission band in QWs can be redshifted not only by including more In, but also by changing the well widths. For this reason, ΔE was plotted against the QW width in Fig. 3.21, where a positive correlation can be seen, which was also shown in [220] and [224]. A few samples appear to be not following the correlation completely (marked by the red ellipse, In3-In5 in Table 1), however this might be explained by more than two times wider barriers (~18 nm) in them as compared to all other samples. It is likely that thick barriers cause a partial strain relaxation in the active layer via the formation of threading dislocations. This enhances the interdiffusion of In atoms, thus making the QW interfaces rough [225], which can be supported by STEM images. It is worth mentioning that in the work [P1] no Stokes shift has been observed at all in a triangular shape single QW structure, emitting at ~460 nm (~2.7 eV), suggesting the importance of an abrupt rectangular shape on the Stokes shift (most of the QW structures in this work have well defined rectangular shapes).

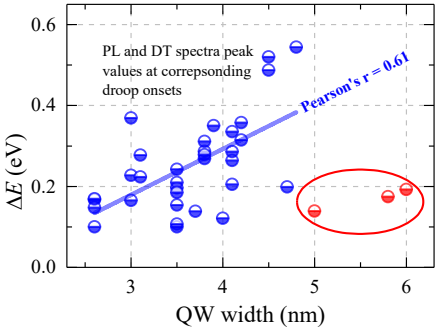

Fig. 3.21. Stokes shift dependence on the QW width. Each data point represents values of separate samples at their specific droop onset carrier densities.

The widening of a rectangular QW increases the spatial separation between the wave functions of electrons and holes. Because of this, a redshift due to QCSE increases as carrier wave functions fall deeper into triangular potential minima at the edges of the well, which was proposed earlier as the origin of the Stokes shift [224]. In the recent work by Zhang et al. [226] it was shown that in semipolar InGaN QWs the Stokes shift is significantly weaker if compared to analogous polar QWs, stating the direct involvement of internal

electric fields. However, in the work by K. Gelžinytė [222], redshifted PL spectra with respect to DT spectra have also been observed in a non-polar SQW sample (represented as a green diamond in Fig. 3.19), where carrier separation along the growth direction due to the absence of parallel electric fields should not occur. Therefore internal electric fields may not be the only possible explanation for large Stokes shifts in QWs.

In a previous chapter it was shown that the diffusion coefficient of carriers scales with QW thickness. Regarding the current topic, higher carrier mobility should lead to an easier redistribution of carriers from the extended states to the localized states (and within them), resulting in a larger Stokes shift. In fact, this can be supported by a positive correlation between the diffusion length and the Stokes shift (Fig. 3.22), meaning that the longer distance that the carriers can travel may promote the occupation of deeper localized states. The mean value of diffusion length increases from ~0.28 μm to ~0.7 μm for the ΔE increase from 0.1 eV to 0.3 eV. Hence, even if the deep localized states are present from high In content fluctuations in the structure, their occupation can be significantly limited if diffusivity of carriers is small, which is inherent to narrow QWs.

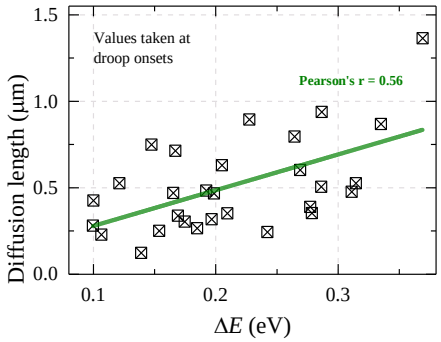

Fig. 3.22. Diffusion length vs the Stokes shift, where each data point represents values of separate samples at their specific droop onset carrier densities.

The next important question is how come do thick InGaN layers can have near zero Stokes shifts? A likely answer to this is the coherent strain throughout the full thickness of a thin layer (like a QW) to match the different lattice parameters of an underlying layer. This can induce significant In content fluctuations, for example, due to compositional pulling effect, or phase separation. In thick epilayers, on the other hand, the strain is relieved as the thickness is increased, and it can totally relax after reaching a critical thickness h_c, which decreases with higher In content [54,94]. Even though this mostly comes at the cost of the increased density of strain-relaxing misfit

dislocations or V-pits, given that the growth conditions are optimal, indium distribution can be much more homogeneous with presumably shallower localized states, meaning a smaller Stokes shift. The role of strain can further be supported by a decrease in the Stokes shift after the insertion of a strain relieving superlattice as seen in Fig. 3.5 from Chapter 3.1. Note that insertion of such an interlayer was accompanied with a decrease of a diffusion coefficient. In the case of a triangular SQW from [P1], the gradient change of In content along the growth direction probably relieved the strain too.

To conclude, potential fluctuations caused by random alloy disorder alone do not determine the magnitude of the Stokes shift in InGaN quantum structures. The positive correlation between the Stokes shift and QW width was observed. This was explained by the increasing redshift caused by QCSE and higher diffusivity that can enhance carrier redistribution to deeper localized states. The abruptness of the QW interfaces appears to be a necessary condition for the Stokes shift as it generates strain, which leads to the internal electric fields and higher fluctuations of In content. Both can be reduced by strain relaxation, which is why in thick InGaN layers the Stokes shift can reach very small values.

3.5. Influence of metalorganics flow interruption on migration of deposited atoms in InGaN LED structures

One of the key objectives in the making of the efficient LEDs is to improve the quality of the materials, especially those used in the active layers. One of the ways to do that is by using the pulsed MOCVD growth mode. During the pulsed growth of an InGaN layer, the supply of TMIn and TMGa precursors to the reactor chamber is periodically interrupted for a preset duration, while the NH_3 supply is kept constant [43,227]. Such a regime promotes the surface migration of the deposited metal atoms and provides additional time for nitrogen deposition, thus improving atomic distribution and suppressing the formation of nitrogen vacancies [43]. In this chapter, the positive impact of the pulsed growth mode is presented [P3]. Furthermore, a deeper insight into the growth process is obtained by studying the impact of the interruption time on diffusivity, the carrier lifetime, and IQE. It is also shown that atom migration, evaporation, and surface nitridization are interconnected processes. The interaction between them defines how the structural quality and localization conditions in a 6 sample set change as the interruption time is increased, which happens in a step-like manner.

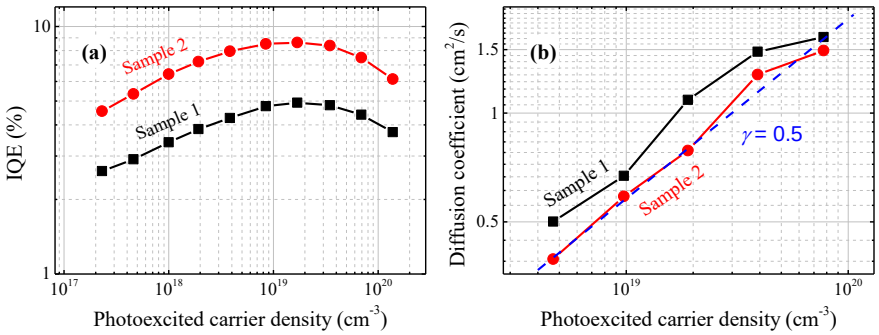

Fig. 3.23. IQE values (a) and the diffusion coefficient (b) as functions of carrier density in the structures grown under continuous (Sample 1) or pulsed growth (Sample 2) [P3].

To begin with, Fig. 3.23(a) shows the comparison of IQE in two samples grown under continuous or pulsed growth mode (Sample 1 and Sample 2 in Table 1, correspondingly), with the same underlying SL structure as described in Chapter 3.1. Their active parts consist of 3–4 nm thick 5 $In_{0.1}Ga_{0.9}N$ QWs, separated by 6 nm thick barriers. During the

pulsed growth, TMIn and TMGa precursors were sent into the chamber for 15 s, and then interrupted by bypassing for 5 s, with the cycle repeated 5 times for each QW. The result is an almost twofold IQE increase with respect to the reference structure. Even though the peaks of IQE curves appear at similar carrier densities of ~2×10^{19} cm^{-3} in both samples, localization is weaker in the reference structure, as evidenced by higher carrier diffusivity with respect to the pulsed growth structure (Fig. 3.23(b)). Interestingly, the reference structure shows a smaller PL blueshift with excitation (30 meV vs 20 meV, Fig. 3.24(a) and (b)). A larger blueshift can be a mixture of larger screening effects due to stronger electric fields and faster saturation of the localized states, with both acting as negative factors. However, their role is diminished by lower carrier diffusivity and a longer lifetime, as evidenced by TRPL measurements: τ values are 13.5 ns and 27 ns at 1.4×10^{18} cm^{-3} in Sample 1 and Sample 2, correspondingly.

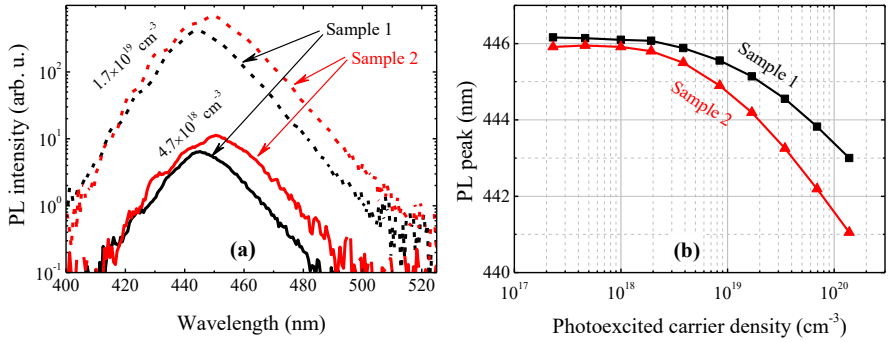

Fig. 3.24. PL spectra (a) and PL peak position vs. carrier density (b) in Sample 1 and Sample 2 [P3].

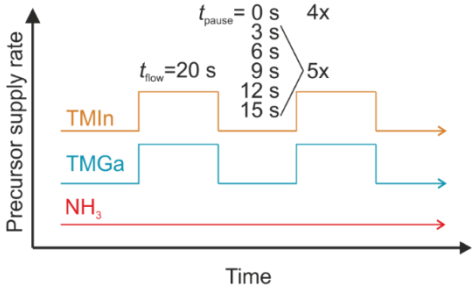

Fig. 3.25. Scheme of a precursor supply timing in a pulsed growth mode of a 6 sample set.

The above presented benefits of a pulsed growth mode invited further research. A set of samples consisting of 6 blue-emitting InGaN/GaN MQWs

structures (tp0-tp15 in Table 1) obtained under various pulsed growth regimes was investigated. The key difference between the samples is that during the growth of each ~4 nm thick QW layer (at 800°C), 20 s duration TMIn and TMGa supplies were interrupted with pauses ranging from 3 to 15 s, a process that took 5 cycles (Fig. 3.25). As for the reference structure (t_{pause} = 0), each QW was continuously grown for 80 s. The barriers in the samples are ~7 nm thick.

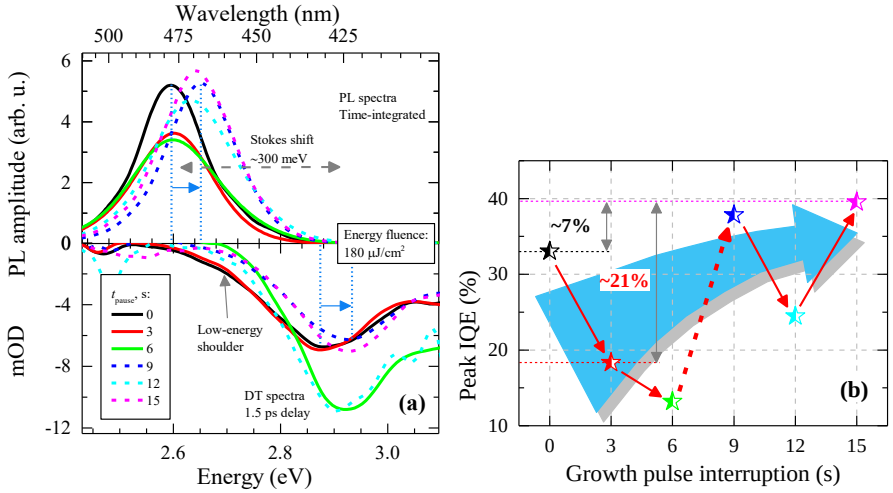

Fig. 3.26. TIPL (upper part) and instantaneous (at 1.5 ps delay) DT spectra (lower part) of the samples at 180 μJ/cm^2 excitation (a). The solid lines correspond to samples with interruption times of up to 6 s, the dashed lines correspond to samples with interruption times longer than 6 s. Peak IQE dependence on the precursor supply interruption time (b). The colors in both graphs are sample-specific to serve as a guide for an eye.

Within the sample set, the PL emission peaks are at 2.6-2.65 eV (477-468 nm, Fig. 3.26(a) upper part), while the absorption – at 2.87-2.93 eV (432-423 nm, Fig. 3.26(a) lower part), which results in a ~300 meV Stokes shift. Despite the relatively high value of this shift, the samples with the longest precursor supply interruption show the peak IQE up to ~40% (Fig. 3.26(b)), which is among the highest values obtained in the thesis. This suggests that the Stokes shift has no negative effect, or even a positive one by diminishing the reabsorption and enhancing IQE. From Fig. 3.26(a) it is also seen that both PL and DT spectra shift to higher energies for interruptions longer than 6 s (marked by blue arrows). This outcome is most likely related to the

evaporation of the deposited indium atoms due to the weak In-N bonds that have low dissociation temperature [227,228], which leaves behind the slightly narrower QWs with lower In content. Since no significant thickness changes were observed by XRD characterization, the blueshift is attributed to the decreased indium content. Additionally, the extra time given for the rearrangement of the surface atoms probably leads to their more uniform distribution and, subsequently, shallower localized states, thus also contributing to the blueshift.

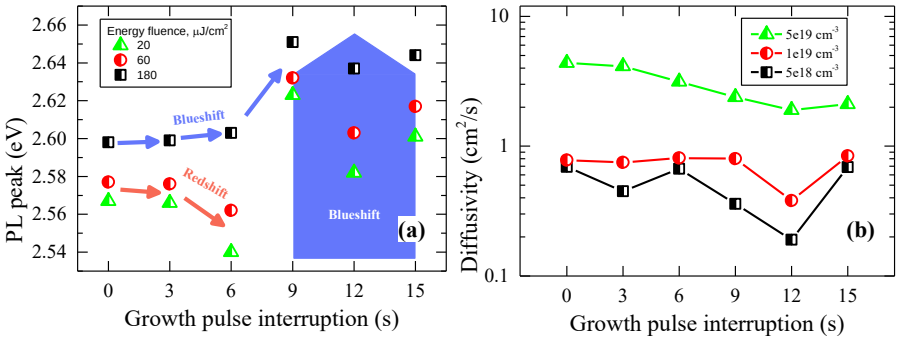

Fig. 3.27. TIPL spectra peaks at different pulse interruption times for three excitation energy densities (a). Carrier diffusivity dependence on growth pulse interruption for three carrier densities (b).

Getting back to the growth pulse interruption time dependence of the peak IQE, a non-monotonous trend is observed – the initial drop switches to a rise after a 6 s interruption time (shown in Fig. 3.26(b) with a dashed line). The enhancement of the peak IQE by ~7% when comparing the reference sample and a sample with t_{pause} = 15 s again proves the positive impact of the pulsed growth mode. This increment is small, however one has to remember that the sample t_{pause} = 0 s differs in the total QW growth time and may not serve as a perfect reference. For instance, the peak IQE difference between the samples with t_{pause} = 3 s and t_{pause} = 15 s is 21%, emphasizing the overall improvement (indicated by a curved cyan arrow). A deeper insight into the mechanism behind the aforementioned non-monotonous trend can be gained from the changes of the peaks of TIPL spectra at different excitation energy densities (Fig. 3.27(a)). When the latter are high (180 μJ/cm^2), PL spectra shift to the blue region as the interruption time increases up to 9 s, after which no further significant changes are observed. Low excitation spectra (20 and 60 μJ/cm^2), on the contrary, demonstrate a redshift up to 6 s, which is replaced by a sudden

shift to higher energies at longer interruption times. To explain these tendencies, one has to take into account that the key processes – surface atom migration, their evaporation, and surface nitridization – are related and happen simultaneously. The small blueshift with the increase in the interruption times up to 6 s implies that only a relatively small number of In (and supposedly other) atoms evaporate, a process which afterwards increases greatly with a step-like change. The initial low-excitation redshift most likely comes from the deeper localized states created by the segregation of In atoms, possibly due to their inefficient migration. The presence of such states can be supported by the low energy shoulders in the short interruption time DT spectra (Fig. 3.26(a)) and larger FWHMs of the respective PL spectra (not shown) [112]. The appearance of a redshift only at the low excitation regime indicates that the density of these localized states is low, and they are easily filled at high excitations where only the blueshift is seen. The initial drop in the peak IQE suggests an increase in the density of defect states, which ceases to be an issue at interruption times above 6 s. The deepening of the localized states and a higher defect density may originate from the low probability of the surface atoms (indium in particular) to find the most energetically favorable lattice positions to attach to [138]. This might be due to the insufficient time for the migration and the competition between the migrating atoms. They just attach wherever they have time and space to do so, which shapes the highly fluctuating energy landscape filled with defects. It is likely that during this initial phase, the additional time simply promotes the segregation of In atoms that fail to find a decent spot in a lattice due to insufficient surface nitridization [43], which is also responsible for the formation of nitrogen vacancies. However, significant changes in the pulsed growth mechanism appear after a 6 s interruption time threshold: the right amount of excess atoms evaporate from the surface, leaving more space for the migration and the attachment of the remaining atoms, which is further enhanced by the extra time for the process; the adequate number of deposited nitrogen atoms reduces the defect formation and In segregation. All these processes combined result in a sudden transition to a crystal lattice with a slightly lower In content but with a smoother atom distribution and with fewer defects, which leads to an increase in the peak IQE. It is worth noting, that diffusion coefficient decreases with longer metalorganics supply interruption times, which is best seen at high carrier densities (5×10^{19} cm^{-3}, Fig. 3.27(b)). Therefore, speculations can be made that a smoother distribution of atoms at longer interruptions gives although shallower, but denser localized states, with such assumption coming

from the narrower FWHM values. These localized states become very important at high carrier densities, especially where the efficiency droop takes place, which in the current samples is between 2-4.5×10^{19} cm^{-3}, and allow to achieve higher peak IQEs by inhibiting carrier diffusion to the non-radiative recombination centers.

The threshold-like transition after a 6 s interruption time could be related to growth parameters, such as V/III ratio and, most importantly, growth temperature. For the current samples, the growth temperature was 800°C, and its increase should lower the threshold, as it would promote all the processes that are related to the pulsed growth. Faster In and other atoms desorption, higher degree of ammonia dissociation, and enhanced atom migration should shift the transition to shorter interruption times. Needless to say that V/III ratio and ambient pressure might as well influence the threshold.

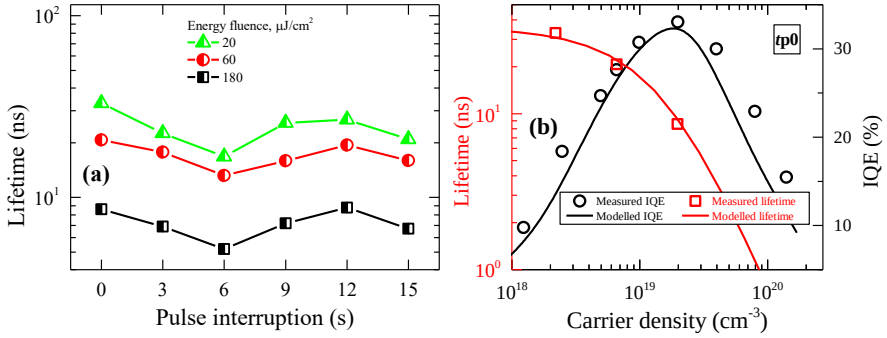

Fig. 3.28. Changes of the spectrally integrated DT lifetimes with the growth pulse interruption at three excitation energy densities (a). An example of a self-consistent fitting of the spectrally-integrated DT lifetime and IQE curves of a reference sample tp0 (b). Open squares and circles show the measured lifetimes and IQEs respectively, while the lines are the fitting results of the ABC model.

A non-monotonous change in DT spectrally integrated carrier lifetimes τ with increasing interruptions of metalorganic precursor supply is observed as well (Fig. 3.28(a)). The initial shortening changes to lengthening after a dip at 6 s, which again reveals the complex nature of the mechanism behind the pulsed growth mode. For a more thorough analysis, a self-consistent ABC modelling was performed. The carrier densities were independently evaluated for all the samples with the individual absorption coefficients obtained from the TIPL measurements in the integrating sphere. The lifetime τ and the IQE curves (Fig. 3.28(b)) were fitted self-consistently using the relations:

$$\frac{1}{\tau} = A + Bn + Cn^2, \tag{3.8}$$

$$IQE = \frac{Bn}{A+Bn+Cn^2}. \tag{3.9}$$

Here, the A term represents the Shockley-Read-Hall, B – bimolecular, C – Auger recombination coefficients. The band-filling effect that was used in Chapter 3.1 was disregarded, as both curves were fitted sufficiently well with the simple model.

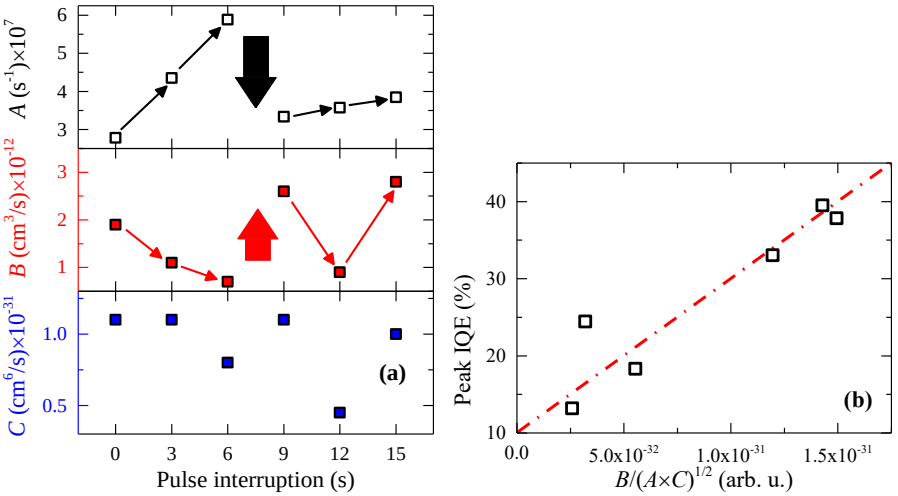

Fig. 3.29. (a) ABC modelling results. The top part represents Shockley-Read-Hall, the middle part – bimolecular, and the bottom part – Auger recombination coefficients vs pulse interruption. (b) Peak IQE vs the dimensionless quality factor ($B/\sqrt{A \times C}$). The line is a guide for an eye.

Modelling results are presented in Fig. 3.29(a). The non-monotonous changes in SRH and bimolecular recombination coefficients support the earlier presented ideas. The initial growth of A from 2.8×10^7 s^{-1} to 5.9×10^7 s^{-1} supports the increase in the defect density, while the decrease of B from 1.9×10^{-12} cm^3/s to 0.7×10^{-12} cm^3/s suggests that the localized states get deeper at the cost of their density, hence the radiative recombination rate drops. Both result in the reduction of the IQE. As expected, the picture changes after the 6 s interruption time, when A returns to nearly the initial value and B increases more than 3 times, indicating improvements in the structural quality as well as in localization conditions. Note that the sample with the 12 s interruption time drops out from the overall tendency with its low B value, possibly due to non-optimized conditions in the formation of localized states during the

growth. As to the Auger recombination coefficient, no clear tendency is observed, except that it appears to be smallest in the least efficient samples. The best sample in terms of the highest peak IQE has the following parameters: A=3.8×10^{7} s^{-1} (1/A=26 ns), B=2.8×10^{-12} cm^{3}/s, C=10^{-31} cm^{6}/s. For comparison, the values from the work [229], obtained in a single QW emitting at 457 nm and having peak EL IQE of about 75%, are: A=2.6×10^{6} s^{-1} (1/A=385 ns), B=3×10^{-12} cm^{3}/s, C=10^{-31} cm^{6}/s. The SRH term which is higher by one order of magnitude in the sample from the current work is most likely responsible for a nearly twice as lower peak IQE.

It is common to use the carrier lifetime as a criteria that shows the quality of a material – a longer lifetime is usually said to be an indication of lower non-radiative losses through defect-related recombination channels. However, from the earlier results of this thesis it is seen, that longest carrier lifetimes do not necessarily lead to the highest peak IQEs. Contribution from all recombination pathways has to be taken into account, as the long lifetime can also be an indication of slow bimolecular recombination. In Fig. 3.29(b) this is reflected by a linear peak IQE dependence on the dimensionless quality factor $B/\sqrt{A \times C}$ [230]. It stresses the competition between radiative and non-radiative channels and, as it is seen in the figure, works very well as a figure of merit for a light emitting material.

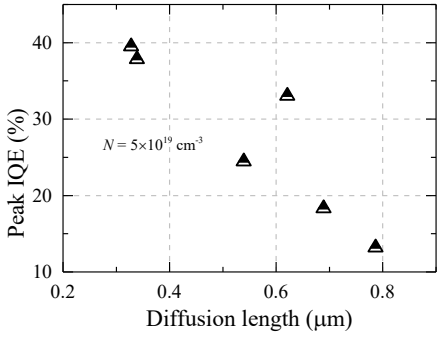

Fig. 3.30. Correlation between the diffusion length at 5×10^{19} cm^{3} carrier density and peak IQE.

A good indicator of improvements in material properties for light emission can be the diffusion length, which is shorter in the samples with higher peak IQEs (Fig. 3.30). The importance of carrier diffusion length can be justified by looking at Fig. 3.31(a), where its dependence on carrier density somewhat resembles the droop curve (as seen in Fig. 3.28(b)) – the initial rise changes into decline, with peak values being reached before each sample's droop onset. This shows that the initial rise in the peak IQE is due to the saturation

of the defects [122,205,231] that are easily accessed at low carrier densities (point defects in particular), which translates into the increasing distance that the charge carriers can travel. The maximum distance depends on both the density of such defects and localization degree. Meanwhile, a further emerging decline is related to the droop process, which effectively reduces the carrier lifetime and, subsequently, diffusion length. In Fig. 3.31(b) the continuously increasing diffusivity even well above the droop onset proposes the diffusion-driven defect recombination as the cause of the droop process. Then again, the Auger term was successfully used in the ABC model to describe both lifetimes and IQE curves of the current samples. Furthermore, LITG carrier lifetimes at high carrier densities above the droop onset scale as $\tau \propto \frac{1}{N^2}$ (Fig. 3.31(b)), which is a clear indication of Auger recombination [N1]. Hence at this point it is reasonable to say that both diffusion-driven and Auger recombination are present, however, the latter appears to be the dominating cause of the droop in the current case.

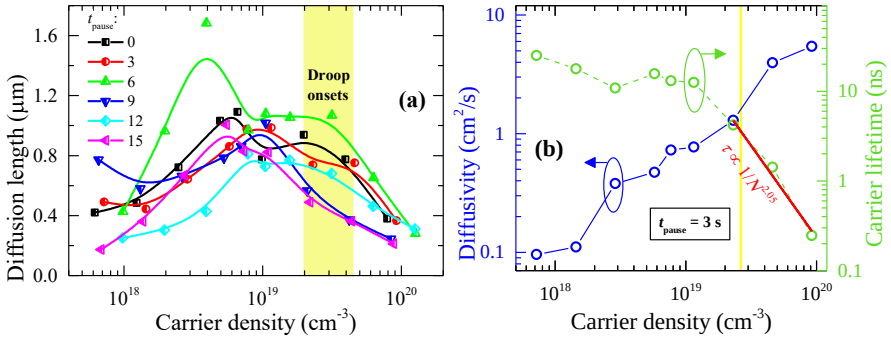

Fig. 3.31. Dependence of the diffusion length on carrier density (a). Diffusivity and the carrier lifetime dependence on carrier density in the sample with a 3 s growth pulse interruption time (b). Yellow stripes indicate the region of droop onsets.

In conclusion, this chapter shows the definite benefits of a pulsed MOCVD growth mode through the improvement in IQE. At the same time, a complex mechanism behind the pulsed growth of InGaN MQWs is unveiled with a study of the non-monotonous changes that the increasing precursor supply interruptions lead to, as evidenced by the non-monotonous peak position shifts and changes in the ABC model coefficients. It appears that migration of deposited atoms leads to their better distribution when there is enough time and there are enough energetically favorable lattice positions to attach to. In the investigated samples, this happens in a threshold-like manner, after a

sufficient number of excess atoms evaporates and the surface gets fairly nitridized. A better quality material with better localization conditions is then obtained, which can be indicated by shorter diffusion lengths. Hence, careful optimization of timing in the pulsed growth regime is necessary to achieve higher efficiencies. A fast recombination process and continuously growing diffusivity at high carrier densities reveal the presence of both Auger and diffusion-driven non-radiative recombination. The former appears to be causing the efficiency droop in the current samples.

3.6. Impact of gross well-width fluctuations on localization conditions

Well-width fluctuations limit the diffusivity of non-equilibrium carriers, one of the key efficiency-determining factors in nitride-based LEDs. These fluctuations result in the typical localization lengths of carriers within the range of 10 nm [80,86,87]. They are generally exceeded by the typical carrier diffusion lengths of the order of tens [61,232] or hundreds [122] of nanometers, therefore it sounds reasonable that the introduction of additional barriers spaced within the two boundaries should improve the overall localization. This was done in the work by Oliver et al. [164], where the presence of gross well-width fluctuations revealed a much higher quantum efficiency as a consequence of diminished non-radiative recombination by creating additional barriers to carrier diffusion. However, this physical model was not complemented up to now by direct measurements of carrier dynamics and diffusivity in these so-called "gappy" QWs. In this chapter, samples with an intentionally highly-fluctuating QW width profile are investigated by LITG, DT and TIPL techniques. It is shown that the fall of diffusivity is connected to the increased peak IQE due to the enhanced rate of radiative recombination, leaving less carriers for the non-radiative recombination channel.

The samples under study are two MQW structures with uniform (1T, Q2T in Table 1) and two MQW structures with highly fluctuating QW width profiles (2T, T-bounce in Table 1). The latter are so thin in some parts that barriers penetrate the wells and form the gaps in them, hence the name gappy. The active layers, consisting of 10 QWs, were grown on 5 μm GaN pseudo-substrates. Gappy MQWs were formed by ramping the temperature up immediately after the completion of each QW growth, which led to the significant loss of indium due to evaporation at certain locations of the exposed InGaN layers. Temperature ramping was performed over a certain period under ammonia without fluxes of metal-organics. After the ramping, either a higher temperature growth of GaN barrier was performed (2T), or the barrier was grown after the temperature was brought back to the initial value (T-bounce). As for the uniform thickness MQWs, either no temperature ramping was done (1T), or prior to it a narrow protective GaN layer was grown (Q2T), wherefore the loss of indium was prevented. Full details on sample growth can be found in [164].

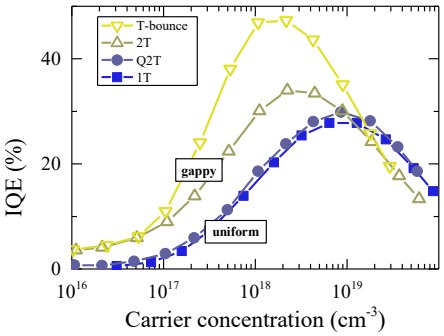

Fig. 3.32. IQEs of gappy and uniform well-width profile samples.

Figure 3.32 shows IQEs as functions of carrier density, evaluated by TIPL measurements. Here gappy samples standout with much higher IQEs at low non-equilibrium carrier concentrations. However, at higher carrier densities (above ~10^{19} cm^{-3}), efficiency curves appear to be converging and show quite similar values. This is in a good agreement with the results reported earlier in [164].

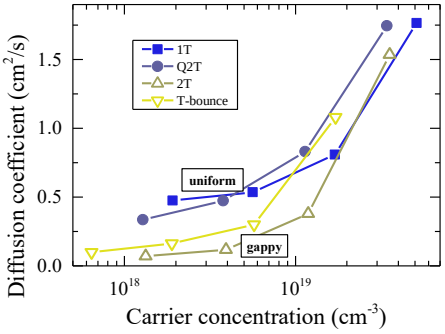

Fig. 3.33. Carrier diffusion coefficient as a function of carrier density.

Lower droop onset carrier densities in gappy samples suggest stronger localization in them, which is evidenced by significantly smaller diffusion coefficients at carrier densities below ~10^{19} cm^{-3} (see Fig. 3.33). At 3×10^{18} cm^{-3}, D is 0.1 and 0.22 cm^2/s in gappy samples, and 0.44 and 0.5 cm^2/s in uniform profile samples. This coincides with up to 4-times larger activation energies for carrier delocalization, as calculated in [164] and [233]. However, at higher carrier densities, there appear to be no systematic differences between the diffusion coefficient values among the samples. This may stem from the delocalized carriers eventually occupying the extended states [183,189] [P2] and is probably the reason why values of IQEs are quite similar at high carrier densities (Fig. 3.32). It once again proves that diffusivity plays

a key role in the nitride-based LED efficiency and nonetheless influences the droop process.

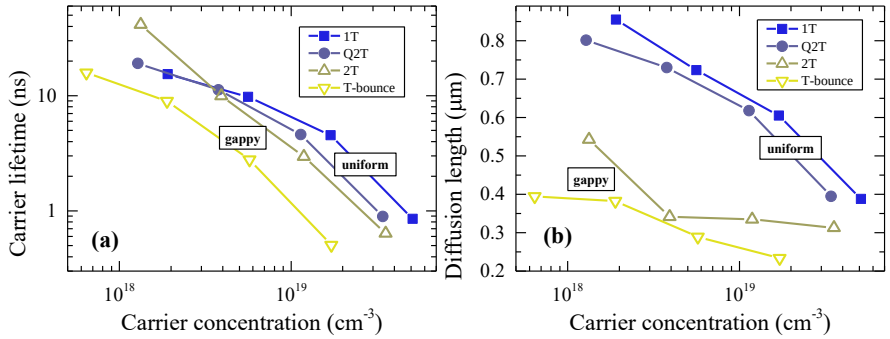

Fig. 3.34. LITG carrier lifetime (a) and diffusion length (b) as functions of carrier density.

Interestingly, carrier lifetimes, contrary to what one would expect in a strongly localized system, are also shorter in gappy QWs (at least at high carrier densities, see Fig. 3.34(a)). Having in mind higher IQEs, this may come from faster recombination through a radiative channel, such as bimolecular recombination. This implies that the decrease of diffusivity promotes the probability for an electron and hole to meet and annihilate radiatively and reduces the effective carrier lifetime. Consequently, this leads to more than 2 times shorter diffusion lengths in gappy samples, which very likely prohibit the carriers from reaching more distant defects (Fig. 3.34(b)). As the TEM images show [164], in the sample with the highest number of gaps (T-bounce), their arrangement in some areas reaches distances even shorter than 50 nm. This may be the origin of the drastic reduction in the diffusion length as carrier movement is restricted by a large amount of potential barriers, which may be too high to hop over.

A simple ABC model with the exact same procedures as in Chapter 3.5 was used to extract the SRH, bimolecular, and Auger recombination coefficients. The carrier lifetime was obtained from spectrally-integrated DT kinetics and used for modelling (Fig. 3.35); modelling results are presented in Table 2. The SRH recombination lifetime ($1/A$) is longest in the sample that was capped prior to the temperature ramping probably due to thermal annealing of defects in InGaN [234]. Meanwhile, B and C coefficients in gappy samples exceed those in the uniform width profile samples by approximately one order of magnitude. This explains an earlier droop onset in

gappy samples and why higher IQE values appear together with shorter carrier lifetimes. Enhanced localization increases the rate of radiative recombination, which effectively leaves less carriers for non-radiative recombination at defects. Defect density may not differ drastically between the samples, but higher population of localized states allows more electrons and holes to recombine radiatively. This can be supported by the fact that more uniform and more intense cathodoluminescence (CL) intensity maps were obtained in gappy QWs [234]. A recent work also showed an increased radiative recombination rate in near-UV LEDs due to higher potential energy fluctuations caused by a higher In content [48].

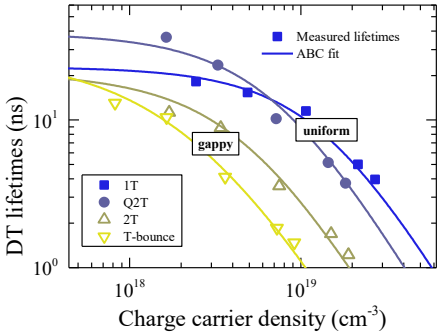

Fig. 3.35. Dependencies of DT spectrally-integrated carrier lifetimes on carrier density with corresponding ABC model fits.

Table 2. ABC modelling results of the samples with uniform and gappy QW width profiles.

QW profile	Sample	Droop onset, $cm^{-3} \times 10^{18}$	1/*A*, ns	*B*, $cm^3/s \times 10^{-12}$	*C*, $cm^6/s \times 10^{-31}$
Uniform	1T	9	23	2.6	2.35
	Q2T	9	39	3.4	5.1
Gappy	2T	3	21	11	20
	T-bounce	2	27	30	56

B and *C* coefficients present a strong linear correlation (Fig. 3.36). Such a connection can mean that the energy transfer to a third particle in a three particle Auger process heavily depends on the initial stage – a two particle process, which can basically be seen as bimolecular recombination. Hence, stronger localization increases the rate of bimolecular recombination and the same applies to Auger recombination. On the other hand, Auger recombination itself can be enhanced by the increased potential fluctuations through scattering [112] and increased uncertainty of the momentum [115],

with both easing the conservation of momentum. Either way the outcome is faster Auger recombination in samples with gross well width fluctuations.

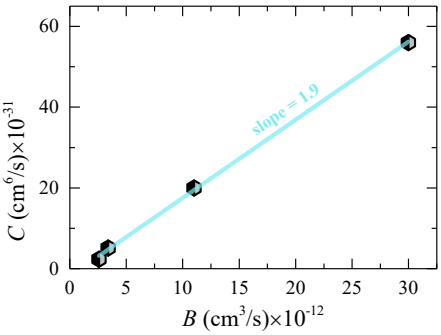

Fig. 3.36. Correlation between Auger (*C*) and bimolecular recombination (*B*) coefficients. The cyan line shows a linear fit.

In conclusion, investigation of carrier dynamics revealed up to nearly 2 times higher peak IQEs in samples with gappy QW width profiles due to up to 4 times reduced carrier diffusivity. This is the outcome of additional barriers provided by gross well-width fluctuations that increase the localization so more carriers get trapped in the localized states. This in turn increases the radiative recombination rate, thus leaving less carriers to reach the defect states. Reduction of the diffusion coefficient and the carrier lifetime gives more than 2 times shorter diffusion lengths in gappy samples. From the simple ABC modelling results, Auger recombination appears to be strongly connected to the magnitude of potential fluctuations.

3.7. Efficiency curve characteristics of an efficient light emitter. Limits of the simple ABC model

PL spectra are often used as the main instrument to get the first impressions about samples as they are relatively easy to obtain and do not require special preparations. They carry information about the peak position, linewidth, intensity, etc. Collecting PL spectra at various excitations allows graphing of the efficiency curves, which can then be used to evaluate the droop onset and other parameters, such as efficiency rise rate and droop rate. However, only PL intensity is usually used to assess improvements in samples without fully exploiting other available data. In this chapter, correlations between the efficiency curve parameters and other important parameters, such as the peak IQE and diffusion coefficient, are investigated in a large array of different InGaN MQWs samples from Table 1. A prognostic potential of the efficiency curve peculiarities is presented. Furthermore, limits of the basic ABC model are discussed in terms of its applicability.

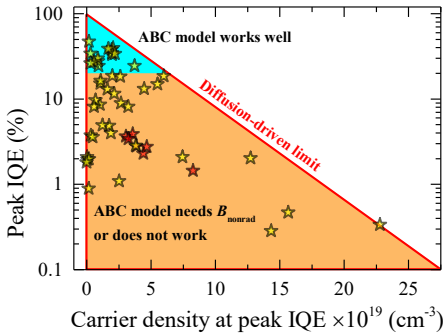

Fig. 3.37. Peak IQE vs the corresponding carrier density at the droop onset. Each data point represents a separate sample. Red interior marks m-plane samples. The red triangle marks the range of possible peak IQE values.

In Fig. 3.37 the peak IQE vs the corresponding carrier density is shown, as extracted from the efficiency curves measured by TIPL in an integrating sphere. An important tendency is seen here – the lower the droop onset carrier density, the higher the peak IQE can be achieved in samples. In other words – there appears to be a certain upper boundary at higher droop onset carrier densities. Because diffusivity directly correlates with carrier density, this may be attributed to the diffusion-driven non-radiative losses at the defects, which fundamentally limit the maximum peak IQE. At the current state of the nitride-based device growth technology, such losses cannot be avoided, as relatively high defect densities are expected even in a high-grade final product. Meanwhile, diffusivity depends on other factors like alloy and well width

fluctuations, not to mention that defectiveness of the materials also has a huge impact on efficiency. Therefore there are peak IQE values that are well below the upper boundary, even at the lowest droop onset carrier densities. Hence the possible peak IQEs are scattered in an area marked by a red triangle in the graph. This suggests that only samples with relatively low defect densities and suitable localization conditions can reach the boundary (but not exceed it), while others will be positioned somewhere within the triangle. Naturally, one finds that keeping the droop onset as low as possible is necessary for the possibility to obtain 100% peak efficiency. Enhancing carrier localization is one way of doing this. This can be supported by the increase of peak IQEs and earlier droop onsets when PL is measured in the same samples but at lower temperatures [66,235]. Reduction of carrier diffusivity in QWs at lower temperatures [121] indicates stronger localization and leads to smaller non-radiative recombination at defects although the material quality remains the same.

The usual processes behind the initial rise of the IQE curve are the increasing with carrier density quadratic bimolecular recombination rate [104,166] [P1,P3] and saturation of non-radiative recombination centers [66,205]. On these basis, the rise rate should be carrying some valuable information, as it is expected that the said processes should give different slopes. For example, in the case of dominating bimolecular recombination, the PL emission intensity would rise with carrier density squared [198] ($I_{PL} \propto BN^2$), whereas the quantum efficiency rise rate should be proportional to carrier density ($IQE_{PL} \propto \frac{I_{PL}}{N} \propto \frac{BN^2}{N} \propto N$). As for other rise rates, they might be indicating the involvement of other mechanisms, such as point defect saturation or exciton recombination. To find the correlation between the peak IQEs and the initial rise rates of IQE curves, the steepest parts of the latter were fitted with a power function (Fig. 3.11 top)

$$IQE_{PL} \propto I_{exc}^{\gamma}. \tag{3.10}$$

The exponent γ will be further regarded as the efficiency rise rate.

In Fig. 3.38(a) the peak IQE vs γ is presented. A general trend of the decreasing peak IQE with a steeper efficiency rise is observed. Some of the samples reach nearly 40% when γ values are below 1, which suggests a significant role of bimolecular and/or exciton-like radiative recombination mechanisms. This can be explained with the fact that the efficiency of the correlated electron-hole pair recombination should stay constant with excitation up till the droop onset, as each generated electron is expected to

recombine with its associated hole, which is usually seen at low temperatures [66,198]. Meanwhile, for bimolecular recombination the rise rate should be proportional to carrier density. SRH recombination, whose efficiency should be independent of carrier density, also takes place, and has a huge impact in samples with low peak IQEs. Therefore, the values of the rise rate fall between 0 and 1 as a result of three competing recombination channels, and dominance of one or another leads to different peak IQEs. However, this cannot explain faster than 1 rise rates.

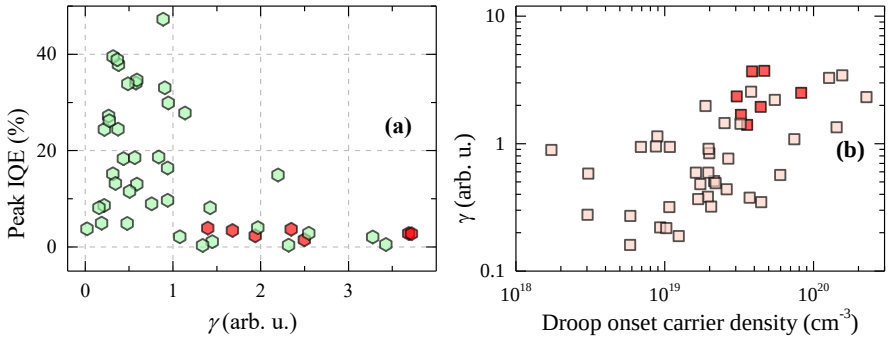

Fig. 3.38. Peak IQE vs the efficiency rise rate γ (a). Correlation between the efficiency rise rate and the droop onset carrier density (b). Red interior marks m-plane samples.

Fig. 3.38(b) shows that higher γ values correlate with higher droop onset carrier densities. As determined from earlier results, a higher droop onset is associated with weaker localization and a faster non-radiative recombination rate. Droop onsets that occur at higher driving currents were also revealed in areas of MQW structure's electroluminescence maps where non-radiative recombination is stronger [234]. All this implies that $\gamma > 1$ is connected to higher order non-radiative losses, very likely diffusion-driven. Then the higher droop onset itself may come from the fact that before reaching the peak IQE value, more charge carriers are needed to saturate the defects [66,205]. This is burdened by the fact that their effective density (that carriers can reach) increases with the filling of the states and subsequently growing delocalization. This leads to the increasing with carrier density non-radiative recombination rate, which is responsible for steeper rise rates.

The relation of efficiency rise rate to localization is evidenced by higher γ values with the increasing diffusion coefficient (Fig. 3.39). These results are interesting in the context of types of droop curves. Generally, there are two of these: type I with a slow efficiency rise and a slow decay, and type II with a

fast rise and a fast decay [205,236]. There have been debates on which is more preferable, even a desirable type III was suggested, with a fast rise and a slow decay. The latter is uncommon, and from the usually observed curves, type I appears to be favorited by the literature, because the droop effect comes at a lower cost at increased carrier densities. However, the curves presented in various works are usually given in arbitrary units and in small sets of quite similar samples, thus choosing such preference may be controversial. In this work, the results in a large array of very diverse samples clearly point out that a slow rise should be the one to seek for the maximum peak IQE, which apparently is a subject to low diffusivity and low droop onsets. In the work [P2], the thresholds of PL and DT (within the PL window) signal saturation, which is closely related to the droop onset, were higher in samples with more indium. This was ascribed to more localized states that need to be saturated (due to higher In content fluctuations). Though in the current context this may also be due to higher number of defects to saturate, as the samples with higher In content showed poor emission outputs. This was also accompanied by a drop of carrier lifetimes in all the electronic states monitored by both TRPL and DT.

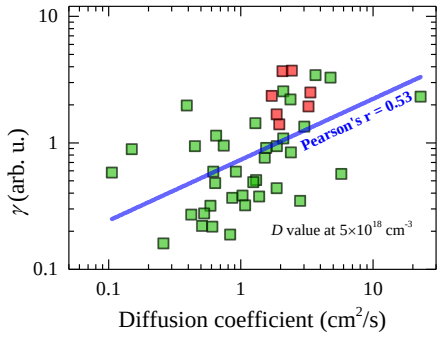

Fig. 3.39. Correlation of γ with carrier diffusion coefficient at 5×10^{18} cm^{-3} carrier density. Red interior marks m-plane samples.

Next the limitations of the standard ABC model with carrier density-independent coefficients are discussed. It was attempted to fit the IQE curves and carrier lifetimes (extracted from the initial parts of the spectrally-integrated DT transients) of 40 c-plane samples from Table 1 (V1-T815) by following the same procedures as in Chapter 3.5. As it turned out, only a part of samples was well described by a simple model, as both the modelled carrier lifetimes and IQEs sufficiently complied with the experimental results (Fig. 3.40(a) and (b)). For other samples, addition of the increasing with carrier density non-radiative recombination term was necessary. In another part of

samples, however, the modelling failed, as it was impossible to find ABC coefficients that would match the measured droop onset. These findings are summarized in Fig. 3.37, where a good match was achieved between the experimental and ABC-modelled curves for all samples with peak IQEs roughly above 20%. For the majority of samples below 20% peak IQE, the standard B coefficient was replaced with $B^* = B_{rad} + B_{nonrad}$, a composition of radiative and non-radiative terms, to reduce the modelled peak IQE values so that they match the experimental ones. Such a modification can be justified by the presence of diffusion-driven non-radiative losses, which scale with excitation due to the increasing density of delocalized carriers. The modified equations are:

$$\frac{1}{\tau} = A + (B_{rad} + B_{nonrad})N + CN^2, \tag{3.11}$$

$$IQE = \frac{B_{rad}}{A+(B_{rad}+B_{nonrad})N+CN^2}. \tag{3.12}$$

Here, the B^* term is assumed to be constant throughout all excitations. In order to better fit inclines and declines of the IQE curves, effects such as the phase-space filling [96] and the associated break-down of quadratic (BN^2) and cubic (CN^3) dependencies [142,237] should be considered, but for the sake of simplicity, they are omitted. Traces of stimulated recombination were not observed, neither in PL spectra nor in DT kinetics even at the highest excitations, therefore this process is not included as well. As for diffusivity – its impact is assumed to be reflected in the used recombination coefficients.

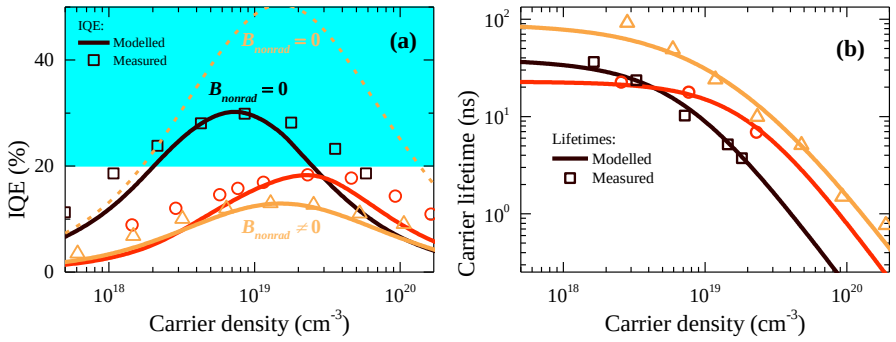

Fig. 3.40. Measured and modelled IQEs (a) and carrier lifetimes (b): data points correspond to the experimental results, curves correspond to the modelled results. The dashed orange line in (a) depicts the overestimated IQE values when $B_{nonrad} = 0$.

The upper results suggest that a simple ABC model is limited only to relatively efficient samples, where Auger recombination is a feasible droop

cause. This makes sense in the context of the results presented in Chapter 3.6: the Auger recombination coefficient directly correlates with the bimolecular recombination coefficient. As the peak IQE decreases, the discrepancy between the measured and modelled values increases. The origin of this could be the emergence of an alternative droop cause, such as diffusion-driven non-radiative recombination. Thus, as the properties of samples deteriorate with the growth of defect density or with the decrease of localization strength, the role of Auger process is reduced. In fact, it was shown that weaker localization correlates with the lower *C* coefficient [112]. Simultaneously, the probability of recombination at the defects increases. At first, only the peak IQE falls behind the initially expected values and B_{nonrad} comes into play, with Auger still remaining the leading droop mechanism. Later the recombination process at the defects intensifies even more and it subsequently starts to dominate over the Auger recombination. This is where the largest discrepancies arise and, depending on other conditions, it may become impossible to describe samples with a simple ABC model.

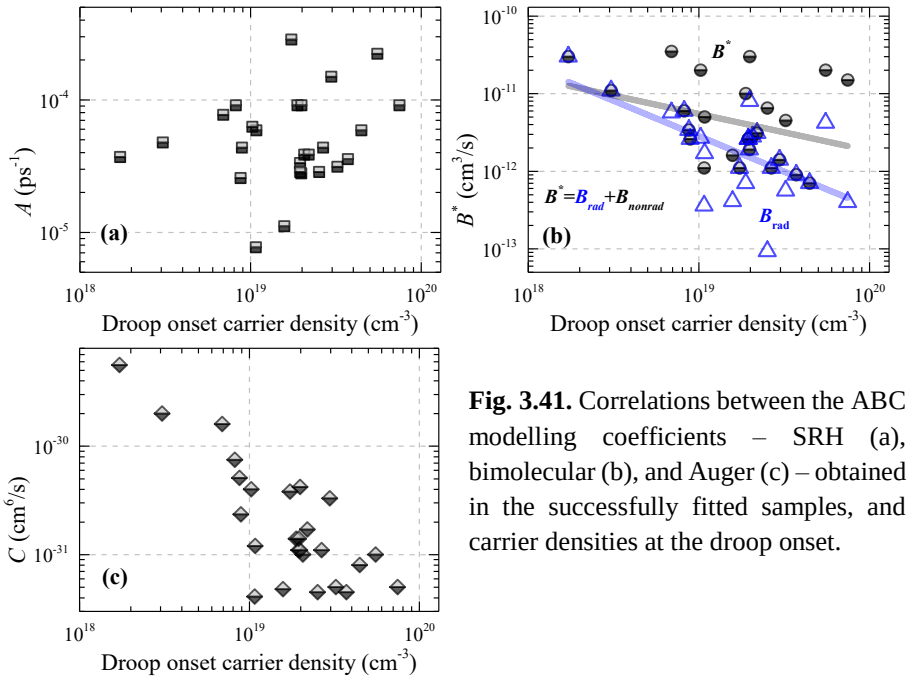

Fig. 3.41. Correlations between the ABC modelling coefficients – SRH (a), bimolecular (b), and Auger (c) – obtained in the successfully fitted samples, and carrier densities at the droop onset.

Modelling coefficients of the well-fitted dependencies demonstrate correlations with droop onset carrier densities. SRH recombination coefficient

values, although fairly scattered, correlate positively (see Fig. 3.41(a)). The higher rate of this recombination can be attributed to weaker localization, inherent to samples with higher droop onset carrier densities, and higher defect densities. Meanwhile, quadratic recombination coefficient B^* tends to decrease in samples with higher droop onsets, as shown in Fig. 3.41(b). In the same graph, B_{rad}, the radiative recombination term in B^*, is also plotted, and the same trend is seen. Linear fits of B^* (black line) and B_{rad} (blue line) reveal a growing separation between the two. This means that not only the quadratic recombination rate decreases with higher droop onset carrier density, but its non-radiative part B_{nonrad} increases as well. All this checks with SRH recombination consuming more carriers and weaker localization leading to higher diffusion-driven non-radiative losses. Auger recombination coefficient also negatively correlates with the droop onset carrier density, which meets the reduction of Auger scattering at the presence of weaker localization (Fig. 3.41(c)). However, this may be an indirect correlation, since theoretical calculations have shown decreased C values in wider wells [114], where higher droop onset carrier density is expected. Nonetheless, the idea that Auger is mostly significant in highly efficient samples is still supported.

In summary, the main peculiarities of the TIPL efficiency curves in samples with high peak IQEs were described. The lower droop onset carrier density accompanied with a slower efficiency rise rate should be favorited and can be used for a quick evaluation of the optimal growth conditions or structural sample parameters on the way to achieve the highest peak IQEs. This is because steeper slopes and higher droop onsets correlate with higher diffusivity, which is an indication of weaker localization and, subsequently, higher non-radiative losses at the defects. All this is confirmed with the simple ABC modelling, performed in a large array of samples, where A coefficient increases, while B and C coefficients decrease with higher droop onset carrier densities. The modelling results also imply that the simple ABC model will most likely work with the highly efficient samples only, where Auger scattering seems to be a valid droop cause, while for other samples with low efficiencies – more variables are needed, as the droop process may be influenced by other complex mechanisms.

3.8. Generalized recommendations for growth

The results from this thesis indicate that suppression of ambipolar in-plane carrier diffusion is necessary to reduce the non-radiative losses at the defects in InGaN QWs. This is relevant to the present technology because currently used solutions to improve material quality, such as the lattice matched substrates or overgrowth techniques, increase cost and complexity. There are several approaches presented in this work, and by combining them together, one should have a strong framework for the growth of an efficient nitride-based light emitting device.

Starting from the underlying layers, insertion of a strain relieving layer like a superlattice before the active layer should be a mandatory procedure, as it reduces the internal electric fields inside QWs and leads to lower carrier delocalization.

Going up to the active layer, thinner wells enhance localization through the increased carrier scattering due to higher potential fluctuations. The wells should be narrow enough (≤3 nm) to provide the optimal localization conditions and the overlap of carrier wave functions, but not too thin (≥2 nm) so that enough of the effective optically active volume is ensured. The QW width also depends on the desired wavelength of emission, however a better approach for longer emission wavelengths is including more indium in a narrow well.

Further improvement of localization can be achieved by using the temperature ramping after the growth of each QW which causes evaporation of the In content at random locations and subsequent gross well width fluctuations. Additional barriers to carrier diffusion enhance the radiative recombination rate and leave less carriers for the non-radiative recombination channels.

Pulsed growth of QWs provides additional surface nitridization, allows the migration of the deposited atoms, as well as evaporation of the excess atoms. The consequential better atom distribution increases localization, as well as the quality of the active layer. Timing should be adjusted carefully for different growth temperatures and precursor partial pressures, however, longer interruption times appear to introduce better changes.

CONCLUSIONS

1. Insertion of a short period superlattice results in lower strain and smaller internal electric fields in the above grown QWs. It is also accompanied by weaker delocalization, which has a crucial influence on IQE and its droop, as evidenced by an inverse correlation between the IQE values and the carrier diffusion coefficient. It was shown that insertion of a SL can increase the IQE several times.

2. The increasing rate of non-radiative recombination with excitation can originate from carrier density dependent non-radiative recombination at the defects. With the addition of saturation of the radiative recombination coefficient due to the phase-space filling, it can be used to successfully describe the IQE droop without using the Auger term.

3. Diffusion-driven non-radiative recombination is evidenced by the increasing ambipolar carrier diffusion coefficient. The latter's increase rate with carrier density was to shown to correlate with the onset of efficiency droop, proving an important role of highly mobile carriers in the efficiency droop process.

4. An untypical redshift of PL peak that emerges at long delays and increases with excitation is a direct observation of carrier redistribution between the localized states of various depths.

5. Higher carrier diffusivity leads to lower peak IQE due to promoted non-radiative recombination of carriers at the defects. This is evidenced by a linear decrease of the carrier lifetime with the increasing diffusion coefficient, obtained at carrier densities corresponding to the droop onset.

6. The ambipolar diffusion coefficient decreases in narrower QWs, which is mainly due to higher well width fluctuation-induced potential energy fluctuations that enhance the scattering of charge carriers.

7. Increased potential fluctuations prohibit the diffusion of carriers to the extended defects, allowing for the localized states to get filled earlier, and enhance the Auger scattering, thus giving rise to an earlier droop onset. The latter is advantageous for peak IQE, since smaller diffusion-driven non-radiative losses are expected at lower carrier densities.

8. The magnitude of the Stokes shift in InGaN QWs is determined by the quantum-confined Stark effect, carrier diffusivity, and random alloy disorder: in wider QWs the carriers fall deeper into triangular potential minima at the edges, while higher diffusivity allows the carriers to reach the

deeper localized states, provided that they are present from random alloy fluctuations. Strain relief reduces the internal electric fields and In content fluctuations, therefore Stokes shift may decrease too.

9. The pulsed MOCVD growth mode is advantageous for increasing the structural quality of the active layer and improving localization conditions, provided that migrating atoms have enough time and enough energetically favorable lattice positions to attach to. This happens after a sufficient number of excess atoms evaporates and the surface gets fairly nitridized. Shorter diffusion length can be an indicator of a better atom distribution.

10. Temperature ramping-induced QW gross well-width fluctuations provide additional barriers to carrier diffusivity. Enhanced localization increases the rate of radiative recombination and prohibits the carriers from reaching the non-radiative recombination centers, as evidenced by reduced carrier lifetimes and significantly shorter diffusion lengths.

11. A fast recombination process and continuously growing diffusivity at high carrier densities reveal the presence of both Auger and diffusion-driven non-radiative recombination. The Auger process alone can be used to describe the droop in QWs with relatively high peak IQE (>20%), while for less efficient QWs diffusion-driven defect recombination has to be included.

12. The lower carrier density droop onset accompanied with a slower quantum efficiency rise rate correlate with stronger localization. They may be used as criteria of the optimal growth conditions or structural sample parameters on the way to achieve the highest peak IQEs.

SUMMARY/SANTRAUKA

ĮVADAS

Šviesos technologijos vaidina labai svarbų vaidmenį mūsų kasdienybėje: bendrasis apšvietimas, indikatoriai ant įvairių elektronikos prietaisų, nuotoliniai pulteliai, mėlynos, raudonos ir infraraudonos spinduliuotės lazeriai atitinkamai BLU-RAY, DVD ir CD įrenginiuose, įvairūs jutikliai, vaizduokliai, automobilinis apšvietimas ir t.t. Didžioji dalis minėtų technologijų yra smarkiai išvystytos, visgi tam prireikė daugiau nei šimto metų ir kelių technologinių proveržių. Tad nenuostabu, jog ir šiomis dienomis mokslininkai ir gamintojai daug dėmesio skiria šviesos technologijų tobulinimui, siekdami dar labiau pagerinti jų našumą ir kokybę, ką papildomai skatina visuomenės rūpinimasis aplinkosauga ir energijos taupymu.

Nuo pat 1879 metų, kuomet Tomas Edisonas pateikė patentą, kaitrinės lemputės buvo vienas iš pagrindinių šviesos šaltinių. Nors ir pigus, tačiau labai nenašus, gebantis šviesa paversti mažiau nei 5% elektros energijos ir turintis mažesnį negu 19 lm/W šviesinį našumą. Kaitrinių lempučių (įskaitant ir halogenines) rinka šiomis dienomis sparčiai mažėja, o daugelis valstybių jau pradėjo drausti tokių lempučių naudojimą bendrajame apšvietime [1]. Tai yra puikiai suprantama, kuomet egzistuoja daug geresnės alternatyvos.

Viena iš jų – 1938 metais sukurti fluorescenciniai šviesos šaltiniai. Jų bendras našumas gali siekti 40% ir daugiau, tipinis šviesinis našumas – 60 lm/W, todėl tokie šviesos šaltiniai yra patrauklūs, ypač komercinės paskirties erdvėse, tokiose kaip prekybos centrai arba biurai. Deja, ši technologija turi tam tikrus trūkumus, iš kurių vienas svarbiausių yra ultravioletinės šviesos konversija fluorescuojančioje dangoje, kuomet ~5.5 eV energijos fotonai yra konvertuojami į ~2.5 eV energijos fotonus, esančius regimojoje srityje. Toks Stokso poslinkis reiškia, jog nedaugiau nei 45% UV spinduliuotės energijos gali būti efektyviai panaudota, tuo tarpu kita dalis yra prarandama kaip šiluma [2]. Kiti nuostoliai moderniose lempose yra susiję su mažesniu negu 90% pačios konversijos kvantiniu našumu fluorescuojančioje dangoje. Negana to, fluorescencinės lemputės kainuoja gerokai daugiau negu kaitrinės (dėl sudėtingesnės konstrukcijos ir didesnio kiekio elektrinių komponentų), dėvisi sparčiau, jei yra dažnai junginėjamos, turi tam tikrą sušilimo laiką, kelia pavojų sveikatai dėl naudojamų gyvsidabrio garų, yra sunkiai perdirbamos ir pritemdomos.

Kalbant apie šviesinį našumą, natrio garų lempos (sukurtos 1965 metais) lenkia anksčiau aptartus šviesos šaltinius su vertėmis iki 200 lm/W. Tačiau tai yra pasiekiama dėl siauro spinduliuotės spektro, esančio prie pat 555 nm bangos ilgio, ties kuriuo žmogaus akis turi didžiausią jautrį [3]. Dėl to spalvų atitikimo rodikliai (angl. *color rendering indexes*, CRI) yra prasti, kas reiškia, jog stebimų objektų, apšviestų natrio garų lempomis, spalvos skiriasi nuo apšviestų natūralia šviesa. Todėl tokia apšvietimo technologija pagrinde yra naudojama lauke (pvz. gatvių apšvietime), kur prioritetas teikiamas geriausiam matomumui už mažiausią kainą, nepaisant spalvų atgavos.

Kietakūnio apšvietimo technologijos pradžia – 1962 metais Nick Holonyak sukurtas raudonas šviestukas (angl. *light emitting diode*, LED). Ši technologija turi didžiulį potencialą užimti visą šviesos technologijų rinką, kadangi neturi griežtų teorinių apribojimų pasiekti beveik 100% vidinį kvantinį našumą, gali laisvai peržengti 100 lm/W ribą [4] (šviestukų gamintojas Cree 2014 metais kambario temperatūroje pasiekė net 303 lm/W [5]), taip pat turi gerokai mažiau trūkumų, lyginant ją su kitomis šviesos technologijomis. Su raudonais, geltonais ir žaliais šviestukais, kurių pagrindas yra tokie puslaidininkiai kaip GaAsP, AlGaInP, bei mėlynais, žaliais ir geltonais, kurių pagrindas – InGaN, galima padengti visą regimąją sritį, kas atveria plačias galimybes: bendrasis ir automobilinis apšvietimai, spalvoti vaizduokliai televizoriams ir mobiliesiems telefonams, projektoriai, adaptyvaus spektro šviesos šaltiniai optimaliai spalvų atgavai [6] arba augalų auginimui, ir t.t. 2016 metais šviestukų rinka buvo įvertinta beveik 30 milijardų JAV dolerių, su prognozėmis iki 2022 metų padvigubėti [7,8].

Pagrindinė medžiaga mėlynos šviesos emisijai – InGaN – šiuo metu yra intensyviai tyrinėjama mokslininkų iš viso pasaulio. Ji yra naudojama našiems mėlyniems, žaliems ir baltiems (pasinaudojant konversija fosforuose, pvz. geltoname YAG:Ce^{3+}) šviestukams. Tačiau, naudojantis draustinio tarpo inžinerija – keičiant junginyje InN ir GaN santykį – yra teorinė galimybė su InGaN padengti ir visą regimosios srities spektrą. Deja, junginiai su didele InN moline dalimi žaliai emisijai pasižymi prasta struktūrine kokybe dėl defektų formavimosi ir dideliais vidiniais elektriniais laukais, o tai lemia mažus vidinius kvantinius našumus (VKN, ~30%, kuomet mėlynuose dariniuose jie gali siekti ~90% [9]). Situacija blogėja slenkant toliau link raudonosios spektro dalies. Tuo tarpu AlGaInP sistemoje defektų tankio augimas yra lydimas perėjimo iš tiesiatarpio puslaidininkio į netiesiatarpį, kuomet keičiant emisijos bangos ilgį nuo raudonos iki žalios ir toliau yra didinamas aliuminio kiekis [10,11]. Šių našumo mažėjimų kombinacija

sudaro tam tikrą sritį (~550-600 nm), kurioje vidiniai kvantiniai našumai yra tokie maži, kad tampa sunku konkuruoti netgi su kaitrinėmis lemputėmis – tai yra efektas, žinomas kaip „žaliojo tarpo“ (angl. “*green gap*”) problema.

Akivaizdu, jog „žaliojo tarpo“ užpildymas yra svarbi užduotis, ir ne tik dėl energijos taupymo sumetimų. Pilnai išnaudoti kietakūnio apšvietimo potencialą galima tik pasitelkus spalvų maišymo metodus be konversijos fosforuose [12]. Taip pat, tai sudarytų galimybes gaminti vaizduoklius šviestukų pagrindu, panašiai kaip ir organinių šviestukų (angl. *organic light emitting diode*, OLED) technologijoje, kuri įgalina daug didesnį kontrasto santykį ir spalvų sodrumą, lyginant su dabar rinkoje dominuojančiais skystųjų kristalų vaizduokliais (angl. *liquid crystal displays*, LCDs), kuriuos riboja tai, jog jų veikimo pagrindą sudaro šviesos iš galinės dalies filtravimas. Tuo tarpu organinių šviestukų vaizduokliai yra brangūs, o juos sudarantys taškai su laiku degraduoja – čia taškai neorganinių šviestukų pagrindu tikrai būtų konkurencingi. Galimybė raudonus, žalius ir mėlynus taškus kurti tos pačios medžiagos pagrindu leistų išvengti keblumų, kylančių dėl skirtingų medžiagų integravimo viename luste, o tai leistų sumažinti gamybos kainą ir sudėtingumą. InGaN šiuo metu yra geriausias kandidatas „žaliojo tarpo“ įveikimui, todėl daug dėmesio yra skiriama paieškai būdų, kurie leistų šios medžiagos kokybę pagerinti.

Deja, InGaN pagrindu kuriami šviestukai turi dar vieną problemą – taip vadinamą našumo krytį (angl. *droop effect*), dėl kurio aukštuose elektros srovės tankiuose sumažėja našumas. Jis tampa ypatingai svarbus kalbant apie didelės galios šviesos šaltinius – tam, kad būtų pasiekti dideli fotonų srautai, tenka leisti stiprias sroves, dėl ko nukenčia našumas, arba tenka naudoti daug lustų, per kuriuos leidžiamos silpnos srovės, dėl ko žymiai išauga sistemos sudėtingumas ir kaina. Nors našumo kryčio problema sulaukia daug dėmesio, tačiau jos kilmei paaiškinti egzistuoja tik teorijos, iš kurių Ožė (angl. *Auger*) rekombinacija [13] turi stipriausią palaikymą, tuo tarpu pilnai veikiančių sprendimo būdų iki šiol nėra pasiūlyta.

Akivaizdu, jog „žaliojo tarpo“ ir našumo kryčio problemas būtina išspręsti tam, kad būtų galimybė pilnai išnaudoti kietakūnio apšvietimo potencialą ir toliau tobulinti apšvietimo technologijas. Sprendimų paieška pastaruoju metu lėtai juda, o per pastarąjį dešimtmetį buvo pasiūlyti daugiausiai tik nedideli patobulinimai. Todėl verta apsvarstyti ir kitus inovatyvius būdus, kurie leistų padidinti našumą. Bet kuriuo atveju, tam yra būtinas pilnas supratimas apie procesus, vykstančius InGaN šviestukuose emisijos metu.

Pagrindinis tikslas

Pagrindinis šio darbo tikslas yra įgyti gilesnes žinias apie spindulinius ir nespindulinius rekombinacijos procesus InGaN kvantinėse sandarose ir apibrėžti struktūrinius bei medžiagos parametrus, kurie šiems procesams turi didžiausią įtaką, pasinaudojant viena kitą papildančiomis nedestruktyviomis optinėmis žadinimo-zondavimo metodikomis. Surinktus rezultatus tikimasi panaudoti šviestukų aktyviosios srities optimizavimui siekiant didžiausio kvantinio našumo bei aiškesniam našumo kryčio supratimui.

Darbo uždaviniai

- Įvertinti absoliutines vidinio kvantinio našumo ir sugerties koeficiento vertes InGaN sandarų su kvantinėmis duobėmis (KD) aktyviosiose srityse. Šios vertės yra reikalingos našiausių bandinių išskyrimui bei tam, kad kuo tiksliau būtų palyginami nuo nepusiausvirųjų krūvininkų tankio priklausantys procesai našiuose ir nenašiuose dariniuose.
- Optiškai ištirti krūvininkų dinamikos kitimą didelėje imtyje $In_xGa_{1-x}N$ darinių, pritaikant platų sužadinimų diapazoną, viršijantį ir neviršijantį našumo kryčio slenkstį.
- Rasti koreliacijas tarp struktūrinių parametrų, medžiagos savybių ir VKN $In_xGa_{1-x}N$ sandarose.
- Siekiant daugiau sužinoti apie galimas našumo kryčio priežastis – sumodeliuoti nuo krūvininkų tankio priklausančius rekombinacijos procesus.
- Apibendrinti gautus rezultatus ir pateikti rekomendacijas InGaN šviestukų aktyviosios srities optimizavimui.

Mokslinis naujumas ir svarba

Šiame darbe ypatingai daug dėmesio yra skiriama tiksliam krūvininkų tankio įvertinimui kiekviename bandinyje su jo specifiniu sugerties koeficientu. Tai leidžia tikslesnį procesų, priklausančių nuo krūvininkų tankio, palyginimą skirtinguose InGaN KD dariniuose, lyginant su krūvininkų tankio skaičiavimu naudojantis literatūroje pateikiamomis vidutinėmis vertėmis – naudojantis pastarosiomis nėra atsižvelgiama į kiekvieno bandinio individualias savybes.

Kambario temperatūros vidiniai kvantiniai našumai tiesiogiai įvertinami integruojančioje sferoje matuojant KD sugertį ir emisiją, papildomai įvertinant sugertį žemiau esančiuose storuose buferiniuose sluoksniuose. Priešingai nei vertinant VKN iš nuo temperatūros priklausančių matavimų, toks metodas yra paprastesnis ir nepasikliauja prielaida, jog žemose temperatūrose nespindulinės rekombinacijos kanalas yra pilnai nuslopinamas.

Optimalaus InGaN šviestuko dizaino paiešką apsunkina didelis kiekis kintamųjų prietaiso gamyboje ir charakterizavime – procesą palengvintų prisirišimas prie vieno parametro, pagal kurį galima būtų tobulinti šviestuko dizainą. Šiame darbe atskleidžiama neigiama koreliacija tarp krūvininkų difuzijos ir kvantinio našumo gali įgalinti tokią koncepciją. Kadangi koreliacija yra stebima tarp didelio kiekio skirtingų bandinių, siūloma difuzijos koeficientą laikyti kaip universalų našumą apribojantį parametrą. Galimybė sumažinti difuzijos koeficientą keičiant KD storį bei modifikuojant auginimo procedūras atrodo perspektyviai tolesniam InGaN šviestukų tobulinimui.

Sunkumai nustatant neabejotiną našumo kryčio priežastį yra tikimai susiję su vienalaikiu kelių mechanizmų pasireiškimu. Eksperimentiniai rezultatai ir modeliavimas rodo tiek difuzijos sąlygotą rekombinaciją defektuose, tiek ir Ožė rekombinaciją. Panašu, kad vyraujantį mechanizmą nulemia lokalizacijos sąlygos ir medžiagos kokybė. Kadangi Ožė rekombinacija vyrauja našiausiuose bandiniuose, tai gali būti paaiškinimas, kodėl standartinis ABC modelis negali būti pritaikytas prastos kokybės bandiniams.

Ginamieji teiginiai

- Didesnė krūvininkų difuzija InGaN KD dariniuose lemia mažesnį maksimalų vidinį kvantinį našumą. Šis fundamentinis apribojimas atsiranda dėl spartesnės nespindulinės delokalizuotų krūvininkų rekombinacijos defektuose, kurią patvirtina tiesiškai mažėjanti krūvininkų gyvavimo trukmė augant difuzijos koeficientui.
- Krūvininkų difuzija mažėja siaurinant InGaN kvantinės duobės storį dėl išaugusių potencialo fluktuacijų, kurias sukelia duobės storio fluktuacijos. Apribodama galimybę pasiekti nespindulinius rekombinacijos centrus, išaugusi krūvininkų lokalizacija sumažina slenkstinę našumo kryčio krūvininkų tankio vertę ir leidžia pasiekti didesnius maksimalius VKN.

- Maksimalus VKN InGaN kvantiniuose dariniuose gali būti padidintas sumažinus difuziją, ką galima pasiekti: (i) įterpus supergardelės tarpsluoksnį, kuris susilpnina krūvininkų delokalizaciją, (ii) pritaikius impulsinio auginimo MOCVD režimą, kuris pagerina lokalizacijos sąlygas dėl geresnio atomų išsidėstymo bei (iii) pakėlus temperatūrą tuoj po KD užauginimo, kas sukuria barjerus krūvininkų difuzijai.
- Dominuojanti našumo kryčio priežastis priklauso nuo medžiagos kokybės, kurią apibrėžia maksimalaus VKN vertė: nustatyta, kad vyraujantis mechanizmas geros kokybės InGaN kvantiniuose dariniuose yra Ožė rekombinacija, kuomet prastos kokybės dariniuose svarbesnis mechanizmas yra krūvininkų delokalizacija ir judėjimas link nespindulinės rekombinacijos centų. Apytikslė maksimalaus VKN riba, skirianti tokius darinius, yra ~20%.

1. METODINĖ DALIS

Šiame darbe pristatyti rezultatai gauti atliekant matavimus keliomis viena kitą papildančiomis optinėmis metodikomis, kurių pagalba bandiniuose stebėtos sugerties/emisijos bei nepusiausvirųjų krūvininkų dinamikos ypatybės.

Eksperimentuose buvo naudojama PHAROS lazerinė sistema, generuojanti 1030 nm (~1.2 eV), 30 kHz pasikartojimo dažnio ir 250 fs trukmės impulsus. Žadinančiojo pluoštelio bangos ilgio parinkimui, šie impulsai buvo leidžiami per ORPHEUS optinį parametrinį stiprintuvą, galintį keisti bangos ilgį 600-2600 nm diapazone, tuomet per antros harmonikos generacijos kristalą. Aktyviosios darinių srities selektyviam žadinimui naudoti ~390-392 nm (~3.18-3.16 eV) impulsai, kurių bangos ilgis parinktas taip, kad būtų viršijama KD esančių būsenų energija, tačiau tiesiogiai nebūtų žadinami kiti greta esantys sluoksniai.

Žadinimo-zondavimo metodikose vėlinimui pasitelktas AEROTECH PRO165LM transliacinis stalas, galintis judėti iki 2 m/s greičiu, 1 μm tikslumu.

Tam, kad būtų užtikrinta sužadinimų atitiktis tarp skirtingų metodikų, žadinančiųjų pluoštelių diametrai buvo išmatuoti su Thorlabs CCD pluošto profiliavimo kamera. Žadinimo galios matuotos OPHIR Nova 2 lazerio galios matuokliu.

Visi matavimai atlikti Vilniaus universiteto Fotonikos ir nanotechnologijų institute, Lietuvoje.

1.1. Laike integruota fotoliuminescencija ir VKN įvertinimas

Laike integruota fotoliuminescencija (LIFL) – viena paprasčiausių darbe naudotų metodikų. Jos metu per nustatytą ekspozicijos trukmę iš sužadinto bandinio yra registruojama emituota šviesa. Šiame darbe ji surenkama šviesolaidžiu į AvaSpec ULS 2048 spektrometrą, turintį 300 linijų/mm difrakcinę gardelę. Kvantinio našumo įvertinimui bandiniai talpinami į 6 colių diametro SphereOptics integruojančią sferą, kurioje pasitelkiamas trijų matavimų metodas (angl. *three measurement approach*) [158]. Jo metu išmatuojami trys spektrai: pirmas – be bandinio sferoje, antras – su nusuktu nuo žadinančiojo pluoštelio bandiniu sferoje, ir trečias – su atsuktu į žadinantįjį pluoštelį bandiniu sferoje. Šio būdo privalumas yra tas, jog yra

įvertinama netiesiogiai sugertos šviesos dalis, atsirandanti nuo žadinančiojo pluoštelio sklaidos ir atspindžių integruojančioje sferoje. Reikia paminėti, jog šiame darbe taip pat įvertinta ir sugertis GaN buferiniame sluoksnyje per donorų-akceptorių poras. Žadinančiajai 390-392 nm spinduliuotei buvo suskaičiuotas 225 cm^{-1} sugerties koeficientas, tai leido tiksliau įvertinti aktyviojoje srityje sugertos šviesos kiekį skaičiuojant kvantinius našumus ir sugerties koeficientus. Pasinaudojant pastaraisiais bandiniuose buvo suskaičiuoti individualūs krūvininkų tankiai.

1.1. Laikinės skyros fotoliuminescencija

Laikinės skyros fotoliuminescencija (LSFL) praplečia LIFL ribas leisdama stebėti, kaip spektrinis emisijos pasiskirstymas kinta per tam tikrą laiką po sužadinimo. Tai suteikia papildomą informaciją apie krūvininkų dinamiką. Šiame darbe naudojamas Hamamatsu C10627 fotochronografas (angl. *streak camera*) su Acton SP2300 monochromatoriumi.

1.2. Skirtuminis pralaidumas

Laikinės skyros skirtuminio pralaidumo (SP) spektroskopija papildo FL metodikas suteikdama galimybę stebėti elektroninių būsenų, tiek dalyvaujančių, tiek ir nedalyvaujančių šviesos emisijoje, užimtumo kitimą nuo laiko. Tai gali duoti vertingą informaciją apie krūvininkų persiskirstymą tarp minėtų būsenų. Metodo esmė – zondo su gana plačiu spektriniu skirstiniu (šiame darbe nuo ~360 iki ~530 nm) sugerties pokytis bandinyje, kuomet šis yra sužadinimas. Sužadintame bandinyje pasikeičia elektroninių būsenų užpilda, todėl tam tikrų bangos ilgių zondo komponentės yra arba stipriau, arba silpniau sugeriamos, lyginant su nesužadintu bandiniu. Vėlinant zondą žadinančiojo pluoštelio atžvilgiu, stebimas laikinis skirtuminio pralaidumo spektrų kitimas. SP signalas, matuojamas OD (angl. *optical density*) vienetais, pateikiamas kaip intensyvumų santykio tarp pro nesužadintą bandinį praėjusio zonduojančio pluoštelio ($T_0(\lambda)$) ir tarp pro sužadintą bandinį praėjusio zonduojančio pluoštelio ($T_p(\lambda, t)$) logaritmas ties tam tikru bangos ilgiu λ ir vėlinimo trukme *t*:

$$T(\lambda, t) = \log\left(\frac{T_0(\lambda)}{T_p(\lambda,t)}\right). \quad (1)$$

1.3. Sugertis laisvaisiais krūvininkais

Sugerties laisvaisiais krūvininkais (SLK) metodikoje, kaip ir SP metodikoje, taip pat registruojamas zondo pralaidumo kitimas. Tačiau SLK atveju zondo sugertis vyksta ne tarp skirtingose juostose esančių elektroninių būsenų, o juostos viduje dėl sugeneruotų nepusiausvirųjų krūvininkų, kadangi zonduojančio pluoštelio fotonų energija (šiame darbe ~1.2 eV) yra gerokai mažesnė už medžiagos draustinio tarpo energiją. SLK signalas vaizduojamas kaip

$$T(t) = \ln\left(\frac{T_0}{T_p(t)}\right), \quad (2)$$

kur T_0 yra praėjusio pro nesužadintą bandinį zondo intensyvumas, $T_p(t)$ – praėjusio pro sužadintą bandinį zondo intensyvumas po tam tikros vėlinimo trukmės.

1.4. Šviesa indukuotos dinaminės difrakcinės gardelės

Šviesa indukuotos dinaminės difrakcinės gardelės (ŠIDDG) yra unikali metodika, vienu metu leidžianti įvertinti nepusiausvirųjų krūvininkų rekombinaciją ir difuziją. Jos pagrindas – dviejų koherentinių žadinančiojo pluoštelio spindulių interferencija bandinyje, taip jame indukuojant periodinį nepusiausvirųjų krūvininkų pasiskirstymą. Šis moduliuoja medžiagos lūžio rodiklį ir sukuria difrakcinę gardelę, nuo kurios dalinai difraguoja zonduojantis spindulys (jo bangos ilgis šiame darbe – 1030 nm). Nutraukus sužadinimą, difrakcinė gardelė pradeda irti dėl krūvininkų rekombinacijos ir difuzijos, todėl zonduojančio spindulio difrakcijos efektyvumas (santykis tarp difragavusio ir nedifragavusio spindulio) pradeda kristi. Tokio proceso laikinę priklausomybę galima stebėti užvėlinus zonduojantį pluoštelį sužadinimo atžvilgiu. Difuzijos įtaka dinaminės gardelės irimo kinetikai yra tuo didesnė, kuo staigesnis nepusiausvirųjų krūvininkų gradientas, t.y. kuo mažesnis indukuotos gardelės periodas Λ. Pastarąjį galima keisti žadinančiuosius pluoštelius į bandinį suvedant skirtingais kampais:

$$\Lambda = \frac{\lambda}{2\sin\left(\frac{\Theta}{2}\right)}, \quad (3)$$

kur λ yra žadinančiųjų pluoštelių bangos ilgis, Θ – kampas tarp jų. Išmatavus dinaminės gardelės irimo kinetikas prie kelių skirtingų periodų ir suskaičiavus

jų irimo trukmes τ_G, galima įsivertinti krūvininkų rekombinacijos trukmę τ_R ir difuzijos koeficientą D, naudojantis formule

$$\frac{1}{\tau_G} = \frac{1}{\tau_R} + \frac{1}{\tau_D} = \frac{1}{\tau_R} + \frac{4\pi^2 D}{\Lambda^2}, \quad (4)$$

kur τ_D – difuzinio irimo trukmė. Reikia paminėti, jog difrakcijos efektyvumas priklauso nuo nepusiausviryjų krūvininkų kvadrato, todėl

$$\eta(t) \propto exp\left(-\frac{2t}{\tau_G}\right). \quad (5)$$

Rekombinacijos trukmės ir difuzijos koeficiento radimo pavyzdys pavaizduotas žemiau esančiame paveikslėlyje (Pav. 1).

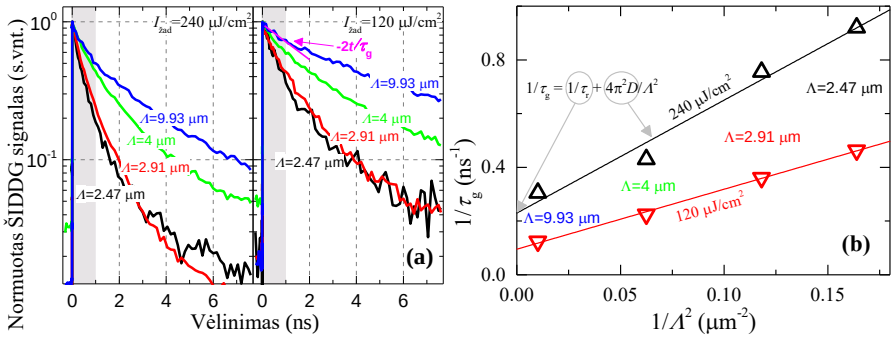

Pav. 1. ŠIDDG kinetikos, išmatuotos su 4 skirtingo periodo indukuotomis gardelėmis Λ (9.93 μm, 4 μm, 2.91 μm ir 2.47 μm) InGaN daugybinių kvantinių duobių bandinyje (tp12 iš Lentelės 1), esant dviem skirtingiems žadinančiojo pluoštelio intensyvumams (a), ir atvirkštinės gardelės irimo trukmės, suskaičiuotos iš pradinių šių kinetikų dalių (pilkai pažymėtos sritys, kuriose skaičiuota), pateiktos kaip funkcijos nuo $1/\Lambda^2$ (b). Juoda linija ($I_{žad}$ = 240 μJ/cm^2) atitinka D = 1.1 cm^2/s, τ_R = 4.4 ns, raudona ($I_{žad}$ = 120 μJ/cm^2) atitinka D = 0.6 cm^2/s, τ_R = 10.5 ns.

1.5. Darbe tirti bandiniai

Šiame darbe tirti bandiniai pagrinde sudaryti iš skirtingų GaN/InGaN daugiasluoksnių šviestuko tipo darinių rinkinių. Jie užauginti metalorganinio cheminio nusodinimo iš garų fazės (angl. *metalorganic chemical vapor deposition*, MOCVD) reaktoriuose. Tą atliko skirtingi augintojai iš Virdžinijos sandraugos universiteto (*Virginia Commonwealth University*, VCU, JAV), Kembridžo universiteto (*University of Cambridge*, CU, Jungtinė Karalystė), kompanijos Aixtron (Vokietija), kompanijos OSRAM Opto Semiconductors (Vokietija), Vilniaus universiteto Fotonikos ir nanotechnologijų instituto (VU FNI, Lietuva) ir Kalifornijos universiteto

(*University of California, Santa Barbara*, UCSB, JAV). Pilnas bandinių sąrašas pateiktas žemiau esančioje lentelėje kartu su esminiais parametrais. Rinkiniuose yra bandiniai su: impulsiniu ir neimpulsiniu auginimo režimu (2.5 skyrius), su didelėmis KD storio fluktuacijomis ir be jų (2.6 skyrius), su skirtingais tarpsluoksniais (2.1 skyrius), su kintančiu In kiekiu aktyviojoje srityje, su skirtingais kvantinių duobių, kvantinių barjerų (KB), dengiančiųjų sluoksnių storiais, su kintančiomis auginimo temperatūromis. Vieną rinkinį sudaro nepoliniai m-plokštumos dariniai (m1-m7 Lentelėje 1), užauginti ant GaN padėklų, tuo tarpu visi kiti dariniai užauginti *c* ašimi ant safyro padėklų. Bandiniai tarp savęs taip pat skiriasi buferinio sluoksnio storiu, legiravimo laipsniu, elektronus blokuojančio sluoksnio buvimu ir pan. Daugiau informacijos apie juos galima rasti atitinkamuose skyriuose arba publikacijų nuorodose Lentelėje 1.

Bandiniuose KD ir barjerų storiai buvo gauti iš elektronų pralaidumo mikroskopo (angl. *transmission electron microscope,* TEM) arba rentgeno spindulių difrakcijos (angl. *X-ray diffraction*, XRD) matavimų, arba įvertinti iš auginimo procedūrų.

Lentelė 1. Šiame darbe tirti bandiniai su jų esminiais parametrais. Kur yra galimybė, nurodyti šaltiniai ir publikacijų nuorodos, kur apie atitinkamus bandinius galima sužinoti daugiau. Spalvos grubiai atitinka FL emisiją. FWHM (angl. *full width at half maximum*) – pilnas plotis pusės maksimumo lygyje.
* – pateikta tik intensyviausios FL smailės vertė.

Bandinio pav.	**KD storis** nm	**KD kiekis** vnt.	**KB storis** nm	**KD In kiekis** %	**FL smailė** eV esant maks. VKN	**FWHM** eV	**Šaltinis/ Nuoroda**
V1	2	6	3	23	3.00	0.14	VCU
V2	2	6	3	20	2.96	0.13	VCU
V3	2	6	12	20	2.93	0.14	VCU[125]
V4	3	6	3	17	2.93	0.13	VCU
Green	3	5		30	2.36	0.12	OSRAM [P5]
Cyan	3	5		26	2.50	0.14	OSRAM [P5]
SQW	4	1		22	2.76	0.14	OSRAM
Blue	3	5			2.79	0.11	OSRAM[165]
Sample A	3.5	5	6	8	2.68	0.16	FNI [P3]
Sample B	3.5	5	6	8	2.81	0.20	FNI [P3]

Sample 1	3.5	5	6	8	2.79	0.12	FNI [P3]
Sample 2	3.5	5	6	8	2.80	0.14	FNI [P3]
Sample 3	3.5	5	6	8	2.80	0.16	FNI [P3]
In1	4.7	5	18	5.1	2.98	0.18	AIXTRON [P2]
In2	4.2	5	18	8.4	2.77	0.22	AIXTRON [P2]
In3	6	5	18	11.3	2.82	0.17	AIXTRON [P2]
In4	5.8	5	18	13.2	2.74	0.17	AIXTRON [P2]
In5	5	5	18	23	2.63	0.20	AIXTRON [P2]
Quad	3.5	4	4.5	15	2.87	0.12	VCU[166]
Hexa	3.5	6	4.5	15	2.81	0.17	VCU[166]
1T	2.6	10	7.1	18.9	2.79	0.10	CU[164]
Q2T	2.6	10	7.1	17.4	2.78	0.11	CU[164]
2T	2.6	10	7.1	18	2.74	0.12	CU[164]
T-bounce	2.6	10	7.1	18	2.74	0.13	CU[164]
S1	3.1	5	7.1	12	2.74	0.15	FNI [P4]
S2	3.7	5	6.6	12	2.66	0.20	FNI [P4]
S3	3.1	5	7.8	12	2.56	0.27	FNI [P4]
S4	3.9	5	7.8	12	2.35	0.29	FNI [P4]
S5	4.2	5	8.7	12	2.31	0.27	FNI [P4]
S6	4.5	5	7.7	12	2.25	0.29	FNI [P4]
S8	4.5	5		12	2.21	0.39	FNI [P4]
S7	4.8	5	9	12	2.13	0.44	FNI [P4]
tp3	4.1	5	6.7	10.5	2.62	0.16	FNI
tp6	4.1	5	6.7	10	2.60	0.17	FNI
tp9	3.8	5	7.2	9.5	2.66	0.15	FNI
tp12	4.1	5	6.7	10	2.65	0.17	FNI
tp15	4.1	5	6.8	9	2.64	0.15	FNI
tp0	3.8	5	6.6	10.5	2.59	0.14	FNI
T810	3.8	5	6.6	10	2.63	0.13	FNI
T815	3.8	5	6.6	10	2.65	0.13	FNI
W1	1	8	12	25	2.90	0.14	UCSB
W2	1	8	12	25	2.86	0.14	UCSB
W3	2	8	12	25	2.51	0.14	UCSB
W4	2.7	8	12	25	2.26	0.13	UCSB
W5	4	8	12	25	2.69*	0.15*	UCSB

m1	8.2	3	8.8	13.3	2.93	0.27	UCSB
m2	8.2	3	8.8	9.2	3.04	0.10	UCSB
m3	6.8	3	8.8	13.1	2.98	0.15	UCSB
m4	7.8	3	8.8	10.4	2.98	0.23	UCSB
m5	8.2	3	14.8	13.2	2.93	0.21	UCSB
m6	4.5	3	14.8	13.5	2.83	0.29	UCSB
m7	4.5	3	14.8	13.5	2.87	0.25	UCSB

2. REZULTATAI IR JŲ APTARIMAS

2.1. Kvantinio našumo pagerinimas InGaN kvantinėse duobėse įterpiant supergardelę

Šviestukų dariniai GaN pagrindu įprastai yra auginami ant safyro padėklų, kadangi šie yra labiau paplitę ir gerokai pigesni negu GaN padėklai. Tačiau dėl gardelių konstantų ir šiluminio plėtimosi koeficientų nesutapimo tarp GaN ir safyro, tokiuose dariniuose susidaro dideli sluoksnių įtempimai, vedantys prie išaugusio dislokacijų tankio ir stiprių vidinių elektrinių laukų, kurie mažina VKN. Tam suvaldyti yra išvystytos kelios technologinės modifikacijos: buferiniai sluoksniai, auginami žemoje temperatūroje [17,171], SiO_2 kaukės šoniniam auginimui [172,173], kintančio In kiekio tarpsluoksniai [P1], arba trumpo periodo supergardelės (SG) [174]. Yra parodyta, jog pastarosios padidina VKN [175,176] ir sumažina FL smailės slinkimąsi didėjant krūvininkų tankiui [174] dėl mažesnio defektų tankio ir silpnesnių vidinių el. laukų.

Pav. 2 pateiktos VKN kreivės ir smailių padėčių kitimas nuo nepusiausviryjų krūvininkų tankio dviejuose identiškuose daugybinių kvantinių duobių dariniuose, viename kurių yra supergardelė (Sample A), kitame – nėra (Sample B). Jų aktyviąsias sritis sudaro penkios 3-4 nm $In_{0.1}Ga_{0.9}N$ KD, atskirtos 6 nm barjerais. Supergardelė – 32 nm tarpsluoksnis tarp buferinio sluoksnio ir aktyviosios srities, kurią sudaro 8 $In_{0.06}Ga_{0.94}N$/GaN heterosandūros. Kaip ir tikėtasi, įterpus supergardelę, VKN išaugo, o smailės slinkimasis gerokai sumažėjo. Didesnis mėlynasis poslinkis gali būti paaiškintas stipresniu vidiniu pjezoelektriniu lauku, tuo tarpu trumpesnis fotoliuminescencijos bangos ilgis atskleidžia mažesnį In kiekį KD dėl lėtesnio In įterpimo įtemptame sluoksnyje [177]. Tačiau vien vidinio elektrinio lauko sumažėjimas negali paaiškinti iki ~3 kartų išaugusio VKN, ypač dideliuose krūvininkų tankiuose.

SLK kinetikos parodė beveik tiesiškai nuo nepusiausviryjų krūvininkų tankio trumpėjančias gyvavimo trukmes, kurias, tikimai, pagrinde lemia spartėjančios spindulinė rekombinacija ($1/\tau_{rad} \sim B_{rad}N$, kur B_{rad} – spindulinės rekombinacijos koeficientas) arba difuzijos įtakota nespindulinė rekombinacija, kuomet krūvininkai palieka potencinius minimumus ir yra pagaunami defektų [120] ($A(N) = B_{nr}N$, kur B_{nr} – minėtos nespindulinės

rekombinacijos koeficientas). Jei abu procesai vyksta vienu metu, tuomet tik dalis krūvininkų rekombinuoja spinduliniu būdu, todėl bendras kvadratinės rekombinacijos narys $B^* = B_{rad} + B_{nr}$.

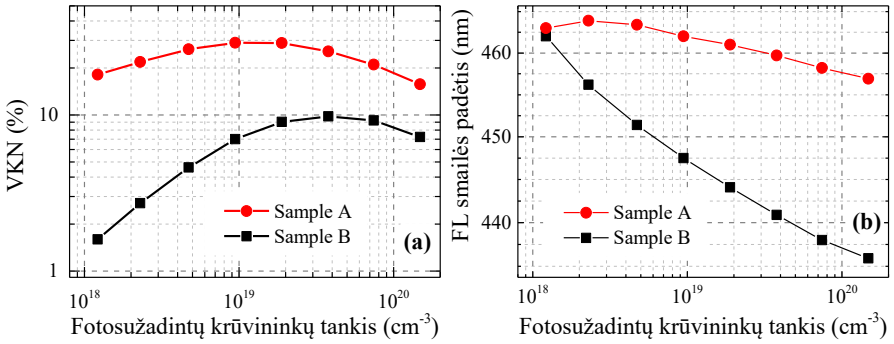

Pav. 2. Fotoliuminescencijos vidinis kvantinis našumas (a) ir smailės padėtis (b) kaip funkcijos nuo fotosužadintų krūvininkų tankio bandiniuose su supergardele (Sample A, raudonos kreivės) ir be supergardelės (Sample B, juodos kreivės) [P3].

Standartinis ABC modelis buvo modifikuotas siekiant sumodeliuoti abiejų bandinių VKN kreives. B narys pakeistas B^*, C narį pasirinkta pašalinti, kadangi jis turėtų būti svarbus tik krūvininkų tankiuose, gerokai didesniuose nei 10^{19} cm^{-3}. Dėl fazinės erdvės pildymo [184] įvertintas nario B_{rad} sotinimasis:

$$B_{rad} = \frac{B_0}{1+\frac{N}{N^*}}, \tag{6}$$

kur B_0 yra neužsotintas rekombinacijos koeficientas, N^*– slenkstinė sotinimo krūvininkų tankio vertė. Kadangi SLK kinetikų irimo sparta neparodė B^* nario sotinimo, todėl laikyta, kad $B^* = B_{rad} + B_{nr} = const$. Pats B^* narys įvertintas iš SLK kinetikų pradinių dalių irimo trukmių pagal $\tau = (A + B^*N)^{-1}$, tuo tarpu nuo krūvininkų tankio nepriklausančios nespindulinės rekombinacijos laikas $\tau_{NR} = 1/A \approx 35$ ns įvertintas iš LSFL kinetikų ties ilgomis vėlinimo trukmėmis (>30 ns). VKN kreivės sumodeliuotos su

$$IQE = \frac{B_{rad}N}{A+(B_{rad}+B_{nr})N}. \tag{7}$$

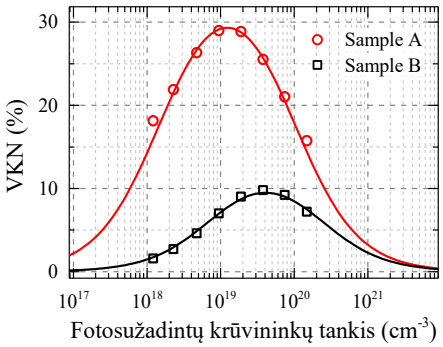

Pav. 3. Sumodeliuotos VKN kreivės naudojantis AB*C modeliu [P3].

Kaip matoma Pav. 3, AB*C modeliu sumodeliuotos abiejų bandinių kreivės gerai atitinka išmatuotąsias, tuo tarpu su standartiniu ABC modeliu ir 2×10^{-31} cm^6/s Ožė koeficientu buvo gautos gerokai per didelės VKN vertės. Panaudoti parametrai: $1/A$=26 ns, B^*=2.4×10^{-11} cm^3/s, N^*=9.4×10^{19} cm^{-3}, B_0=0.9×10^{-11} cm^3/s (Sample A); $1/A$=15 ns, B^*=0.8×10^{-11} cm^3/s, N^*=20×10^{19} cm^{-3}, B_0=0.11×10^{-11} cm^3/s (Sample B). Akivaizdu, kad maksimalią VKN vertę lemia B_{rad}/B_{nr} santykis, kuris yra 0.6 ir 0.16 atitinkamai bandinyje su supergardele ir be jos. Su tuo koreliuoja atitinkami maksimalūs VKN – 30% ir 10%. Našumo krytis bandiniuose atsiranda dėl B_{rad} sotinimo [185] ir B_{nr} augimo didėjant krūvininkų tankiui [121,122].

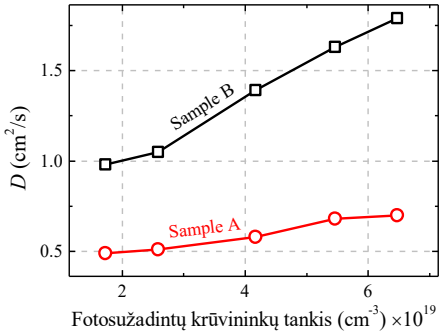

Pav. 4. Difuzijos koeficiento priklausomybė nuo sužadintų krūvininkų tankio [P3].

Skirtumą tarp B_{rad} galima paaiškinti stipresniu vidiniu elektriniu lauku bandinyje be supergardelės, dėl kurio atskiriamos elektronų ir skylių banginės funkcijos ir sumažėja spindulinės rekombinacijos sparta. Tuo tarpu stipresnę delokalizuotų krūvininkų nespindulinės rekombinacijos įtaką tame pačiame bandinyje galima paaiškinti gerokai didesniu krūvininkų difuzijos koeficientu (Pav. 4). Jis parodo, jog didesnė dalis krūvininkų užima ištęstines (aukštesnės energijos) būsenas, iš kurių yra lengviau pasiekiami defektai. Lėtesnis

difuzijos koeficiento augimas bandinyje su supergardele rodo, jog šios įterpimas ne tik pagerino lokalizacijos sąlygas, bet ir sumažino delokalizacijos spartą. Pats difuzijos koeficiento augimas nuo krūvininkų tankio patvirtina B_{nr} nario buvimą, kuris yra galima našumo kryčio priežastis.

2.2. Krūvininkų lokalizacijos ir difuzijos įtaka fotoliuminescencijai smarkiai sužadintuose InGaN dariniuose žydriems ir žaliems šviestukams

Krūvininkų lokalizacija yra vienas svarbiausių reiškinių InGaN šviestukuose, kadangi ji nulemia krūvininkų pernašos ypatybes ir užtikrina didelį spindulinį našumą. Lokalizacijos įtaka didėja augant In kiekiui dėl didesnės netvarkos In atomų pasiskirstyme [93]. Stipresnė lokalizacija gali efektyviau atskirti krūvininkus nuo defektų, kita vertus ji gali sumažinti spindulinės rekombinacijos spartą dėl nekoreliuotų valentinės ir laidumo juostos potencialo fluktuacijų [93,186] ir mažesnės banginių funkcijų sanklotos [74,156]. Krūvininkų lokalizacija taip pat gali keisti SRH ir Ožė rekombinacijų koeficientus [186,187]. Dideliuose nepusiausvirųjų krūvininkų tankiuose vyksta priešingas reiškinys – delokalizacija, galinti paskatinti našumo kryčio atsiradimą mažesniuose, negu Ožė rekombinacijai įprasta, krūvininkų tankiuose [120,122,188].

Pav. 5 pateikti LIFL ir momentiniai SP spektrai dviejuose bandiniuose, turinčiuose FL smailes ties ~500 nm (žydras – cyan) ir ~530 nm (žalias – green). Bandinius sudaro buferinis nelegiruotas GaN sluoksnis, vidutiniškai legiruotas n-tipo GaN:Si srovės plėtimo sluoksnis, smarkiai legiruotas GaN:Si kontaktinis sluoksnis, aktyvioji sritis, sudaryta iš penkių InGaN 3 nm storio KD (In kiekis ~26% ir ~30% atitinkamai žydrai ir žaliai emisijai), atskirtų GaN barjerais, p-tipo AlGaN:Mg elektronus blokuojantis sluoksnis (angl. *electron blocking layer*, EBL) ir p-tipo GaN:Mg viršutinis kontaktinis sluoksnis. Skirtumas tarp FL ir SP spektrų, arba Stokso poslinkis, yra didesnis žaliame bandinyje, kas rodo stipresnę lokalizacijos įtaką [195] – to ir tikimasi bandinyje su didesniu In kiekiu [192]. Keliant žadinimo intensyvumą, stebimas neįprastas reiškinys – FL smailės raudonasis poslinkis, pereinantis į mėlynąjį poslinkį. Šis reiškinys yra ryškesnis žydrame bandinyje ir yra neįprastas todėl, kad poliniuose KD dariniuose tikimasi matyti tik mėlynąjį poslinkį dėl vidinių elektrinių laukų ekranavimo ir būsenų pildymo [197], ir tik labai aukštuose krūvininkų tankiuose dėl draustinės juostos tarpo renormalizacijos yra stebėtas raudonasis poslinkis [180].

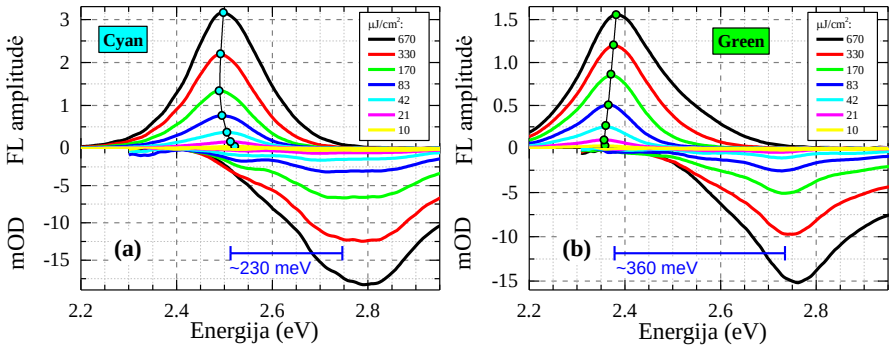

Pav. 5. LIFL (viršus) ir momentiniai (ties 120 ps vėlinimu) SP (apačia) spektrai žydrame (cyan, (a)) ir žaliame (green, (b)) KD dariniuose esant skirtingiems žadinimams [P5]. Neigiamas SP signalas rodo sugerties praskaidrėjimą.

Keliant žadinimo intensyvumą, pilnas FL spektrų plotis pusės maksimumo aukštyje didėja – tai vyksta dėl seklių lokalizuotų būsenų pildymo ir tolesnio aukštesnės ir žemesnės energijos būsenų pildymo [181,196]. Iš laikinių LSFL ir SP charakteristikų nustatyta, jog raudonasis poslinkis pradeda dominuoti tarp 7 ns ir 10 ns po sužadinimo, tuo tarpu iki tol stebimas mėlynasis poslinkis. Todėl raudonojo poslinkio priežastimi negali būti draustinio tarpo renormalizacija, kuri vyksta iškart po sužadinimo. Kvantinės sąspraudos Štarko efektą taip pat galima atmesti, kadangi raudonasis poslinkis ilgose vėlinimo trukmėse viršija pradinį mėlynąjį poslinkį – mažėjant krūvininkų tankiui, vidinis elektrinis laukas turėtų atsistatyti į pradinę būseną.

Taigi stebėto raudonojo poslinkio priežastis – krūvininkų persiskirstymas tarp skirtingo gylio lokalizuotų būsenų. Žemuose sužadinimuose elektronai ir skylės yra pagaunami atsitiktinių fluktuojančio potencialo vietų ir jose lieka. Keliant žadinimą, seklios būsenos yra užpildomos, todėl krūvininkai iš jų gali lengviau pabėgti į gilesnes lokalizuotas būsenas. Tokią teoriją patvirtina ir pasiūlymas, jog lokalizacija į gilesnes būsenas užima daugiau laiko, negu į seklesnes [181]. Todėl net ir sumažėjus krūvininkų tankiui, gilesnių būsenų pildymas tęsiasi toliau ir pradinis mėlynasis poslinkis yra viršijamas. Galiausiai aukščiausiuose sužadinimuose yra užpildomos ir giliausios lokalizuotos būsenos, todėl stebimas mėlynasis poslinkis.

Būsenų pildymą patvirtina ŠIDDG metodika išmatuotas ambipolinės difuzijos koeficientas, nemonotoniškai augantis nuo nepusiausviųjų krūvininkų tankio (Pav. 6(a)). To priežastis – augantis krūvininkų skaičius judresnėse ištęstinėse būsenose, skatinantis nuo žadinimo spartėjančią

nespindulinę rekombinaciją [122]. Tą patį parodė ir spartėjanti rekombinacijos sparta mėlynajame FL spektrų šlaite. Delokalizuotų krūvininkų pernašos įtaka našumo kryčiui yra pavaizduota Pav. 6(b). Čia kreivės su tuščiaviduriais simboliais žymi darinių FL kvantinius našumus, o kreivės su pilnaviduriais simboliais – FL intensyvumus, sunormuotus į atitinkamą difuzijos koeficientą. Matyti, jog abiejų tipų kreivės virš našumo kryčio slenksčio elgiasi panašiai. Tai rodo, jog dėl delokalizacijos augantis krūvininkų judris yra susijęs su našumo kryčio atsiradimu duotuose bandiniuose. Pagal P. Dawson et al. darbą [89], didžioji dalis elektronų yra delokalizuoti plačiame sužadinimų diapazone, kuomet skylės net ir kambario temperatūroje lieka lokalizuotos. Todėl našumo kryčiui didžiausią įtaką daro auganti nuo nepusiausvirųjų krūvininkų tankio skylių delokalizacija.

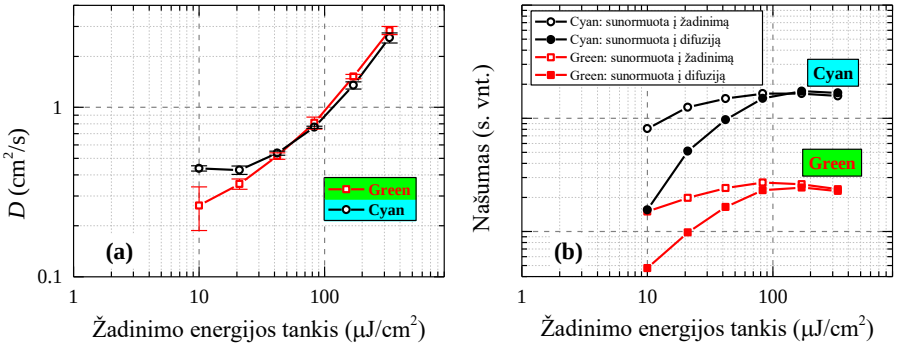

Pav. 6. (a) Difuzijos koeficientas žydrame ir žaliame KD dariniuose kaip funkcija nuo sužadinimo energijos tankio. (b) FL signalo intensyvumas, sunormuotas į žadinimo energijos tankį (tuščiaviduriai simboliai) arba į difuzijos koeficientą (pilnaviduriai simboliai), žydrame (juoda spalva) ir žaliame (raudona spalva) dariniuose. Našumo kreivės viena kitos atžvilgiu yra perstumtos ordinačių ašyje dėl aiškumo [P5].

2.3. Krūvininkų difuzijos apribotas vidinis kvantinis našumas skirtingo storio InGaN kvantinėse duobėse

Kaip rodo ankstesni skyriai, krūvininkų lokalizacija turi didžiulę įtaką emisijai iš InGaN kvantinių duobių. Tai yra pagrindinė priežastis, kodėl daug defektų turinti medžiaga gali našiai šviesti, kadangi krūvininkams yra sudaromos kliūtys pasiekti nespindulinės rekombinacijos centrus (NRC) [59]. Deja, lokalizacija yra sudėtingas ir iki galo nesuprastas reiškinys. Iki šiol trūksta žinių apie tai, kokią įtaką jai daro struktūriniai ir/arba medžiagos

parametrai. Kita vertus, krūvininkų difuzija ir gyvavimo trukmė yra glaudžiai su lokalizacija susiję parametrai, kadangi apribojamas krūvininkų, kurie turi įveikti aukštesnius potencialo netolygumus, judėjimas ir jie linkę ilgiau gyvuoti, kas buvo parodyta nemažame skaičiuje darbų [121,122] [P2, P5].

Pagrindinis dėmesys šioje darbo dalyje yra skiriamas parametrams esant nepusiausvirųjų krūvininkų tankiui, kuriame prasideda našumo krytis (t.y. turimas maksimalus VKN). Pav. 7(a) pateiktos kiekvieno bandinio (iš Lentelės 1) difuzijos koeficiento ir gyvavimo trukmės vertės (suskaičiuotos iš ŠIDDG kinetikų pradinių dalių iki 1 ns vėlinimo) ties specifiniu našumo kryčio slenksčiu, įvertintu iš LIFL matavimų. Matyti, jog gyvavimo trukmė tiesiškai mažėja nuo krūvininkų tankio, todėl galima laikyti, kad esant maksimaliam VKN dar nėra įsijungęs spartus rekombinacijos procesas. Pagal ABC modelį, Ožė rekombinacijai polinkis turėtų būti -2 [207] [N1]). Tuo tarpu difuzijos koeficientas tiesiškai auga, kas žymi augančią krūvininkų delokalizaciją. Pav. 7(b) stebima koreliacija tarp gyvavimo trukmės ir difuzijos koeficiento rodo, jog judresni krūvininkai nyksta sparčiau. Taigi krūvininkų dinamiką ties našumo kryčio slenksčiu apsprendžia difuzijos įtakotas mechanizmas, kuris priklauso nuo krūvininkų tankio ir yra universalus dėl jo stebėjimo tarp skirtingų bandinių.

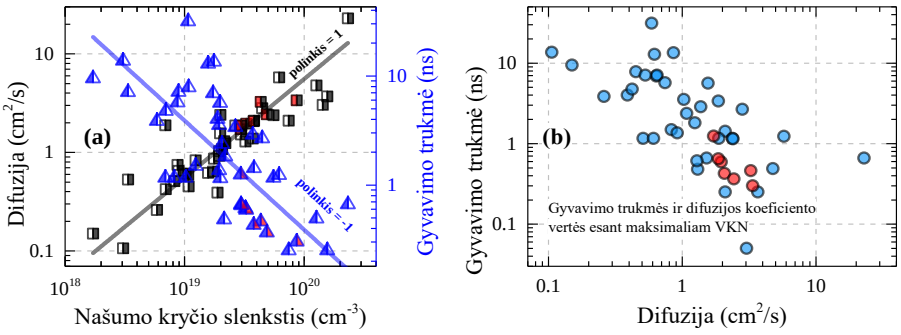

Pav. 7. Difuzijos koeficiento ir gyvavimo trukmės priklausomybės nuo specifinio krūvininkų tankio, ties kuriuo prasideda našumo krytis (turimas maksimalus VKN), ir jas atitinkančios tiesinės funkcijos (a). Gyvavimo trukmė kaip funkcija nuo difuzijos koeficiento (b). Kiekvienas taškas atitinka atskiro bandinio vertes. Raudonas taškų užpildymas žymi m-plokštumos bandinius, kuriuose dinaminės difrakcinės gardelės buvo indukuotos statmenai *c*-ašiai, kas reiškia, jog išmatuotos vertės susijusios su krūvininkų difuzija išilgai *a*-ašies.

Spartesnės krūvininkų nykimo spartos priežastimi gali būti tiek nespindulinė, tiek ir spindulinė rekombinacija. Pirmuoju atveju krūvininkai

lengviau pasiekia defektus, tuo tarpu antruoju atveju – kitas lokalizuotas būsenas [P5], kas padidina tikimybę susitikti ir spinduliniu būdu rekombinuoti nekoreliuotai pasiskirsčiusiems priešingo ženklo krūvininkams [74,196]. Tačiau žiūrint į Pav. 8(a) ir (b), matyti, jog antrasis atvejis mažai tikėtinas, kadangi maksimalus VKN atvirkščiai koreliuoja su difuzijos koeficientu ir tiesiogiai koreliuoja su gyvavimo trukme. Maksimaliam VKN nukritus nuo ~47% iki mažiau nei 1%, difuzijos koeficientas padidėja nuo ~0.1 cm^2/s iki daugiau nei 6 cm^2/s, kai tuo tarpu gyvavimo trukmė sumažėja nuo daugiau nei 10 ns iki šimtų ps. Didesnį negu 30% VKN pasiekia tik tie bandiniai, kuriuose gyvavimo trukmė perkopia 1 ns ties našumo kryčio slenksčiu. Taigi spartesnė rekombinacija vyksta dėl stipriau delokalizuotų krūvininkų, kurie lengviau pasiekia taškinius arba ištęstinius defektus. Apibendrinant galima teigti, jog vidinį kvantinį našumą riboja krūvininkų difuzija, kas neseniai buvo stebėta ir perovskituose [208]. Kadangi tipiškai difuzija auga nuo krūvininkų tankio, didesnis maksimalus VKN yra labiau tikėtinas esant mažesniems našumo kryčio slenksčiams, kas bus parodyta 2.7 skyriuje.

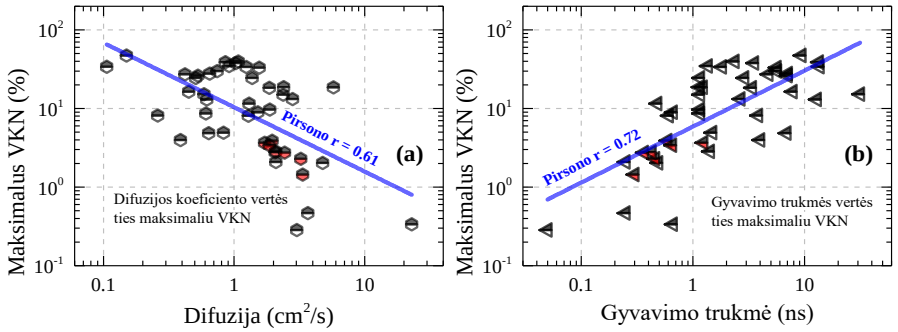

Pav. 8. Koreliacija tarp maksimalaus VKN ir: krūvininkų difuzijos (a), gyvavimo trukmės (b). Kiekvienas taškas atitinka atskiro bandinio vertę ties specifiniu krūvininkų tankiu, atitinkančiu maksimalų VKN. Raudonas užpildymas žymi m-plokštumos bandinius.

Maksimalaus VKN apribojimas dėl krūvininkų difuzijos reiškia, jog šią sumažinus, turėtų išaugti šviesos išeiga ties našumo kryčio slenksčiu. Vienas iš būdų tą padaryti – sumažinti krūvininkų tankį, ties kuriuo našumo krytis prasideda. Ieškant įvairių koreliacijų pastebėta, jog našumo krytis anksčiausiai prasideda dariniuose su siauresnėmis KD (Pav. 9(a)). Taip pat pastebėta, jog difuzijos koeficiento vertė ties visiems bandiniams vienoda 5×10^{18} cm^{-3}

krūvininkų koncentracija yra mažesnė siauresnėse duobėse (Pav. 9(b)). Tai atskleidžia, jog tarp minėtų trijų parametrų yra tam tikras ryšys.

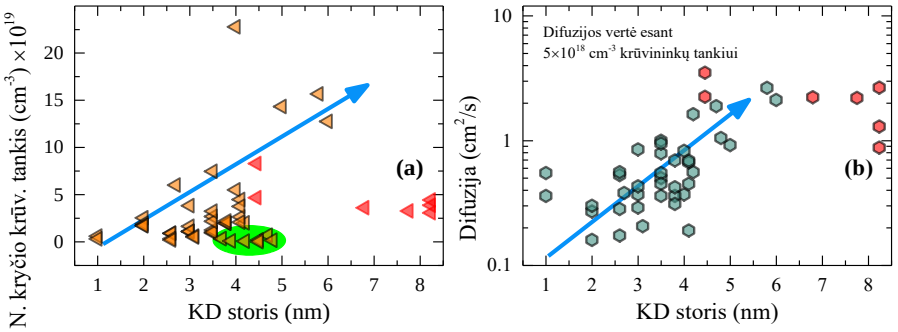

Pav. 9. Koreliacija tarp krūvininkų tankio, atitinkančio našumo kryčio atsiradimą, ir KD storio (a). Krūvininkų difuzijos priklausomybė nuo KD storio esant vienodam 5×10^{18} cm^{-3} krūvininkų tankiui (b). Raudonas užpildymas žymi m-plokštumos bandinius; žalia elipsė žymi bandinius iš [P4].

Kalbant apie KD storio ir difuzijos koreliaciją, tikimiausias paaiškinimas yra duobės storio fluktuacijų sukeltos potencialo fluktuacijos [85], kurios išauga siauresnėse duobėse [211]. Tą galima paaiškinti atvirkštine kvadratine kvantinėse sąspraudos energijos lygmenų priklausomybe nuo KD storio, naudojantis paprastu dalelės dėžėje su begalinio aukščio barjerais modeliu [157]:

$$E_n = \frac{h^2 n^2}{8 m^* L^2}. \quad (8)$$

Čia h – Planko konstanta, m^* – dalelės efektinė masė, n – energijos lygmuo, L – duobės plotis. Lygtis 8 duoda gerokai didesnes energijos lygmens vertes, kuomet L yra mažesnis. Atitinkamai yra ir su duobės storio fluktuacijų ΔL sukeltomis energijos fluktuacijomis ΔE, dėl ko susidaro didesni potencialo netolygumai, vedantys į stipresnę lokalizaciją. Stipresnė lokalizacija jau anksčiau stebėta siauresnėse InGaN [207,212] ir AlGaN [14] kvantinėse duobėse. Pridedant arba atimant prie nominalaus KD storio L pačią mažiausią galimą ΔL vertę, kuri atitinka 0.259 nm atominį monosluoksnį [80,91], pirmasis ($n = 1$) skylių energijos lygmuo E_{h1} pasikeičia 6-8 meV ir 1-2 meV, kai KD storis atitinkamai yra 3 ir 5 nm, o efektinė skylių masė m^* yra $1.1m_0$ [29]. Pritaikant tą patį elektronams su $0.18m_0$ efektine mase [29], E_{n1} pasikeičia 35-46 meV ir 12-15 meV, kai KD storis atitinkamai yra 3 ir 5 nm. Skaičiavimų rezultatai atvaizduoti Pav. 10, kur matyti, jog efektas pradeda reikštis esant mažesniam nei ~6 nm storiui. Nors šie skaičiavimai yra labai

supaprastinti, jie kiekybiškai parodo išaugusį storio fluktuacijų sukeltų potencialo fluktuacijų dydį siauresnėje KD. Jų vertės elektronams yra palyginamos su šilumine ~25 meV energija kambario temperatūroje, todėl elektronų judėjimas šokuojant per būsenas turėtų būti smarkiai apribojamas, be to, esant dviejų arba daugiau monosluoksnių fluktuacijoms, efektas dar labiau sustiprėtų. Panašiai turėtų būti ir su stipriai lokalizuotomis skylėms.

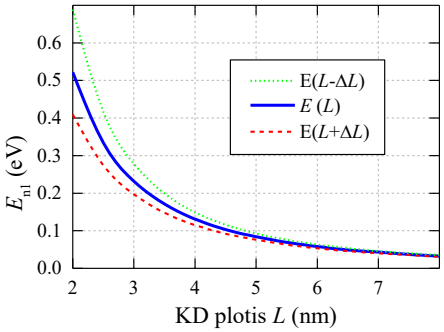

Pav. 10. Suskaičiuotos pirmojo elektronų lygmens energijos $E(L)$ vertės stačiakampėje kvantinėje duobėje su begalinio aukščio barjerais. Raudona brūkšninė kreivė $E(L+\Delta L)$ vaizduoja sumažėjusią sąspraudos energiją, kuomet monosluoksnis (0.259 nm) yra pridedamas prie nominalaus storio L, žalia taškuota kreivė $E(L-\Delta L)$ vaizduoja padidėjusią sąspraudos energiją, kuomet monosluoksnis yra atimamas.

Žinant, kad krūvininkų lokalizacija yra stipresnė siauresnėse kvantinėse duobėse, galima paaiškinti ankstesnį našumo kryčio atsiradimą jose (Pav. 9(a)). Vienas iš paaiškinimų gali būti tas, jog esant stipresnei lokalizacijai, mažėja tikimybė pasiekti nespindulinės rekombinacijos centrus, todėl lokalizuotos būsenos yra lengviau užpildomos. Krūvininkų tankis šiose būsenose lokaliai yra didesnis, negu kitose terpės vietose, todėl toks netolygus pasiskirstymas sumažina efektyvų, optiškai aktyvų tūrį [104]. Tai paskatina ankstesnį našumo kryčio atsiradimą, kurį sukelia spartus, smarkiai nuo krūvininkų tankio priklausantis, nespindulinis procesas, toks kaip Ožė rekombinacija (arba kitas). Kitas paaiškinimas gali būti tas, kad išaugusios fluktuacijos palengvina sąlygas impulso momento tvermės dėsnio patenkinimui Ožė rekombinacijos procese [112,115], kas šiam leidžia atsirasti prie mažesnių krūvininkų tankių. Anksčiau stebėtas augantis našumo kryčio slenkstis AlGaN KD silpnėjant lokalizacijai paremia šiuos paaiškinimus [215]. Taip pat darbe [P4] buvo parodyta stipri lokalizacijos įtaka Pav. 9(a) žalia elipse pažymėtuose bandiniuose, kuriuose stebėtas anomaliai ankstyvas našumo krytis.

2.4. Stokso poslinkis InGaN kvantiniuose dariniuose

Sugerto ir išspinduliuoto fotonų energijų skirtumas, kitaip žinomas kaip Stokso poslinkis, yra stebėtas dideliame skaičiuje darinių InGaN pagrindu, tokių kaip epitaksiniai sluoksniai, šviestukai bei lazeriniai diodai (LD) [59,122,195,198,219,220]. Esant šiam poslinkiui, su emisijos spektru dažniausiai persikloja tik mažose energijose esantis sugerties kraštas. Tas pats yra matoma ir šiame darbe tirtuose InGaN kvantiniuose dariniuose, kuriuose stebimas raudonasis LIFL spektrų poslinkis lyginant juos su momentiniais SP spektrais [P2-P5]. Energijos skirtumas (ΔE) tarp FL ir SP spektrų smailių padėčių tiesiškai mažėja didėjant FL smailės energijai (šiame darbe nuo $\Delta E = 0.54$ eV, esant 2.2 eV) ir konverguoja į nulį ties GaN draustinės juostos tarpu (juodi pusiau užpildyti deimantai Pav. 11). Šis reiškinys yra svarbus šviestukams ir LD, kadangi dėl jo kvantinėse duobėse išspinduliuotų fotonų reabsorbcija tarpjuostiniu būdu yra labai silpna – dėl to pagerėja šviesos ištrūka [221]. Kita vertus, darbe [P3] nukritęs VKN buvo priskirtas mažesniam FL ir SP spektrų persiklojimui. Bet kuriuo atveju, Stokso poslinkis iki šiol nėra galutinai suprastas reiškinys, o paskutiniai dideli darbai šioje srityje atlikti tūkstantmečių sandūroje.

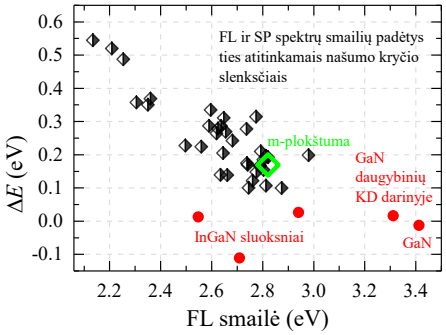

Pav. 11. Energijos skirtumas tarp LIFL ir SP spektrų smailių padėčių (Stokso poslinkis) kaip funkcija nuo FL emisijos smailės energijos. Kiekvienas taškas atitinka atskiro bandinio vertes ties specifiniais našumo kryčio slenkstį atitinkančiais krūvininkų tankiais. Juodi deimantai atitinka KD darinius, raudoni skrituliai – epitaksinius sluoksnius, žalias deimantas – nepolinį vienos 10 nm storio KD darinį iš K. Gelžinytės darbo [222].

Stokso poslinkio kilmė III-nitriduose įprastai yra siejama su lokalizacija, dėl kurios sugertis vyksta aukštesnės energijos būsenose, iš kurių krūvininkai relaksuoja į lokalizuotas būsenas ir ten rekombinuoja spinduliniu būdu [59] [P3]. Lokalizacijos stipris bendrai didėja augant In fluktuacijoms [44,76], todėl natūralu tikėtis ryškesnio Stokso poslinkio bandiniuose su didesne In koncentracija [44]. Deja, šiame darbe tirtuose KD dariniuose bendra

tendencija nėra stebima– tarp atskirų bandinių grupių galima įžiūrėti tiek augimą, tiek ir mažėjimą. Nemonotoniška ΔE priklausomybė nuo In kiekio jau anksčiau buvo stebėta InGaN epitaksiniuose sluoksniuose [219]. Šiame darbe taip pat papildomai buvo ištirti keli epitaksiniai GaN ir InGaN sluoksniai, kurie parodė artimą nulinei vertei raudonąjį FL spektrų poslinkį SP spektrų atžvilgiu (Pav. 11 raudoni skrituliai). Mažas Stokso poslinkis (<80 meV) anksčiau buvo stebėtas ir storuose bei homogeniškuose InGaN sluoksniuose su iki 17% siekiančiu In kiekiu ir emisijos smaile iki 448 nm (2.7 eV) [223]. Pagal [38], Stokso poslinkio nebuvimas rodo juosta-juosta arba eksitoninio šuolio dominavimą. Kalbant apie lokalizaciją, taip greičiausiai yra dėl tolygaus In pasiskirstymo [223], arba mechanizmo, neleidžiančio užimti gilias lokalizuotas būsenas. Atsižvelgiant į šiuos faktus ir į tai, jog Stokso poslinkis kvantinėse duobėse yra universali tiesinė emisijos energijos funkcija, lokalizacija dėl atsitiktinių lydinio fluktuacijų negali būti vienintelis mechanizmas, sukeliantis šį poslinkį.

Kadangi emisijos juostą galima stumti į raudonąją pusę platinant kvantinę duobę, Pav. 12 ΔE vertė yra atidėta nuo KD storio. Čia yra matoma teigiama koreliacija, kuri anksčiau stebėta darbuose [220] ir [224]. Bandiniai, pažymėti raudonai (In3-In5 iš Lentelės 1), iš koreliacijos iškrenta. Taip gali būti dėl storų kvantinių barjerų juose, dėl ko, formuojantis dislokacijoms, dalinai relaksuoja įtempimai aktyviojoje srityje. Tai paskatina In atomų interdifuziją, dėl ko KD ir barjerų sandūra tampa grubi [225]. Reikia paminėti, jog darbe [P1] Stokso poslinkis nebuvo stebėtas trikampio profilio kvantinėje duobėje, šviečiančioje ties ~460 nm (~2.7 eV). Tai rodo stačiakampės KD su aiškiomis ir staigiomis ribomis svarbą Stokso poslinkiui.

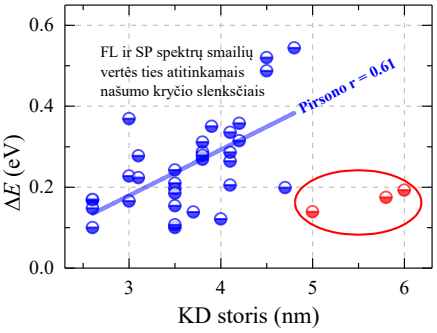

Pav. 12. Stokso poslinkio priklausomybė nuo KD storio. Kiekvienas taškas atitinka atskirą bandinį ties specifinį našumo kryčio slenkstį atitinkančiu krūvininkų tankiu.

Stačiakampės kvantinės duobės platinimas didina erdvinį elektronų ir skylių banginių funkcijų atskyrimą. Tai padidina raudonąjį poslinkį dėl

kvantinės sąspraudos Štarko efekto, kadangi krūvininkai sukrenta giliau į trikampio potencialo minimumus duobių kraštuose, kas jau anksčiau buvo pasiūlyta kaip galima Stokso poslinkio priežastis [224]. Neseniai publikuotame Zhang et al. darbe [226] buvo parodyta, jog pusiau polinėse InGaN kvantinėse duobėse Stokso poslinkis yra gerokai mažesnis, negu analogiškose polinėse KD, kas byloja apie tiesioginę vidinių elektrinių laukų įtaką. Kita vertus, K. Gelžinytės darbe [222] į raudonąją pusę paslinkti FL spektrai atžvilgiu SP spektrų buvo stebėti vienoje nepoline kryptimi augintoje KD (žalias deimantas Pav. 11), kur elektriniai laukai išilgai auginimo krypties neturėtų susidaryti. Taigi vidiniai elektriniai laukai negali būti vienintelė priežastis, atsakinga už didelį Stokso poslinkį kvantinėse duobėse.

Praeitame skyrelyje buvo parodyta, jog difuzijos koeficientas auga platinant KD, o tai turėtų palengvinti krūvininkų persiskirstymą iš seklesnių lokalizuotų būsenų į gilesnes ir padidinti Stokso poslinkį. Teigiama koreliacija tarp difuzijos ilgio ir ΔE vertės tą patvirtina ir parodo, jog ilgesnis atstumas, kurį krūvininkai gali nukeliauti, paskatina gilesnių būsenų pildymą. Taigi, net jei gilios lokalizuotos būsenos dėl In kiekio fluktuacijų ir susidaro, jų pildymas gali būti apribotas dėl silpnos difuzijos, kas yra būdinga siauroms kvantinėms duobėms.

Kalbant mažą Stokso poslinkį storuose InGaN sluoksniuose, tą galima paaiškinti relaksavusiu sluoksnio įtempimu po tam tikro kritinio storio h_c, kuris mažėja nuo In koncentracijos [54,94]. Kitaip negu koherentiškai įtemptame sluoksnyje, kuriame dėl kompozicinio traukimo (angl. *compositional pulling*) ir fazės atskyrimo gali susidaryti ryškios In kiekio fluktuacijos, relaksavusiame sluoksnyje In pasiskirstymas gali būti gerokai homogeniškesnis, su seklesnėmis lokalizuotomis būsenomis. Darbe [P3] sumažėjęs Stokso poslinkis stebėtas po supergardelės įterpimo, kuris tikimai sumažino įtempimus.

2.5. Metalorganikos tiekimo nutraukimo įtaka nusodintų atomų migracijai InGaN šviestukų dariniuose

Vienas svarbiausių uždavinių gaminant našius šviestukus yra medžiagos kokybės pagerinimas. Vienas iš būdų tam pasiekti yra impulsinis MOCVD auginimo režimas. Jo metu auginant InGaN sluoksnį, TMIn ir TMGa prekursorių tiekimas į reaktorių yra periodiškai nutraukiamas tam tikram laikui, tuo tarpu NH_3 yra tiekiamas pastoviai [43,227]. Toks režimas paskatina

paviršinių atomų migraciją ir suteikia papildomo laiko azoto atomų nusodinimui, kas pagerina atomų išsidėstymą ir gerokai sumažina azoto vakansijų formavimąsi [43].

Pav. 13(a) pateiktas dviejų identiškų bandinių, kurių vienas augintas pastoviu, o kitas – impulsiniu MOCVD auginimo režimu (atitinkamai Sample 1 ir Sample 2 Lentelėje 1), VKN palyginimas. Abiejuose bandiniuose yra įterptos 2.1 skyriuje aprašytos supergardelės, o jų aktyvioji sritis sudaryta iš 3-4 nm storio $In_{0.1}Ga_{0.9}N$ kvantinių duobių, atskirtų 6 nm storio barjerais. Impulsinio auginimo metu TMIn ir TMGa prekursoriai buvo paduodami į auginimo kamerą 15 s, tuomet 5 s tiekimas buvo pertraukiamas, o toks ciklas kartojamas 5 kartus kiekvienai KD. Rezultatas – beveik dvigubai išaugęs VKN ir sumažėjusi krūvininkų difuzija bandinyje, augintame impulsiniu režimu. LSFL matavimai tame pačiame bandinyje parodė dvigubai ilgesnes gyvavimo trukmes (atitinkamai 27 ns ir 13.5 ns, esant 1.4×10^{18} cm^{-3} krūvininkų tankiui).

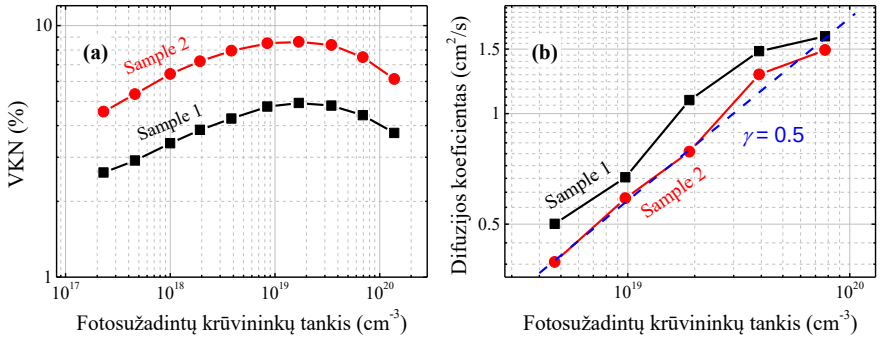

Pav. 13. VKN vertės (a) ir difuzijos koeficientas (b) kaip funkcijos nuo krūvininkų tankio dariniuose, augintuose pastoviu (Sample 1) arba impulsiniu (Sample 2) auginimo režimu [P3].

Siekiant detaliau išnagrinėti pertrūkio trukmės įtaką, buvo ištirtas 6 mėlynai šviečiančių InGaN/GaN daugybinių kvantinių duobių darinių rinkinys (tp0-tp15 Lentelėje 1). Šiame rinkinyje kiekviena ~4 nm pločio KD buvo auginama 20 s trunkantį TMIn ir TMGa tiekimą nutraukiant nuo 3 iki 15 s trukmei, tokį ciklą kartojant 5 kartus. Kaip etalonas buvo paimtas bandinys, kurio kvantinės duobės augintos nenutrūkstamai 80 s ($t_{pauzės} = 0$). Visų darinių barjerai – 7 nm pločio.

Bandiniuose FL emisijos smailės padėtys išsidėsčiusios ties 2.6-2.65 eV (477-468 nm, Pav. 14(a) viršutinė dalis), tuo tarpu sugerties – ties 2.87-2.93

eV (432-423 nm, Pav. 14(a) apatinė dalis), kas reiškia ~300 meV Stokso poslinkį. Nepaisant pastarojo didelės vertės, bandinys su ilgiausia prekursorių tiekimo pertrūkio trukme pasiekia beveik 40% maksimalų VKN (Pav. 14(b)), kuris yra vienas didžiausių iš šiame darbe nagrinėtų bandinių. Iš Pav. 14(a) matyti, jog tiek FL, tiek ir SP spektrai pasislenka į aukštesnes energijas, kuomet pertrūkio trukmė viršija 6 s (parodyta mėlynomis linijomis). To priežastis – nusodintų atomų nugaravimas nuo paviršiaus dėl silpnų In-N jungčių, turinčių žemą disociacijos temperatūrą [227,228]. Sprendžiant iš XRD matavimų, duobės storis pastebimai nepakinta, todėl mėlynasis spektrų poslinkis pagrinde yra nulemtas mažesnės In koncentracijos KD. Taip pat, papildomas laikas atomų migracijai veda prie tolygesnio atomų pasiskirstymo ir seklesnių lokalizuotų būsenų susidarymo, kas galimai duoda papildomą įnašą mėlynajam poslinkiui.

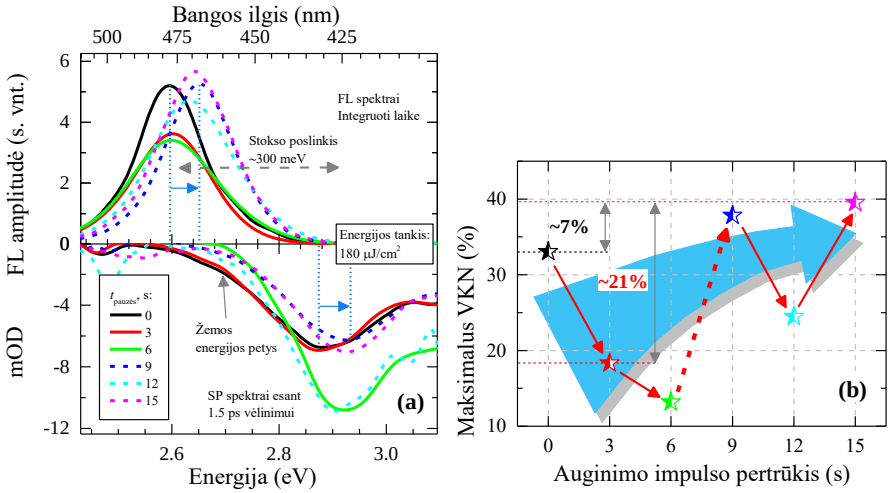

Pav. 14. LIFL (viršutinė dalis) ir momentiniai (esant 1.5 ps vėlinimui) SP (apatinė dalis) bandinių spektrai, esant 180 μJ/cm^2 žadinimo energijos tankiui (a). Vientisos linijos atitinka darinius su pertrūkio trukmėmis iki 6 s, brūkšninės linijos atitinka darinius su ilgesnėmis negu 6 s pertrūkio trukmėmis. Maksimalaus VKN priklausomybė nuo prekursorių tiekimo pertrūkio trukmės (b). Spalvos abiejuose paveiksluose žymi atitinkamus bandinius.

Kalbant apie maksimalaus VKN priklausomybę nuo auginimo impulso pertrūkio trukmės, čia stebimas nemonotoniškas kitimas – pradinis kritimas pereina į augimą po 6 s pertrūkio (Pav. 14(b) brūkšninė linija). Maksimalaus VKN pagerinimas 7%, lyginant etaloninį bandinį ir bandinį su $t_{pauzės}$ = 15 s,

patvirtina teigiamą impulsinio auginimo įtaką. Nors šis pagerinimas ir mažas, tačiau reikia turėti omenyje, kad etaloninis bandinys šiek tiek skiriasi nuo kitų bendra KD auginimo trukme. Palyginus tarpusavyje bandinius su $t_{pauzės}$ = 3 s ir $t_{pauzės}$ = 15 s, skirtumas siekia net 21%, kas išryškina bendrą pagerinimą (Pav. 14(b) žymi lenkta žydra strėlė). Gilesnį supratimą apie prieš tai minėtą nemonotonišką tendenciją galima įgyti iš LIFL spektrų smailių padėčių kitimo. Pav. 15(a) pavaizduota, jog esant 180 μJ/cm^2 žadinimo energijos tankiui, FL spektrų smailės slenkasi į mėlynąją pusę, kuomet pertrūkio trukmė ilginama iki 9 s, po ko didesni pokyčiai nevyksta. Mažų sužadinimų (20 ir 60 μJ/cm^2) spektrų padėtys iš pradžių rodo raudonąjį poslinkį iki 6 s, kuris pereina į staigų mėlynąjį poslinkį ilgesnėse auginimo impulso pertrūkio trukmėse. Tą galima paaiškinti trijų procesų – paviršinių atomų migracijos, jų nugaravimo ir paviršiaus nitridizacijos – vienalaikiškumu ir sąsaja. Silpnas mėlynasis poslinkis iki 6 s pertrūkio trukmės rodo, jog tik santykinai nedidelė In (ir kitų) atomų dalis nugaruoja. Vėliau šis procesas smarkiai išauga. Pradinis žemų sužadinimų raudonasis poslinkis teigia apie gilesnių lokalizuotų būsenų formavimąsi dėl In segregacijos, greičiausiai dėl nepakankamai efektyvios šių atomų migracijos. Raudonojo poslinkio buvimas tik žemuose žadinimuose byloja apie mažą gilių lokalizuotų būsenų tankį, dėl ko jos yra lengvai užpildomos dideliuose žadinimuose, kur stebimas tik mėlynasis poslinkis. Pradinis VKN kritimas galimai yra nulemtas defektų tankio augimo iki 6 s pertrūkio trukmės. Lokalizuotų būsenų gilėjimas ir didesnis defektų tankis greičiausiai atsiranda dėl mažos tikimybės paviršiaus atomams (pagrinde In) įsitvirtinti energiškai patogiose kristalinės gardėlės vietose [138]. Tai galimai vyksta dėl nepakankamo laiko migracijai ir konkurencijos tarp migruojančių atomų, todėl jie įsikabina ten, kur nukeliauti užtenka laiko ir yra laisvos vietos. Tai formuoja smarkiai fluktuojantį potencialo reljefą, kuriame gausu defektų. Panašu, jog papildomas laikas per šią pradinę fazę tiesiog paskatina In atomų segregaciją, kuomet šie negali rasti geros vietos gardelėje dėl skurdžios paviršiaus nitridizacijos [43], kuri taip pat atsakinga už azoto vakansijų formavimąsi. Tačiau viskas pasikeičia po slenkstinės 6 s pertrūkio trukmės: nugaruoja pakankamai perteklinių atomų, kurie palieka daugiau vietos likusiųjų migracijai ir prisikabinimui, tuo tarpu šiems procesams taip pat suteikiamas papildomas laikas; nusodinama pakankamai azoto atomų, kurie sumažina defektų formavimąsi ir In segregaciją. Šių procesų bendras efektas – staigus perėjimas į kristalinę gardelę, turinčią mažesnį In kiekį, tačiau su tolygesniu atomų pasiskirstymu ir

mažesniu defektų tankiu, kas veda link išaugusio maksimalaus VKN. Verta paminėti, jog difuzijos koeficientas mažėja dariniuose ilginant metalorganikos prekursorių tiekimo pertrūkio trukmę, kas geriausiai matoma esant dideliems krūvininkų tankiams (5×10^{19} cm^{-3}, Pav. 15(b)). Todėl galima teigti, jog tolygesnis atomų pasiskirstymas sukuria nors ir seklesnes, bet gausesnes lokalizuotas būsenas. Šių svarba tampa akivaizdi dideliuose krūvininkų tankiuose, kuriuose prasideda našumo krytis – mažesnė krūvininkų difuzija leidžia pasiekti aukštesnius vidinius kvantinius našumus. Vienalaikis VKN kreivių ir krūvininkų gyvavimo trukmių modeliavimas standartiniu ABC modeliu patvirtinta visas šias prielaidas.

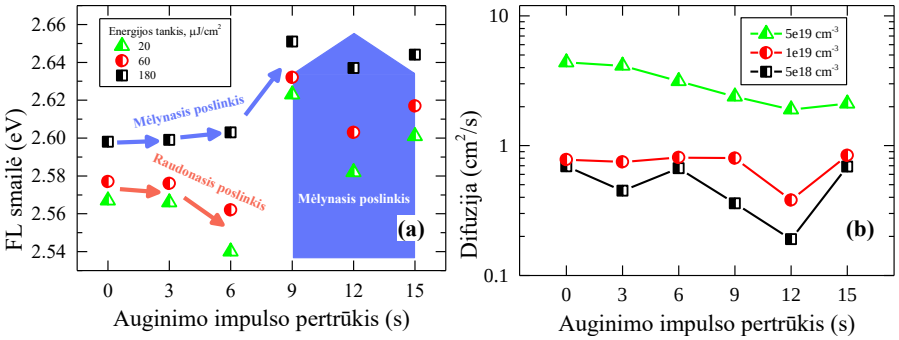

Pav. 15. LIFL spektrų smailių padėtys esant skirtingoms auginimo pertrūkio trukmėms ir trims skirtingiems žadinimo energijos tankiams (a). Krūvininkų difuzijos prieklausa nuo auginimo pertrūkio trukmės, esant trims skirtingiems krūvininkų tankiams (b).

Geras indikatorius atomų išsidėstymo pagerinime – difuzijos ilgis. Jis yra trumpesnis bandiniuose su didesniais maksimaliais VKN (Pav. 16).

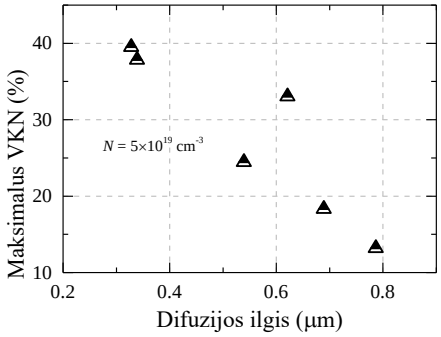

Pav. 16. Koreliacija tarp difuzijos ilgio, esant 5×10^{19} cm^3 krūvininkų tankiui, ir maksimalaus VKN.

2.6. Didelių duobės storio fluktuacijų įtaka lokalizacijos sąlygoms

KD storio fluktuacijos riboja nepusiausvirųjų krūvininkų difuziją – vieną svarbiausių faktorių, nulemiančių našumą šviestukuose nitridų pagrindu. Dėl šių fluktuacijų krūvininkų lokalizacijos ilgiai tipiškai yra 10 nm ir mažiau [80,86,87]. Tuo tarpu tipiniai krūvininkų difuzijos ilgiai siekia dešimtis [61,232] arba šimtus [122] nanometrų, todėl racionalu manyti, jog lokalizaciją galima būtų pagerinti sukūrus tam tikrus barjerus difuzijai, išsidėsčiusius tarp minėtų dviejų ribų. Tai buvo padaryta Oliver et al. [164] darbe, kur didelės duobės storio fluktuacijos sukūrė barjerus krūvininkų difuzijai, kas susilpnino krūvininkų nespindulinę rekombinaciją ir žymiai padidino vidinį kvantinį našumą. Tačiau iki šiol šis fizikinis modelis nebuvo pagrįstas tiesioginiais krūvininkų dinamikos tyrimais taip vadinamose „skylėtose“ (angl. *gappy*) kvantinėse duobėse.

Šioje darbo dalyje tirti du daugybinių KD dariniai su tolygaus (1T, Q2T Lentelėje 1) ir du daugybinių KD dariniai su smarkiai fluktuojančio (2T, T-Bounce Lentelėje 1) kvantinės duobės storio profiliais. Pastaruosiuose KD storis kai kuriose vietose yra tiek mažas, jog atskiri barjerai tarpusavyje susisiekia, todėl šie dariniai pavadinti „skylėtais“. Aktyviosios bandinių sritys buvo augintos ant 5 μm GaN pseudo-padėklų, jas sudaro 10 KD. „Skylėtos“ kvantinės duobės formuotos iškart po kiekvienos iš jų auginimo pakėlus temperatūrą, kas sukėlė žymų In nugaravimą atsitiktinėse atidengto InGaN sluoksnio vietose. Temperatūros kėlimas vykdytas per tam tikrą laiką amoniako aplinkoje, nutraukus metalorganikos tiekimą į reaktoriaus kamerą. GaN barjerai buvo auginami arba pakeltoje temperatūroje (2T), arba grąžinus ją į pradinę vertę (T-bounce). Auginant tolygaus storio KD, temperatūra arba nebuvo didinama (1T), arba tai buvo vykdoma prieš tai užauginus ploną apsauginį GaN sluoksnį (Q2T), kuris neleido In nugaruoti. Visos darinių auginimo detalės pateiktos [164].

Pav. 17 pateikti vidiniai kvantiniai našumai kaip funkcijos nuo krūvininkų tankio (iš LIFL matavimų). Matyti, kaip „skylėti“ dariniai išsiskiria gerokai didesnėmis VKN vertėmis žemose nepusiausvirųjų krūvininkų koncentracijose. Tiesa, didesnėse koncentracijose (virš ~10^{19} cm^{-3}) našumo kreivės rodo panašias vertes. Rezultatai sutampa su publikuotais anksčiau [164].

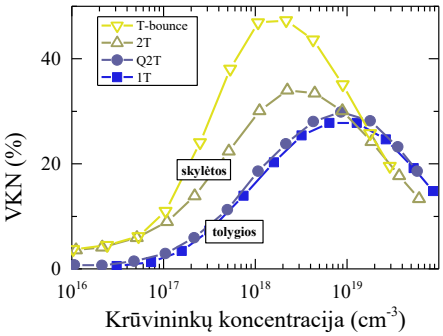

Pav. 17. Vidiniai kvantiniai našumai bandiniuose su „skylėtomis“ ir tolygaus storio kvantinėmis duobėmis.

Mažesni našumo kryčio atsiradimo slenksčiai „skylėtose“ KD byloja apie stipresnę lokalizaciją, ką patvirtina mažesnis difuzijos koeficientas, esant krūvininkų koncentracijai žemiau ~10^{19} cm^{-3} (Pav. 18). Kai pastarosios vertė yra 3×10^{18} cm^{-3}, *D* yra 0.1 ir 0.22 cm^2/s „skylėtose“ ir 0.44 ir 0.5 cm^2/s tolygaus storio kvantinėse duobėse. Tai sutampa su iki 4 kartus didesnėmis aktyvacijos energijomis, suskaičiuotomis [164] ir [233]. Aukštesnėse koncentracijose esminių skirtumų tarp difuzijos koeficiento verčių nebelieka, kas greičiausiai nulemia labai panašius VKN (Pav. 17).

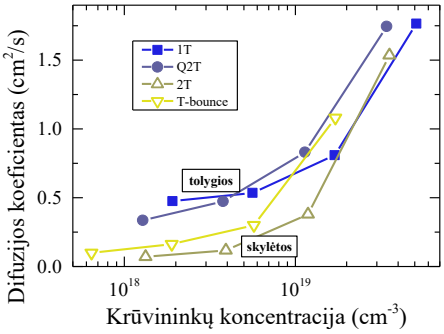

Pav. 18. Krūvininkų difuzijos koeficientas kaip funkcija nuo krūvininkų tankio.

Įdomu tai, jog krūvininkų gyvavimo trukmės „skylėtose“ KD yra trumpesnės (Pav. 19(a)), priešingai, negu galima tikėtis stipriai lokalizuotoje sistemoje. Kadangi maksimalus VKN taip pat yra didesnis „skylėtuose“ dariniuose, to priežastis greičiausiai yra spartesnė spindulinė rekombinacija. Ją lemia sumažėjusi difuzija, dėl kurios padidėja tikimybė elektronams ir skylėms susitikti ir anihiliuoti spinduliniu būdu. Tai veda link daugiau nei 2 kartus trumpesnių difuzijos ilgių „skylėtose“ duobėse (Pav. 19(b)), kas trukdo krūvininkams pasiekti toliau esančius defektus. Vienalaikis gyvavimo trukmių ir našumo kreivių modeliavimas patvirtina šias išvadas. Kitas svarbus

momentas – eile išaugęs Ožė rekombinacijos koeficientas „skylėtuose“ bandiniuose. To priežastis – taip pat išaugusi lokalizacija, dėl kurios krūvininkai yra stipriau sklaidomi potencialo fluktuacijų [112] bei išauga judesio kiekio neapibrėžtumas [115], o kartu tai palengvina judesio kiekio tvermės dėsnio patenkinimą.

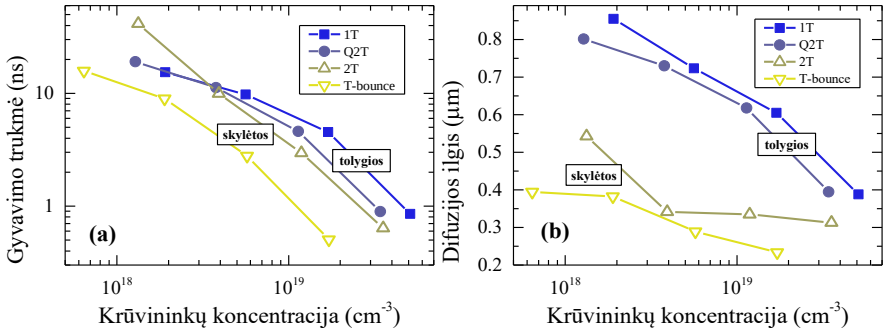

Pav. 19. ŠIDDG krūvininkų gyvavimo trukmė (a) ir difuzijos ilgis (b) kaip funkcijos nuo krūvininkų tankio.

2.7. Našumo kreivių charakteristikos našiuose šviestukuose. ABC modelio pritaikomumo ribos

Pirminė informacija apie bandinius dažniausiai yra gaunama iš FL matavimų, kurie yra santykinai paprasti ir nereikalauja specialaus paruošimo. FL spektrai suteikia informaciją apie smailės padėtį, juostos plotį, intensyvumą ir pan. Turint FL spektrus prie skirtingų sužadinimo lygių, galima nubraižyti našumo kreives, kurios suteikia informaciją apie našumo kryčio slenkstį bei apie kitus parametrus, tokius kaip našumo augimo ar kritimo sparta. Deja, vertinant patobulinimus dariniuose, dažniausiai yra atsižvelgiama tik į emisijos intensyvumą, tuo tarpu kiti parametrai lieka nuošalyje. Tačiau pastarieji taip pat gali suteikti naudingos informacijos, pagal kurią galima prognozuoti tam tikras medžiagos savybes.

Pav. 20 pateikti maksimalūs vidiniai kvantiniai našumai ties atitinkamais krūvininkų tankiais (viskas įvertinta iš LIFL matavimų integruojančioje sferoje). Čia matoma svarbi tendencija – kuo mažesnis našumo kryčio slenkstis, tuo didesnis maksimalus VKN gali būti pasiektas. Kitaip sakant – aukštesniuose našumo kryčio slenksčiuose yra tam tikra viršutinė riba. Kadangi krūvininkų difuzija tiesiogiai koreliuoja su jų tankiu, ši riba gali būti

priskirta difuzijos sąlygotiems nespinduliniams nuostoliams defektuose, kurie apriboja maksimalų VKN. Kadangi difuzija priklauso ir nuo kitų faktorių, tokių kaip atsitiktinės lydinio ar duobės storio fluktuacijos, o defektų tankis medžiagose taip pat gali būti labai skirtingas, maksimalių VKN vertės yra išsibarsčiusios srityje, apibrėžtoje raudonu trikampiu. Tai reiškia, kad tik bandiniai, turintys santykinai mažus defektų tankius ir pakankamas lokalizacijos sąlygas, gali pasiekti difuzijos sąlygotą ribą (bet jos neviršyti). Taip pat tam, kad būtų galima pasiekti 100% VKN, reikia kuo mažesnio našumo kryčio slenksčio. Geriausia strategija tam pasiekti – difuzijos koeficiento mažinimas.

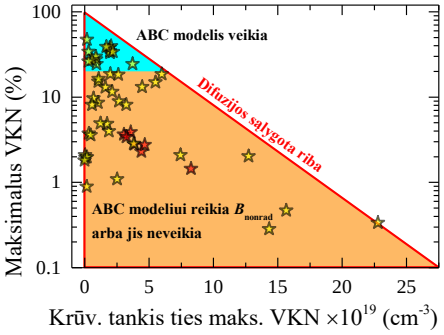

Pav. 20. Maksimalus VKN ties specifiniais, našumo kryčio slenkstį atitinkančiais, krūvininkų tankiais. Kiekvienas taškas atitinka atskirą bandinį. Raudonas užpildymas žymi m-plokštumos darinius. Raudonas trikampis žymi galimų maksimalių VKN verčių sritį.

Pagrindiniai procesai, lemiantys pradinį VKN kreivės kilimą, yra spartėjanti nuo krūvininkų tankio bimolekulinė rekombinacija [104,166] [P1,P3] ir nespindulinės rekombinacijos centrų sotinimas [66,205]. Atsižvelgiant į tai, kilimo sparta gali turėti naudingos informacijos, kadangi minėti procesai lems skirtingus VKN kreivės polinkius. Pvz. dominuojant bimolekulinei rekombinacijai, FL intensyvumas turėtų augti nuo krūvininkų tankio kvadrato [198] ($I_{PL} \propto BN^2$), tuo tarpu kvantinio našumo augimas turėtų būti tiesiogiai proporcingas ($IQE_{PL} \propto \frac{I_{PL}}{N} \propto \frac{BN^2}{N} \propto N$). Koreliacijos paieškai tarp maksimalaus VKN ir našumo kilimo spartos, stačiausios VKN kreivių dalys buvo įvertintos naudojantis laipsnine funkcija

$$IQE_{PL} \propto I_{exc}^{\gamma}. \quad (9)$$

Laipsnio rodiklis γ toliau bus vadinamas našumo kilimo sparta.

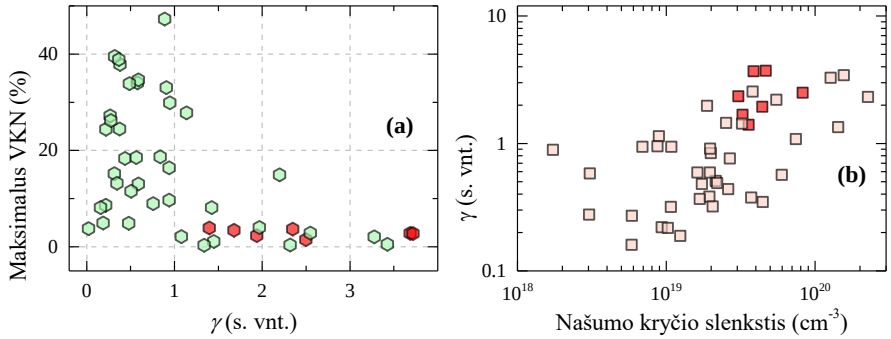

Pav. 21. Maksimalus VKN ties atitinkama našumo kilimo sparta γ (a). Koreliacija tarp našumo kilimo spartos ir našumo kryčio slenksčio (b). Raudona spalva žymi m-plokštumos bandinius.

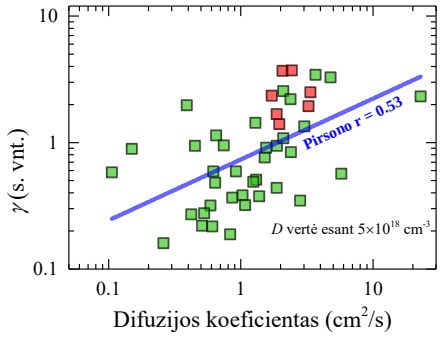

Pav. 22. Koreliacija tarp γ ir difuzijos koeficiento, esant 5×10^{18} cm^{-3} krūvininkų tankiui. Raudona spalva žymi m-plokštumos bandinius.

Pav. 21(a) atvaizduotas maksimalus VKN ties atitinkama γ verte. Matoma bendra tendencija, jog maksimalus VKN mažėja, kuomet našumo kilimo sparta auga. Kai kurie bandiniai pasiekia beveik 40%, kai γ vertės neviršija 1, kas greičiausiai byloja apie ryškų įnašą iš bimolekulinės arba eksitoninės rekombinacijos kanalų. Pav. 21(b) rodo, jog staigesnis našumo kilimas koreliuoja su didesniu našumo kryčio slenksčiu. Kaip jau minėta anksčiau, didesnis našumo kryčio slenkstis yra susijęs su silpnesne lokalizacija ir išaugusia nespindulinės rekombinacijos sparta. Todėl didesnės γ vertės greičiausiai yra susijusios su aukštesnės eilės nespinduliniais nuostoliais. Labiausiai tikėtina, kad juos sąlygoja krūvininkų difuzija. Tą patvirtina Pav. 22, kur stebima tiesioginė γ ir difuzijos koeficiento koreliacija. Taigi didesnis našumo kryčio slenkstis reiškia ir didesnį skaičių defektų, kuriuos reikia užsotinti prieš pasiekiant maksimalų VKN [66,205]. Tą apsunkina efektyviojo defektų tankio, kurį krūvininkai gali pasiekti, didėjimas dėl būsenų pildymo ir

augančios delokalizacijos. Tai sukelia nuo krūvininkų tankio spartėjančią nespindulinę rekombinaciją, kuri atsakinga už greitesnį našumo kilimą.

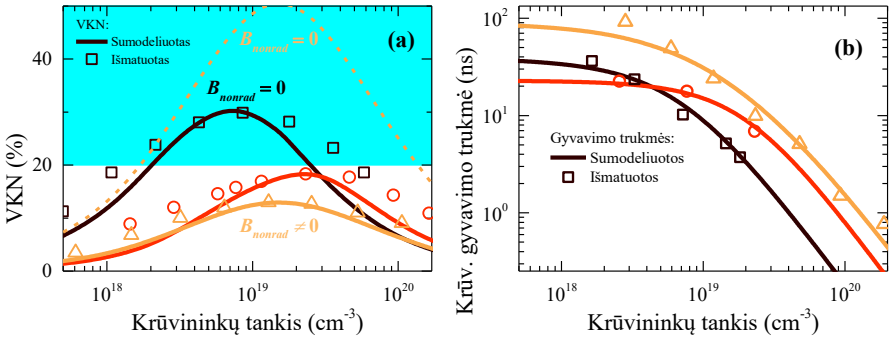

Pav. 23. Išmatuoti ir sumodeliuoti VKN (a) ir krūvininkų gyvavimo trukmės (b): taškai atitinka eksperimentinius rezultatus, kreivės atvaizduoja modeliavimo rezultatus.

Toliau aptariamos standartinio ABC modelio su nuo krūvininkų tankio nekintančiais koeficientais galiojimo ribos. Tuo tikslu buvo pamėginta sumodeliuoti 40-ies polinių bandinių iš Lentelės 1 (V1-T815) VKN kreives ir krūvininkų gyvavimo trukmes (gautas iš spektre integruotų SP kinetikų pradinių dalių). Išaiškėjo, jog naudojantis tuo pačiu *A*, *B* ir *C* koeficientų (atitinkančių SRH, bimolekulinę ir Ožė rekombinacijas) rinkiniu, sumodeliuoti gyvavimo trukmes ir VKN kreives paprastu ABC modeliu pavyko tik daliai bandinių (Pav. 23(a) ir (b)). Kitiems bandiniams prireikė papildomo, nuo krūvininkų tankio augančio, nespindulinės rekombinacijos dėmens. Dar kitiems bandiniams modeliavimas nepavyko, kadangi nesigavo parinkti ABC koeficientų, kurie atitiktų išmatuotą našumo kryčio slenkstį. Šie rezultatai atvaizduoti Pav. 20, kur geras atitikimas tarp eksperimentinių ir sumodeliuotų kreivių pasiektas dariniuose su maksimaliu VKN, viršijančiu 20%. Didžiajai daliai bandinių su maks. VKN <20%, standartinis *B* koeficientas buvo pakeistas į $B^* = B_{rad} + B_{nonrad}$, kurį sudaro spindulinė ir nespindulinė dalys, kas leido sumažinti sumodeliuotas VKN vertes, taip jas sutapatinant su eksperimentinėmis. Tokią modifikaciją galima pagrįsti difuzijos sąlygotais nespinduliniais nuostoliais, kurie didėja su žadinimu dėl augančio delokalizuotų krūvininkų tankio. Modifikuotos lygtys yra:

$$\frac{1}{\tau} = A + (B_{rad} + B_{nonrad})N + CN^2, \tag{10}$$

$$IQE = \frac{B_{rad}}{A+(B_{rad}+B_{nonrad})N+CN^2}. \tag{11}$$

B^* narys laikomas pastoviu visiems žadinimams. Geresniam VKN kreivių atitikimui reikėtų įskaityti tokius efektus kaip fazinės erdvės pildymas [96] ir su tuo susijęs kvadratinės (BN^2) bei kubinės (CN^3) priklausomybių neišsilaikymas [142,237], tačiau dėl paprastumo tai nebuvo daryta.

Viršutiniai rezultatai rodo, jog paprastas ABC modelis yra pritaikomas tik santykinai našiems bandiniams, kuriuose Ožė rekombinacija yra pagrindinė našumo kryčio priežastis. Krentant maksimaliam VKN, neatitikimas tarp sumodeliuotų ir išmatuotų verčių didėja. Galima to priežastis – kito proceso, tokio kaip difuzijos sąlygota nespindulinė rekombinacija, atsiradimas. Todėl, prastėjant darinio kokybei dėl išaugusio defektų tankio arba susilpnėjusios lokalizacijos, Ožė proceso vaidmuo mažėja. Silpnesnė lokalizacija jau seniau buvo pristatyta kaip sumažėjusio C koeficiento priežastis [112].

2.8. Bendros rekomendacijos auginimui

Šioje disertacijoje pateikti rezultatai rodo, jog ambipolinės krūvininkų difuzijos apribojimas KD plokštumoje yra būtinas siekiant sumažinti nuostolius dėl nespindulinės rekombinacijos defektuose. Tai yra svarbu šiandieninei technologijai, kadangi dabartiniai sprendimai medžiagos kokybei pagerinti, tokie kaip padėklai su suderintomis gardelės konstantomis arba šoninis auginimas, padidina kainą ir daro visą auginimo procesą sudėtingesniu. Šiame darbe pateikti keli būdai, kuriuos kombinuodamas augintojas gali turėti stiprų pagrindą našaus šviestuko nitridų technologijos pagrindu kūrimui.

Pradedant nuo apatinių sluoksnių, įtempimus mažinančio sluoksnio, tokio kaip supergardelė, įterpimas turėtų būti standartinė procedūra, kadangi tai susilpnina vidinius elektrinius laukus ir mažina krūvininkų delokalizaciją.

Einant link aktyviosios srities, čia stipresnė lokalizacija gali būti pasiekta auginant siauresnes kvantines duobes, kuriose stipresnę krūvininkų sklaidą sukelia didesnės potencialo fluktuacijos. KD turėtų būti pakankamai siauros ($\leq$3 nm), kad būtų užtikrintos optimalios lokalizacijos sąlygos ir krūvininkų banginių funkcijų persiklojimas, bet ne per siauros ($\geq$2 nm), kad būtų užtikrintas pakankamas efektyvios optiškai aktyvios terpės tūris. KD storis priklauso ir nuo planuojamo emisijos bangos ilgio, tačiau geresnė strategija ilginant bangos ilgį yra įterpti daugiau In siauroje kvantinėje duobėje.

Tolesnis lokalizacijos pagerinimas gali būti pasiektas pakeliant temperatūrą po KD užauginimo, dėl ko atsitiktinėse vietose nugaruoja In

atomai ir susidaro didelės duobės storio fluktuacijos. Papildomi barjerai krūvininkų difuzijai paspartina spindulinės rekombinacijos spartą ir palieka mažiau krūvininkų nespindulinės rekombinacijos kanalams.

Impulsinis KD auginimas pagerina paviršiaus nitridizaciją, įgalina nusodintų atomų migraciją, taip pat ir perteklinių atomų nugaravimą. Susidaręs geresnis atomų išsidėstymas sustiprina lokalizaciją ir sluoksnio kokybę. Laiko intervalai turėtų būti atidžiai patrinkti esant skirtingoms auginimo temperatūroms ir prekursorių daliniams slėgiams, tačiau ilgesnės pertrūkio trukmės rodo geresnius rezultatus.

IŠVADOS

1. Trumpo periodo supergardelės įterpimas sumažina įtempimus ir vidinius elektrinius laukus aukščiau auginamose kvantinėse duobėse. Taip pat susilpninama delokalizacija, turinti didelę įtaką VKN ir našumo kryčiui, ką įrodo atvirkštinė koreliacija tarp VKN verčių ir difuzijos koeficiento. Parodyta, kad supergardelės įterpimas gali padidinti VKN kelis kartus.
2. Nuo žadinimo intensyvumo spartėjanti nespindulinė rekombinacija gali būti susijusi su defektuose vykstančia ir nuo krūvininkų tankio priklausančia nespinduline rekombinacija. Pritaikius ją ir spindulinės rekombinacijos sotinimą dėl fazinės erdvės pildymo, galima sėkmingai aprašyti našumo kryčio reiškinį nenaudojant Ožė rekombinacijos dėmens.
3. Difuzijos sąlygotą nespindulinę rekombinaciją įrodo augantis difuzijos koeficientas. Parodyta, jog pastarojo augimo nuo krūvininkų tankio sparta koreliuoja su našumo kryčio atsiradimu, kas patvirtina svarbų smarkiai judrių krūvininkų vaidmenį našumo kryčio procese.
4. Netipinis raudonasis poslinkis, stebimas ilguose vėlinimuose ir didėjantis nuo žadinimo intensyvumo, yra tiesiogiai stebimas krūvininkų persiskirstymas tarp skirtingo gylio lokalizuotų būsenų.
5. Didesnė krūvininkų difuzija lemia mažesnį maksimalų vidinį kvantinį našumą dėl spartesnės nespindulinės delokalizuotų krūvininkų rekombinacijos defektuose. Tą patvirtina universalus tiesiškas krūvininkų gyvavimo trukmė mažėjimas augant difuzijos koeficientui.
6. Ambipolinės difuzijos koeficientas mažėja siauresnėse kvantinėse duobėse dėl didesnių duobės storio fluktuacijų sukeltų potencinės energijos fluktuacijų, kurios padidina krūvininkų sklaidą.
7. Išaugusios potencialo fluktuacijos trukdo krūvininkams judėti link ištęstinių defektų, dėl ko yra greičiau užpildomos lokalizuotos būsenos, ir skatina Ožė rekombinaciją – tai nulemia ankstesnį našumo kryčio slenkstį. Pastarasis yra naudingas maksimaliam VKN, kadangi esant mažesniems krūvininkų tankiams tikėtini mažesni nuostoliai dėl difuzijos sąlygotos nespindulinės rekombinacijos.
8. Stokso poslinkio dydį InGaN kvantinėse duobėse lemia kvantinės sąspraudos Štarko efektas, krūvininkų difuzija ir atsitiktinės lydinio fluktuacijos: platesnėse duobėse krūvininkai sukrenta į kraštuose esančius gilesnius trikampio potencialo minimumus, tuo tarpu išaugusi difuzija leidžia krūvininkams pasiekti gilesnes lokalizuotas būsenas, jei šios susidarė dėl

atsitiktinių lydinio fluktuacijų. Įtempimų medžiagoje atpalaidavimas mažina vidinius elektrinius laukus ir In kiekio fluktuacijas, dėl ko gali sumažėti ir Stokso poslinkis.

9. Impulsinis MOCVD auginimo režimas auginamame aktyviajame sluoksnyje padidina struktūrinę kokybę ir pagerina lokalizacijos sąlygas, jei paviršiuje migruojantiems atomams yra suteikiama pakankamai laiko ir susidaro pakankamai energiškai patogių gardelės vietų atomų prisitvirtinimui. Tai įvyksta, kuomet nugaruoja pakankamas kiekis perteklinių atomų ir paviršius yra pakankamai nitridizuojamas. Trumpesnis difuzijos nuotolis gali parodyti geresnį atomų išsidėstymą.

10. Didelės KD storio fluktuacijos, kurias sukuria auginimo temperatūros pakėlimas, sukuria papildomus barjerus krūvininkų difuzijai. Sustiprinta lokalizacija padidina spindulinės rekombinacijos spartą ir neleidžia krūvininkams pasiekti nespindulinės rekombinacijos centrų, ką rodo sutrumpėjusios gyvavimo trukmės ir gerokai mažesni difuzijos nuotoliai.

11. Spartus rekombinacijos procesas ir tolydžiai auganti difuzija aukštuose nepusiausvirųjų krūvininkų tankiuose atskleidžia tiek Ožė, tiek ir difuzijos sąlygotos nespindulinės rekombinacijos buvimą. Vien Ožė procesas yra tinkamas našumo kryčio aprašymui kvantinėse duobėse su santykinai aukštu VKN (>20%), tuo tarpu mažiau našiose KD reikia įskaityti ir difuzijos sąlygotą rekombinaciją defektuose.

12. Našumo krytis, atsirandantis mažesniuose krūvininkų tankiuose, ir lėtesne kvantinio našumo augimo sparta koreliuoja su stipresne lokalizacija. Šie kriterijai gali būti panaudoti ieškant optimalių auginimo sąlygų ar struktūrinių darinių parametrų, kai yra siekiama kuo didesnio VKN.

[1] Phase-out of incandescent light bulbs, (2019). https://en.wikipedia.org/wiki/Phase-out_of_incandescent_light_bulbs.
[2] Fluorescent lamp, (2019). https://en.wikipedia.org/wiki/Fluorescent_lamp.
[3] P. Pust, P.J. Schmidt, W. Schnick, A revolution in lighting, Nat. Mater. 14 (2015) 454–458. doi:10.1038/nmat4270.
[4] C. Koekemoer, Here are some lumen per watt (LPW) targets for common LEDs, (2017). https://insights.regencylighting.com/lpw-targets-for-led-lamp-types.
[5] Cree First to Break 300 Lumens-Per-Watt Barrier, (2014). http://www.cree.com/news-media/news/article/cree-first-to-break-300-lumens-per-watt-barrier.
[6] A. Žukauskas, R. Vaicekauskas, P. Vitta, A. Tuzikas, M.S. Shur, Polychromatic solid-state light sources for the control of colour saturation of illuminated surfaces, US 2014/0167646 A1, 2014. https://patents.google.com/patent/US20140167646A1/en (accessed January 22, 2018).
[7] LED Lighting Market To Drive Speedily And Reach USD 54.28 Billion By 2022, (2018). https://www.zionmarketresearch.com/news/led-lighting-market.
[8] LED Lighting Market Size, Trends, Growth, Industry Report, 2018-2025, (2018). https://www.grandviewresearch.com/industry-analysis/led-lighting-market.
[9] C. Weisbuch, M. Piccardo, L. Martinelli, J. Iveland, J. Peretti, J.S. Speck, The efficiency challenge of nitride light-emitting diodes for lighting, Phys. Status Solidi Appl. Mater. Sci. 212 (2015) 899–913. doi:10.1002/pssa.201431868.
[10] J.S. Cheong, A.N.A.P. Baharuddin, J.S. Ng, A.B. Krysa, J.P.R. David, Absorption coefficients in AlGaInP lattice-matched to GaAs, Sol. Energy Mater. Sol. Cells. 164 (2017) 28–31. doi:10.1016/j.solmat.2017.01.042.
[11] D. Zhu, C.J. Humphreys, Solid-state lighting based on light emitting diode technology, in: M. Al-Amri, M. El-Gomati, M. Zubairy (Eds.), Opt. Our Time, Springer, Cham, 2016: pp. 87–118. doi:10.1007/978-3-319-31903-2.
[12] M. Auf Der Maur, A. Pecchia, G. Penazzi, W. Rodrigues, A. Di Carlo, Efficiency Drop in Green InGaN/GaN Light Emitting Diodes: The Role of Random Alloy Fluctuations, Phys. Rev. Lett. 116 (2016) 1–5. doi:10.1103/PhysRevLett.116.027401.

[13] J. Iveland, J.S. Speck, L. Martinelli, J. Peretti, C. Weisbuch, Auger effect identified as main cause of efficiency droop in LEDs, SPIE Newsroom. 1 (2014) 2–5. doi:10.1117/2.1201406.005109.
[14] J. Jurkevičius, Photoluminescence efficiency in wide-band-gap III-nitride semiconductors and their heterostructures: Doctoral Dissertation, Vilnius University, 2016. https://elaba.lvb.lt/permalink/f/1gjkcsi/ELABAETD18323372.
[15] J.I. Pankove, E.A. Miller, J.E. Berkeyheiser, GaN electroluminescent diodes, in: 1971 Int. Electron Devices Meet., IRE, 1971: pp. 78–78. doi:10.1109/IEDM.1971.188400.
[16] H. Amano, M. Kito, K. Hiramatsu, I. Akasaki, P-Type Conduction in Mg-Doped GaN Treated with Low-Energy Electron Beam Irradiation (LEEBI), Jpn. J. Appl. Phys. 28 (1989) L2112–L2114. doi:10.1143/JJAP.28.L2112.
[17] S. Nakamura, GaN Growth Using GaN Buffer Layer, Jpn. J. Appl. Phys. 30 (1991) L1705–L1707. doi:10.1143/JJAP.30.L1705.
[18] S. Nakamura, N. Iwasa, M. Senoh, T. Mukai, Hole Compensation Mechanism of P-Type GaN Films, Jpn. J. Appl. Phys. 31 (1992) 1258–1266. doi:10.1143/JJAP.31.1258.
[19] S. Nakamura, T. Mukai, M. Senoh, Candela-class high-brightness InGaN/AlGaN double-heterostructure blue-light-emitting diodes, Appl. Phys. Lett. 64 (1994) 1687–1689. doi:10.1063/1.111832.
[20] The 2014 Nobel Prize in Physics - Press release, (2018). https://www.nobelprize.org/prizes/physics/2014/press-release/.
[21] L.E. Ramos, L.K. Teles, L.M.R. Scolfaro, J.L.P. Castineira, A.L. Rosa, J.R. Leite, Structural, electronic, and effective-mass properties of silicon and zinc-blende group-III nitride semiconductor compounds, Phys. Rev. B. 63 (2001) 1–10. doi:10.1103/PhysRevB.63.165210.
[22] T. Mattila, A. Zunger, Predicted bond length variation in wurtzite and zinc-blende InGaN and AlGaN alloys, J. Appl. Phys. 85 (1999) 160–167. doi:10.1063/1.369463.
[23] K.A. Jones, T.P. Chow, M. Wraback, M. Shatalov, Z. Sitar, F. Shahedipour, K. Udwary, G.S. Tompa, AlGaN devices and growth of device structures, J. Mater. Sci. 50 (2015) 3267–3307. doi:10.1007/s10853-015-8878-3.
[24] M. Stutzmann, O. Ambacher, M. Eickhoff, U. Karrer, A.L. Pimenta, R. Neuberger, J. Schalwig, R. Dimitrov, P.J. Schuck, R.D. Grober, Playing with polarity, Phys. Status Solidi Basic Res. 228 (2001) 505–512. doi:10.1002/1521-3951(200111)228:2<505::AID-PSSB505>3.0.CO;2-U.
[25] Z.Y. Al Balushi, J.M. Redwing, The effect of polarity on MOCVD growth of thick InGaN, Appl. Phys. Lett. 110 (2017) 022101. doi:10.1063/1.4972967.

[26] S.-H. Wei, A. Zunger, Valence band splittings and band offsets of AlN, GaN, and InN, Appl. Phys. Lett. 69 (1996) 2719–2721. doi:10.1063/1.117689.
[27] X. Wang, S. Liu, N. Ma, L. Feng, G. Chen, F. Xu, N. Tang, S. Huang, K.J. Chen, S. Zhou, B. Shen, High-electron-mobility InN layers grown by boundary-temperature-controlled epitaxy, Appl. Phys. Express. 5 (2012) 015502. doi:10.1143/APEX.5.015502.
[28] Band structure for Wurtzite GaN, (n.d.). http://www.ioffe.ru/SVA/NSM/Semicond/GaN/bandstr.html.
[29] M. Suzuki, T. Uenoyama, A. Yanase, First-principles calculations of effective-mass parameters of AlN and GaN, Phys. Rev. B. 52 (1995) 8132–8139. doi:10.1103/PhysRevB.52.8132.
[30] V. Pishchik, L.A. Lytvynov, E.R. Dobrovinskaya, Properties of sapphire, in: Sapphire Mater. Manuf. Appl., Springer US, Boston, MA, 2009: pp. 55–176. doi:10.1007/978-0-387-85695-7.
[31] O.K. Jani, Development Of Wide-Band Gap InGaN Solar Cells For High-Efficiency Photovoltaics: Doctoral Dissertation, Georgia Tech, 2008. http://smartech.gatech.edu/handle/1853/29627.
[32] V. Tassev, Heteroepitaxy, an Amazing Contribution of Crystal Growth to the World of Optics and Electronics, Crystals. 7 (2017) 178. doi:10.3390/cryst7060178.
[33] V.P. Kladko, A. V. Kuchuk, N. V. Safryuk, V.F. MacHulin, A.E. Belyaev, H. Hardtdegen, S.A. Vitusevich, Mechanism of strain relaxation by twisted nanocolumns revealed in AlGaN/GaN heterostructures, Appl. Phys. Lett. 95 (2009). doi:10.1063/1.3184569.
[34] J.T. Griffiths, S. Zhang, B. Rouet-Leduc, W.Y. Fu, A. Bao, D. Zhu, D.J. Wallis, A. Howkins, I. Boyd, D. Stowe, M.J. Kappers, C.J. Humphreys, R.A. Oliver, Nanocathodoluminescence Reveals Mitigation of the Stark Shift in InGaN Quantum Wells by Si Doping, Nano Lett. 15 (2015) 7639–7643. doi:10.1021/acs.nanolett.5b03531.
[35] GaN on Silicon, (n.d.). https://www.gan.msm.cam.ac.uk/projects/silicon.
[36] A.J. Ptak, L.J. Holbert, L. Ting, C.H. Swartz, M. Moldovan, N.C. Giles, T.H. Myers, P. Van Lierde, C. Tian, R.A. Hockett, S. Mitha, A.E. Wickenden, D.D. Koleske, R.L. Henry, Controlled oxygen doping of GaN using plasma assisted molecular-beam epitaxy, Appl. Phys. Lett. 79 (2001) 2740–2742. doi:10.1063/1.1403276.
[37] J. Piprek, How to decide between competing efficiency droop models for GaN-based light-emitting diodes, Appl. Phys. Lett. 107 (2015). doi:10.1063/1.4927202.
[38] E.F. Schubert, I.D. Goepfert, W. Grieshaber, J.M. Redwing, Optical properties of Si-doped GaN, Appl. Phys. Lett. 71 (1997) 921–923. doi:10.1063/1.119689.

[39] I. Shalish, L. Kronik, G. Segal, Y. Rosenwaks, Y. Shapira, U. Tisch, J. Salzman, Yellow luminescence and related deep levels in unintentionally doped GaN films, Phys. Rev. B. 59 (1999) 9748–9751. doi:10.1103/PhysRevB.59.9748.

[40] H. Amano, I. Akasaki, K. Hiramatsu, N. Koide, N. Sawaki, Effects of the buffer layer in metalorganic vapour phase epitaxy of GaN on sapphire substrate, Thin Solid Films. 163 (1988) 415–420. doi:10.1016/0040-6090(88)90458-0.

[41] S.T. Pendlebury, P.J. Parbrook, D.J. Mowbray, D.A. Wood, K.B. Lee, InGaN/GaN quantum wells with low growth temperature GaN cap layers, J. Cryst. Growth. 307 (2007) 363–366. doi:10.1016/j.jcrysgro.2007.07.018.

[42] A.G. Bhuiyan, A. Hashimoto, A. Yamamoto, Indium nitride (InN): A review on growth, characterization, and properties, J. Appl. Phys. 94 (2003) 2779–2808. doi:10.1063/1.1595135.

[43] A. Kadys, T. Malinauskas, T. Grinys, M. Dmukauskas, J. Mickevičius, J. Aleknavičius, R. Tomašiūnas, A. Selskis, R. Kondrotas, S. Stanionytė, H. Lugauer, M. Strassburg, Growth of InN and In-Rich InGaN Layers on GaN Templates by Pulsed Metalorganic Chemical Vapor Deposition, J. Electron. Mater. 44 (2015) 188–193. doi:10.1007/s11664-014-3494-6.

[44] F.B. Naranjo, M.A. Sánchez-García, F. Calle, E. Calleja, B. Jenichen, K.H. Ploog, Strong localization in InGaN layers with high In content grown by molecular-beam epitaxy, Appl. Phys. Lett. 80 (2002) 231–233. doi:10.1063/1.1432751.

[45] Ž. Gačević, V.J. Gómez, N.G. Lepetit, P.E.D. Soto Rodríguez, A. Bengoechea, S. Fernández-Garrido, R. Nötzel, E. Calleja, A comprehensive diagram to grow (0001)InGaN alloys by molecular beam epitaxy, J. Cryst. Growth. 364 (2013) 123–127. http://dx.doi.org/10.1016/j.jcrysgro.2012.11.031 (accessed September 24, 2018).

[46] D.C. Oh, S.W. Lee, H. Goto, S.H. Park, I.H. Im, T. Hanada, M.W. Cho, T. Yao, Impact of V/III ratio on electrical properties of GaN thick films grown by hydride vapor-phase epitaxy, Appl. Phys. Lett. 91 (2007) 132112. doi:10.1063/1.2786851.

[47] L. Cai, C. Feng, Effect of vacancy defects on the mechanical properties of carbon nanotube reinforced polypropylene, J. Nanotechnol. 2017 (2017) 1–6. doi:10.1155/2017/6987430.

[48] A. Islam, D.-S. Shim, J.-I. Shim, A.B.M.H. Islam, D.-S. Shim, J.-I. Shim, Enhanced Radiative Recombination Rate by Local Potential Fluctuation in InGaN/AlGaN Near-Ultraviolet Light-Emitting Diodes, Appl. Sci. 9 (2019) 871. doi:10.3390/app9050871.

[49] Y.-S. Lin, K.-J. Ma, C. Hsu, S.-W. Feng, Y.-C. Cheng, C.-C. Liao,

C.C. Yang, C.-C. Chou, C.-M. Lee, J.-I. Chyi, Dependence of composition fluctuation on indium content in InGaN/GaN multiple quantum wells, Appl. Phys. Lett. 77 (2000) 2988. doi:10.1063/1.1323542.

[50] C. Bazioti, E. Papadomanolaki, T. Kehagias, T. Walther, J. Smalc-Koziorowska, E. Pavlidou, P. Komninou, T. Karakostas, E. Iliopoulos, G.P. Dimitrakopulos, Defects, strain relaxation, and compositional grading in high indium content InGaN epilayers grown by molecular beam epitaxy, J. Appl. Phys. 118 (2015) 155301. doi:10.1063/1.4933276.

[51] Y. Inatomi, Y. Kangawa, T. Ito, T. Suski, Y. Kumagai, K. Kakimoto, A. Koukitu, Theoretical study of the composition pulling effect in InGaN metalorganic vapor-phase epitaxy growth, Jpn. J. Appl. Phys. 56 (2017) 078003. doi:10.7567/JJAP.56.078003.

[52] K. Hiramatsu, Y. Kawaguchi, M. Shimizu, N. Sawaki, T. Zheleva, R.F. Davis, H. Tsuda, W. Taki, N. Kuwano, K. Oki, The Composition Pulling Effect in MOVPE Grown InGaN on GaN and AlGaN and its TEM Characterization, MRS Internet J. Nitride Semicond. Res. 2 (1997) e6. doi:10.1557/S1092578300001320.

[53] G.B. Stringfellow, Microstructures produced during the epitaxial growth of InGaN alloys, J. Cryst. Growth. 312 (2010) 735–749. doi:10.1016/J.JCRYSGRO.2009.12.018.

[54] H. Wang, D.S. Jiang, U. Jahn, J.J. Zhu, D.G. Zhao, Z.S. Liu, S.M. Zhang, Y.X. Qiu, H. Yang, Investigation on the strain relaxation of InGaN layer and its effects on the InGaN structural and optical properties, Phys. B Condens. Matter. 405 (2010) 4668–4672. doi:10.1016/j.physb.2010.08.058.

[55] J. Neugebauer, Surfactants and antisurfactants on group-III-nitride surfaces, in: Phys. Status Solidi C Conf., Wiley-Blackwell, 2003: pp. 1651–1667. doi:10.1002/pssc.200303132.

[56] C.E. Dreyer, A. Alkauskas, J.L. Lyons, J.S. Speck, C.G. Van De Walle, Gallium vacancy complexes as a cause of Shockley-Read-Hall recombination in III-nitride light emitters, Appl. Phys. Lett. 108 (2016) 141101. doi:10.1063/1.4942674.

[57] F.C. Massabuau, P. Chen, M.K. Horton, S.L. Rhode, C.X. Ren, T.J. O'Hanlon, A. Kovács, M.J. Kappers, C.J. Humphreys, R.E. Dunin-Borkowski, R.A. Oliver, Carrier localization in the vicinity of dislocations in InGaN, J. Appl. Phys. 121 (2017) 013104. doi:10.1063/1.4973278.

[58] A. Vaitkevičius, J. Mickevičius, D. Dobrovolskas, Ö. Tuna, C. Giesen, M. Heuken, G. Tamulaitis, Influence of quantum-confined Stark effect on optical properties within trench defects in InGaN quantum wells with different indium content, J. Appl. Phys. 115 (2014).

doi:10.1063/1.4881776.
[59] S. Nakamura, The Roles of Structural Imperfections in InGaN-Based Blue Light-Emitting Diodes and Laser Diodes, Science (80-.). 281 (1998) 956–961. doi:10.1126/science.281.5379.956.
[60] F. Hitzel, G. Klewer, S. Lahmann, U. Rossow, A. Hangleiter, Localized high-energy emissions from the vicinity of defects in high-efficiency Gax In1-x N GaN quantum wells, Phys. Rev. B - Condens. Matter Mater. Phys. 72 (2005) 1–4. doi:10.1103/PhysRevB.72.081309.
[61] A. Kaneta, M. Funato, Y. Kawakami, Nanoscopic recombination processes in InGaN/GaN quantum wells emitting violet, blue, and green spectra, Phys. Rev. B - Condens. Matter Mater. Phys. 78 (2008) 1–7. doi:10.1103/PhysRevB.78.125317.
[62] Y.H. Choi, M.H. Kim, J.H. Yi, J. Jeon, S. Khym, J. Lee, H.K. Yuh, H.S. Song, S.J. Leem, Characteristics of nitride-based laser diode grown on SiO2-removed laterally overgrown GaN, J. Korean Phys. Soc. 42 (2003) S129–S133.
[63] A. Knigge, M. Brendel, F. Brunner, S. Einfeldt, A. Knauer, V. Kueller, M. Weyers, AlGaN photodetectors for the UV-C spectral region on planar and epitaxial laterally overgrown AlN/sapphire templates, Phys. Status Solidi Curr. Top. Solid State Phys. 10 (2013) 294–297. doi:10.1002/pssc.201200636.
[64] C.H. Wang, C.C. Ke, C.H. Chiu, J.C. Li, H.C. Kuo, T.C. Lu, S.C. Wang, Study of the internal quantum efficiency of InGaN / GaN UV LEDs on patterned sapphire substrate using the electroluminescence method, J. Cryst. Growth. 315 (2011) 242–245. doi:10.1016/j.jcrysgro.2010.09.046.
[65] S. Tanaka, Y. Zhao, I. Koslow, C.-C. Pan, H.-T. Chen, J. Sonoda, S.P. DenBaars, S. Nakamura, Droop improvement in high current range on PSS-LEDs, Electron. Lett. 47 (2011) 335. doi:10.1049/el.2010.3306.
[66] T. Kohno, Y. Sudo, M. Yamauchi, K. Mitsui, H. Kudo, H. Okagawa, Y. Yamada, Internal quantum efficiency and nonradiative recombination rate in InGaN-based near-ultraviolet light-emitting diodes, Jpn. J. Appl. Phys. 51 (2012) 072102. doi:10.1143/JJAP.51.072102.
[67] S.J. Chang, Y.C. Lin, Y.K. Su, C.S. Chang, T.C. Wen, S.C. Shei, J.C. Ke, C.W. Kuo, S.C. Chen, C.H. Liu, Nitride-based LEDs fabricated on patterned sapphire substrates, Solid. State. Electron. 47 (2003) 1539–1542. doi:10.1016/S0038-1101(03)00073-X.
[68] Y. Narukawa, M. Ichikawa, D. Sanga, M. Sano, T. Mukai, White light emitting diodes with super-high luminous efficacy, J. Phys. D. Appl. Phys. 43 (2010) 354002. doi:10.1088/0022-3727/43/35/354002.
[69] I.S. Romanov, I.A. Prudaev, V. V. Kopyev, Effects of GaN barrier

thickness on built-in electric field and internal quantum efficiency of blue InGaN/GaN multiple quantum wells LED structures, Jpn. J. Appl. Phys. 55 (2016). doi:10.7567/JJAP.55.05FJ15.

[70] E.T. Yu, X.Z. Dang, P.M. Asbeck, S.S. Lau, G.J. Sullivan, Spontaneous and piezoelectric polarization effects in III–V nitride heterostructures, J. Vac. Sci. Technol. B Microelectron. Nanom. Struct. 17 (1999) 1742. doi:10.1116/1.590818.

[71] O. Ambacher, J. Smart, J.R. Shealy, N.G. Weimann, K. Chu, M. Murphy, W.J. Schaff, L.F. Eastman, R. Dimitrov, L. Wittmer, M. Stutzmann, W. Rieger, J. Hilsenbeck, Two-dimensional electron gases induced by spontaneous and piezoelectric polarization charges in N- and Ga-face AlGaN/GaN heterostructures, J. Appl. Phys. 85 (1999) 3222–3233. doi:10.1063/1.369664.

[72] S.F. Chichibu, H. Marchand, M.S. Minsky, S. Keller, P.T. Fini, J.P. Ibbetson, S.B. Fleischer, J.S. Speck, J.E. Bowers, E. Hu, U.K. Mishra, S.P. DenBaars, T. Deguchi, T. Sota, S. Nakamura, Emission mechanisms of bulk GaN and InGaN quantum wells prepared by lateral epitaxial overgrowth, Appl. Phys. Lett. 74 (1999) 1460–1462. doi:10.1063/1.123581.

[73] S. Schulz, O. Marquardt, C. Coughlan, M.A. Caro, O. Brandt, E.P. O'Reilly, Atomistic description of wave function localization effects in In x Ga 1-x N alloys and quantum wells, in: Phys. Simul. Optoelectron. Devices XXIII, 2015: p. 93570C. doi:10.1117/12.2084800.

[74] T.J. Badcock, P. Dawson, M.J. Davies, M.J. Kappers, F.C.P. Massabuau, F. Oehler, R.A. Oliver, C.J. Humphreys, Low temperature carrier redistribution dynamics in InGaN/GaN quantum wells, J. Appl. Phys. 115 (2014) 113505. doi:10.1063/1.4868628.

[75] R. Ivanov, Impact of carrier localization on recombination in InGaN quantum wells with nonbasal crystallographic orientations: Doctoral Dissertation, KTH Royal Institute of Technology, 2017. https://kth.diva-portal.org/smash/get/diva2:1142091/FULLTEXT02.pdf.

[76] K.P. O'donnell, R.W. Martin, P.G. Middleton, Origin of luminescence from ingan diodes, Phys. Rev. Lett. 82 (1999) 237–240. doi:10.1103/PhysRevLett.82.237.

[77] J.R. Jinschek, R. Erni, N.F. Gardner, A.Y. Kim, C. Kisielowski, Local indium segregation and bang gap variations in high efficiency green light emitting InGaN/GaN diodes, Solid State Commun. 137 (2006) 230–234. doi:10.1016/j.ssc.2005.10.030.

[78] T.M. Smeeton, C.J. Humphreys, J.S. Barnard, M.J. Kappers, The impact of electron beam damage on the detection of indium-rich localisation centres in InGaN quantum wells using transmission

electron microscopy, J. Mater. Sci. 41 (2006) 2729–2737. doi:10.1007/s10853-006-7876-x.
[79] T.M. Smeeton, M.J. Kappers, J.S. Barnard, M.E. Vickers, C.J. Humphreys, Electron-beam-induced strain within InGaN quantum wells: False indium "cluster" detection in the transmission electron microscope, Cit. Appl. Phys. Lett. 83 (2003) 2988. doi:10.1063/1.1636534.
[80] D.M. Graham, A. Soltani-Vala, P. Dawson, M.J. Godfrey, T.M. Smeeton, J.S. Barnard, M.J. Kappers, C.J. Humphreys, E.J. Thrush, Optical and microstructural studies of InGaNGaN single-quantum-well structures, J. Appl. Phys. 97 (2005) 103508. doi:10.1063/1.1897070.
[81] C.J. Humphreys, Does In form In-rich clusters in InGaN quantum wells?, Philos. Mag. 87 (2007) 1971–1982. doi:10.1080/14786430701342172.
[82] W.R. Zhao, G.E. Weng, J.Y. Wang, J.Y. Zhang, H.W. Liang, T. Sekiguchi, B.P. Zhang, Enhanced Light Emission due to Formation of Semi-polar InGaN/GaN Multi-quantum Wells, Nanoscale Res. Lett. 10 (2015) 459. doi:10.1186/s11671-015-1171-1.
[83] S.H. Han, D.Y. Lee, H.W. Shim, J. Wook Lee, D.J. Kim, S. Yoon, Y. Sun Kim, S.T. Kim, Improvement of efficiency and electrical properties using intentionally formed V-shaped pits in InGaN/GaN multiple quantum well light-emitting diodes, Appl. Phys. Lett. 102 (2013) 251123. doi:10.1063/1.4812810.
[84] P.A. Dróżdż, K.P. Korona, M. Sarzyński, S. Grzanka, R. Czernecki, T. Suski, Direct observation of long distance lateral transport in InGaN/GaN quantum wells, J. Appl. Phys. 125 (2019) 55702. doi:10.1063/1.5052312.
[85] R. a Oliver, S.E. Bennett, T. Zhu, D.J. Beesley, M.J. Kappers, D.W. Saxey, a Cerezo, C.J. Humphreys, Microstructural origins of localization in InGaN quantum wells, J. Phys. D. Appl. Phys. 43 (2010) 354003. doi:10.1088/0022-3727/43/35/354003.
[86] S. Schulz, M.A. Caro, C. Coughlan, E.P. O'Reilly, Atomistic analysis of the impact of alloy and well-width fluctuations on the electronic and optical properties of InGaN/GaN quantum wells, Phys. Rev. B - Condens. Matter Mater. Phys. 91 (2015) 1–12. doi:10.1103/PhysRevB.91.035439.
[87] D. Watson-Parris, M.J. Godfrey, R.A. Oliver, P. Dawson, M.J. Galtrey, M.J. Kappers, C.J. Humphreys, Energy landscape and carrier wave-functions in InGaN/GaN quantum wells, Phys. Status Solidi Curr. Top. Solid State Phys. 7 (2010) 2255–2258. doi:10.1002/pssc.200983516.
[88] S. Schulz, D.P. Tanner, E.P. O'Reilly, M.A. Caro, T.L. Martin, P.A.J.

Bagot, M.P. Moody, F. Tang, J.T. Griffiths, F. Oehler, M.J. Kappers, R.A. Oliver, C.J. Humphreys, D. Sutherland, M.J. Davies, P. Dawson, Structural, electronic, and optical properties of m -plane InGaN/GaN quantum wells: Insights from experiment and atomistic theory, Phys. Rev. B - Condens. Matter Mater. Phys. 92 (2015) 235419. doi:10.1103/PhysRevB.92.235419.

[89] P. Dawson, S. Schulz, R.A. Oliver, M.J. Kappers, C.J. Humphreys, The nature of carrier localisation in polar and nonpolar InGaN/GaN quantum wells, J. Appl. Phys. 119 (2016) 181505. doi:10.1063/1.4948237.

[90] D.S.P. Tanner, M.A. Caro, E.P. O'Reilly, S. Schulz, Random alloy fluctuations and structural inhomogeneities in c-plane InxGa1-xN quantum wells: Theory of ground and excited electron and hole states, RSC Adv. 6 (2016) 64513–64530. doi:10.1039/c6ra07540a.

[91] M.J. Galtrey, R.A. Oliver, M.J. Kappers, C.J. Humphreys, P.H. Clifton, D. Larson, D.W. Saxey, A. Cerezo, Three-dimensional atom probe analysis of green- and blue-emitting InxGa1-xNGaN multiple quantum well structures, J. Appl. Phys. 104 (2008). doi:10.1063/1.2938081.

[92] D. Watson-Parris, M.J. Godfrey, P. Dawson, R.A. Oliver, M.J. Galtrey, M.J. Kappers, C.J. Humphreys, Carrier localization mechanisms in InxGa1-xN/GaN quantum wells, Phys. Rev. B - Condens. Matter Mater. Phys. 83 (2011) 1–7. doi:10.1103/PhysRevB.83.115321.

[93] M. Auf Der Maur, A. Pecchia, G. Penazzi, W. Rodrigues, A. Di Carlo, Unraveling the "Green Gap" problem: The role of random alloy fluctuations in InGaN/GaN light emitting diodes, Phys. Rev. Lett. 116 (2015). doi:10.1103/PhysRevLett.116.027401.

[94] D. Holec, P.M.F.J. Costa, M.J. Kappers, C.J. Humphreys, Critical thickness calculations for InGaN/GaN, J. Cryst. Growth. 303 (2007) 314–317. doi:10.1016/j.jcrysgro.2006.12.054.

[95] T. Langer, A. Kruse, F.A. Ketzer, A. Schwiegel, L. Hoffmann, H. Jönen, H. Bremers, U. Rossow, A. Hangleiter, Origin of the "green gap": Increasing nonradiative recombination in indium-rich GaInN/GaN quantum well structures, Phys. Status Solidi Curr. Top. Solid State Phys. 8 (2011) 2170–2172. doi:10.1002/pssc.201001051.

[96] E. Kioupakis, Q. Yan, D. Steiauf, C.G. Van De Walle, Temperature and carrier-density dependence of Auger and radiative recombination in nitride optoelectronic devices, New J. Phys. 15 (2013) 125006. doi:10.1088/1367-2630/15/12/125006.

[97] S.Y. Karpov, Strategies for creating efficient, beautiful whites, Compd. Semicond. (2015). https://compoundsemiconductor.net/article/96572/Strategies_For_Cre

ating_Efficient_Beautiful_Whites.
[98] D. Schiavon, M. Binder, M. Peter, B. Galler, P. Drechsel, F. Scholz, Wavelength-dependent determination of the recombination rate coefficients in single-quantum-well GaInN/GaN light emitting diodes, Phys. Status Solidi Basic Res. 250 (2013) 283–290. doi:10.1002/pssb.201248286.
[99] I.A. Lamkin, S.A. Tarasov, A. V Solomonov, I.I. Mikhailov, Influence of the composition of the GaAsP solid solution on the Ag-GaAsP barrier height, in: J. Phys. Conf. Ser., 2016: p. 12037. doi:10.1088/1742-6596/690/1/012037.
[100] Y. Jiang, Y. Li, Y. Li, Z. Deng, T. Lu, Z. Ma, P. Zuo, L. Dai, L. Wang, H. Jia, W. Wang, J. Zhou, W. Liu, H. Chen, Realization of high-luminous-efficiency InGaN light-emitting diodes in the “green gap” range, Sci. Rep. 5 (2015) 1–7. doi:10.1038/srep10883.
[101] G. Franssen, T. Suski, P. Perlin, R. Bohdan, A. Bercha, W. Trzeciakowski, I. Makarowa, P. Prystawko, M. Leszczyński, I. Grzegory, S. Porowski, S. Kokenyesi, Fully-screened polarization-induced electric fields in blueviolet InGaNGaN light-emitting devices grown on bulk GaN, Appl. Phys. Lett. 87 (2005) 41109. doi:10.1063/1.2000331.
[102] J. Piprek, Efficiency droop in nitride-based light-emitting diodes, Phys. Status Solidi Appl. Mater. Sci. 207 (2010) 2217–2225. doi:10.1002/pssa.201026149.
[103] A. Dunn, B.F. Spencer, S.J.O. Hardman, D.M. Graham, S. Hammersley, M.J. Davies, P. Dawson, M.J. Kappers, R.A. Oliver, C.J. Humphreys, Investigating efficiency droop in InGaN/GaN quantum well structures using ultrafast time-resolved terahertz and photoluminescence spectroscopy, Phys. Status Solidi C. 13 (2016) 252–255. doi:10.1002/pssc.201510193.
[104] G. Verzellesi, D. Saguatti, M. Meneghini, F. Bertazzi, M. Goano, G. Meneghesso, E. Zanoni, Efficiency droop in InGaN/GaN blue light-emitting diodes: Physical mechanisms and remedies, J. Appl. Phys. 114 (2013). doi:10.1063/1.4816434.
[105] G. Tamulaitis, J. Mickevičius, D. Dobrovolskas, E. Kuokštis, M.S. Shur, M. Shatalov, J. Yang, R. Gaska, Carrier dynamics and efficiency droop in AlGaN epilayers with different Al content, Phys. Status Solidi Curr. Top. Solid State Phys. 9 (2012) 1677–1679. doi:10.1002/pssc.201100550.
[106] Y.C. Shen, G.O. Mueller, S. Watanabe, N.F. Gardner, A. Munkholm, M.R. Krames, Auger recombination in InGaN measured by photoluminescence, Appl. Phys. Lett. 91 (2007) 141101. doi:10.1063/1.2785135.
[107] J. Iveland, L. Martinelli, J. Peretti, J.S. Speck, C. Weisbuch, Direct

measurement of Auger electrons emitted from a semiconductor light-emitting diode under electrical injection: identification of the dominant mechanism for efficiency droop, Phys. Rev. Lett. 110 (2013) 1–5. doi:10.1103/PhysRevLett.110.177406.
[108] L. Martinelli, C. Weisbuch, J. Peretti, K. Gelžinytė, W.Y. Ho, J.S. Speck, D.J. Myers, J. Iveland, Identification of low-energy peaks in electron emission spectroscopy of InGaN/GaN light-emitting diodes, J. Appl. Phys. 124 (2018) 055703. doi:10.1063/1.5030208.
[109] E. Kioupakis, P. Rinke, K.T. Delaney, C.G. Van De Walle, Indirect Auger recombination as a cause of efficiency droop in nitride light-emitting diodes, Appl. Phys. Lett. 98 (2011) 16–18. doi:10.1063/1.3570656.
[110] K.T. Delaney, P. Rinke, C.G. Van de Walle, Auger recombination rates in nitrides from first principles, Appl. Phys. Lett. 94 (2009) 191109. doi:10.1063/1.3133359.
[111] F. Bertazzi, M. Goano, E. Bellotti, A numerical study of Auger recombination in bulk InGaN, Appl. Phys. Lett. 97 (2010) 231118. doi:10.1063/1.3525605.
[112] M. Shahmohammadi, W. Liu, G. Rossbach, L. Lahourcade, A. Dussaigne, C. Bougerol, R. Butté, N. Grandjean, B. Deveaud, G. Jacopin, Enhancement of Auger recombination induced by carrier localization in InGaN/GaN quantum wells, Phys. Rev. B. 95 (2017) 1–10. doi:10.1103/PhysRevB.95.125314.
[113] A.S. Polkovnikov, G.G. Zegrya, Auger recombination in semiconductor quantum wells, Phys. Rev. B - Condens. Matter Mater. Phys. 58 (1998) 4039–4056. doi:10.1103/PhysRevB.58.4039.
[114] F. Bertazzi, X. Zhou, M. Goano, G. Ghione, E. Bellotti, Auger recombination in InGaN/GaN quantum wells: A full-Brillouin-zone study, Appl. Phys. Lett. 103 (2013). doi:10.1063/1.4819129.
[115] C.K. Tan, W. Sun, J.J. Wierer, N. Tansu, Effect of interface roughness on Auger recombination in semiconductor quantum wells, AIP Adv. 7 (2017) 35212. doi:10.1063/1.4978777.
[116] E. Kioupakis, Q. Yan, C.G. Van De Walle, Interplay of polarization fields and Auger recombination in the efficiency droop of nitride light-emitting diodes, Appl. Phys. Lett. 101 (2012) 231107. doi:10.1063/1.4769374.
[117] H.Y. Ryu, G.H. Ryu, Y.H. Choi, B. Ma, Modeling and simulation of efficiency droop in GaN-based blue light-emitting diodes incorporating the effect of reduced active volume of InGaN quantum wells, Curr. Appl. Phys. 17 (2017) 1298–1302. doi:10.1016/j.cap.2017.06.014.
[118] M. Zhang, P. Bhattacharya, J. Singh, J. Hinckley, Direct measurement of auger recombination in In0.1Ga0.9N/GaN quantum wells and its

impact on the efficiency of In0.1Ga0.9N/GaN multiple quantum well light emitting diodes, Appl. Phys. Lett. 95 (2009) 201108. doi:10.1063/1.3266520.
[119] M. Meneghini, N. Trivellin, G. Meneghesso, E. Zanoni, U. Zehnder, B. Hahn, A combined electro-optical method for the determination of the recombination parameters in InGaN-based light-emitting diodes, J. Appl. Phys. 106 (2009) 114508. doi:10.1063/1.3266014.
[120] J. Hader, J. V. Moloney, S.W. Koch, Density-activated defect recombination as a possible explanation for the efficiency droop in GaN-based diodes, Appl. Phys. Lett. 96 (2010) 221106. doi:10.1063/1.3446889.
[121] R. Aleksiejūnas, P. Ščajev, S. Nargelas, T. Malinauskas, A. Kadys, K. Jarašiūnas, Impact of Diffusivity to Carrier Recombination Rate in Nitride Semiconductors: From Bulk GaN to (In,Ga)N Quantum Wells, Jpn. J. Appl. Phys. 52 (2013) 08JK01. doi:10.7567/JJAP.52.08JK01.
[122] R. Aleksiejūnas, K. Gelžinyte, S. Nargelas, K. Jarašiūnas, M. Vengris, E.A. Armour, D.P. Byrnes, R.A. Arif, S.M. Lee, G.D. Papasouliotis, Diffusion-driven and excitation-dependent recombination rate in blue InGaN/GaN quantum well structures, Appl. Phys. Lett. 104 (2014) 022114. doi:10.1063/1.4862026.
[123] Y. Yan Zhang, Y. An Yin, Performance enhancement of blue light-emitting diodes with a special designed AlGaN/GaN superlattice electron-blocking layer, Appl. Phys. Express. 99 (2011) 221103. doi:10.1063/1.3653390.
[124] S.-H. Han, D.-Y. Lee, S.-J.P. Lee, C.-Y. Cho, M.-K. Kwon, S.-J.P. Lee, D.Y. Noh, D.-J. Kim, Y.C. Kim, S.-J. Park, Effect of electron blocking layer on efficiency droop in InGaN/GaN multiple quantum well light-emitting diodes, Appl. Phys. Lett. 94 (2009) 231123. doi:10.1063/1.3153508.
[125] X. Ni, Q. Fan, R. Shimada, Ü. Özgür, H. Morkọ, Reduction of efficiency droop in InGaN light emitting diodes by coupled quantum wells, Appl. Phys. Lett. 93 (2008) 91–94. doi:10.1063/1.3012388.
[126] J. Xie, X. Ni, Q. Fan, R. Shimada, Ü. Özgür, H. Morkọ, On the efficiency droop in InGaN multiple quantum well blue light emitting diodes and its reduction with p-doped quantum well barriers, Appl. Phys. Lett. 93 (2008) 121107. doi:10.1063/1.2988324.
[127] X. Ni, X. Li, J. Lee, S. Liu, V. Avrutin, Ü. Özgür, H. Morkoç, A. Matulionis, T. Paskova, G. Mulholland, K.R. Evans, InGaN staircase electron injector for reduction of electron overflow in InGaN light emitting diodes, Appl. Phys. Lett. 97 (2010) 3–5. doi:10.1063/1.3465658.
[128] N.I. Bochkareva, V. V Voronenkov, R.I. Gorbunov, A.S. Zubrilov, Y.S. Lelikov, P.E. Latyshev, Y.T. Rebane, A.I. Tsyuk, Y.G. Shreter,

Defect-related tunneling mechanism of efficiency droop in III-nitride light-emitting diodes, Appl. Phys. Lett. 96 (2010) 71101. doi:10.1063/1.3367897.
[129] J. Piprek, S. Li, Electron leakage effects on GaN-based light-emitting diodes, Opt. Quantum Electron. 42 (2010) 89–95. doi:10.1007/s11082-011-9437-z.
[130] C.K. Li, Y.R. Wu, Study on the current spreading effect and light extraction enhancement of vertical GaN/InGaN LEDs, IEEE Trans. Electron Devices. 59 (2012) 400–407. doi:10.1109/TED.2011.2176132.
[131] T. Sadi, P. Kivisaari, J. Oksanen, J. Tulkki, On the correlation of the Auger generated hot electron emission and efficiency droop in III-N light-emitting diodes, Appl. Phys. Lett. 105 (2014) 71101. doi:10.1063/1.4894862.
[132] J. Mickevičius, J. Jurkevičius, M.S. Shur, J. Yang, R. Gaska, G. Tamulaitis, Photoluminescence efficiency droop and stimulated recombination in GaN epilayers, Opt. Express. 20 (2012) 25195. doi:10.1364/OE.20.025195.
[133] M. Rumi, J.W. Perry, Two-photon absorption: an overview of measurements and principles, Adv. Opt. Photonics. 2 (2010) 451. doi:10.1364/AOP.2.000451.
[134] R. Paschotta, Multiphoton absorption, RP Photonics Encycl. (2008). https://www.rp-photonics.com/multiphoton_absorption.html.
[135] S.H. Simon, The Oxford solid state basics (1st ed.), Oxford University Press, 2013.
[136] A. Avramescu, T. Lermer, J. Müller, C. Eichler, G. Bruederl, M. Sabathil, S. Lutgen, U. Strauss, True green laser diodes at 524 nm with 50 mW continuous wave output power on c-plane GaN, Appl. Phys. Express. 3 (2010) 5–8. doi:10.1143/APEX.3.061003.
[137] K. Jarašiūnas, R. Aleksiejūnas, T. Malinauskas, M. Sūdžius, S. Miasojedovas, S. Juršėnas, A. Žukauskas, R. Gaska, J. Zhang, M.S. Shur, J.W. Yang, E. Kuokštis, M.A. Khan, Carrier diffusion and recombination in highly excited InGaN/GaN heterostructures, Phys. Status Solidi Appl. Mater. Sci. 202 (2005) 820–823. doi:10.1002/pssa.200461351.
[138] W. Liu, D. Zhao, D. Jiang, D. Shi, J. Zhu, Z. Liu, P. Chen, J. Yang, F. Liang, S. Liu, Y. Xing, L. Zhang, W. Wang, M. Li, Y. Zhang, G. Du, Effect of carrier transfer process between two kinds of localized potential traps on the spectral properties of InGaN/GaN multiple quantum wells, Opt. Express. 26 (2018) 3427. doi:10.1364/OE.26.003427.
[139] D. Kovalev, B. Averboukh, D. Volm, B. Meyer, H. Amano, I. Akasaki, Free exciton emission in GaN, Phys. Rev. B - Condens. Matter Mater.

Phys. 54 (1996) 2518–2522. doi:10.1103/PhysRevB.54.2518.
[140] S.L. Chuang, Optical gain of strained wurtzite GaN quantum-well lasers, IEEE J. Quantum Electron. 32 (1996) 1791–1800. doi:10.1109/3.538786.
[141] M. Kuik, L.J.A. Koster, G.A.H. Wetzelaer, P.W.M. Blom, Trap-assisted recombination in disordered organic semiconductors, Phys. Rev. Lett. 107 (2011) 256805. doi:10.1103/PhysRevLett.107.256805.
[142] J. Hader, J. V. Moloney, S.W. Koch, Beyond the ABC: carrier recombination in semiconductor lasers, (2006) 61151T. doi:10.1117/12.641744.
[143] M.A. Green, Solar cells: operating principles, technology, and system applications, 1982. http://adsabs.harvard.edu/abs/1982ph...book.....G (accessed October 1, 2018).
[144] R. Aleksiejūnas, M. Sūdžius, T. Malinauskas, J. Vaitkus, K. Jarašiūnas, S. Sakai, Determination of free carrier bipolar diffusion coefficient and surface recombination velocity of undoped GaN epilayers, Appl. Phys. Lett. 83 (2003) 1157–1159. doi:10.1063/1.1599036.
[145] V.N. Abakumov, V.I. Perel, I.N. Yassievich, Nonradiative recombination in semiconductors, North-Holland, Amsterdam, 1991.
[146] A. Haug, Auger recombination in direct-gap semiconductors : band-structure effects, J. Phys. C Solid State Phys. 16 (1983) 4159–4172. doi:10.1088/0022-3719/16/21/017.
[147] A.D. Andreev, G.G. Zegrya, Auger recombination in strained quantum wells, Semiconductors. 3 (1997) 297–303. doi:10.1103/PhysRevB.58.4039.
[148] C.M. Jones, C.H. Teng, Q. Yan, P.C. Ku, E. Kioupakis, Impact of carrier localization on recombination in InGaN quantum wells and the efficiency of nitride light-emitting diodes: Insights from theory and numerical simulations, Appl. Phys. Lett. 111 (2017) 1–6. doi:10.1063/1.5002104.
[149] P.T. Landsberg, Trap-Auger recombination in silicon of low carrier densities, Appl. Phys. Lett. 50 (1987) 745–747. doi:10.1063/1.98086.
[150] S. Nargelas, Investigation of carrier dynamics in InN, InGaN, and GaAsBi by optical pump-probe techniques: Doctoral Dissertation, Vilnius University, 2013. https://elaba.lvb.lt/permalink/f/16nmo04/ELABAETD2042818.
[151] M. Ansari-Rad, J.A. Anta, J. Bisquert, Interpretation of diffusion and recombination in nanostructured and energy-disordered materials by stochastic quasiequilibrium simulation, J. Phys. Chem. C. 117 (2013) 16275–16289. doi:10.1021/jp403232b.
[152] Z.I. Alferov, The double heterostructure: concepts and its applications in physics, electronics and technology, Int. J. Mod. Phys. B. 16 (2002)

647–675. doi:10.1142/S0217979202010233.
[153] H. Kroemer, A Proposed Class of Hetero-junction Injection Lasers, Proc. IEEE. 51 (1963) 1782–1783. doi:10.1109/PROC.1963.2706.
[154] ALFEROV, Z. I., AlAs-GaAs heterojunction injection lasers with a low room-temperature threshold, Fiz, Tekh. Poluprov. 3 (1969) 1328–1332. https://ci.nii.ac.jp/naid/20001362117/ (accessed October 1, 2018).
[155] H. Morkoç, Handbook of Nitride Semiconductors and Devices Vol. 2: Electronic and Optical Processes in Nitrides, Wiley-VCH, 2008. doi:10.1002/9783527628414.
[156] A. Morel, P. Lefebvre, S. Kalliakos, T. Taliercio, T. Bretagnon, B. Gil, Donor-acceptor-like behavior of electron-hole pair recombinations in low-dimensional (Ga,In)N/GaN systems, Phys. Rev. B. 68 (2003) 1–6. doi:10.1103/PhysRevB.68.045331.
[157] D.A.B. Miller, Optical Physics of Quantum Wells, in: Quantum Dyn. Simple Syst. Proc. Forty Fourth Scottish Univ. Summer Sch. Physics, Stirling, August 1994, 1997: pp. 239–266. https://ee.stanford.edu/~dabm/181.pdf.
[158] S. Leyre, E. Coutino-Gonzalez, J.J. Joos, J. Ryckaert, Y. Meuret, D. Poelman, P.F. Smet, G. Durinck, J. Hofkens, G. Deconinck, P. Hanselaer, Absolute determination of photoluminescence quantum efficiency using an integrating sphere setup, Rev. Sci. Instrum. 85 (2014) 123115. doi:10.1063/1.4903852.
[159] Guide to streak cameras, HAMAMATSU PHOTONICS K.K. (2008) 12. https://www.hamamatsu.com/resources/pdf/sys/SHSS0006E_STREAK.pdf.
[160] J.C. Dainty, H.J. Eichler, P. Günter, D.W. Pohl, Laser-Induced Dynamic Gratings, Springer-Verlag, 1986. doi:10.1007/978-3-540-39662-8.
[161] T. Malinauskas, S. Nargelas, R. Aleksiejūnas, K. Jarašiūnas, Heterodyne detection scheme for light-induced transient grating experiment, Opt. Commun. 281 (2008) 6061–6064. doi:10.1016/j.optcom.2008.09.007.
[162] K. Jarašiūnas, Šiuolaikinių puslaidininkinių darinių optinė diagnostika, Progretus, Vilnius, 2008.
[163] Application Note – The Raman Spectrum of Water, (2019). https://www.stellarnet.us/application-note-raman-spectrum-water/.
[164] R.A. Oliver, F.C.P. Massabuau, M.J. Kappers, W.A. Phillips, E.J. Thrush, C.C. Tartan, W.E. Blenkhorn, T.J. Badcock, P. Dawson, M.A. Hopkins, D.W.E. Allsopp, C.J. Humphreys, The impact of gross well width fluctuations on the efficiency of GaN-based light emitting diodes, Appl. Phys. Lett. 103 (2013) 7–11. doi:10.1063/1.4824193.

[165] I. Reklaitis, R. Kudžma, S. Miasojedovas, P. Vitta, A. Žukauskas, R. Tomašiūnas, I. Pietzonka, M. Strassburg, Photoluminescence Decay Dynamics in Blue and Green InGaN LED Structures Revealed by the Frequency-Domain Technique, J. Electron. Mater. 45 (2016) 3290–3299. doi:10.1007/s11664-016-4557-7.
[166] X. Li, S. Okur, F. Zhang, S.A. Hafiz, V. Avrutin, Ü. Özgür, H. Morkoc, K. Jarašiūnas, Improved quantum efficiency in InGaN light emitting diodes with multi-double-heterostructure active regions, Appl. Phys. Lett. 101 (2012) 041115. doi:10.1063/1.4739419.
[167] S. Yao, T. Lan, G. Zhou, Y. Li, L. Lang, H. Yu, Z. Lv, Z. Wang, Effect of strain modification on crystallinity and luminescence of InGaN/GaN multiple quantum wells grown by MOCVD, Appl. Phys. A. 124 (2018) 619. doi:10.1007/s00339-018-1958-x.
[168] E. Matioli, C. Weisbuch, Active Region Part A. Internal Quantum Efficiency in LEDs, in: T.-Y. Seong, H. Jung, A. Hiroshi, M. Hadis (Eds.), III-Nitride Based Light Emit. Diodes Appl., Springer, 2013: pp. 121–153. doi:10.1007/978-94-007-5863-6_7.
[169] Y.-H. Kwon, S.K. Shee, G.H. Gainer, G.H. Park, S.J. Hwang, J.J. Song, Time-resolved study of yellow and blue luminescence in Si- and Mg-doped GaN, Appl. Phys. Lett. 76 (2000) 840. doi:10.1063/1.125602.
[170] D. Brunner, H. Angerer, E. Bustarret, F. Freudenberg, R. Höpler, R. Dimitrov, O. Ambacher, M. Stutzmann, Optical constants of epitaxial AlGaN films and their temperature dependence, J. Appl. Phys. 82 (1997) 5090–5096. doi:10.1063/1.366309.
[171] S.D. Hersee, J. Ramer, K. Zheng, C. Kranenberg, K. Malloy, M. Banas, M. Goorsky, The role of the low temperature buffer layer and layer thickness in the optimization of OMVPE growth of GaN on sapphire, 24 (1995) 1519–1523. doi:10.1007/BF02676804.
[172] A. Knigge, M. Brendel, F. Brunner, S. Einfeldt, A. Knauer, V. Kueller, M. Weyers, AlGaN photodetectors for the UV-C spectral region on planar and epitaxial laterally overgrown AlN/sapphire templates, Phys. Status Solidi. 10 (2013) 294–297. doi:10.1002/pssc.201200636.
[173] A. Sakai, H. Sunakawa, A. Usui, Defect structure in selectively grown GaN films with low threading dislocation density, Appl. Phys. Lett. 71 (1997) 2259–2261. doi:10.1063/1.120044.
[174] S.J. Leem, Y.C. Shin, K.C. Kim, E.H. Kim, Y.M. Sung, Y. Moon, S.M. Hwang, T.G. Kim, The effect of the low-mole InGaN structure and InGaN/GaN strained layer superlattices on optical performance of multiple quantum well active layers, J. Cryst. Growth. 311 (2008) 103–106. doi:10.1016/j.jcrysgro.2008.10.047.
[175] S.P. Chang, C.H. Wang, C.H. Chiu, J.C. Li, Y.S. Lu, Z.Y. Li, H.C. Yang, H.C. Kuo, T.C. Lu, S.C. Wang, Characteristics of efficiency

droop in GaN-based light emitting diodes with an insertion layer between the multiple quantum wells and n-GaN layer, Appl. Phys. Lett. 97 (2010) 251114. doi:10.1063/1.3531957.
[176] W.V. Lundin, A.E. Nikolaev, A.V. Sakharov, E.E. Zavarin, G.A. Valkovskiy, M.A. Yagovkina, S.O. Usov, N.V. Kryzhanovskaya, V.S. Sizov, P.N. Brunkov, A.L. Zakgeim, A.E. Cherniakov, N.A. Cherkashin, M.J. Hytch, E.V. Yakovlev, D.S. Bazarevskiy, M.M. Rozhavskaya, A.F. Tsatsulnikov, Single quantum well deep-green LEDs with buried InGaN/GaN short-period superlattice, J. Cryst. Growth. 315 (2011) 267–271. doi:10.1016/J.JCRYSGRO.2010.09.043.
[177] S. Valdueza-Felip, E. Bellet-Amalric, A. Núñez-Cascajero, Y. Wang, M.-P. Chauvat, P. Ruterana, S. Pouget, K. Lorenz, E. Alves, E. Monroy, High In-content InGaN layers synthesized by plasma-assisted molecular-beam epitaxy: Growth conditions, strain relaxation, and In incorporation kinetics, J. Appl. Phys. 116 (2014) 233504. doi:10.1063/1.4903944.
[178] S.H. Park, T.H. Chung, J.H. Baek, D. Ahn, Reduction of efficiency droop in green strain-compensated InGaN/InGaN light-emitting diodes grown on InGaN substrate, Jpn. J. Appl. Phys. 54 (2015) 022101. doi:10.7567/JJAP.54.022101.
[179] Y.L. Li, Y.R. Huang, Y.H. Lai, Efficiency droop behaviors of InGaN/GaN multiple-quantum-well light-emitting diodes with varying quantum well thickness, Appl. Phys. Lett. 91 (2007) 181113. doi:10.1063/1.2805197.
[180] G. Sun, G. Xu, Y.J. Ding, H. Zhao, G. Liu, J. Zhang, N. Tansu, Investigation of fast and slow decays in InGaN/GaN quantum wells, Appl. Phys. Lett. 99 (2011) 10–13. doi:10.1063/1.3627166.
[181] N.I. Bochkareva, Y.T. Rebane, Y.G. Shreter, Efficiency droop and incomplete carrier localization in InGaN/GaN quantum well light-emitting diodes, Appl. Phys. Lett. 103 (2013) 191101. doi:10.1063/1.4828780.
[182] M.J. Davies, T.J. Badcock, P. Dawson, M.J. Kappers, R.A. Oliver, C.J. Humphreys, High excitation carrier density recombination dynamics of InGaN/GaN quantum well structures: Possible relevance to efficiency droop, Appl. Phys. Lett. 102 (2013) 022106. doi:10.1063/1.4781398.
[183] T. Malinauskas, A. Kadys, T. Grinys, S. Nargelas, R. Aleksiejūnas, S. Miasojedovas, J. Mickevičius, R. Tomašiūnas, K. Jarašiūnas, M. Vengris, S. Okur, V. Avrutin, X. Li, F. Zhang, Ü. Özgür, H. Morkoç, Impact of carrier localization, recombination, and diffusivity on excited state dynamics in InGaN/GaN quantum wells, in: Proc. Vol. 8262, Gall. Nitride Mater. Devices VII, International Society for

Optics and Photonics, 2012: p. 82621S. doi:10.1117/12.906488.
[184] A. David, M.J. Grundmann, Droop in InGaN light-emitting diodes: A differential carrier lifetime analysis, Appl. Phys. Lett. 96 (2010) 1–4. doi:10.1063/1.3330870.
[185] S. Jong-In, K. Hyungsung, S. Dong-Soo, Y. Han-Youl, An Explanation of Efficiency Droop in InGaN-based Light Emitting Diodes: Saturated Radiative Recombination Rate at Randomly Distributed In-Rich Active Areas, J. Korean Phys. Soc. 58 (2011) 503. doi:10.3938/jkps.58.503.
[186] F. Nippert, S.Y. Karpov, G. Callsen, B. Galler, T. Kure, C. Nenstiel, M.R. Wagner, M. Straßburg, H.J. Lugauer, A. Hoffmann, Temperature-dependent recombination coefficients in InGaN light-emitting diodes: Hole localization, Auger processes, and the green gap, Appl. Phys. Lett. 109 (2016) 161103. doi:10.1063/1.4965298.
[187] S.Y. Karpov, Effect of localized states on internal quantum efficiency of III-nitride LEDs, Phys. Status Solidi - Rapid Res. Lett. 4 (2010) 320–322. doi:10.1002/pssr.201004325.
[188] G. Pozina, R. Ciechonski, Z. Bi, L. Samuelson, B. Monemar, Dislocation related droop in InGaN/GaN light emitting diodes investigated via cathodoluminescence, Appl. Phys. Lett. 107 (2015) 251106. doi:10.1063/1.4938208.
[189] A. Vertikov, I. Ozden, A. V Nurmikko, Diffusion and relaxation of excess carriers in InGaN quantum wells in localized versus extended states, J. Appl. Phys. 86 (1999) 4697–4699. doi:10.1063/1.371423.
[190] S. Marcinkevičius, K. Gelžinytė, Y. Zhao, S. Nakamura, S.P. DenBaars, J.S. Speck, Carrier redistribution between different potential sites in semipolar ($20\bar{2}1$) InGaN quantum wells studied by near-field photoluminescence, Appl. Phys. Lett. 105 (2014) 111108. doi:10.1063/1.4896034.
[191] H.M. Solowan, J. Danhof, U.T. Schwarz, Direct observation of charge carrier diffusion and localization in an InGaN multi quantum well, Jpn. J. Appl. Phys. 52 (2013) 4–9. doi:10.7567/JJAP.52.08JK07.
[192] S.-W. Feng, Y.-C. Cheng, Y.-Y. Chung, C.C. Yang, Y.-S. Lin, C. Hsu, K.-J. Ma, J.-I. Chyi, Impact of localized states on the recombination dynamics in InGaN/GaN quantum well structures, J. Appl. Phys. 92 (2002) 4441. doi:10.1063/1.1506393.
[193] H. Jeong, H.J. Jeong, H.M. Oh, C.H. Hong, E.K. Suh, G. Lerondel, M.S. Jeong, Carrier localization in In-rich InGaN/GaN multiple quantum wells for green light-emitting diodes, Sci. Rep. 5 (2015) 9373. doi:10.1038/srep09373.
[194] F. Chen, M.C. Cheung, P.M. Sweeney, W.D. Kirkey, M. Furis, A.N. Cartwright, Ultrafast differential transmission spectroscopy of excitonic transitions in InGaN/GaN multiple quantum wells, J. Appl.

Phys. 93 (2003) 4933–4935. doi:10.1063/1.1559432.
[195] R.W. Martin, P.G. Middleton, K.P.O. Donnell, W. Van Der Stricht, Exciton localization and the Stokes' shift in InGaN epilayers, Appl. Phys. Lett. 74 (1999) 263. doi:10.1063/1.123275.
[196] M.J. Davies, T.J. Badcock, P. Dawson, R.A. Oliver, M.J. Kappers, C.J. Humphreys, High excitation density recombination dynamics in InGaN/GaN quantum well structures in the droop regime, Phys. Status Solidi Curr. Top. Solid State Phys. 11 (2014) 694–697. doi:10.1002/pssc.201300498.
[197] E. Kuokštis, J.W. Yang, G. Simin, M.A. Khan, R. Gaska, M.S. Shur, Two mechanisms of blueshift of edge emission in InGaN-based epilayers and multiple quantum wells, Appl. Phys. Lett. 80 (2002) 977–979. doi:10.1063/1.1433164.
[198] K. Jarašiūnas, S. Nargelas, R. Aleksiejūnas, S. Miasojedovas, M. Vengris, S. Okur, H. Morkoç, Ü. Özgür, C. Giesen, Ö. Tuna, M. Heuken, Spectral distribution of excitation-dependent recombination rate in an In0.13Ga0.87N epilayer, J. Appl. Phys. 113 (2013) 0–9. doi:10.1063/1.4793637.
[199] B.R. Bennett, R.A. Soref, J.A. Del Alamo, Carrier-induced change in refractive index of InP, GaAs and InGaAsP, IEEE J. Quantum Electron. 26 (1990) 113–122. doi:10.1109/3.44924.
[200] Y. Cho, G.H. Gainer, a J. Fischer, J.J. Song, S. Keller, U.K. Mishra, S.P. DenBaars, "S-shaped" temperature-dependent emission shift and carrier dynamics in InGaN/GaN multiple quantum wells, Appl. Phys. Lett. 73 (1998) 1370–1372. doi:10.1063/1.122164.
[201] Q. Li, S.J. Xu, M.H. Xie, S.Y. Tong, Origin of the 'S-shaped' temperature dependence of luminescent peaks from semiconductors, J. Phys. Condens. Matter. 17 (2005) 4853–4858. doi:10.1088/0953-8984/17/30/011.
[202] S.F. Chichibu, T. Azuhata, T. Sota, T. Mukai, S. Nakamura, Localized quantum well excitons in InGaN single-quantum-well amber light-emitting diodes, J. Appl. Phys. 88 (2000) 5153. doi:10.1063/1.1314906.
[203] R. Aleksiejūnas, M. Sūdžius, V. Gudelis, T. Malinauskas, K. Jarašiūnas, Q. Fareed, R. Gaska, M.S. Shur, J. Zhang, J. Yang, E. Kuokštis, M.A. Khan, Carrier transport and recombination in InGaN/GaN heterostructures, studied by optical four-wave mixing technique, Phys. Status Solidi C Conf. 2690 (2003) 2686–2690. doi:10.1002/pssc.200303261.
[204] M. Binder, A. Nirschl, R. Zeisel, T. Hager, H.J. Lugauer, M. Sabathil, D. Bougeard, J. Wagner, B. Galler, Identification of nnp and npp Auger recombination as significant contributor to the efficiency droop in (GaIn)N quantum wells by visualization of hot carriers in

photoluminescence, Appl. Phys. Lett. 103 (2013). doi:10.1063/1.4818761.
[205] Y. Lin, Y. Zhang, Z. Liu, L. Su, J. Zhang, T. Wei, Z. Chen, Spatially resolved study of quantum efficiency droop in InGaN light-emitting diodes, Appl. Phys. Lett. 101 (2012). doi:10.1063/1.4772549.
[206] C.H. Wang, S.P. Chang, W.T. Chang, J.C. Li, Y.S. Lu, Z.Y. Li, H.C. Yang, H.C. Kuo, T.C. Lu, S.C. Wang, Efficiency droop alleviation in InGaN/GaN light-emitting diodes by graded-thickness multiple quantum wells, Appl. Phys. Lett. 97 (2010) 181101. doi:10.1063/1.3507891.
[207] T. Malinauskas, S. Miasojedovas, R. Aleksiejūnas, S. Juršėnas, K. Jarašiūnas, M. Nomura, Y. Arakawa, T. Shimura, K. Kuroda, Direct study of nonlinear carrier recombination in InGaN quantum well structures, Phys. Status Solidi. 8 (2011) 2381–2383. doi:10.1002/pssc.201000997.
[208] P. Ščajev, C. Qin, R. Aleksiejūnas, P. Baronas, S. Miasojedovas, T. Fujihara, T. Matsushima, C. Adachi, S. Juršėnas, Diffusion Enhancement in Highly Excited MAPbI 3 Perovskite Layers with Additives, J. Phys. Chem. Lett. 9 (2018) 3167–3172. doi:10.1021/acs.jpclett.8b01155.
[209] Ü. Özgür, H. Liu, X. Li, X. Ni, H. Morkoç, GaN-based light-emitting diodes: Efficiency at high injection levels, Proc. IEEE. 98 (2010) 1180–1196. doi:10.1109/JPROC.2010.2043210.
[210] C.H. Wang, S.P. Chang, P.H. Ku, J.C. Li, Y.P. Lan, Hole transport improvement in InGaN/GaN light-emitting diodes by graded-composition multiple quantum barriers, Appl. Phys. Lett. 99 (2011) 171106. doi:https://doi.org/10.1063/1.3655903.
[211] D. Zanato, S. Gokden, N. Balkan, B.K. Ridley, W.J. Schaff, The effect of interface-roughness and dislocation scattering on low temperature mobility of 2D electron gas in GaN/AlGaN, Semicond. Sci. Technol. 19 (2004) 427–432. doi:10.1088/0268-1242/19/3/024.
[212] J. Bai, T. Wang, S. Sakai, Influence of the quantum-well thickness on the radiative recombination of InGaN/GaN quantum well structures, J. Appl. Phys. 88 (2000) 4729. doi:10.1063/1.1311831.
[213] R. Aleksiejūnas, M. Sūdžius, T. Malinauskas, J. Vaitkus, K. Jarašiūnas, S. Sakai, Determination of free carrier bipolar diffusion coefficient and surface recombination velocity of undoped GaN epilayers, Appl. Phys. Lett. 83 (2003) 1157–1159. doi:10.1063/1.1599036.
[214] T.J. Yang, R. Shivaraman, J.S. Speck, Y.R. Wu, The influence of random indium alloy fluctuations in indium gallium nitride quantum wells on the device behavior, J. Appl. Phys. 116 (2014). doi:10.1063/1.4896103.

[215] J. Mickevičius, J. Jurkevičius, A. Kadys, G. Tamulaitis, M. Shur, M. Shatalov, J. Yang, R. Gaska, Temperature-dependent efficiency droop in AlGaN epitaxial layers and quantum wells, AIP Adv. 6 (2016) 045212. doi:10.1063/1.4947574.
[216] K. Zhao, X. Yang, B. Xu, D. Li, C. Wang, L. Feng, Well Thickness Dependence of the Internal Quantum Efficiency and Carrier Concentration in GaN-Based Multiple Quantum Well Light-Emitting Diodes, J. Electron. Mater. (2015) 1–5. doi:10.1007/s11664-015-4203-9.
[217] T. Sugahara, H. Sato, M. Hao, Y. Naoi, S. Kurai, S. Tottori, K. Yamashita, K. Nishino, L.T. Romano, S. Sakai, Direct Evidence that Dislocations are Non-Radiative Recombination Centers in GaN, Jpn. J. Appl. Phys. 37 (1998) L398–L400. doi:10.1143/JJAP.37.L398.
[218] S. Hammersley, D. Watson-Parris, P. Dawson, M.J. Godfrey, T.J. Badcock, M.J. Kappers, C. McAleese, R.A. Oliver, C.J. Humphreys, The consequences of high injected carrier densities on carrier localization and efficiency droop in InGaN/GaN quantum well structures, J. Appl. Phys. 111 (2012). doi:10.1063/1.3703062.
[219] H.P.D. Schenk, M. Leroux, P. de Mierry, Luminescence and absorption in InGaN epitaxial layers and the van Roosbroeck–Shockley relation, J. Appl. Phys. 88 (2000) 1525. doi:10.1063/1.373850.
[220] J. Kvietkova, L. Siozade, P. Disseix, a. Vasson, J. Leymarie, B. Damilano, N. Grandjean, J. Massies, Optical Investigations and Absorption Coefficient Determination of InGaN/GaN Quantum Wells, Phys. Status Solidi. 190 (2002) 135–140. doi:10.1002/1521-396X(200203)190:1<135::AID-PSSA135>3.0.CO;2-1.
[221] E. Matioli, C. Weisbuch, Active Region Part A. Internal Quantum Efficiency in LEDs, in: T.-Y. Seong, J. Han, H. Amano, H. Morkoç (Eds.), III-Nitride Based Light Emit. Diodes Appl., Springer, Dordrecht, 2013: p. 390. doi:10.1007/978-981-10-3755-9.
[222] K. Gelžinytė, Study of excess carrier dynamics in nonpolar InGaN/GaN quantum wells: Master's Thesis, Vilnius University, 2015.
[223] S. Srinivasan, F. Bertram, A. Bell, F.A. Ponce, S. Tanaka, H. Omiya, Y. Nakagawa, Low Stokes shift in thick and homogeneous InGaN epilayers, Appl. Phys. Lett. 80 (2002) 550–552. doi:10.1063/1.1436531.
[224] S.F. Chichibu, A.C. Abare, M.S. Minsky, S. Keller, S.B. Fleischer, Effective band gap inhomogeneity and piezoelectric field in InGaN / GaN multiquantum well structures, Appl. Phys. Lett. 73 (1998) 1–4. doi:10.1063/1.122350.
[225] D.K. Im, Y.M. Oon, K.S. Ong, S.P. Ark, T. Gan, Effect of Barrier

Thickness on the Interface and Optical Properties of InGaN / GaN Multiple Quantum Wells, Appl. Phys. 40 (2001) 3085–3088.
[226] Y. Zhang, R.M. Smith, Y. Hou, B. Xu, Y. Gong, J. Bai, T. Wang, Stokes shift in semi-polar (112¯2) InGaN/GaN multiple quantum wells, Appl. Phys. Lett. 108 (2016) 031108. doi:10.1063/1.4940396.
[227] M. Dmukauskas, A. Kadys, T. Malinauskas, T. Grinys, I. Reklaitis, K. Badokas, M. Skapas, R. Tomašiūnas, D. Dobrovolskas, S. Stanionytė, I. Pietzonka, M. Strassburg, H.J. Lugauer, Influence of metalorganic precursors flow interruption timing on green InGaN multiple quantum wells, J. Phys. D. Appl. Phys. 49 (2016) 505107. doi:10.1088/0022-3727/49/50/505101.
[228] O. Tuna, H. Behmenburg, C. Giesen, H. Kalisch, R.H. Jansen, G.P. Yablonskii, M. Heuken, Dependence of InN properties on MOCVD growth parameters, Phys. Status Solidi Curr. Top. Solid State Phys. 8 (2011) 2044–2046. doi:10.1002/pssc.201001004.
[229] J. Piprek, F. Römer, B. Witzigmann, On the uncertainty of the Auger recombination coefficient extracted from InGaN/GaN light-emitting diode efficiency droop measurements, Appl. Phys. Lett. 106 (2015). doi:10.1063/1.4914833.
[230] S. Karpov, ABC-model for interpretation of internal quantum efficiency and its droop in III-nitride LEDs: a review, Opt. Quantum Electron. 47 (2015) 1293–1303. doi:10.1007/s11082-014-0042-9.
[231] T.H. Gfroerer, Y. Zhang, M.W. Wanlass, A comparison of photoluminescence imaging and confocal photoluminescence microscopy in the study of diffusion near isolated extended defects in GaAs, in: 2012 38th IEEE Photovolt. Spec. Conf., IEEE, 2012: pp. 001624–001626. doi:10.1109/PVSC.2012.6317907.
[232] J. Danhof, U.T. Schwarz, A. Kaneta, Y. Kawakami, Time-of-flight measurements of charge carrier diffusion in InxGa1-xN/GaN quantum wells, Phys. Rev. B - Condens. Matter Mater. Phys. 84 (2011) 035324. doi:10.1103/PhysRevB.84.035324.
[233] D. Dargis, Carrier dynamics in InGaN quantum wells with gross well width fluctuations: Master's Thesis, Vilnius University, 2016.
[234] M.J. Wallace, P.R. Edwards, M.J. Kappers, M.A. Hopkins, F. Oehler, S. Sivaraya, R.A. Oliver, C.J. Humphreys, D.W.E. Allsopp, R.W. Martin, Effect of the barrier growth mode on the luminescence and conductivity micron scale uniformity of InGaN light emitting diodes, J. Appl. Phys. 117 (2015). doi:10.1063/1.4915628.
[235] I.E. Titkov, S.Y. Karpov, A. Yadav, V.L. Zerova, M. Zulonas, B. Galler, M. Strassburg, I. Pietzonka, H.J. Lugauer, E.U. Rafailov, Temperature-Dependent internal quantum efficiency of blue high-brightness light-emitting diodes, IEEE J. Quantum Electron. 50 (2014) 911–920. doi:10.1109/JQE.2014.2359958.

[236] J. Mickevičius, Ž. Podlipskas, R. Aleksiejūnas, A. Kadys, J. Jurkevičius, G. Tamulaitis, M.S. Shur, M. Shatalov, J. Yang, R. Gaska, Podlipskas, R. Aleksiejūnas, A. Kadys, J. Jurkevičius, G. Tamulaitis, M.S. Shur, M. Shatalov, J. Yang, R. Gaska, Nonradiative Recombination, Carrier Localization, and Emission Efficiency of AlGaN Epilayers with Different Al Content, J. Electron. Mater. 44 (2015) 4706–4709. doi:10.1007/s11664-015-4132-7.

[237] Ž. Podlipskas, J. Jurkevičius, A. Kadys, M. Kolenda, V. Kovalevskij, D. Dobrovolskas, R. Aleksiejūnas, G. Tamulaitis, Extreme radiation resistance in InN, J. Alloys Compd. 789 (2019) 48–55. doi:10.1016/j.jallcom.2019.03.108.

CURRICULUM VITAE

Vardas, pavardė	Kazimieras Nomeika
Gimimo data	1989/05/23
El. paštas	kazimieras.nomeika@ff.vu.lt

Išsilavinimas

Nuo 2008 iki 2012	Fizikos bakalauras, Fizikos fakultetas, Vilniaus universitetas
Nuo 2012 iki 2014	Medžiagų technologijų magistras, Fizikos fakultetas, Vilniaus universitetas
Nuo 2014 iki 2018	Medžiagų inžinerijos doktorantūros studijos, Fizikos fakultetas, Vilniaus universitetas

Darbo patirtis

Nuo 2015	Jaunesnysis mokslo darbuotojas, Fotonikos ir nanotechnologijų institutas, Vilniaus universitetas
Nuo 2014 iki 2016	Inžinierius, Fotonikos ir nanotechnologijų institutas, Vilniaus universitetas

Dalyvavimas moksliniuose projektuose

Nuo 2011 iki 2012	SMT-021/SMT11R-081
2015	SVE-02/2012
Nuo 2016 iki 2018	LAT-05/2016
2017	CERN-VU-2016-1
2018	P-LLT-18-6
Nuo 2017	S-MIP-17-75
Nuo 2018	LMT-K-712-01-0013
Nuo 2018	LMT-L-718-01-0041
Nuo 2018	CPVA-K-703-02-0002

Apdovanojimai Geriausias stendinis pranešimas (konferencija Open Readings 2014)

LIST OF PUBLICATIONS AND THEIR COPIES / PUBLIKACIJŲ SĄRAŠAS IR JŲ KOPIJOS

P1. A. Kadys, T. Malinauskas, M. Dmukauskas, I. Reklaitis, **K. Nomeika**, V. Gudelis, R. Aleksiejūnas, P. Ščajev, S. Nargelas, S. Miasojedovas, K. Jarašiūnas, Photoluminescence features and carrier dynamics in InGaN heterostructures with wide staircase interlayers and differently shaped quantum wells, Lith. J. Phys. 54 (2014) 187–198.

P2. R. Aleksiejūnas, **K. Nomeika**, S. Miasojedovas, S. Nargelas, T. Malinauskas, K. Jarašiūnas, Ö. Tuna, M. Heuken, Carrier dynamics in blue and green emitting InGaN MQWs, Phys. Status Solidi. 252 (2015) 977–982.

P3. **K. Nomeika**, M. Dmukauskas, R. Aleksiejūnas, P. Ščajev, S. Miasojedovas, A. Kadys, S. Nargelas, K. Jarašiūnas, Enhancement of quantum efficiency in InGaN quantum wells by using superlattice interlayers and pulsed growth, Lith. J. Phys. 55 (2016) 255–263.

P4. J. Mickevičius, D. Dobrovolskas, R. Aleksiejūnas, **K. Nomeika**, T. Grinys, A. Kadys, G. Tamulaitis, Influence of growth temperature on carrier localization in InGaN/GaN MQWs with strongly redshifted emission band, J. Cryst. Growth. 459 (2017) 173–177.

P5. **K. Nomeika**, R. Aleksiejūnas, S. Miasojedovas, R. Tomašiūnas, K. Jarašiūnas, I. Pietzonka, M. Strassburg, H.-J. Lugauer, Impact of carrier localization and diffusion on photoluminescence in highly excited cyan and green InGaN LED structures, J. Lumin. 188 (2017) 301–306.

1st publication / 1 publikacija

Photoluminescence features and carrier dynamics in InGaN heterostructures with wide staircase interlayers and differently shaped quantum wells

A. Kadys, T. Malinauskas, M. Dmukauskas, I. Reklaitis, **K. Nomeika**, V. Gudelis, R. Aleksiejūnas, P. Ščajev, S. Nargelas, S. Miasojedovas, K. Jarašiūnas

Lithuanian Journal of Physics **54** (2014) 187–198
DOI:10.3952/physics.v54i3.2959

Lithuanian Journal of Physics, Vol. **54**, No. 3, pp. 187–198 (2014)

PHOTOLUMINESCENCE FEATURES AND CARRIER DYNAMICS IN InGaN HETEROSTRUCTURES WITH WIDE STAIRCASE INTERLAYERS AND DIFFERENTLY SHAPED QUANTUM WELLS

A. Kadys, T. Malinauskas, M. Dmukauskas, I. Reklaitis, K. Nomeika, V. Gudelis,

R. Aleksiejūnas, P. Ščajev, S. Nargelas, S. Miasojedovas, and K. Jarašiūnas

Institute of Applied Research, Vilnius University, Saulėtekio 9-III, LT-10222 Vilnius, Lithuania
E-mail: kestutis.jarasiunas@ff.vu.lt

Received 22 April 2014; revised 15 June 2014; accepted 23 September 2014

We present a comprehensive study of photoexcited carrier dynamics in differently grown InGaN/InGaN multiple quantum well (MQW) structures, modified by insertion of a wide interlayer structure and subsequent growth of differently shaped quantum wells (rectangular, triangular, trapezoidal). This approach of strain management allowed the reduction of dislocation density due to gradually increasing In content in the interlayer and shaping the smooth quantum well/barrier interfaces. A set of c-oriented MQW structures emitting at 470 nm were grown at Vilnius University, Institute of Applied Research, using a closed coupled showerhead type MOCVD reactor. Photoluminescence (PL) spectra of MQW structures were analysed combining continuous wave and pulsed PL measurements. Reactive ion etching of the structures enabled discrimination of PL signals originated in the InGaN interlayer structure, underlying quantum wells, and quantum barriers, thus providing growth-related conditions for enhanced carrier localization in the wells. Time-resolved PL and differential transmission kinetics provided carrier lifetimes and their spectral distribution, being the longest in triangular-shape QWs which exhibited the highest PL intensity. The light-induced transient grating (LITG) technique was used to determine the spatially averaged carrier lifetime in the entire heterostructure, in this way unravelling the electronic quality of the LED internal structure at conditions similar to device performance. LITG decay rates at low and high excitation energy densities revealed increasing with photoexcitation nonradiative recombination rate in the triangular and trapezoidal wells.

Keywords: light emitting diodes, nitride semiconductors, photoluminescence, carrier recombination

PACS: 73.21.Fg; 78.67.-n; 78.47.-p

1. Introduction

Despite extensive research efforts for a decade, the physical origin of the dominant mechanism of emission efficiency droop in InGaN light emitting diodes (LEDs) has not been clarified. Physical mechanisms which may lead to droop at high injection levels are reviewed and classified [1–3]. They discriminate internal mechanisms of nonradiative losses in the active region of a LED and those caused by the carrier leakage. The former case deals with a problem why all carriers injected into the active region are not consumed by radiative recombination and what are the nonradiative recombination pathways that contribute at high injections (e. g. Auger recombination in the InGaN wells was invoked [3, 4]). It was also suggested that additional nonradiative losses may appear at high injections due to carrier delocalization from the states within the potential minima where they recombine radiatively at low injections. The delocalized carriers are mobile and can occupy the extended states as well as diffuse to the defect sites and recombine nonradiatvely (a hypothesis of defect-activated nonradiative recombination was proposed by Hader [5] and verified experimentally in violet and blue LEDs [6, 7]). Saturation of a radiative recombination rate cannot be excluded as well [8].

Other processes deal with nonradiative losses outside the active region, and they may have a number of forms leading to enhanced droop. The electron leakage in a biased device can be promoted by the carrier spillover above the barriers, while experimental data have shown that the effect is not large enough to singlehandedly explain the efficiency droop [9]. Besides that, electron overshooting has been suggested as the dominant mechanism [2, 10]. Here, the electrons injected from the n-GaN layer into the well gain high kinetic

energy and become hot; therefore, only a part of them can contribute to radiative (or nonradiative) recombination in the active layer. The rest of the electrons can cross the active region and reach the p-GaN layer by ballistic transport. Correspondingly, several technological modifications to the GaN LED structure have been proposed as droop remedies of the later effect. It has been shown that insertion of a few rather thick InGaN layers with increasing In content (the so-called InGaN staircase electron injector, SEI) provides conditions for electron thermalization before they reach the active region [10]. Other technological approaches include variation of the thickness, the number, and the shape of QWs, engineering the quantum barriers, insertion of the electron blocking layer, or growth of the wells along semi- and non-polar orientations [1].

We note that up to now an impact of the SEI structure on emission efficiency was revealed by measuring electroluminescence and external quantum efficiency (EQE) dependence in a biased LED structure. Despite some previous reports that the droop of internal quantum efficiency (IQE) was not observed under optical carrier generation at rates comparable to those under electrical injection [11], a clear correlation of the EQE onset with saturation of IQE gives strong evidence that the QW properties strongly contribute to the photo- and electroluminescence efficiency. Therefore, investigation of photoexcited carrier dynamics in the entire LED structure (including SEI layers) needs further studies to determine the InGaN alloy related radiative and nonradiative recombination rates.

In this work we present several technological modifications of the active LED region and subsequent comprehensive analysis of it by means of various optical techniques. To reduce dislocation density, strain relaxation management was realized by inserting thick InGaN layers with gradually increasing In content as well growing the smooth quantum well/barrier interfaces (instead of abrupt change of In content). Therefore, a SEI structure with gradual increase of In density was grown on the n-GaN template layer before the growth of a QW structure. Secondly, shaping of the spatial profile of the wells is supposed to improve shape-dependent overlap of electron-hole wave functions and enhance the radiative emission efficiency [12, 13]. For evaluation of the LED active region quality, the structural and optical properties of the grown heterostructures were analysed using X-ray diffraction (XRD) and atomic force microscopy (AFM) data, PL spectra at low continuous wave (CW) injections as well as at higher photoexcitations by using picosecond and femtosecond pulses, also investigating carrier dynamics. For the latter goal, carrier recombination pathways in the structures were investigated by applying various time-resolved techniques: photoluminescence spectroscopy (PL), differential transmission (DT), and light-induced transient gratings (LITG). These techniques allowed us to investigate PL spectra and spectral distribution of the carrier recombination rate, discriminate growth-dependent contribution of SEI or QW to the entire PL spectrum, verify the higher quantum efficiency in non-rectangular quantum wells, and evaluate the electronic quality of the entire heterostructure at conditions similar to device performance.

2. Samples and techniques

The MQW structures were grown using an *AIXTRON* CCS (closed coupled showerhead) MOCVD reactor at Vilnius University. Trimetilindium (TMI), trimetilgalium (TMG), and ammonia were used as precursors for In, Ga, and N, accordingly. An undoped ~3 μm thick GaN layer (see Fig. 1) was deposited on a sapphire substrate with the c (0001) crystallographic

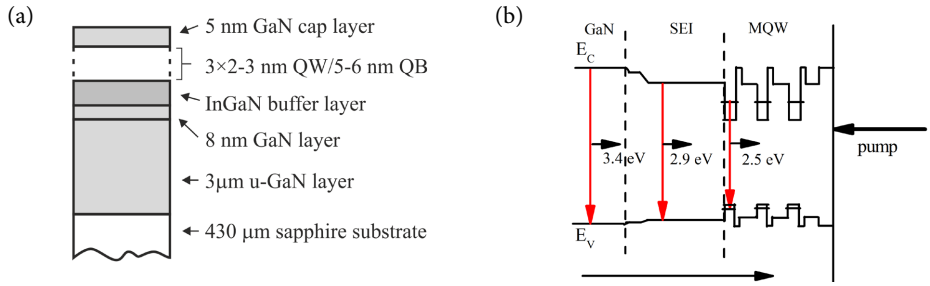

Fig. 1. (a) Scheme of the grown heterostructure. (b) Profiles of conduction E_C and valence E_V band edges in the absence of polarization fields, obtained using $In_xGa_{1-x}N$ band-gap dependence on In concentration E_G (eV) = 3.4(1–x) + 0.7 x – bx(1–x) with the bowing parameter b = 2.5 eV [20] and the valence band offset ΔE_V(eV) = 0.7x.

orientation, tilted by 0.25–0.35 degree with respect to the m-plane. The sapphire substrate was initially decontaminated at 1800 °C, then its surface was nitridized, and a thin (20–5 nm) amorphic GaN layer was grown at 530 °C. During the next step, the temperature was raised to 1070 °C leading to the crystallization of the layer, which then was used to deposit a 3.5 μm thick crystalline GaN buffer layer. It had an electron density of $n_e \approx 10^{17}$ cm^{-3} and electron mobility μ_e ~200 cm^2/Vs.

A wide InGaN buffer layer, or the so-called SEI structure, was grown on the GaN layer before deposition of a LED active region, composed of three quantum wells and three barriers. The SEI structure consisted of three layers (see Fig. 2(a)) – a 2 nm thick layer with low indium content grown at 950 °C, a 5–6 nm thick In layer with gradually increasing In content, and the final 90 nm thick InGaN layer grown at 800 °C with the highest In content (4–11% of In as determined by XRD). A rather thick interlayer was chosen to obtain fully relaxed and less defective InGaN layers, taking into account that critical thickness of $In_xGa_{1-x}N$ on GaN for x in the range from 5% to 15% is around 50 nm [14, 15]. The In content in the layers was changed by varying growth temperature as the TMI/TMG = 1.5 ratio was kept constant.

The QWs were grown at around 700 °C to reach high In content (up to ~25%). Three periods of 2–3 nm thick wells and ~6 nm barriers were grown. After each QW, a protective 1 nm thick GaN layer was deposited at 700 °C to prevent the In evaporation from the QW during the temperature ramp-up for barrier growth. The In concentration profile of QWs in A, B, and C structures was nominally rectangular, as the growth temperature was kept constant during the well growth to get constant In concentration. On the other hand, the D and E structures were grown by ramping temperatures during the well growth that led to the triangular (D) or trapezoidal (E) In concentration and band-gap profile in QWs. The gradient increase of In at the interfaces allowed to accommodate stress and avoid generation of additional structural defects in the wells. The intended structure, growth temperatures, and thicknesses are shown in Fig. 2(a). On the top of each active structure a 5 nm thick GaN cap layer was deposited. QW and barrier thicknesses were estimated from XRD $\omega/2\theta$ scans using (0002) reflection (Fig. 2(b)). We note that a reference $In_xGa_{1-x}N$ MQW structure (sample F, not shown in Fig. 2(a); the wells are the same as in the sample A) was also grown directly on the GaN template without the SEI interlayer under the same growth conditions.

A number of techniques were used for optical characterization of the LED structures. A standard set-up of time-integrated PL spectroscopy was employed using ~355 nm excitation pulses from a picosecond YAG:Nd^{3+} laser and detecting the PL spectra by a thermoelectrically cooled *Princeton Instruments* CCD camera. For low excitation CW PL measurements, a fluorimeter LS–55 was used, where samples were excited at 380 nm. For time-resolved PL

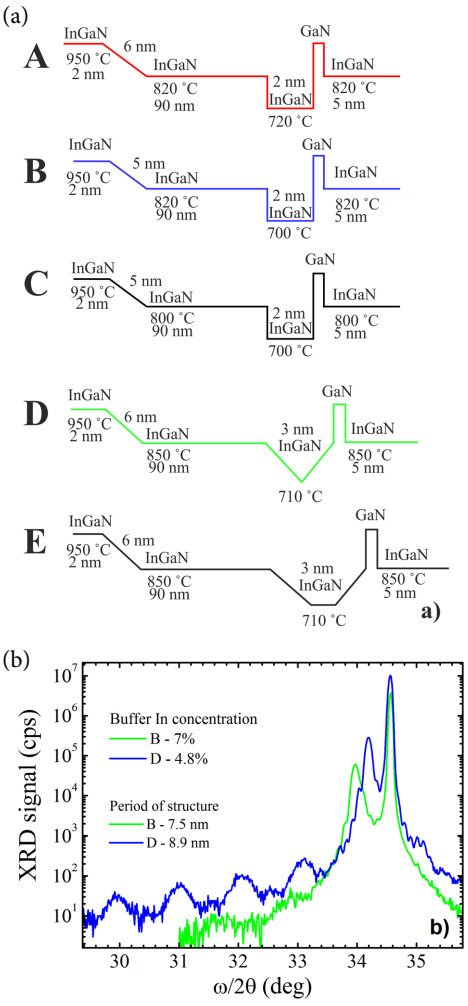

Fig. 2. (a) Band-gap profile with the corresponding growth algorithm in the investigated structures; for simplicity, only the first quantum well and quantum barrier is shown in the drawing. A, B, and C are the structures with rectangular shape, while D and E with triangular and trapezoidal shape of quantum wells. (b) XRD $\omega/2\theta$ scan data in samples B and D.

measurements, a picosecond YAG:Nd^{3+} laser (emitting at 355 nm and water Raman-shifted 405 nm wavelengths) was combined with an *Hamamatsu* C10627 streak camera and Acton SP2300 monochromator, providing the temporal resolution of 20 ps.

The experimental set-up for spectrally and time-resolved DT was based on a commercial Ti:Sapphire femtosecond laser (Spitfire, *Spectra Physics*) delivering 800 nm pulses of 120 fs duration at a 1 kHz repetition rate (Fig. 3(a)). The output of the laser was split into two equal parts. One was used to pump the optical parametric amplifier (TOPAS, *Light Conversion*) providing 120 fs pulses at wavelengths continuously tunable between 1200–2500 nm. The pump was set to 400 nm (3.1 eV) and absorbed in the QWs and SEI, avoiding carrier photogeneration in the GaN buffer layer. The second beam was delayed and focused on a CaF_2 window generating a short pulse of white light. This spectrally broad pulse (330–700 nm) was used to probe changes in absorption spectra at various times after the photoexcitation. The differential transmission spectrum is presented as instantaneous optical density $OD(\lambda,t) = \log(T_0(\lambda)/T(\lambda,t))$; where $T_0(\lambda)$ and $T(\lambda,t)$ stand for the sample transmittance spectrum without and with the pump pulse at a time instant t. In this way, DT technique provided means to observe evolution of state occupancy in InGaN QWs with high temporal and spectral resolution.

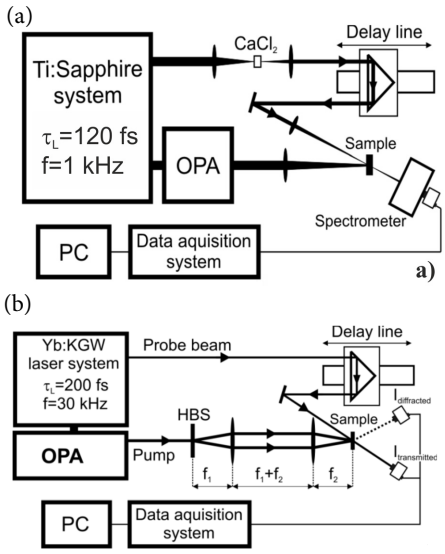

Fig. 3. Experimental set-ups of (a) DT and (b) LITG techniques.

Unlike the conventional pump-probe set-up, where samples are excited by the Gaussian-like spatial profile, LITG technique for photoexcitation uses the interference field of two coherent beams [16] (Fig. 3(b)). This results in recording of a free-carrier grating with period Λ and carrier density spatial modulation ΔN_0, the decay of which can be probed by diffraction of a delayed probe beam, providing an instantaneous diffraction efficiency $\eta(t) \sim \Delta N_0^2 \exp(-2t/\tau_G)$. The grating decay time τ_G at different grating periods allows determination of the carrier diffusion coefficient D and the carrier lifetime τ_R according to the $1/\tau_G = 1/\tau_R + 4\pi^2 D/\Lambda^2$ relationship. Such an approach has several advantages, one of which being the ability to measure the time evolution of the overall free carrier density.

3. Results and discussion

3.1. Sample morphology and structural quality

The structural quality and surface morphology of the grown structures was evaluated by scanning electron microscopy (SEM, Fig. 4) and atomic force microscopy (AFM, Fig. 5). SEM and AFM images showed that samples D and E with the triangular and trapezoidal wells, correspondingly, have the significantly smoother surfaces. The surface roughness measured by AFM decreased down to around 3 nm in D and E samples with respect to the rectangular ones with the roughness of 7 nm. Also, the AFM scans showed that the dislocation density (dark spots) was lower by a factor of 2 in the graded quantum wells (samples D and E) if compared to the reference sample with the constant In concentration (the dark spot density was 5×10^8 cm^{-2} (sample A) and $2–3 \times 10^8$ cm^{-2} (samples D and E). Also, the observed hexagons were much larger in the samples D and E.

3.2. PL emission at steady state conditions: PL spectra

In order to optimize the growth parameters, continuous wave (CW) PL spectra were recorded and PL output at the QW peak position (~470 nm) was compared between the variously grown structures (Fig. 6). The weaker additional bands appearing at ~370 and 400 nm were attributed to GaN buffer and interlayer emission, correspondingly, and will be addressed in the later section.

Among the rectangular QWs grown at different temperatures, the most intensive PL output at 470 nm was found in structure A (Fig. 6(a)). Therefore, the lower growth temperature of ~720 °C was assumed as a more suitable one for growth of the rectangular QWs. Then the PL efficiency was maximized by varying the well shape, and the highest PL signal was

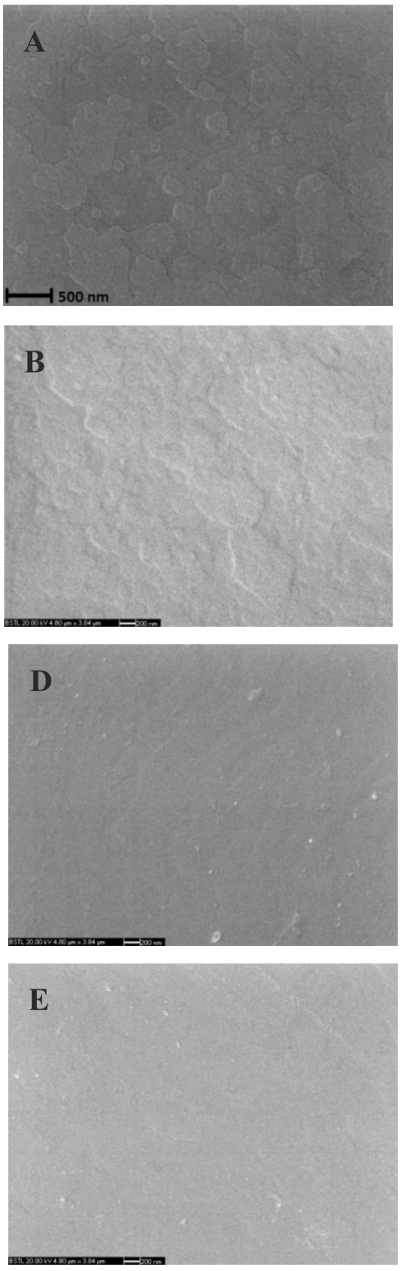

Fig. 4. SEM surface images of samples A, B, D, and E taken at the same magnification ratio. The surface roughness in samples A and B is noticeably larger than that in samples D and E.

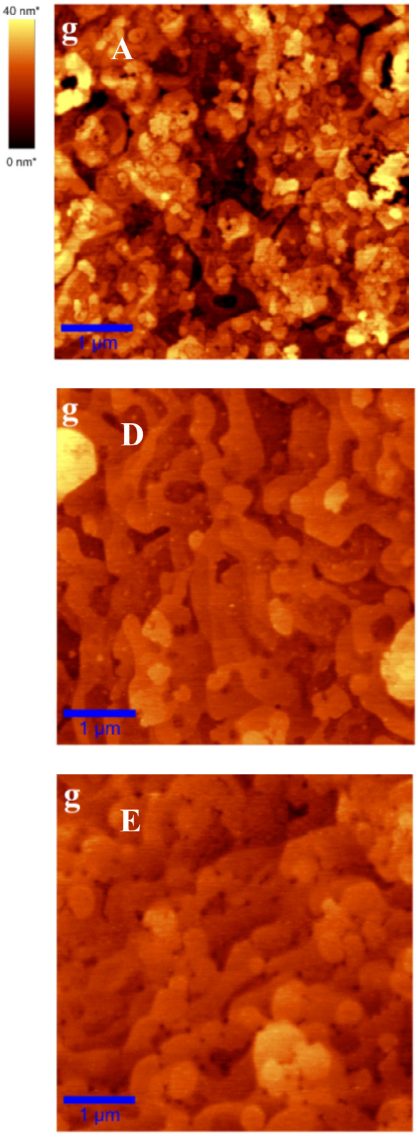

Fig. 5. AFM scans of samples A, D, and E.

obtained for the triangular QWs (sample D in Fig. 6(b)). This can be explained by better In incorporation and its weaker segregation due to continuous change of strain [12, 13]. Also, it has been shown that the e-h wave function overlap is better in the triangular and trapezoidal QWs [12, 13].

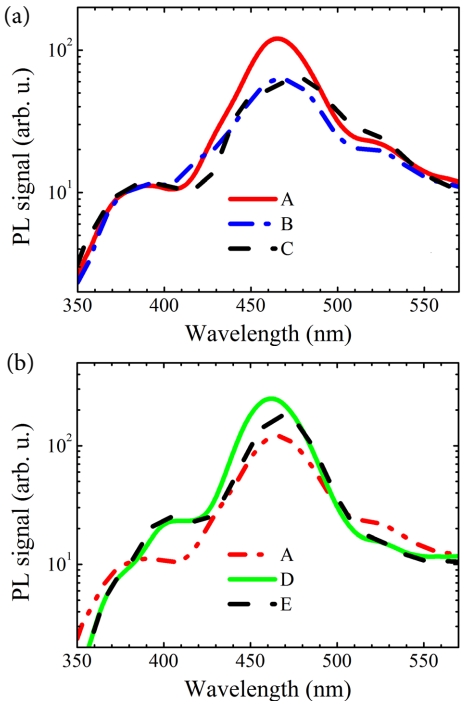

Fig. 6. Comparison of CW photoluminescence spectra in the structures with the rectangular QWs grown at various temperatures (a) and for differently shaped wells (b). For growth conditions, see Fig. 2(a). The used excitation power density was 20 μW/cm^2 at 380 nm.

3.3. PL characteristics at pulsed excitation

To get a deeper insight into PL features at higher free carrier densities, PL measurements were performed under pulsed 355 nm excitation (Fig. 7). Three distinct peaks were identified in the PL spectra. A wide peak at 450–470 nm saturating with excitation was attributed to the emission from the wells. The second stronger peak was blue-shifted with respect to QW emission. Its origin can be related to the emission from the thick SEI layer, since such a peak was absent in sample F without the SEI. In addition, variation of In content in the SEI leads to the shift of this peak position from 395 to 415 nm. The strongest SEI-related emission was observed in sample B at 420 nm (having the In concentration of about 7%, as the In content above 10% causes degradation of the InGaN epilayer and decrease of its PL intensity [6]). The third peak at 370 nm arises from the GaN barrier, as its position coincides with that from the bulk GaN [17].

To confirm the origin of the strong PL peaks in the 390–420 nm range, two steps of the reactive ion etching were performed on the LED structures, after which the PL spectra were measured again (see Fig. 8). Each step removed ~36 nm from the top of

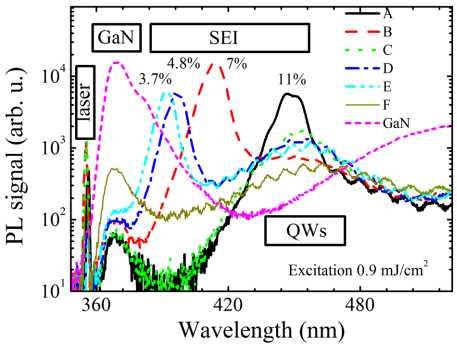

Fig. 7. Comparison of photoluminescence spectra in the studied samples using the picosecond pulses at 355 nm with energy density of I_0 = 0.9 mJ/cm^2. In content in the SEI layers is indicated in the figure. PL of bulk GaN shows the spectral position of the quantum barriers in the structures. The sample without the SEI (sample F) is also shown for comparison.

the structure. The first etching removed the 5 nm thick cap layer and the 25–30 nm thick QW structure (3 periods of QWs with barriers). The second etching removed a part of the SEI structure.

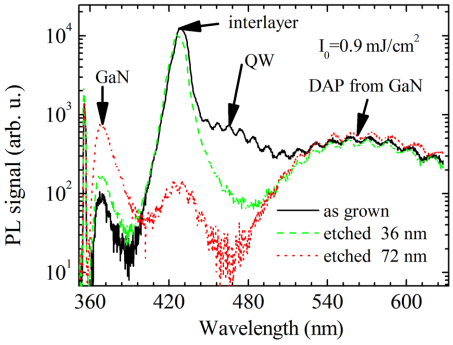

Fig. 8. PL spectra in the as-grown sample B (black line online), after the etching out the QWs (green line online), and the part of the SEI structure (red line online).

It was observed that after etching out the QWs the wide band at 470 nm almost disappeared, which proves that this band is caused by the emission from the wells. After the second etching step, the band at 420 nm also almost disappeared. The latter peak can be attributed to luminescence of the upper part of the InGaN SEI layer that has a better structural quality (critical depth for the InGaN alloy with 7% of In is expected to be 50 nm [14]). The lower part of SEI is believed to contain a high density of point defects and dislocations, which results in a weaker and broader PL spectrum [6, 18]. The emission at 370 nm from the GaN buffer increased after the etching due to reduced re-absorption by the InGaN layers. The 600 nm peak did not considerably change after the etching and was probably related to donor-acceptor pair (DAP) recombination in the GaN buffer (called yellow luminescence [19]).

The In composition in the wells can be estimated using the emission wavelengths and the well thickness. In all cases, QW emission peaks at ~470 nm (2.6 eV, Fig. 6) indicating the similar In content in all QWs. According to calibration, 25% of indium should be present in QWs grown at 710 ± 10 °C temperature. Relying on dependence of InGaN band-gap energy, it would provide 2.3 eV InGaN band-gap [20], whereas carrier confinement in the 3 nm thick well shifts up the lowest transition energy; therefore, PL occurs at 2.5 eV (estimation of the first electronic level position in the well according to $E_1 = h^2/(8m_e d^2)$ relationship [21] provided 0.22 eV shift). The large width (~240 meV) of the emission peak can be explained by thermal broadening, variations of QW thickness and In content in the wells.

The PL spectra dependence on excitation fluence is provided in Fig. 9. It was observed that PL peak intensities in both the GaN buffer and SEI interlayer continuously increase with the excitation, while the QW peak almost saturates. Fig. 10 shows the dependence of PL peak intensity versus excitation for various spectral regions of the grown structures. These dependences were fitted by power functions with the different indices that reflect carrier generation and recombination peculiarities. At high excitations, the sublinear dependence $I_{PL} \sim I_0^{0.4}$ for the QW emission points out the saturation of the PL signal, while the superlinear growth $I_{PL} \sim I_0^{1.4}$ is observed for the SEI interlayer.

In the QWs, PL intensity increases linearly at low excitations indicating the excitonic emission in QW band tails. At higher excitations, saturation of PL emission intensity from the wells can be explained by filling of the localized states (Fig. 10(a)). PL dependence in the interlayer exhibits much steeper dependence on excitation, which is typical of bulk GaN (slope of 2 corresponds to quadratic increase of PL signal with excitation, as the linear increase of electron-hole concentration, $N_{eh} \propto \alpha I_0$, leads to the bimolecular recombination, $I_{PL} \propto N_{eh}^2$). The decrease of the slope value at high injections (I_0>1 mJ/cm^2) is a typical case for bulk semiconductors indicating interaction of various recombination mechanisms and saturation of the radiative recombination rate [8].

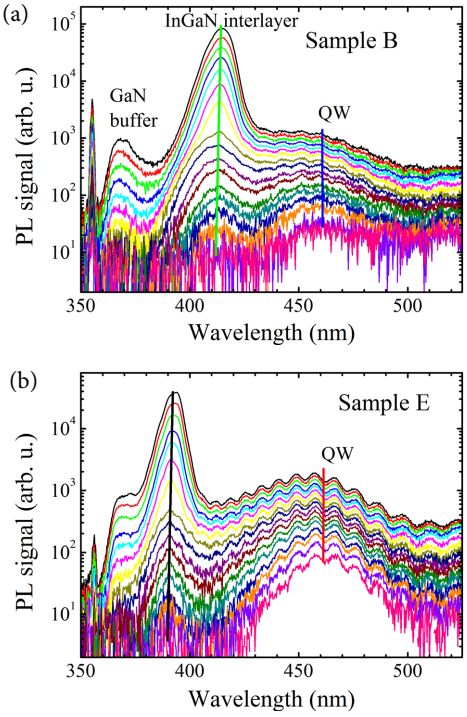

Fig. 9. PL spectra: (a) in the rectangular QW (sample B) and (b) in the trapezoidal QW (sample E) under the pulsed excitation at 355 nm.

It was observed that PL emission from the samples with profiled QWs (D and E samples, Fig. 10(a)) at pulsed excitation has the highest PL efficiency, thus confirming PL measurements under steady-state excitation conditions. In the latter structures, In concentration in the SEI interlayer is lower, thus favouring better carrier localization in QWs. In A and C samples, the QW spectral position overlaps with the SEI emission peak (Fig. 7), indicating weak localization in the wells; therefore, emission from the well and SEI cannot be separated, especially at high excitations (Fig. 10(b)). Consequently, too high concentration of In in the SEI layer leads to rather weak localization of carriers in the wells and rather weak emission from the wells. It is worth noting that the F sample exhibits only the QW

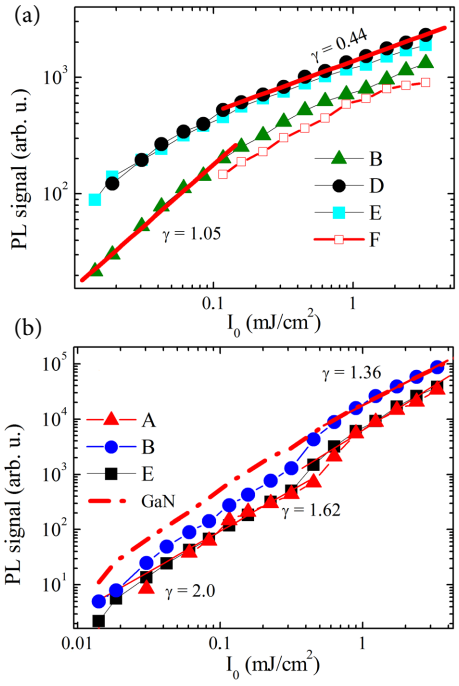

Fig. 10. PL intensity vs. excitation energy fluence at 355 nm for emission from the QWs at 470 nm (a) and from the SEI peaks (b). Saturation of PL ($\gamma = 0.44$, (a)) indicates filling of the localized states in the QWs; PL superlinear increase in (b) reveals its origin in the bipolar carrier recombination from the weakly localized states in the SEI.

peak, as there is no SEI interlayer. A comparison of PL signal from the rectangular wells F with respect to B (which has the SEI interlayer) points out to a positive impact of the interlayer, i. e. increase of the structural quality of the subsequently grown quantum wells.

The further PL measurements used selective photoexcitation of quantum wells at 405 nm; at this wavelength, the photon energy was sufficient to excite the quantum wells but not enough to excite the barriers and interlayers. This was confirmed by measurements of PL spectra at selective photoexcitation (Fig. 11(a)), and time-resolved PL kinetics provided carrier lifetimes in the differently shaped quantum wells (Fig. 11(b)).

It was observed that the blue-shift of PL appears due to screening of the quantum confinement Stark effect (QCSE) and filling of the localized states (Fig. 11(a)). Carrier lifetime of the sample D is ~4 times larger with respect to sample B, indicating the enhanced carrier localization in the former structure. Consequently, a few times longer lifetime provides ~3 times higher PL intensity (see Fig. 10(a)). Rather weak dependence of PL lifetime on excitation (at excitation above 0.1 mJ/cm^2) in D and E samples indicated the dominant channel of nonradiative recombination in the wells; here, a twice higher PL efficiency at 0.1 mJ/cm^2 with respect to 0.01 mJ/cm^2 excitation correlated with corresponding lifetime increase (from 0.2 to 0.4 ns) in sample D, indicating saturation of point defects [7]. A similar effect was also observed in sample E. A shorter carrier lifetime of 47 ps in sample F without SEI structure indicated a positive role of the SEI layer. We also note that at 355 nm excitation the PL decay time in the wells was also weakly dependent on excitation, while the PL decay times in the interlayers were shorter (e. g. 50 ps in sample E and

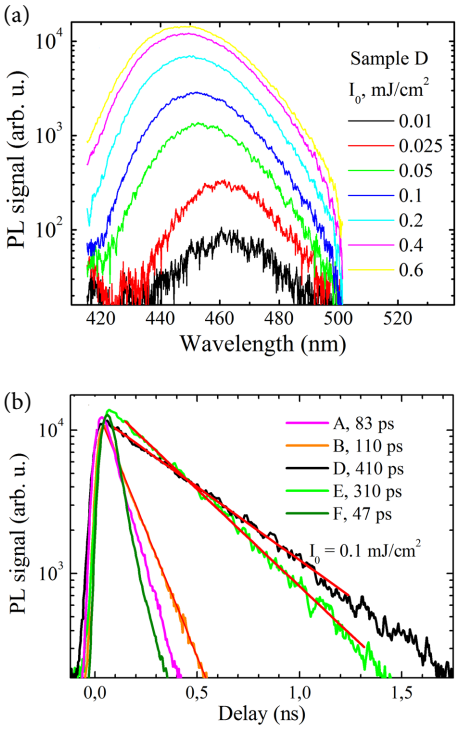

Fig. 11. (a) PL spectra in the triangular QWs at various excitations. (b) Comparison of PL decay kinetics of the QW emission in the samples. Excitation wavelength was set to 405 nm to avoid carrier excitation in the GaN buffer and barriers.

110 ps in sample B). Thus, a two times longer lifetime in sample B explained a two times stronger PL in it (see Fig. 10(b)).

3.4. DT spectra and LITG kinetics

In Fig. 12(a), a comparison between instantaneous DT and PL spectra is presented for sample D at selective photoexcitation. Within the entire spectral range the absorption decreases after the excitation (providing a negative DT signal) due to the state filling effect. Two distinct peaks in DT spectra are seen within the sub-nanosecond delay times range and are attributed, correspondingly, to absorption bleaching in the SEI interlayer (415 nm) and in the quantum wells (460 nm). The overlap of DT and PL spectra at the QW position indicates a strong photoexcitation absorption of QWs and, thus, sufficiently high density of states in quantum wells. During the first ~50 ps after the excitation, carrier transfer from higher to lower energy states occurs (compare the DT spectra at 0 ps and 50 ps in Fig. 12(a)). Later on, the DT signal decays due to carrier recombination; here, a shift of DT and PL spectra towards the longer wavelengths with time is attributed to rebuilding of initially screened polarization electric fields in QWs.

Figure 12(b) shows DT decay transients at various spectral positions within the PL band of QWs in sample D. Two decay components are present in these transients. The time decay constant of the faster component is shown in Fig. 12(c) (black squares online). It varies within 200–400 ps at given excitation and is close to the time constant of PL decay obtained from time-resolved PL measurements (red circles online in Fig. 12(c)). In addition, the spectral distributions of PL and DT decay times are very similar. This allows attributing this component to the radiative recombination of carriers that gives rise to photoluminescence. We note that PL time constant does not necessarily correspond to the radiative decay time, but is instead a result of radiative and nonradiative processes, $1/\tau_{PL} = 1/\tau_{rad} + 1/\tau_{nonrad}$. Therefore, the initial decay constants of DT and the PL decay time represent the fast nonradiative recombination time after the photoexcitation. At higher photoexcitations, PL decay time increases (see Fig. 12(c), red triangles online), as the nonradiative recombination centres are partially filled (a similar increase of the fast PL decay component was also observed in Ref. [7]). After carrier localization in the lowest energy states, the DT decay time becomes slower (note the second DT decay component with decay time constant well above 10 ns, Fig. 12(b)). We did not find a slow component in PL spectra and thus conclude that thermally activated carrier transfer from these

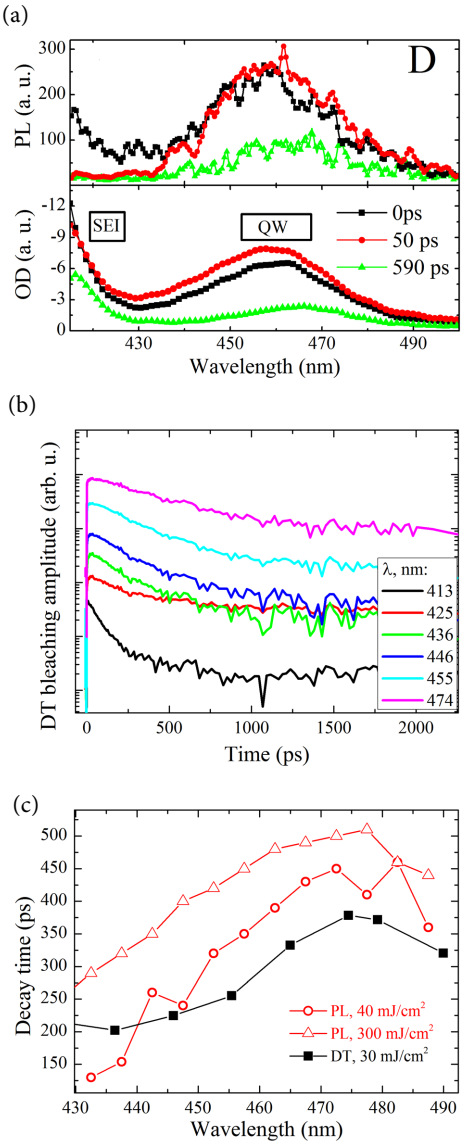

Fig. 12. Comparison of PL and DT data in sample D for a moderate excitation of 30–40 μJ/cm^2: (a) instantaneous PL and DT spectra of quantum wells at several delay times, (b) DT decay transients at various spectral positions (the transients are arbitrarily shifted with respect to each other for the sake of visibility), and (c) decay time constants of PL and DT signals against the spectral position.

localized states to nonradiative recombination centres is more efficient than the radiative recombination. We note that in less defective QWs the long lasting PL decay component is present [7]. As the long-decay DT signature is seen both in SEI and QWs (Fig. 12(b)), we attribute this component to nonradiative carrier recombination from deeply localized states, which are present both in the QW and SEI region. The DT decay time constants shorter than those of PL can be explained within the latter assumption since part of the carriers are being transferred to these immobile localized states.

The above-given PL and DT measurements pointed out that radiative processes were more efficient in the structures with non-rectangular-shape QWs. To compare the average carrier lifetime in differently shaped QWs, LITG measurements were performed at 387 nm excitation and 1030 nm probing. The pump wavelength was chosen to ensure photoexcitation of QWs and InGaN staircase and to avoid creation of excess carriers in the buffer GaN layer (selection of lower quantum energy would be preferable, but it provides less excess carriers and does not favour measurements in a wide dynamic range). Since LITG signal is proportional to the density of excited carriers integrated over the sample depth, the nonequilibrium carriers in the interlayer and in the QWs contribute to the measured diffraction signal. This approach allows evaluating the electronic quality of the grown structures at conditions similar to device performance at electrical carrier injection.

The kinetics of LITG decay for the differently shaped QWs are presented in Fig. 13 at low and high excitation energy densities. Here, the used low injection case was favourable to reveal processes of carrier transfer to localized states in QWs with the subsequent slower decay, while the high injection regime reveals the processes in higher energy states when the carriers are able to occupy the extended dates (in the given case, they may occupy the states in a wide SEI layer). In the structures D and E, the carrier lifetime peaks at ~300 ps, while in the structures A and B with standard well shape the carrier lifetime drops down to ~100 ps. At higher excitation, the lifetime in samples D and E also decreases to ~100 ps as the delocalized carriers occupy the extended states and face a higher number of fast nonradiative recombination centres. Therefore, carrier lifetime becomes similar to the one typical of the interlayer or the quantum well barriers.

The low-injection carrier lifetimes (~300 ps) coincide well with the PL decay times (300–400 ps in the QWs of D and E structures (Fig. 11(b)) and indicate the nonradiative recombination time in localized states. Despite that the average carrier lifetime of the heterostructure decreases with excitation, the PL decay time at the QW does not change significantly at even

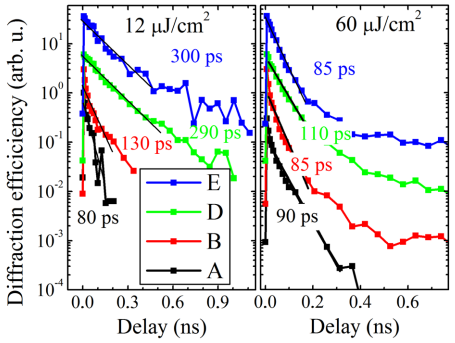

Fig. 13. LITG kinetics in differently shaped MQW structures at low and high excitation energy densities (grating period equals 7.27 μm). Kinetics are vertically displaced for clarity. The excitation quantum energy of 3.2 eV generates carriers in the entire heterostructure and monitors the spatially averaged carrier lifetime.

higher excitation which is a consequence of localized state saturation. This is an indication that localized state lifetime is weakly injection-dependent, i. e. the contribution of radiative emission with carrier density dependent recombination rate was not observed in the given set of samples.

4. Conclusions

Varying the growth regime, the active region of LED structure was modified by inserting a wide interlayer structure with gradual In concentration increase and subsequent growth of differently shaped InGaN quantum wells (rectangular, triangular, trapezoidal). Growth temperature variation allowed to obtain different In content in the quantum wells and formation of smooth quantum well barriers.

Measurements of photoluminescence spectra combined with the reactive-ion etching of the structure were applied for discrimination of PL signals originated in the InGaN interlayer structure, underlying quantum wells, and quantum barriers. Analysis of PL intensity dependence on excitation density provided technologically tailored conditions for enhanced carrier localization in the wells. The highest PL intensity was obtained in the heterostructure with triangularly shaped QWs.

Carrier dynamics was studied by TRPL, differential transmission, and light-induced transient grating techniques, providing carrier lifetimes, their spectral distribution, and revealing shorter carrier lifetime on the high-energy wing. Light-induced transient grating

technique was used to determine the average carrier lifetime in the entire heterostructure, in this way unravelling the electronic quality of the internal LED structure at conditions similar to device performance. Grating decay rates at low and high excitation energy densities revealed increasing with photoexcitation nonradiative recombination rate in the triangular and trapezoidal wells. This study proved that the implemented strain management led to the lower dislocation density, smoother surface, longer localized carrier lifetime, and eventually the highest PL intensity in the triangularly shaped quantum wells.

Acknowledgement

The authors acknowledge support of the European Social Fund under Project VP1-3.1-ŠMM-07K-02-006.

References

[1] G. Verzellesi, D. Saguatti, M. Meneghini, F. Bertazzi, M. Goano, G. Meneghesso, and E. Zanoni, Efficiency droop in InGaN/GaN blue light-emitting diodes: Physical mechanisms and remedies, J. Appl. Phys. **114**, 071101 (2013).

[2] V. Avrutin, S.A. Hafiz, F. Zhang, Ü. Özgür, H. Morkoç, and A. Matulionis, InGaN light-emitting diodes: Efficiency-limiting processes at high injection, J. Vac. Sci. Technol. A **31**, 050809 (2013).

[3] J. Piprek, Efficiency droop in nitride-based light-emitting diodes, Phys. Status Solidi A **207**, 2217–2225 (2010).

[4] E. Kioupiakis, P. Rinke, K.T. Delaney, and C.G. Van de Walle, Indirect Auger recombination as a cause of efficiency droop in nitride light-emitting diodes, Appl. Phys. Lett. **98**, 161107 (2011).

[5] J. Hader, J.V. Moloney, and S.W. Koch, Density-activated defect recombination as a possible explanation for the efficiency droop in GaN-based diodes, Appl. Phys. Lett. **96**, 221106 (2010).

[6] T. Malinauskas, A. Kadys, T. Grinys, S. Nargelas, R. Aleksiejūnas, S. Miasojedovas, J. Mickevičius, R. Tomašiūnas, K. Jarašiūnas, M. Vengris, S. Okur, V. Avrutin, X. Li, F. Zhang, Ü. Özgür, and H. Morkoç, Impact of carrier localization, recombination, and diffusivity on excited state dynamics in InGaN/GaN quantum wells, Proc. SPIE **8262**, 82621S-1 (2012).

[7] R. Aleksiejūnas, K. Gelžinytė, S. Nargelas, K. Jarašiūnas, M. Vengris, E.A. Armour, D.P. Byrnes, R.A. Arif, S.M. Lee, and G.D. Papasouliotis, Diffusion-driven and excitation-dependent recombination rate in blue InGaN/GaN quantum well structures, Appl. Phys. Lett. **104**, 022114 (2014).

[8] J.I. Shim, H. Kim, D.S. Shin, and H.Y. Yoo, An explanation of efficiency droop in InGaN-based light emitting diodes: saturated radiative recombination rate at randomly distributed In-rich active areas, J. Korean Phys. Soc. **58**, 503–508 (2011).

[9] B.-J. Ahn, T.-S. Kim, Y. Dong, M.-T. Hong, J.-H. Song, J.-H. Song, H.-K. Yuh, S.-C. Choi, D.-K. Bae, and Y. Moon, Experimental determination of current spill-over and its effect on the efficiency droop in InGaN/GaN blue-light-emitting diodes, Appl. Phys. Lett. **100**, 031905 (2012).

[10] X. Ni, X. Li, J. Lee, S. Liu, V. Avrutin, Ü. Özgür, H. Morkoç, A. Matulionis, T. Paskova, G. Mulholland, and K.R. Evans, InGaN staircase electron injector for reduction of electron overflow in InGaN light emitting diodes, Appl. Phys. Lett. **97**, 031110 (2010).

[11] M.H. Kim, M.F. Schubert, Q. Dai, J.K. Kim, E.F. Schubert, J. Piprek, and Y. Park, Origin of efficiency droop in GaN-based light-emitting diodes, Appl. Phys. Lett. **91**, 183507 (2007).

[12] S.-H. Han, D.-Y. Lee, H.-W. Shim, G.-Ch. Kim, Y.S. Kim, S.-T. Kim, S.-J. Lee, Ch.-Y. Cho, and S.-J. Park, Improvement of efficiency droop in InGaN/GaN multiple quantum well light-emitting diodes with trapezoidal wells, J. Phys. Appl. Phys. **43**, 354004 (2010).

[13] H. Zhao, G. Liu, J. Zhang, J.D. Poplawsky, V. Dierolf, and N. Tansu, Approaches for high internal quantum efficiency green InGaN light-emitting diodes with large overlap quantum wells, Opt. Express **19**, A991–A1007 (2011).

[14] M. Leyer, J. Stellmach, Ch. Meissner, M. Pristovsek, and M. Kneissl, The critical thickness of InGaN on (0001) GaN, J. Cryst. Growth **310**, 4913–4915 (2008).

[15] K. Pantzas, G. Patriarche, G. Orsal, S. Gautier, T. Moudakir, M. Abid, V. Gorge, Z. Djebbour, P.L. Voss, and A. Ougazzaden, Investigation of a relaxation mechanism specific to InGaN for improved MOVPE growth of nitride solar cell materials, Phys. Status Solidi A **209**(1), 25–28 (2012).

[16] K. Jarašiūnas, R. Aleksiejūnas, T. Malinauskas, V. Gudelis, T. Tamulevičius, S. Tamulevičius, A. Guobienė, A. Usikov, V. Dmitriev, and H.J. Gerritsen, Implementation of diffractive optical element in four-wave mixing scheme for *ex situ* characterization of hydride vapor phase epitaxy-grown GaN layers, Rev. Sci. Instrum. **78**, 033901 (2007).

[17] P. Ščajev, K. Jarašiūnas, S. Okur, Ü. Özgür, and H. Morkoç, Carrier dynamics in bulk GaN, J. Appl. Phys. **111**, 023702 (2012).

[18] P. Ščajev, A. Usikov, V. Soukhoveev, R. Aleksiejūnas, and K. Jarašiūnas, Diffusion-limited nonradiative recombination at extended defects in hydride vapor phase epitaxy GaN layers, Appl. Phys. Lett. **98**, 202105 (2011).

[19] G. Li, S.J. Chua, S.J. Xu, W. Wang, P. Li, B. Beaumont, and P. Gibart, Nature and elimination of yellow-band luminescence and donor–acceptor emission of undoped GaN, Appl. Phys. Lett. **74**, 2821–2823 (1999).

[20] V.Yu. Davydov, A.A. Klochikhin, V.V. Emtsev, D.A. Kurdyukov, S.V. Ivanov, V.A. Vekshin, F. Bechstedt, J. Furthmüller, J. Aderhold, J. Graul, A.V. Mudryi, H. Harima, A. Hashimoto, A. Yamamoto, and E.E. Haller, Band gap of hexagonal InN and InGaN alloys, Phys. Status Solidi B **234**(3), 787–795 (2002).

[21] N. Peyghambarian, S.W. Koch, and A. Mysyrowicz, *Introduction to Semiconductor Optics* (Prentice Hall, 1993).

FOTOLIUMINESCENCIJOS YPATUMAI IR KRŪVININKŲ DINAMIKA InGaN HETEROSANDAROSE SU PLAČIU LAIPTUOTU TARPSLUOKSNIU IR SKIRTINGO PROFILIO KVANTINĖMIS DUOBĖMIS

A. Kadys, T. Malinauskas, M. Dmukauskas, I. Reklaitis, K. Nomeika, V. Gudelis, R. Aleksiejūnas, P. Ščajev, S. Nargelas, S. Miasojedovas, K. Jarašiūnas

Vilniaus universiteto Taikomųjų mokslų institutas, Vilnius, Lietuva

Santrauka

Pristatome išsamius fotosužadintų krūvininkų dinamikos tyrimus daugialypėse InGaN kvantinėse sandarose su plačiu laiptuotu tarpsluoksniu ir skirtingo profilio kvantinėmis duobėmis (stačiakampėmis, trikampėmis, trapecinėmis). Šis įtempimų valdymo būdas dėl palaipsniui didėjančio In kiekio tarpsluoksnyje ir sklandaus sandūrų tarp kvantinių duobių bei barjerų formavimo leido sumažinti dislokacijų tankį. Daugialypės kvantinės sandaros, orientuotos išilgai c ašies ir šviečiančios ties 470 nm, buvo pagamintos Vilniaus universiteto Taikomųjų mokslų instituto MOCVD reaktoriuje. Fotoliuminescencijos (FL) spektrų matavimai buvo atlikti nuolatinės veikos ir impulsinio žadinimo sąlygomis. Bandinių reaktyvus joninis ėsdinimas leido identifikuoti FL atsaką iš InGaN tarpsluoksnio, kvantinių duobių ir kvantinių barjerų, tokiu būdu parodant su auginimu susijusias sąlygas, lemiančias geresnę krūvininkų lokalizaciją duobėse. Iš laikinės skyros FL ir skirtuminio pralaidumo kinetikų įvertintos krūvininkų gyvavimo trukmės (ir jų spektrinis pasiskirstymas) buvo ilgiausios trikampėse kvantinėse duobėse, kuriose taip pat stebėtas didžiausias FL intensyvumas. Šviesa indukuotų difrakcinių gardelių metodika panaudota nustatant erdviškai suvidurkintą krūvininkų gyvavimo trukmę visoje heterostruktūroje, tai leido įvertinti vidinės šviestuko struktūros kokybę panašiomis prietaisų veiklai sąlygomis. Gardelių irimo spartos esant žemam ir aukštam žadinimo energijos tankiui atskleidė su fotosužadinimu augančią nespindulinės rekombinacijos spartą trikampio ir trapecinio profilio duobėse.

2nd publication / 2 publikacija

Carrier dynamics in blue and green emitting InGaN MQWs

R. Aleksiejūnas, **K. Nomeika**, S. Miasojedovas, S. Nargelas, T. Malinauskas, K. Jarašiūnas, Ö. Tuna, M. Heuken

Physica Status Solidi (b) **252** (2015) 977–982
DOI:10.1002/pssb.201451583

Wiley Online Library
Early View publication on www.wileyonlinelibrary.com
(issue and page numbers not yet assigned;
citable using Digital Object Identifier – **DOI**)

Phys. Status Solidi B, 1–6 (2015) / **DOI** 10.1002/pssb.201451583

physica status solidi b
www.pss-b.com
basic solid state physics

Carrier dynamics in blue and green emitting InGaN MQWs

R. Aleksiejūnas*[,1], K. Nomeika[1], S. Miasojedovas[1], S. Nargelas[1], T. Malinauskas[1], K. Jarašiūnas[1], Ö. Tuna[2], and M. Heuken[2]

[1] Institute of Applied Research, Vilnius University, Saulėtekio al. 9-3, Vilnius LT-10222, Lithuania
[2] AIXTRON SE, Kaiserstr. 98, D-52134 Herzogenrath, Germany

Received 30 September 2014, revised 14 November 2014, accepted 28 November 2014
Published online 23 January 2015

Keywords charge carrier diffusion, charge carrier recombination, InGaN, photoluminescence, quantum wells, transient gratings

* Corresponding author: e-mail ramunas.aleksiejunas@ff.vu.lt, Phone: +370 5 236 6037

Spectrally and spatially-resolved nonlinear optical techniques were combined with the photoluminescence spectroscopy to study carrier dynamics and photoluminescence efficiency in highly excited blue- and green-emitting InGaN/GaN quantum wells. The differential transmission and transient grating techniques provided carrier lifetimes and diffusivity in the extended states with energies above the photoluminescence emission band and revealed their dependences on excess carrier density. At high excitation conditions, an increase of diffusivity led to the increase of nonradiative recombination rate, being more pronounced in the green QW structures with respect to the blue ones. Enhancement of these processes in the extended states has a strong impact on diminishing the photoluminescence efficiency in the localized states.

1 Introduction Progress of InGaN-based light emitting diodes (LED) is facing two main issues limiting their efficiency. From one side, LED efficiency starts to decline at high carrier densities (efficiency droop problem). Still a subject of debates, the efficiency droop seems to be caused by internal processes in the nitride material. Auger recombination, carrier delocalization, saturation of radiative emission, and electron leakage are named as the most probable mechanisms behind the efficiency droop (an overview can be found in [1, 2]). The second major problem is deterioration of InGaN LED performance with the increasing emission wavelength (i.e., with the increasing In content). The increasing Stokes' shift of In rich alloys [3] and subsequent increase of the number of localized states below the absorption edge should play a greater role in carrier localization, redistribution, and recombination. Recent photoluminescence (PL) studies of multiple quantum wells (MQWs) with a low ($x = 0.18$) and high ($x = 0.31$) In content at selective excitation [4] showed that the emission reduction at longer wavelengths (525 nm) was caused by thermal activation of nonradiative processes (what resulted in 200 ps PL lifetimes in the green QW) rather than by decreasing overlap of electron-hole wave functions. Quasi-stationary multimode SNOM measurements at a selective excitation of violet-to-green LEDs suggested a longer diffusion length in the green LEDs due to the presumably longer carrier lifetime [5], but this contradicts the decreasing crystalline quality of the green-emitting wells [4, 6]. Earlier studies of two nominally similar InGaN QWs with $x \approx 0.3$ revealed either nonexponential PL decay time and a small diffusion length or the exponential decay and large diffusion length [7] while both samples exhibited long lifetimes up to 100 ns. The diffusivity features demonstrated a profound involvement of localized states, which disappeared at high excitations when carrier transport in the extended states dominated. Moreover, CL measurements of the yellow-emitting InGaN/GaN LEDs in quasi-stationary conditions [8] (using 100 ns duration pulses) revealed an absence of strong exciton localization and pointed out to dominant impact of nonradiative recombination at 300 K.

Therefore, to clarify the differences of carrier diffusion and recombination dynamics with increase of In content, we performed a study of excess carrier spatial and temporal dynamics in InGaN QW structures emitting from UV to green. To discriminate between the recombination and diffusion processes, we used light-induced transient grating (LITG) technique [9, 10], which directly provided the

diffusion coefficient of excess carriers at selective excitation. Time-resolved spectroscopy of differential transmission (DT) enabled an access to the localized and extended states in a wide spectral range [11, 12], including the states well above the PL emission band [13]. The standard time-resolved PL (TRPL) measurements were also performed to study the excitation dependent PL decay times, spectra, and efficiencies. We focus on the fast dynamics of non-equilibrium carriers that is revealed as fast transients in all used techniques. It may enlighten the roots of carrier delocalization processes that eventually determine PL saturation at quasi-stationary conditions.

2 Samples and experimental techniques A set of five samples, each consisting of five InGaN quantum wells and GaN barriers, was grown by metalorganic chemical vapor deposition on c-plane sapphire substrate, buffered by 3 μm thick n-GaN buffer layer, doped to 5×10^{18} cm^{-3}. Indium content in the wells was 5.1% (sample A), 8.4% (sample B), 11.3% (sample C), 13.2% (sample D), and 23% (sample E). The thickness was ~5 nm for the quantum wells and ~18 nm for the GaN barriers. The well width was measured using TEM, while the composition was estimated from X-ray diffraction measurements. To estimate In content optically, PL emission was measured under continuous-wave (cw) and pulsed excitations; the latter time-integrated spectra are shown in Fig. 1. We note that very broad spectrum in the sample E indicates poor compositional and probably structural quality of QWs; however, we include it into further analysis. Cw PL peaks ranged in the samples from 2.98 eV (416 nm, sample A) to 2.16 eV (575 nm, sample E), while under pulsed excitation (i.e., at much higher photoexcited carrier density) the spectra appeared at higher photon energies from 2.33 eV to 2.94 eV. In content in the QWs was estimated from PL peak positions at both low and high excitations using Vegard's law for bowing parameter values ranging from 1.32 to 2.87 [14, 15]. Good agreement with XRD estimation was achieved with pulsed PL data, while the cw-PL peak values resulted in overestimation of In content.

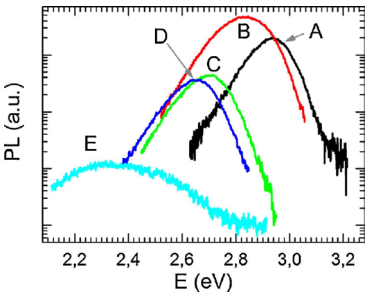

Figure 1 Time-integrated PL spectra under pulsed excitation (25 ps pulse at 355 nm, 160 μJ/cm^2). Letters indicate the samples.

Several optical techniques were employed in this study. In TRPL, the samples were non-selectively excited using the 25 ps duration Nd:YAG laser pulses at 355 nm (3.49 eV) and 10 Hz repetition rate. A Hamamatsu streak camera along with a spectrometer was used for the measurements of PL spectra and kinetics. The experimental setup for time-resolved differential transmittance (DT) consisted of a PHAROS (Light Conversion) laser, delivering 1030 nm and 200 fs duration pulses at 30 kHz repetition rate and an ORPHEUS (Light Conversion) optical parametric amplifier (OPA), generating wavelengths within 630–2600 nm range. Frequency-doubled OPA pulses at 382 nm (3.25 eV) were used for selective excitation of the QWs. The white light continuum pulse served to probe the DT spectra and their decay in a 380–480 nm spectral window, using a spectrograph with 300 lines/mm grating and a CCD camera. A chopper was used to periodically close the pump pulse and measure the DT with and without excitation ($T_p(\lambda, t)$ and $T_0(\lambda)$, correspondingly) at various probe delays, providing the instantaneous $T(\lambda, t)$ spectra (in mOD units): $T(\lambda, t) = 1000 \times \log(T_0(\lambda)/T_p(\lambda, t))$.

The same laser and OPA were employed for the selective excitation of QWs in LITG measurements. Two coherent pump pulses (at 385 nm for the sample A and 399 nm for the other samples) intersected at an angle θ in a sample creating a transient pattern of spatially-modulated density of free carriers $N(x) = N_0 + \Delta N(1 + \cos[2\pi x/\Lambda])$ with a spacing $\Lambda \approx \lambda/\sin\theta$. In turn, the carrier density modulation caused spatial modulation of a refractive index $\Delta n(x)$, which amplitude was proportional to the photo-excited carrier density, $\Delta n(x) \propto \Delta N(x)$, hence a transient diffraction grating was recorded. A delayed pulse at 1030 nm served as a probe that partially diffracted on the transient diffraction grating. Time-dependent diffraction efficiency η (t) can be expressed as $\eta(t) = (2\pi n_{eh} \Delta N d/\lambda_{probe})^2 \exp(-2t/\tau_G)$, where n_{eh} is the refractive index change per one electron-hole pair, d is the layer thickness, and τ_G is the grating decay time. τ_G is composed of recombination τ_R and diffusion τ_G time components: $1/\tau_G = 1/\tau_R + 1/\tau_D$. The diffusive decay time $\tau_D = \Lambda^2/(4\pi D_a)$ depends on Λ, so values of bipolar diffusion coefficient D_a and carrier lifetime τ_R can be determined from $\tau_G(\Lambda, t)$ measurements. All the reported experiments were carried out at room temperature.

3 Results and discussion To clarify the origin of large blue shift of the PL peak with excitation, we carried out TRPL measurements for various excitation fluences. As an example, in Fig. 2a we show PL spectra in sample B at several excitations; the spectra are time-integrated over one nanosecond after excitation. With excitation, the PL peak blue-shifts from 2.69 eV to 2.90 eV (i.e., by 210 meV). The instantaneous peak position at zero time delay shifts even more (by 260 meV), as it is shown in Fig. 2b where we plot the instantaneous PL peak position as a function of

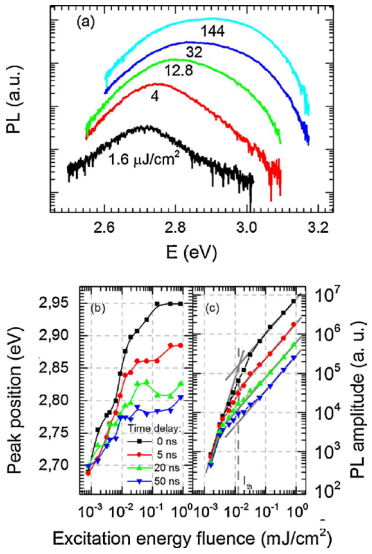

Figure 2 PL spectra recorded at various excitation energy fluences (a) and the dynamics of instantaneous PL peak position (b) and spectrally-integrated amplitude (c) with excitation for several delay times in the sample B. I_{th} indicates the threshold fluence corresponding to saturation of localized states. The spectra were integrated over 1 ns after the pump pulse. The zero delay time stands for PL signal after the end of excitation pulse.

excitation energy fluence for several delays. A closer look reveals that the peak position of the overall spectrum moves because the low energy PL peak saturates with the excitation, thus the high energy shoulder of the spectra becomes dominant approximately at 40–50 μJ/cm^2, which corresponds to ∼(3–4) × 10^{18} cm^{-3} of photoexcited carriers (assuming absorption coefficient $\alpha = 5 \times 10^4$ cm^{-1} [16] and reflection coefficient of 0.2). The blue shift of PL peak position was observed in all samples; energy span between the low and high emission peak values increased almost linearly with indium content, from 230 meV in the sample A to 500 meV in the sample E.

Temporal behavior of the PL spectra in the sample B can be seen in Fig. 2b and c, where we plot PL peak position and PL amplitude as functions of excitation energy fluence at several fixed time delays. Two excitation regions with different relaxation rates can be distinguished. Below ∼10 μJ/cm^2, PL emission is dominated by the low energy component characterized by slow relaxation of PL peak position and amplitude. At higher pump fluences, appearance of high energy component in Fig. 2a is followed by much faster relaxation of amplitude and peak position, indicating higher carrier recombination rate at the high energy wing of PL spectrum. Using one-dimensional Schrödinger-Poisson solver we estimated the PL peak shift due to the screening of the built-in electrical field (we considered a large value of 1.15 MV/cm). We estimated that with excitation increase from 2 to 200 μJ/cm^2 in a 5 nm wide QW with 10% indium, the shift should not exceed 150 meV, which is considerably less than the experimentally observed 260 meV in the sample B. This shows that while the peak shift of ∼70 meV at high excitations (20–200 μJ/cm^2) may be assigned to the electrical field screening, the shift of 190 meV at low excitations (1–20 μJ/cm^2) must be caused by other reasons.

Based on the experimental data shown in Fig. 2, we attribute the low and high energy spectral components to emission from the deeply localized and extended/shallow-localized QW states, correspondingly. This conclusion agrees with the results reported in [17–19], where similar spectral broadening at high electrical and optical injection was also observed at low temperatures and attributed to delocalized carriers. In [20] both PL emission peaks were ascribed to localized carriers; however, the energy span between the peaks did not exceed ∼40 meV in latter case.

Due to the limited density of localized states, emission from them dominates only at low carrier densities. Change in slope at zero delay time in Fig. 2c corresponds to energy fluence I_{th} when the saturation of localized states occurs; similar saturation was also observed in DT data. In Fig. 3 the threshold carrier density evaluated from I_{th} is shown for all studied samples; DT threshold was evaluated from the spectra integrated within the PL spectral region. The threshold increases with In content, which can be attributed to higher density of localized states in QWs with higher In composition. Saturation of absorption in PL spectral range allows estimation of injected carrier density that efficiently contributes to PL emission. As it is seen from Fig. 3, this density is limited to (5–15) × 10^{18} cm^{-3}, depending on In content. The integral value of the entire DT spectrum (not shown here) reveal much weaker saturation indicating that at high densities carriers are being photoexcited to the states with energies above those of the PL band.

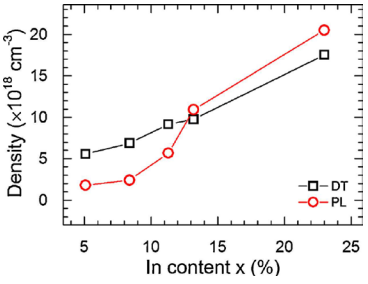

Figure 3 Photoexcited carrier density at which saturation of pulsed PL (red circles) and DT signal (black squares) occurs.

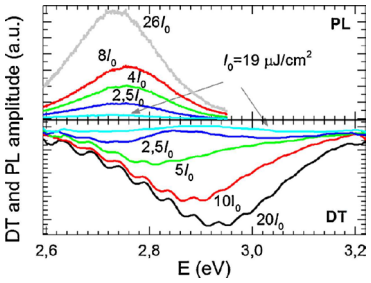

Figure 4 Time-integrated PL spectra (top) and DT spectra at 10 ps delay (bottom) for the sample D, recorded under pulsed excitation at various pump energy fluences represented in multiples of $I_0 = 19\,\mu J/cm^2$, which corresponds to 1.44×10^{18} cm^{-3} carrier density.

DT measurements were performed to collect more detailed information about the physical origin limiting the PL signal at high carrier densities. In Fig. 4 we compare PL and DT spectra in the sample D recorded at various excitations. PL spectra provide information about the electronic states participating in radiative recombination, while the differential absorption signal is sensitive to the changes in occupancy of all states, including those not seen in the PL spectra. The DT spectra have a negative sign ($T_p(\lambda, t) > T_0(\lambda)$) indicating the absorption bleaching of the photoexcited sample due to the state filling and subsequent decrease in electronic transition probability to these states. At carrier densities bellow $(3–5) \times 10^{18}$ cm^{-3} (i.e., below the PL saturation density in the sample D, see Fig. 3b), at least two components can be seen in DT spectra. One with lower energy (~2.73 eV) coincides with the PL line, while the second (~3.14 eV) appears at photon energies above the PL emission band. While the lower energy DT component can be attributed to absorption bleaching in localized and ground extended states of QW, the origin of the second band is not clear. Judging by the energy separation from the PL peak (~400 meV in Fig. 4) it could be ascribed to electronic transition between the higher order QW extended states like hh2–e2 [21]. On the other hand, the rate of e2–hh2 transition is expected to be much higher than that of the e1-hh1 one, but both DT components exhibited similar decay times on nanosecond scale. Presence of two emission bands separated spatially and spectrally has been previously observed by SNOM measurements in InGaN QWs while at low temperatures [22]. The latter data revealed a main low-energy emission region and a much weaker higher-energy region, and hence suggested that the weak-emitting areas are close to defects. The energy barrier around these defects (presumably, dislocations) allowed the carriers to avoid recombination at dislocation sites (at least at low temperatures and low excitations). Two peaks in DT spectra tentatively might be attributed to absorption bleaching in such different areas of a sample. Our measurements, performed at 300 K and at high carrier densities, were favorable for carrier thermal and optical activation, thus the higher-energy PL emission band vanished (see Fig. 4), leaving a signature of the latter band in the DT spectra. We also would like to note that the instantaneous spectra are insensitive for weak but long lasting emission.

Increasing excitation results in the broadening and blue-shift of the DT spectra, since absorption saturates at low energy side but increases at higher photon energies. In turn, this indicates the saturation of localized and probably main extended states in the QWs. It is interesting to note that carrier densities at which both PL saturation and DT broadening begin are around $(5–10) \times 10^{18}$ cm^{-3}. In addition, PL saturation is accompanied by the appearance of fast decay transients in PL and DT kinetics. In Fig. 5 we plot the decay transients of DT (left) and PL (right) signals at several spectral positions for moderate and high excitation levels. Fast component appears in both DT and PL kinetics at high excitation and is more pronounced at higher photon energies. This component is often attributed to the manifestation of enhanced radiative recombination, which rate linearly increases with carrier density. However, a simple estimation shows that this initial decay component is way too fast to be related to band-to-band recombination. Assuming carrier density of 1.3×10^{19} cm^{-3} at 160 μJ/cm^2 and a standard value of radiative recombination coefficient, $B = 5 \times 10^{-11}$ cm^3/s [23], the radiative recombination time $\tau_{rad} = 1/BN = 1.6$ ns should be expected, but the measured decay time of fast PL component at 2.88 eV is 80 ps (see Fig. 5). Therefore, this fast decay should be attributed to non-radiative recombination instead. Similar consideration excludes Auger recombination as well, since at given carrier density the characteristic Auger decay time $\tau_{Auger} = 1/CN^2$ should exceed 1 ns even assuming C as high as 1×10^{-30} cm^6/s [24, 25]. We note that the qualitative picture in all samples was similar to that described for the sample D, i.e., fast PL and DT transients appear in the spectral region of the extended states at the carrier densities close to the threshold value (Fig. 3b).

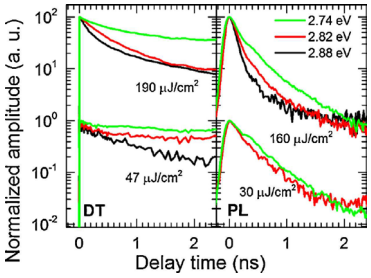

Figure 5 Decay transients of PL and DT signal at several spectral positions for two excitations in the sample D.

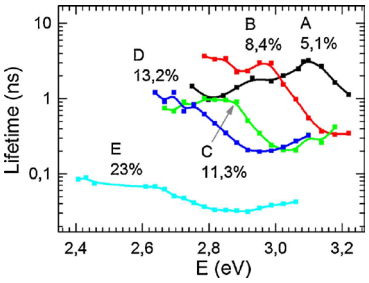

Figure 6 Spectral distribution of carrier lifetime, obtained from the DT decay measurements in all samples at 160 μJ/cm^2. Indium content of QWs is indicated in the plot.

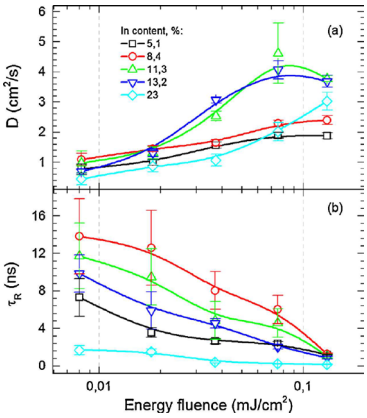

Figure 7 Diffusion coefficient D (a) and carrier lifetime τ_R (b) determined simultaneously from the LITG measurements as a function of excitation energy fluence.

Figure 6 summarizes the spectral dependence of DT decay times in the investigated samples at relatively high carrier density. Decay time at PL position (i.e., at the localized states) obviously correlates with the PL intensity of the QWs (compare with Fig. 1). Increase in indium content apparently introduces more defects, which results in lifetime drop in all the states. Wide spectrum of short lifetimes in sample E indicates a probably partially-relaxed and highly-defective structure. It is interesting to note that even some high energy states show longer decay time in the sample A if compared to the sample B, but the localized states recombine slower in the latter sample and that is reflected in its higher PL emission efficiency (as the time integrated PL efficiency is proportional to carrier lifetime). The similar situation is observed between the samples C and D (Fig. 1). It allows to conclude that PL efficiency mostly benefits from the slow recombination of carriers in the localized states within the red wing of a PL line rather than from fast band-to-band recombination of free carriers in the higher energy extended states, as one could expect keeping in mind that $I_{PL} \sim BN^2$. The presented experimental facts can be explained within the framework of density-activated non-radiative recombination [26]. At low densities, when localized (and maybe low-energy extended) states are only partially filled, the photoexcited carriers tend to occupy them, which spatially separates the carriers from the recombination centers and leads to efficient radiative recombination. As these states become filled, the carriers remain longer in the high-energy extended states [19], allowing them to diffuse to the non-radiative recombination centers. It is interesting to note that a large part of these high energy states contribute to absorption but are well above the PL emission energies, which means that with excitation the increasing part of carriers do not contribute to radiative emission.

Direct measurements of carrier lifetime and diffusion coefficient using the LITG technique (Fig. 7) provide indication that high-energy states are spatially separated from the states that determine the PL emission spectrum. Note that LITG signal is inversely proportional to the effective mass of carriers, $\eta(t) \propto N_e^2/m_e^* + N_p^2/m_p^*$, i.e., the strongest input comes from free electrons, but ambipolar diffusion is driven by both electrons and holes. In Fig. 7, an inverse correlation between D and τ_R values is seen, similarly as it was observed in other InGaN QWs and thick layers [12, 27, 28]. Carrier diffusion coefficient varies from 0.4 to 1 cm^2/s at 8 μJ/cm^2 for QWs with different In content, while it increases up to 1.9–4.6 cm^2/s at 80 μJ/cm^2. Mobility enhancement again can be understood in terms of increasing quasi-Fermi level in the bands resulting in the increasing amount of carriers in extended and, thus, mobile states. Increase in carrier mobility leads to enhanced carrier diffusion and capture by non-radiative recombination centers, what is reflected in lifetime reduction with excitation. Such a mechanism also could explain the existence of long-lasting component at energies above the PL line in DT spectra at low carrier densities – spatially separated carriers cannot relax to lower energy states. Strongest dependence of diffusivity on excitation fluence in the samples C and D, which have higher In content, pointed out that carriers become delocalized at higher excitations more easily in highly defective areas. Further analysis of this tendency requires more detailed microstructural characterization of QW, understanding its origin [29], and correlation with fast carrier transfer from the localized areas to neighbor defect regions under strong photoexcitation conditions. These studies may also be helpful to link the impact of QW microstructures with the LED efficiency droop.

4 Conclusions We performed time and spectrally resolved photoluminescence and differential transmission measurements combined with light induced transient gratings technique to study correlations in carrier well structures with x varying from 5.1% to 23%. PL saturation has been observed at carrier densities from 2 to 20 × 10^{18}

cm^{-3}. It was related to the filling of localized and low-energy extended electronic states, located within the PL band, and carrier transfer to the higher energy extended states. Fast recombination transients appearing at high carrier density correlated with the lifetime in extended states and thus were attributed to density-activated non-radiative carrier capture from the latter states by defect sites. Inverse correlation between the carrier diffusion coefficient and lifetime confirmed that the rate of non-radiative recombination in quantum well increases as more carriers are transferred to mobile extended states, thus diffusion length is getting shorter in green-emitting QWs. Time-integrated PL efficiency at high excitations is strongly influenced by the decreasing carrier lifetime in the extended states.

Acknowledgements This work at Vilnius University was supported by the European Social Fund under Project VP1-3.1-ŠMM-07-K-02-006.

References

[1] J. Piprek, Phys. Status Solidi A **207**, 2217 (2010).
[2] G. Verzellesi, D. Saguatti, M. Meneghini, F. Bertazzi, M. Goano, G. Meneghesso, and E. Zanoni, J. Appl. Phys. **114**, 071101 (2013).
[3] R. W. Martin, P. G. Middleton, K. P. O'Donnell, and W. Van der Stricht, Appl. Phys. Lett. **74**, 263 (1999).
[4] T. Langer, A. Kruse, F. A. Ketzer, A. Schwiegel, L. Hoffmann, H. Jönen, H. Bremers, U. Rossow, and A. Hangleiter, Phys. Status Solidi C **8**, 2170 (2011).
[5] A. Kaneta, M. Funato, and Y. Kawakami, Phys. Rev. B **78**, 125317 (2008).
[6] A. Avramescu, T. Lermer, J. Müller, C. Eichler, G. Bruederl, M. Sabathil, S. Lutgen, and U. Strauss, Appl. Phys. Express **3**, 061003 (2010).
[7] A. Vertikov, I. Ozden, and A. V. Nurmikko, J. Appl. Phys. **86**, 4697 (1999).
[8] T. Li, A. M. Fischer, Q. Y. Wei, F. A. Ponce, T. Detchprohm, and C. Wetzel, Appl. Phys. Lett. **96**, 031906 (2010).
[9] R. Aleksiejūnas, M. Sūdžius, T. Malinauskas, J. Vaitkus, K. Jarašiūnas, and S. Sakai, Appl. Phys. Lett. **83**, 1157 (2003).
[10] K. Jarašiūnas, T. Malinauskas, R. Aleksiejūnas, M. Sūdžius, E. Frayssinet, B. Beaumont, J.-P. Faurie, and P. Gibart, Phys. Status Solidi A **202**, 566 (2005).
[11] A. Kaneta, T. Mutoh, Y. Kawakami, S. Fujita, G. Marutsuki, Y. Narukawa, and T. Mukai, Appl. Phys. Lett. **83**, 3462 (2003).
[12] R. Aleksiejūnas, K. Gelžinytė, S. Nargelas, K. Jarašiūnas, M. Vengris, E. A. Armour, D. P. Byrnes, R. A. Arif, S. M. Lee, and G. D. Papasouliotis, Appl. Phys. Lett. **104**, 022114 (2014).
[13] Özgür, H. O. Everitt, S. Keller, and S. P. DenBaars, Appl. Phys. Lett. **82**, 1416 (2003).
[14] R. R. Pela, C. Caetano, M. Marques, L. G. Fereira, J. Furthmüller, and L. K. Teles, Appl. Phys. Lett. **98**, 151907 (2011).
[15] G. Orsal, Y. El Gmili, N. Fressengeas, J. Streque, R. Djerboub, T. Moudakir, S. Sundaram, A. Ougazzaden, and J. P. Salvestrini, Opt. Mater. Express **4**, (2014).
[16] M. Nawaz and A. Ashfaq, Semicond. Sci. Technol. **27**, 035019 (2012).
[17] G. Sun, G. Xu, Y. J. Ding, H. Zhao, G. Liu, J. Zhang, and N. Tansu, Appl. Phys. Lett. **99**, 081104 (2011).
[18] M. J. Davies, T. J. Badcock, P. Dawson, M. J. Kappers, R. A. Oliver, and C. J. Humphreys, Appl. Phys. Lett. **102**, 022106 (2013).
[19] N. I. Bochkareva, Y. T. Rebane, and Y. G. Shreter, Appl. Phys. Lett. **103**, 191101 (2013).
[20] Z. Li, J. Kang, B. W. Wang, H. Li, Y. H. Weng, Y.-C. Lee, Z. Liu, X. Yi, Z. C. Feng, and G. Wang, J. Appl. Lett. **115**, 083112 (2014).
[21] T. Schulz, A. Nirschl, P. Drechsel, F. Nippert, T. Markurt, M. Albrecht, and A. Hoffman, Appl. Phys. Lett. **105**, 181109 (2014).
[22] F. Hitzel, G. Klewer, S. Lahmann, U. Rossow, and A. Hangleiter, Phys. Rev. B **72**, 0813 (2005).
[23] X. Li, S. Okur, F. Zhang, V. Avrutin, Özgür, H. Morkoç, S. M. Hong, S. H. Yen, T. C. Hsu, and A. Matulionis, J. Appl. Phys. **111**, 063112 (2012).
[24] S. Xia, Z. M. S. Li, W. Lu, Z. H. Zhang, Y. Sheng, and L. W. Cheng, Appl. Phys. Lett. **99**, 233501 (2011).
[25] T. Sadi, P. Kivisaari, J. Oksanen, and J. Tulkki, Appl. Phys. Lett. **105**, 091106 (2014).
[26] J. Hader, J. V. Moloney, and S. W. Koch, Appl. Phys. Lett. **96**, 221106 (2010).
[27] K. Jarašiūnas, S. Nargelas, R. Aleksiejūnas, S. Miasojedovas, M. Vengris, S. Okur, H. Morkoç, Ü. Özgür, C. Giesen, Ö. Tuna, and M. Heuken, J. Appl. Phys. **113**, 103701 (2013).
[28] T. Malinauskas, A. Kadys, T. Grinys, S. Nargelas, R. Aleksiejūnas, S. Miasojedovas, J. Mickevičius, R. Tomašiūnas, K. Jarašiūnas, M. Vengris, S. Okur, V. Avrutin, X. Li, F. Zhang, U. Özgür, and H. Morkoç, Proc. SPIE **8622**, 82621S (2012).
[29] R. A. Oliver, S. E. Bennett, T. Zhu, D. J. Beesley, M. J. Kappers, D. W. Saxey, A. Cerezo, and C. J. Humphreys, J. Phys. D, Appl. Phys. **43**, 354003 (2010).

3rd publication / 3 publikacija

Enhancement of quantum efficiency in InGaN quantum wells by using superlattice interlayers and pulsed growth

K. Nomeika, M. Dmukauskas, R. Aleksiejūnas, P. Ščajev, S. Miasojedovas, A. Kadys, S. Nargelas, K. Jarašiūnas

Lithuanian Journal of Physics **55** (2016) 255–263
DOI:10.3952/physics.v55i4.3221

Lithuanian Journal of Physics, Vol. **55**, No. 4, pp. 255–263 (2015)

ENHANCEMENT OF QUANTUM EFFICIENCY IN InGaN QUANTUM WELLS BY USING SUPERLATTICE INTERLAYERS AND PULSED GROWTH

K. Nomeika, M. Dmukauskas, R. Aleksiejūnas, P. Ščajev, S. Miasojedovas, A. Kadys, S. Nargelas, and K. Jarašiūnas

Institute of Applied Research, Vilnius University, Saulėtekio 9, LT-10222 Vilnius, Lithuania
E-mail: kazimieras.nomeika@tmi.vu.lt

Received 22 June 2015; revised 21 July 2015; accepted 29 September 2015

Enhancement of internal quantum efficiency (IQE) in InGaN quantum wells by insertion of a superlattice interlayer and applying the pulsed growth regime is investigated by a set of time-resolved optical techniques. A threefold IQE increase was achieved in the structure with the superlattice. It was ascribed to the net effect of decreased internal electrical field due to lower strain and altered carrier localization conditions. Pulsed MOCVD growth also resulted in twice higher IQE, presumably due to better control of defects in the structure. An LED (light emitting diode) structure with a top p-type contact GaN layer was manufactured by using both growth techniques with the peak IQE equal to that in the underlying quantum well structure. The linear recombination coefficient was found to gradually increase with excitation due to carrier delocalization, and the latter dependence was successfully used to fit the IQE droop.

Keywords: light emitting diodes, nitride semiconductors, photoluminescence, carrier recombination, carrier diffusion

PACS: 73.21.Fg, 78.67.-n, 78.47.-p

1. Introduction

GaN-based structures for light emitting diodes (LEDs) and other optoelectronic devices are grown predominantly on sapphire substrates by the MOCVD technique, because GaN substrates for homoepitaxial growth remain to be expensive and difficult to obtain. A large mismatch of the lattice constants and the thermal expansion coefficients between GaN and sapphire result in considerable strain, which in turn gives rise to a large amount of dislocations and an internal piezoelectric field. The high internal electric field quenches the internal quantum efficiency (IQE) in GaN-based quantum structures due to the quantum confined Stark effect. Therefore, several technological modifications of the LED structure have been developed to relieve the strain in the material. Most of these approaches involve inserting a buffer layer between the sapphire wafer and LED active structure, like a low-temperature GaN layer [1], AlN or AlGaN layer [2], SiO_2 layer with openings for overgrowth [3], or a short period superlattice (SL) [4]. It has been demonstrated that the SL insertion layer results in increase of IQE [5, 6] and smaller photoluminescence (PL) peak shift with injection [4] due to supposedly smaller defect density and lower internal electrical fields. SL was also used to improve the electroluminescence due to better hole injection and current spreading [7–9].

On the other hand, IQE depends on structural quality of InGaN quantum wells that determine the amount of defects and, consequently, nonradiative recombination time. It is well known that IQE drops as the In content is increased, mostly due to lower growth temperatures needed to achieve larger In amount in the layers. A promising technique for achieving metal rich InGaN layers of good quality is a pulsed growth. This technique was mainly used for InN growth, but it has also been demonstrated as a promising tool for InGaN growth by metal-modulated epitaxy [10], high-pressure MOCVD [11, 12], and recently by low pressure MOCVD [13].

In this paper, we analyze the effects of SL insertion and the pulsed growth on IQE by monitoring carrier dynamics in the InGaN quantum well (QW) structures

emitting at 450–460 nm. Optical properties and carrier dynamics features are compared between (i) QW structures with and without an SL interlayer and (ii) identical QW samples grown by continuous or pulsed growth. We employ a number of time-resolved techniques like light-induced transient gratings (LITG), differential transmission (DT), free carrier absorption (FCA), and photoluminescence (PL) to obtain a detailed picture of carrier recombination pathways. We demonstrate a three-fold increase in IQE in the structure with an SL and a two-fold one in the pulsed grown sample, as compared to that of the corresponding reference structures. We analyze the effects of changes in the internal electrical field and carrier delocalization on the IQE in the structures. We also demonstrate that a full LED structure with a p-contact layer may reach the peak IQE equal to that of the underlying MQW structure.

2. Samples and measurement techniques

Two sets of MQWs structures under investigation were grown by MOCVD on (0001) sapphire with a ~3 μm thick GaN template. Ammonia (NH_3), trimethylgallium (TMG), trimethylindium (TMI), trimethylaluminum (TMA), silane, and magnesium bispentacyclodienyl (Cp_2Mg) were used as source compounds, nitrogen and hydrogen were used as carrier gases.

In the first set of MQWs samples (samples *A* and *B*) we investigated an impact of InGaN/GaN SL as a crystal grating stress modified interlayer between the GaN template and MQWs. The SL growth parameters in sample *A* were optimized: the SL structure consists of 8 periods of $In_{0.06}Ga_{0.94}N$/GaN heterostructures with a total thickness of 30–35 nm. The active regions of the structures contained five (3–4) nm wide $In_{0.1}Ga_{0.9}N$ QWs separated by 6 nm wide GaN quantum barriers. The whole structure is capped by a 30 nm thick GaN layer. Sample *B* was grown under identical conditions, but without SL.

In the second set of 3 samples (samples *1*, *2*, *3*) we analyzed impact of the pulsed growth on QW and full LED quantum efficiency. All samples were grown on a 3 μm thick GaN template on sapphire together with an optimized SL interlayer which has been described above. The active part consisted of 5 periods $In_{0.1}Ga_{0.9}N$/GaN multiple QW structure 3–4 nm thick wells and 6 nm thick barriers. A reference InGaN/GaN MQW structure (sample *1*) was grown in a conventional precursor continuous-flux mode. In the pulsed growth mode, NH_3 was constantly flowing, while TMI and TMG were sent into a chamber for 15 s, and then bypassed for 5 s (sample *2*). More details of the pulsed growth MOCVD can be found in Ref. [14]. Finally, a full LED structure with a top 40 nm thick p-type $Al_{0.1}Ga_{0.9}N$ blocking layer and a 300 nm thick p-type GaN layer was grown (sample *3*).

The experimental set-up for the time-resolved DT consisted of a PHAROS (*Light Conversion*) laser, delivering 1030 nm and 200 fs duration pulses at the 30 kHz repetition rate and an ORPHEUS (*Light Conversion*) optical parametric amplifier (OPA), generating wavelengths in the 630–2600 nm range. Frequency doubling of OPA pulses was used to set the wavelength of one of the split beams from the laser for the selective excitation (382 nm, 3.25 eV) of the QWs in the samples while the other delayed beam was passed through a sapphire crystal to generate a white light continuum probe. A spectrograph with the 300 lines/mm grating and a CCD camera spectrometer provided means to observe the evolution of DT spectra in a 380–480 nm window. A chopper was used to periodically close the pump pulse and measure the DT with and without excitation ($T_p(\lambda, t)$ and $T_0(\lambda)$, respectively) at various probe delays, providing the instantaneous $T(\lambda, t)$ spectra (in mOD units): $T(\lambda, t) = 1000 \times \log(T_0(\lambda)/T_p(\lambda, t))$.

FCA and PL IQE measurements were carried out using the same laser system as in DT. In FCA, the second OPA was used for a probe beam. The probe was tuned to 1.65 μm (0.75 eV). An integrating sphere with the three-measurement approach was used for the evaluation of PL IQE [15]. In the three-measurement approach 3 PL spectra are taken: one with an empty sphere, one with the sample in the sphere but out of the path of the pump beam and one with the sample in the sphere and in the path of the pump beam. For both experiments, the pump was 390 nm (3.18 eV).

The YAG:Nd^{3+} laser with 25 ps pulse duration and 10 Hz repetition rate was combined with a *Hamamatsu* C10627 streak camera and an *Acton* SP2300 monochromator for TRPL measurements, providing a temporal resolution of 20 ps. With the water Raman-shift of the third laser harmonic (355 nm) the wavelength of the pump beam was 405 nm (3.06 eV).

For the LITG experiment, the same YAG:Nd^{3+} laser with the water Raman-shifted pump to 405 nm was used. The principle of the technique is the excitation of the sample by an interference field of two coherent pump beams, creating a transient spatially modulated free carrier pattern $N(x) = N_0 + \Delta N(1 + \cos[2\pi x/\Lambda])$ with spacing Λ, which modulates the refractive index $\Delta n(x) \propto \Delta N(x)$ and diffracts a delayed probe beam (1064 nm – 1.17 eV, fundamental laser harmonic). Diffraction efficiency of a transient grating $\eta(t) \propto (\Delta Nd)^2$ and its decay $1/\tau_g = 1/\tau_R + 1/\tau_D$ provided a convenient way to determine the recombination-governed

grating decay time τ_R and the diffusive decay time $\tau_D = \Lambda^2/(4\pi^2 D_a)$. The latter is Λ dependent, therefore the bipolar diffusion coefficient D_a was determined by performing measurements with different induced grating periods at various photoexcited carrier densities.

The reflectivity of the samples was 0.3 for the FCA experiment (because of the Brewster's angle of the sample in respect of the pump beam) and 0.2 for other techniques. For the calculations of photoexcited carrier densities the absorption coefficient $\alpha = 10^5$ cm^{-1} was taken, which resulted in 1.35×10^{19} cm^{-3} for the 100 μJ/cm^2 excitation energy fluence.

3. Results and discussion

Figure 1(a) shows the IQE as a function of photoexcited carrier density in the samples with and without an SL layer. Both IQE curves reveal the typical features of "efficiency droop" in InGaN QWs: the IQE value increases up to carrier densities of $(1–3) \times 10^{19}$ cm^{-3} and starts to decline at higher excitations. SL insertion resulted in threefold increase of the peak IQE value (30% in sample *A* versus 10% in sample *B*) and much "flatter" IQE vs the excitation curve. We note a rather large blueshift of the PL peak position with excitation in sample *B* (170 meV), compared to the shift by 40 meV in sample *A* (Fig. 1(b)). Consequently, a full width at the half maximum (FWHM) of the PL spectrum in sample *B* became considerably broader at high excitations, while at low ones the FWHM values were similar in both structures (Fig. 1(c)). Different blueshift and emission wavelengths can be attributed to the effects of the internal electrical field. A larger blueshift with excitation indicates a stronger internal piezo electrical field in sample *B* due to larger strain, while much shorter emission wavelengths at high carrier densities point out a smaller indium amount in this structure. The reported strain relaxation due to the SL [4] and slower indium incorporation in the compressively strained QWs [16] support the latter assumption. In addition, TEM and XRD data (to be reported elsewhere) suggest that the QW growth rate is larger in more strained structures. As a result, thinner QWs with higher In content can be expected in sample *A*, which is favourable for higher IQE [17, 18] and smaller efficiency droop. The impact of

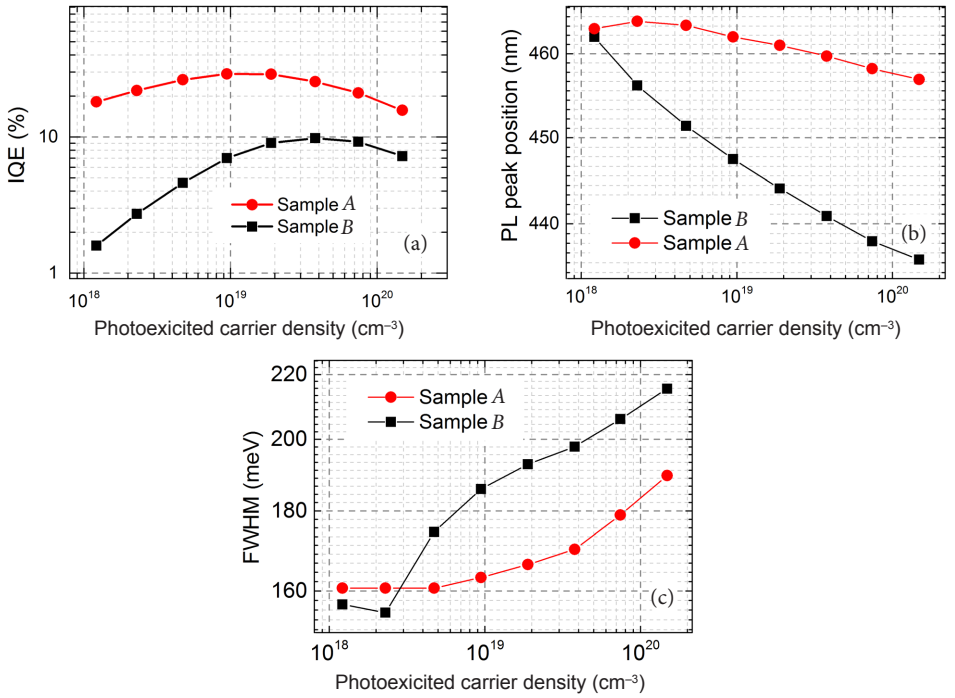

Fig. 1. Photoluminescence quantum efficiency (a), peak position of PL spectra (b), and FWHM (c) as a function of photoexcited carrier density in the structures with SL (sample *A*, red) or without SL (sample *B*, black).

the internal electrical field, however, cannot fully account for differences in IQE, especially at high carrier densities. Also, large PL peak shift can be caused by saturation of localized states at a low energy side of the PL spectrum [19–22].

Time-resolved FCA, PL, and DT measurements were carried out for a direct observation of carrier dynamics and discrimination between the radiative and non-radiative recombination pathways. The FCA technique allowed determination of the average lifetime of the net carrier population, while DT provided complementary information on temporal changes in the occupancy of particular states. Figure 2(a) shows the FCA kinetics recorded in sample *A* for various excitation energy densities within the 30–890 μJ/cm^2 range. The peak amplitude of the transients increases linearly with the carrier density within the entire excitation range, thus confirming a linear increase of the photoexcited carrier density and the absence of absorption bleaching. A precise calibration of the carrier density N and density-dependent recombination constants of the ABC model [23] is feasible under this condition. For the sake of estimation simplicity, an instantaneous decay time at the very initial part of the kinetics (within 90–200 ps after the pump) was calculated as a function of N (Fig. 2(b)). The latter dependence revealed a close to the linear decrease of lifetime with excitation which may be attributed either to the increase of the radiative recombination rate ($1/\tau_{rad} \sim B_{rad}N$, where B_{rad} is the radiative recombination coefficient) or to the density-activated nonradiative recombination after carriers escape from the potential minima and are captured by traps [24], which can be expressed by the nonradiative recombination rate $A(N) = B_{nr}N$. If both processes take place simultaneously, only a part of the total density-dependent recombination rate can contribute to the radiative decay, i. e. $B^* = B_{rad} + B_{nr}$, in agreement with our previous observations [25, 26].

We applied the described models for the analysis of the excitation-dependent carrier lifetime. Following the standard ABC model, the constant non-radiative recombination coefficient A (or excitation-independent nonradiative lifetime $\tau_{NR} = 1/A$) and the effective recombination coefficient $B^* \sim 1/N$ can be obtained from the fitting of the decay time $\tau = (A + B^*N + CN^2)^{-1}$, where C is the Auger recombination term. The Auger term is considered as a possible mechanism of non-radiative losses; however, it should be important only at carrier densities well above 10^{19} cm^{-3} due to a small value (~10^{-31} cm^6/s) in InGaN [27]. For both samples $\tau_{NR} = 1/A \approx 35$ ns was estimated from TRPL transients at long delay times (>30 ns); this term is dominant at carrier densities below 10^{18} cm^{-3}. The values of the recombination coefficient B^* were estimated from Fig. 2(b) as 0.8×10^{-11} cm^3/s and 2.4×10^{-11} cm^3/s for samples *B* and *A*, respectively. The ratio of three between the B^* as well the IQE values agrees quite well for these samples, suggesting that competition between the radiative and nonradiative processes varies with excitation and depends on the sample structural quality. On the other hand, different IQE values may be a consequence of different density of carriers contributing to radiative recombination. We fitted the measured IQE curves with the modified AB*C model:

$$IQE = \frac{B_{rad}N}{A + (B_{rad} + B_{nr})N}. \quad (1)$$

To better account for the IQE droop, saturation of B_{rad} with the excitation due to the phase-state filing was included [28]:

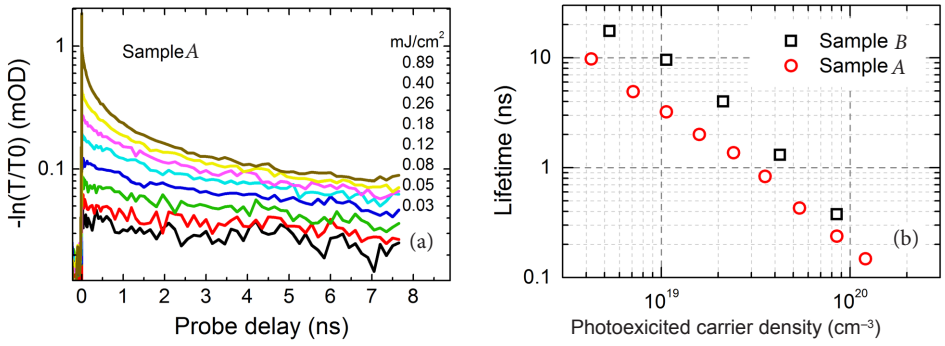

Fig. 2. (a) FCA kinetics in sample *A* at various excitations. (b) Instantaneous carrier lifetime at 100–200 ps delay as a function of photoexcited carrier density.

$$B_{\mathrm{rad}} = \frac{B_0}{1+\frac{N}{N^*}}. \qquad (2)$$

Here, B_0 is the unsaturated recombination coefficient and N^* is the threshold carrier density of saturation. $B^* = B_{\mathrm{rad}} + B_{\mathrm{nr}} = \mathrm{const}$ was also assumed since FCA measurements showed no saturation of the net B^* term. A good fit of IQE curves was obtained under these assumptions, without adding the Auger term (Fig. 3). Equation (1) allowed obtaining exact absolute IQE values, while the standard ABC with the C term of 2×10^{-31} cm^6/s yields in an overestimated IQE. Fitting parameters were as follows: $1/A$ = 26 ns, $B^* = 2.4 \times 10^{-11}$, $N^* = 9.4 \times 10^{19}$ cm^{-3}, $B_0 = 0.9 \times 10^{-11}$ cm^3/s (sample A); $1/A$ = 15 ns, $B^* = 0.8 \times 10^{-11}$, $N^* = 20 \times 10^{19}$ cm^{-3}, $B_0 = 0.11 \times 10^{-11}$ cm^3/s (sample B). Net B^* values were taken from the fit in Fig. 2(b). The analysis of Eq. (1) shows that the peak IQE value is governed by the ratio of $B_{\mathrm{rad}}/B_{\mathrm{nr}}$: this ratio is 0.6 and 0.16 in samples A and B, which correlates with the IQE peak values of 30 and 10%. The efficiency droop occurs due to the expected saturation of B_{rad} [29] and predominantly due to the increase of B_{nr} [26, 30]. The initially constant A term, being relatively small in the samples, has some impact only at lower excitations. Different values of the radiative recombination efficiency B_{rad} in the samples can be attributed to the quantum confined Stark effect: stronger electrical field results in larger separation of electron-hole wave functions and smaller radiative recombination in sample B. We note that N^* values can also be affected by the electrical field, since it is not accounted for in the simplistic model (1).

To assess the physical reasons behind the lower radiative recombination rate in sample B, we measured and compared the PL and DT spectra at various excitations and delay time instants (Fig. 4). The DT signal has a negative sign indicating the bleaching of absorption in the bandgap vicinity. A shift between the spectral positions of DT and PL spectra indicates that absorption occurs in higher energy states (presumably in the extended states of a QW), then carriers relax in low energy localized states, where radiative recombination occurs. An overlap between the DT and PL spectra pointed out to the most efficient spectral range of carrier transfer from high to low energy states. This process may influence the PL efficiency, since the PL efficiency from the high energy states is low if compared to that from the localized low energy states [31]. At the 46 μJ/cm^2 excitation (corresponding to 6.2×10^{18} cm^{-3} carrier density), the shift between PL and DT spectra is 25 and 31 nm in samples A and B, respectively. Larger separation between the absorption and PL peaks results in smaller IQE in sample B, especially at lower excess carrier densities. With increasing excitation,

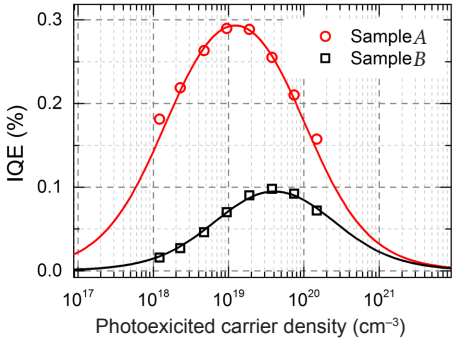

Fig. 3. Fitted IQE curves using the (1) model.

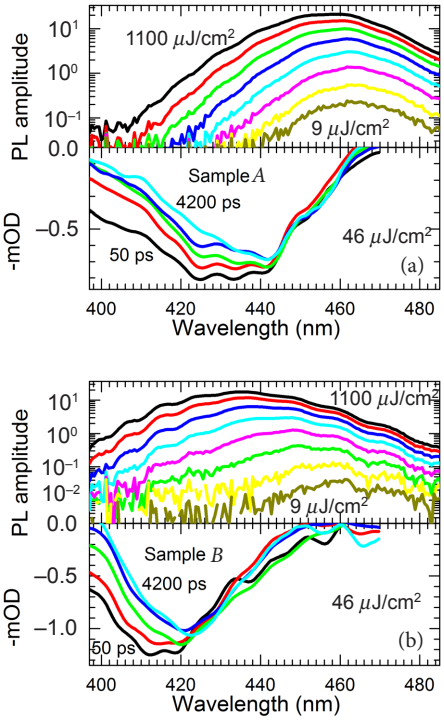

Fig. 4. Time-integrated PL spectra at various excitations (top figures, excitation range is indicated on the plot) and differential transmission (DT) spectra at various delay times (bottom figures) in samples with SL (a) and without SL (b).

the PL spectra broaden as the localized states get saturated and the fast PL transients point to emission from the higher energy. This broadening is larger in sample *B* (Fig. 1(c)), pointing out to lower density of the localized states in it with respect to sample *A*.

Stronger carrier localization in sample A is further evidenced by the dependence of the diffusion coefficient *D* on carrier density (Fig. 5). *D* is equal to 0.5 cm^2/s and 1 cm^2/s at carrier density of 1 × 10^{19} cm^{-3} in samples *A* and *B*, respectively. It increases with excitation in both samples, but the increase is more pronounced in sample *B*. LITG gives the bipolar diffusion coefficient, which under the used experimental conditions is proportional to the hole mobility [32]. We explain higher mobility of free carriers (holes) in sample *B* by a larger part of free carriers occupying the extended states in QWs, as compared to that of sample *A*. With increasing excitation, a relatively larger part of carriers is being transferred to the extended states, and this is reflected in asymmetrical broadening of DT and PL spectra towards higher energies. A similar effect has been reported previously [26]. Therefore, it can be suggested that larger increase in the *D* value is also a signature of faster non-radiative recombination and, thus, lower IQE at high excitations. Delocalization of presumably holes and subsequent increase of non-radiative recombination of carriers with increasing density is the physical origin of the term B_{nr} and a possible reason for IQE droop.

An impact of the pulsed MOCVD growth on the IQE of QW structures was investigated by performing similar measurements of IQE, time-resolved PL, DT spectra, and LITG kinetics. Here a set of 3 samples was analyzed.

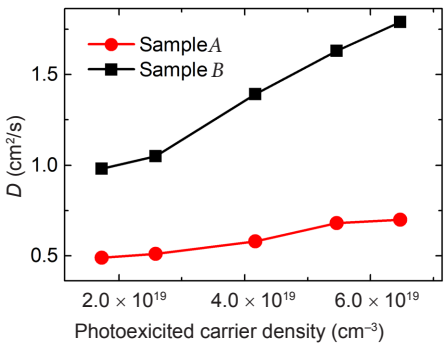

Fig. 5. Diffusion coefficient as a function of photoexcited carrier density.

Figure 6(a) shows the comparison of IQE in the samples grown under continuous or pulsed growth mode (sample *1* and sample *2*, respectively). The pulsed growth resulted in almost twofold IQE increase with respect to the reference structure. In contrast to the previous set, the peaks of the IQE curves appear at similar carrier density of ~2 × 10^{19} cm^{-3} in both samples. This value is close to that in sample *A*, which confirms that the droop threshold density is closely related to the structure of the sample, since the latter determines the strain, internal electrical field strength, and carrier localization. The latter is weaker in the reference structure, as evidenced by higher carrier diffusivity with respect to the pulsed growth structure (Fig. 6(b)). Moreover, even slightly weaker carrier localization and higher *D* value in the LED structure lead to its low IQE value at low excitations (sample *3*). The LED structure also exhibits larger PL blueshift with excitation (~70 meV) if compared to sample *2* (30 meV, Fig. 7). Similarly

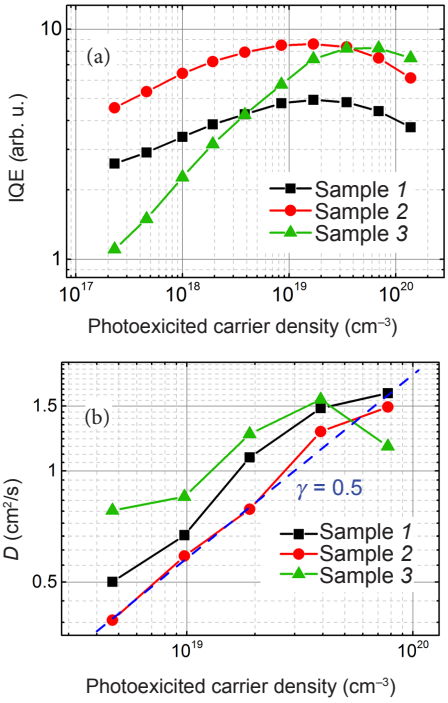

Fig. 6. IQE values (a) and diffusion coefficient (b) as a function of carrier density in the structures grown under continuous (sample *1*) or pulsed growth (sample *2*), and in the full LED structure (sample *3*).

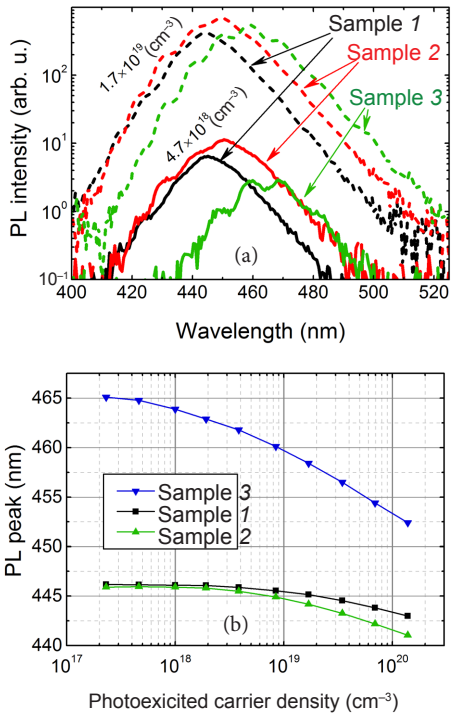

Fig. 7. PL spectra (a) and PL peak position vs carrier density (b) in samples *1*, *2* and *3*.

like in the previous set, a larger blueshift can be a mixture of larger screening effects due to stronger electric fields and saturation of localized states. Both effects, however, have a similar negative influence on IQE at low excitations and are eliminated at high carrier densities, where IQE of the LED structure reaches the same peak value as in sample *2*. The latter fact indicates a relatively low defect density and low non-radiative recombination rate A. It is evidenced by TRPL measurements: $1/A = \tau$ values are 13.5, 27, and 49 ns at 1.4×10^{18} cm^{-3} in samples *1*, *2*, and *3*, respectively. Long lifetime and high IQE at high excitations indicate that the top p-GaN layer has a negligible negative effect on LED performance, which is often the case due to diffusion of Mg dopants to the active MQW area [33].

4. Conclusions

Insertion of the superlattice interlayer and the pulsed MOCVD growth were employed and yielded three- and two-fold enhancement of IQE in InGaN/GaN QWs, respectively. A detailed investigation by time-resolved transient grating, photoluminescence, free carrier absorption, and differential transmission techniques was employed to analyze the physical origins of IQE increment and IQE droop at high carrier densities. The superlattice interlayer resulted in lower strain and smaller internal electrical field in the MQW samples. A crucial influence of carrier delocalization to IQE and its droop was evidenced by an inverse correlation between the IQE values and carrier diffusion coefficient: the increase in diffusivity resulted in the drop of IQE in all samples. A simple model based on the modified ABC rate equation with the excitation-dependent A term was used to account for increasing rate of nonradiative recombination with the excitation. The IQE droop was explained assuming the linear increase of both radiative and nonradiative recombination rates, together with the saturation of the radiative recombination coefficient due to phase-space filling. Finally, a LED structure with a p-type contact layer was grown with the peak IQE similar to that of the underlying MQW structure.

Acknowledgements

This work at Vilnius University was supported by the European Social Fund under Project VP1-3.1-ŠMM-07-K-02-006.

References

[1] S. Nakamura, GaN growth using GaN buffer layer, Jpn. J. Appl. Phys. **30**(10A), L1705 (1991), http://dx.doi.org/10.1143/JJAP.30.L1705

[2] H. Amano, N. Sawaki, I. Akasaki, and Y. Toyoda, Metalorganic vapor phase epitaxial growth of a high quality GaN film using an AlN buffer layer, Appl. Phys. Lett. **48**(5), 353–355 (1986), http://dx.doi.org/10.1063/1.96549W

[3] A. Sakai, H. Sunakawa, and A. Usui, Defect structure in selectively grown GaN films with low threading dislocation density, Appl. Phys. Lett. **71**(5), 2259–2261 (1997), http://dx.doi.org/10.1063/1.120044

[4] S.J. Leem, Y.C. Shin, K.C. Kim, E.H. Kim, Y.M. Sung, Y. Moon, S.M. Hwang, and T.G. Kim, The effect of the low-mole InGaN structure and InGaN/GaN strained layer superlattices on optical performance of multiple quantum well active layers, J. Cryst. Growth **311**(1), 103–106 (2008), http://dx.doi.org/10.1016/j.jcrysgro.2008.10.047

[5] S.P. Chang, C.H. Wang, C.H. Chiu, J.C. Li, Y.S. Lu, Z.Y. Li, H.C. Yang, H.C. Kuo, T.C. Lu, and S.C. Wang, Characteristics of efficiency droop in GaN-based light emitting diodes with an insertion layer between the multiple quantum wells and

n-GaN layer, Appl. Phys. Lett. **97**(25), 251114 (2010), http://dx.doi.org/10.1063/1.3531957

[6] W.V. Lundin, A.E. Nikolaeva, A.V. Sakharova, E.E. Zavarina, G.A. Valkovskiy, M.A. Yagovkina, S.O. Usov, N.V. Kryzhanovskaya, V.S. Sizov, P.N. Brunkov, A.L. Zakgeim, A.E. Cherniakov, N.A. Cherkashin, M.J. Hytch, E.V. Yakovlev, D.S. Bazarevskiy, M.M. Rozhavskaya, and A.F. Tsatsulnikov, J. Cryst. Growth **315**(1), 267–271 (2011), http://dx.doi.org/10.1016/j.jcrysgro.2010.09.043

[7] T.C. Wen, S.J. Chang, C.T. Lee, W.C. Lai, and J.K. Sheu, Nitride-based LEDs with modulation-doped $Al_{0.12}Ga_{0.88}N$-GaN superlattice structures, IEEE Trans. Electron Dev. **51**(10), 1743–1746 (2004), http://dx.doi.org/10.1109/TED.2004.835985

[8] Y.J. Liu, T.Y. Tsai, C.H. Yen, L.Y. Chen, T.H. Tsai, and W.C. Liu, Characteristics of a GaN-based light-emitting diode with an inserted p-GaN/i-InGaN superlattice structure, IEEE J. Quantum Electron. **46**(4), 492–498 (2010), http://dx.doi.org/10.1109/JQE.2009.2037337

[9] T. Jeong, H.J. Park, J.W. Ju, H.S. Oh, J.H. Baek, J.S. Ha, G.H. Ryiu, and H.Y. Ryu, High efficiency InGaN blue light-emitting diode with >4 W output power at 3 A, IEEE Photon. Technol. Lett. **26**(7), 649–652 (2014), http://dx.doi.org/10.1109/LPT.2014.2301874

[10] M. Moseley, B. Gunning, J. Greenlee, J. Lowder, G. Namkoong, and W.A. Doolittle, Observation and control of the surface kinetics of InGaN for the elimination of phase separation, J. Appl. Phys. **112**(1), 014909 (2012), http://dx.doi.org/10.1063/1.4733347

[11] N. Dietz, M. Alevli, V. Woods, M. Strassburg, H. Kang, and I.T. Ferguson, The characterization of InN growth under high-pressure CVD conditions, Phys. Status Solidi B **242**(15), 2985–2994 (2005), http://dx.doi.org/10.1002/pssb.200562246

[12] V. Woods and N. Dietz, InN growth by high-pressures chemical vapor deposition: Real-time optical growth characterization, Mater. Sci. Eng. B **127**(2–3), 239–250 (2006), http://dx.doi.org/10.1016/j.mseb.2005.10.032

[13] A. Kadys, T. Malinauskas, M. Dmukauskas, I. Reklaitis, K. Nomeika, V. Gudelis, R. Aleksiejūnas, P. Ščajev, S. Nargelas, S. Miasojedovas, and K. Jarašiūnas, Photoluminescence features and carrier dynamics in InGaN heterostructures with wide staircase interlayers and differently shaped quantum wells, Lith. J. Phys. **54**(3), 187–198 (2014), http://dx.doi.org/10.3952/physics.v54i3.2959

[14] A. Kadys, T. Malinauskas, T. Grinys, M. Dmukauskas, J. Mickevičius, J. Aleknavičius, R. Tomašiūnas, A. Selskis, R. Kondrotas, S. Stanionytė, H. Lugauer, and M. Strassburg, Growth of InN and In-rich InGaN layers on GaN templates by pulsed metal-organic chemical vapor deposition, J. Electron. Mater. **44**(1), 188–193 (2015), http://dx.doi.org/10.1007/s11664-014-3494-6

[15] S. Leyre, E. Coutino-Gonzalez, J.J. Joos, J. Ryckaert, Y. Meuret, D. Poelman, P.F. Smet, G. Durinck, J. Hofkens, G. Deconinck, and P. Hanselaer, Absolute determination of photoluminescence quantum efficiency using an integrating sphere setup, Rev. Sci. Instrum. **85**(12), 123115 (2014), http://dx.doi.org/10.1063/1.4903852

[16] S. Valdueza-Felip, E. Bellet-Amalric, A. Núñez-Cascajero, Y. Wang, M.-P. Chauvat, P. Ruterana, S. Pouget, K. Lorenz, E. Alves, and E. Monroy, High In-content InGaN layers synthesized by plasma-assisted molecular-beam epitaxy: Growth conditions, strain relaxation, and In incorporation kinetics, J. Appl. Phys. **116**(23), 233504 (2014), http://dx.doi.org/10.1063/1.4903944

[17] S. Park, T. Chung, J.H. Baek, and D. Ahn, Reduction of efficiency droop in green strain-compensated InGaN/InGaN light-emitting diodes grown on InGaN substrate, Jpn. J. Appl. Phys. **54**(2), 022101 (2015), http://dx.doi.org/10.7567/JJAP.54.022101

[18] Y.L. Li, Y.R. Huang, and Y.H. Lai, Efficiency droop behaviors of InGaN/GaN multiple-quantum-well light-emitting diodes with varying quantum well thickness, App. Phys. Lett. **91**(18), 181113 (2007), http://dx.doi.org/10.1063/1.2805197

[19] G. Sun, G. Xu, Y.J. Ding, H. Zhao, G. Liu, J. Zhang, and N. Tansu, Investigation of fast and slow decays in InGaN/GaN quantum wells, Appl. Phys. Lett. **99**(8), 081104 (2011), http://dx.doi.org/10.1063/1.3627166

[20] M.J. Davies, T.J. Badcock, P. Dawson, M.J. Kappers, R.A. Oliver, and C.J. Humphreys, High excitation carrier density recombination dynamics of InGaN/GaN quantum well structures: Possible relevance to efficiency droop, Appl. Phys. Lett. **102**(2), 022106 (2013), http://dx.doi.org/10.1063/1.4781398

[21] N.I. Bochkareva, Y.T. Rebane, and Y.G. Shreter, Efficiency droop and incomplete carrier localization in InGaN/GaN quantum well light-emitting diodes, Appl. Phys. Lett. **103**(19), 191101 (2013), http://dx.doi.org/10.1063/1.4828780

[22] R. Aleksiejūnas, K. Nomeika, S. Miasojedovas, S. Nargelas, T. Malinauskas, K. Jarašiūnas, Ö. Tuna, and M. Heuken, Carrier dynamics in blue and green emitting InGaN MQWs, Phys. Status Solidi B **252**(5) 977–982 (2015), http://dx.doi.org/10.1002/pssb.201451583

[23] J. Piprek, Efficiency droop in nitride-based light-emitting diodes, Phys. Status Solidi A **207**(10), 2217–2225 (2010), http://dx.doi.org/10.1002/pssa.201026149

[24] J. Hader, J.V. Moloney, and S.W. Koch, Density-activated defect recombination as a possible explanation for the efficiency droop in GaN-based diodes, Appl. Phys. Lett. **96**(22), 221106 (2010), http://dx.doi.org/10.1063/1.3446889

[25] T. Malinauskas, A. Kadys, T. Grinys, S. Nargelas, R. Aleksiejūnas, S. Miasojedovas, J. Mickevičius, R. Tomašiūnas, K. Jarašiūnas, M. Vengris, S. Okur, V. Avrutin, X. Li, F. Zhang, Ü. Özgür, and H. Morkoç,

Impact of carrier localization, recombination, and diffusivity on excited state dynamics in InGaN/GaN quantum wells, Proc. SPIE **8262**, 82621S–1 (2012), http://dx.doi.org/10.1117/12.906488

[26] R. Aleksiejūnas, K. Gelžinytė, S. Nargelas, K. Jarašiūnas, M. Vengris, E.A. Armour, D.P. Byrnes, R.A. Arif, S.M. Lee, and G.D. Papasouliotis, Diffusion-driven and excitation-dependent recombination rate in blue InGaN/GaN quantum well structures, Appl. Phys. Lett. **104**(2), 022114 (2014), http://dx.doi.org/10.1063/1.4862026

[27] T. Sadi, P. Kivisaari, J. Oksanen, and J. Tulkki, On the correlation of the Auger generated hot electron emission and efficiency droop in III-N light-emitting diodes, Appl. Phys. Lett. **105**(9), 091106 (2014), http://dx.doi.org/10.1063/1.4894862

[28] A. David and M.J. Grundmann, Droop in InGaN light-emitting diodes: A differential carrier lifetime analysis, Appl. Phys. Lett. **96**(10), 103504 (2010), http://dx.doi.org/10.1063/1.3330870

[29] J.I. Shim, H.S. Kim, D.S. Shin, and H.Y. Yoo, An explanation of efficiency droop in InGaN-based light emitting diodes: Saturated radiative recombination rate at randomly distributed In-rich active areas, J. Korean Phys. Soc. **58**(3), 503–508 (2011), http://dx.doi.org/10.3938/jkps.58.503

[30] R. Aleksiejūnas, P. Ščajev, S. Nargelas, T. Malinauskas, A. Kadys, and K. Jarašiūnas, Impact of diffusivity to carrier recombination rate in nitride semiconductors: from bulk GaN to (In, Ga)N quantum wells, Jpn. J. Appl. Phys. **52**(8 S), 08JK01 (2013), http://dx.doi.org/10.7567/JJAP.52.08JK01

[31] F. Hitzel, G. Klewer, S. Lahmann, U. Rossow, and A. Hangleiter, Localized high-energy emissions from the vicinity of defects in high-efficiency $Ga_xIn_{1-x}N$/GaN quantum wells, Phys. Rev. B **72**, 081309(R) (2005), http://dx.doi.org/10.1103/PhysRevB.72.081309

[32] R. Aleksiejūnas, M. Sūdžius, T. Malinauskas, J. Vaitkus, K. Jarašiūnas, and S. Sakai, Determination of free carrier bipolar diffusion coefficient and surface recombination velocity of undoped GaN epilayers, Appl. Phys. Lett. **83**(6), 1157–1159 (2003), http://dx.doi.org/10.1063/1.1599036

[33] D.M. Graham, P. Dawson, Y. Zhang, P.M.F.J. Costa, M.J. Kappers, C.J. Humphreys, and E.J. Thrush, The effect of a Mg-doped GaN cap layer on the optical properties of InGaN/AlGaN multiple quantum well structures, Phys. Status Solidi B **3**(6), 2005–2008 (2006), http://dx.doi.org/10.1002/pssc.200565246

KVANTINIO NAŠUMO PAGERINIMAS InGaN KVANTINĖSE DUOBĖSE ĮTERPIANT SUPERGARDELĘ IR NAUDOJANTIS IMPULSINIU AUGINIMU

K. Nomeika, M. Dmukauskas, R. Aleksiejūnas, P. Ščajev, S. Miasojedovas, A. Kadys, S. Nargelas, K. Jarašiūnas

Vilniaus universiteto Taikomųjų mokslų institutas, Vilnius, Lietuva

Santrauka

Vidinio kvantinio našumo (VKN) pagerinimas InGaN kvantinėse duobėse dėl supergardelės įterpimo ir impulsinio auginimo pritaikymo ištirtas laikinės skyros optinių metodikų kombinacija. Supergardelės tarpsluoksnio įterpimas padidino VKN tris kartus, tai gali būti aiškinama sumažėjusiu vidiniu elektriniu lauku dėl mažesnių įtempimų ir pakeistų lokalizacijos sąlygų. Impulsinio auginimo dėka VKN padidėjo dvigubai, tikimiausiai dėl geresnės defektų kontrolės struktūros. Šviesos diodo darinys su viršutiniu p-tipo GaN kontaktiniu sluoksniu buvo pagamintas naudojant supergardelės tarpsluoksnį ir impulsinį auginimą, tokiu būdu gautas toks pats maksimalus VKN kaip ir darinyje be kontaktinio sluoksnio. Tiesinės rekombinacijos koeficientas augo palaipsniui nuo žadinimo intensyvumo dėl krūvininkų delokalizacijos. Pasinaudojus tokia priklausomybe, buvo sėkmingai sumodeliuotas VKN smukimas.

4th publication / 4 publikacija

Influence of growth temperature on carrier localization in InGaN/GaN MQWs with strongly redshifted emission band

J. Mickevičius, D. Dobrovolskas, R. Aleksiejūnas, **K. Nomeika**, T. Grinys, A. Kadys, G. Tamulaitis

Journal of Crystal Growth **459** (2017) 173–177
DOI:10.1016/j.jcrysgro.2016.12.008

Journal of Crystal Growth 459 (2017) 173–177

Contents lists available at ScienceDirect

Journal of Crystal Growth

journal homepage: www.elsevier.com/locate/jcrysgro

Influence of growth temperature on carrier localization in InGaN/GaN MQWs with strongly redshifted emission band

J. Mickevičius*, D. Dobrovolskas, R. Aleksiejūnas, K. Nomeika, T. Grinys, A. Kadys, G. Tamulaitis

Institute of Applied Research and Semiconductor Physics Department, Vilnius University, Saulėtekio al. 3, LT-10257 Vilnius, Lithuania

ARTICLE INFO

Communicated by T.F. Kuech

Keywords:
A1. Carrier localization
A3. MOCVD
A3. Quantum wells
A3. SPSL
B1. Nitrides

ABSTRACT

To shift the emission band to long wavelength side, InGaN/GaN multiple quantum wells were grown by metalorganic chemical vapor deposition (MOCVD) using pulsed delivery of the metalorganic precursors at fixed parameters of the pulses but variable growth temperatures and by introducing short-period superlattices (SPSL) as buffer layers. By decreasing the growth temperatures for both SPSL and quantum wells down to 800 °C, a considerable shift of the photoluminescence (PL) band peak down to ~2 eV is achieved at reasonably acceptable decrease in PL intensity at low carrier density. However, increase in the carrier density resulted in considerable blue shift of the band, and the efficiency droop onset occurred at rather low carrier densities. The comparison of the data on PL and differential optical transmittance, which were supported by structural analysis, revealed that the large red shift in the PL band position is predominantly caused by an increasing tail of localized states. Meanwhile, the efficiency droop effect in the samples under study is caused predominantly by the enhancement of nonradiative carrier recombination.

1. Introduction

The efficiency of InGaN-based light-emitting diodes (LEDs) and laser diodes rapidly decreases as the emission wavelength is increased above ~500 nm, resulting in a so-called "green gap" [1]. A few effects are responsible for this strong deterioration of emission efficiency in the InGaN multiple quantum wells (MQWs) used as active regions. First of all, the large mismatch of lattice constants and thermal expansion coefficients between GaN or InGaN and sapphire, which is commonly used as a substrate in III-nitride technology, results in considerable strain. The strain facilitates formation of structural defects and gives rise to strong built-in piezoelectric field, which diminishes the internal quantum efficiency (IQE) due to the quantum confined Stark effect (QCSE). Moreover, to shift the emission wavelength to green spectral region, the incorporation of higher In content in the active layers is required. Due to the reduced thermal stability of InN, the high-In-content InGaN has to be deposited at rather low growth temperatures [2,3]. Moreover, the strain inhibits the incorporation of In due to the compositional pulling effect [4,5]. Therefore, even lower growth temperatures are needed. The combination of a low growth temperature and an increasing strain energy leads to the formation of a number of structural defects [6–8], which deteriorate the structural quality of the active region, while the well-known inherent tendency of InGaN for compositional fluctuations might result in the formation of large defect-rich clusters [8].

To improve the crystal quality and reduce the strain, several technological approaches have been proposed [9–18]. These approaches focus primarily on inserting and optimizing an intermediate layer between GaN buffer layer and InGaN/GaN active region. InGaN/GaN short-period superlattices (SPSL) [9–12], low-In-content InGaN layers [10,13], step-graded InGaN/GaN superlattice [14], or low-temperature n-GaN layer [11,15] have been studied as prospective intermediate layers. Generally, an increase in IQE [9,11–14] and smaller photoluminescence (PL) band shift with increasing carrier injection [10,14,15] have been demonstrated in the structures with such intermediate layers. On the other hand, pulsed growth mode is proved to be a promising approach to improve the quality of active high-In-content InGaN layers. This technique was mainly used for InN growth, but was also demonstrated as a prospective tool for InGaN growth by metal-modulated epitaxy [16], high-pressure metalorganic chemical vapor deposition (MOCVD) [17], and, recently, low-pressure MOCVD [18].

In this work, we grow InGaN/GaN MQWs emitting in a wide spectral range by using both SPSL and pulsed growth approaches. We study how the variations of the temperatures for growing SPSL and active InGaN QWs influence the long-wavelength shift of the emission.

* Corresponding author.
E-mail address: juras.mickevicius@ff.vu.lt (J. Mickevičius).

http://dx.doi.org/10.1016/j.jcrysgro.2016.12.008
Received 28 September 2016; Received in revised form 15 November 2016; Accepted 1 December 2016
Available online 02 December 2016

The comparison of the results obtained using PL spectroscopy, nonlinear absorption and structural characterization enabled us to link the PL band position, band gap, and indium content with the technological conditions used for the deposition of the structures. A drastic contribution of carrier localization increasing in the samples emitting at longer wavelengths is demonstrated.

2. Experimental

InGaN/GaN MQWs under study were grown using MOCVD technique in a close-coupled showerhead 3×2″ reactor (*AIXTRON*). Trimethylgallium (TMGa), trimethylindium (TMIn), and ammonia (NH_3) were used as Ga, In, and N precursors, respectively. N_2 was used as ambient and carrier gas.

3-μm-thick c-plane GaN templates on sapphire were used as substrates. Initially, the strain-relieving SPSL consisting of 8–15 periods of alternating low-In-content $In_xGa_{1-x}N$ (x=4–7%) and GaN layers was grown. The thickness of one superlattice period was 4 nm. The temperature of the SPSL growth was varied in the range from 860 to 800 °C. On top of the SPSL, five pairs of InGaN/GaN quantum wells and barriers were deposited. The QWs were grown using a pulsed growth regime, which was accomplished by modulating the flow of In and Ga precursors into the reactor chamber, while maintaining the flow of NH_3 constant. Both metalorganic precursors have been delivered synchronously for the duration of 15 s and the delivery pulses have been followed by 12-s-long pauses. The on-off cycle was repeated 14 times in fabrication of all the samples under study. The growth temperature of QWs was varied in the range from 810 to 800 °C. The GaN barriers were grown in the usual constant TMGa flow regime. The growth parameters for the samples under study are provided in Table 1.

The structural characterization of the structures was performed using transmission electron microscopy (TEM) (*FEI Tecnai G2 F20 X-TWIN*) and X-ray diffraction (XRD) (*Rigaku SmartLab*) techniques. Photoluminescence of the samples was studied under steady- and quasi-steady-state conditions using CW He-Cd laser (325 nm) and the 3rd harmonic (355 nm) of the Q-switched YAG laser radiation (pulse duration 4 ns) for low- and high-intensity excitation, respectively. The luminescence signal was analyzed by a double monochromator (*Jobin Yvon HRD-1*) and detected by a photomultiplier (*Hamamatsu*). The measurements were performed in a wide range of excitation power densities from 4 W/cm^2 to 10 MW/cm^2 to cover the excitation conditions corresponding low carrier densities, which are convenient for sample characterization, and the densities similar to those in operating light emitting devices. The carrier lifetimes were estimated using time-resolved photoluminescence (TRPL) spectroscopy. The samples were excited at 405 nm using a femtosecond laser (pulse duration 250 fs). The TRPL spectra and kinetics were recorded by a streak camera (*Hamamatsu*).

Free carrier dynamics was studied using time-resolved differential transmission (DT) spectroscopy. The experimental setup consisted of a femtosecond laser delivering 200 fs duration pulses at 1030 nm and an optical parametric amplifier (OPA) generating light in the range from 630 to 2600 nm. The output of OPA was split into two beams. The 2nd harmonic (391 nm) of one of the beams was used for excitation, while the other variably delayed beam was passed through a sapphire crystal to generate a white light continuum probe. The evolution of DT spectra was observed using a spectrometer with a CCD camera (*Harpia, Light Conversion*). A chopper was used to periodically close the pump pulse and ensure measuring the transmission with and without excitation ($T_P(\lambda,t)$ and $T_0(\lambda)$, respectively) at various probe delays to obtain the instantaneous DT spectra: $OD(\lambda, t) = -\log(T_p/T_0)$.

All the measurements were performed at room temperature.

Table 1
Growth conditions of the InGaN/GaN MQWs under study: growth temperatures for short-period superlattice (T_{SPSL}) and quantum well (T_{QW}), the number of SPSL periods, QW and barrier widths.

Sample	T_{SPSL} (°C)	T_{QW} (°C)	SPSL periods	QW width (nm)	Barrier width (nm)
S1	860	808	8	3.1	7.1
S2	820	810	8	3.7	6.6
S3	825	805	12	3.1	7.8
S4	810	800	8	3.9	7.8
S5	800	805	12	4.2	8.7
S6	800	800	12	4.5	7.7
S7	800	800	15	4.8	9.0

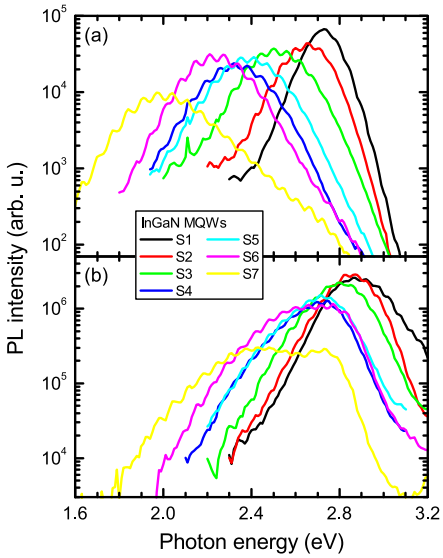

Fig. 1. PL spectra of InGaN/GaN MQWs measured under (a) low (4 W/cm^2) and (b)

3. Results and discussion

Fig. 1(a) presents the PL spectra of the InGaN/GaN MQWs structures under study measured at excitation power density of 4 W/cm^2. The PL spectra cover a wide range from 2.8 to 2.0 eV. As the PL band shifts to lower energies, the PL intensity initially decreases only slightly (samples S1-S2), then stays almost constant in samples S2-S6, and strongly decreases in the sample with the PL band peaked at ~2.0 eV (sample S7). The shift of the PL band is accompanied by the increase in the band width from 175 meV to 370 meV (in samples S1 and S7, respectively), and the more pronounced contribution of the high-energy component.

A red shift of the PL band can be achieved by increasing the QW width and/or In content in the QWs. The structural characterization was performed to estimate these parameters. Fig. 2 shows a cross-section TEM image of sample S1. This is a typical TEM image similar to those for other InGaN/GaN MQWs under study. Five QWs can be identified in the image despite the nonuniform shade in the QWs, which is probably caused by fluctuations in indium composition [19]. The well and barrier thicknesses estimated using the TEM images of all the samples under study are provided in Table 1. The trend can be observed that the QW width increases as the PL band shifts to lower energies. Note that all the QWs were fabricated at a constant number of

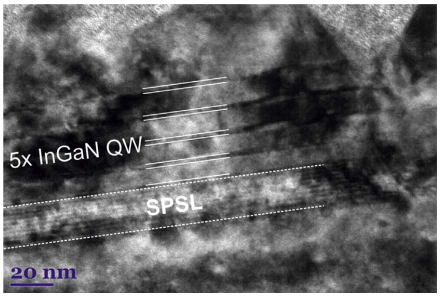

Fig. 2. TEM image of InGaN/GaN MQWs sample S4.

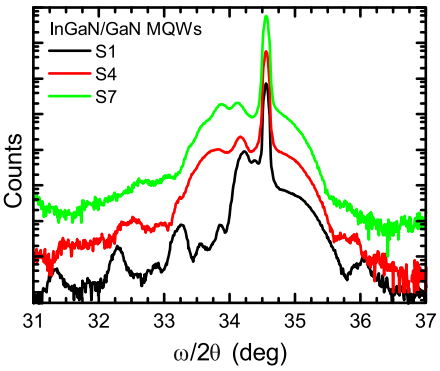

Fig. 3. XRD scans of three samples under study. The curves are vertically shifted for clarity.

on-off cycles in delivering pulses of metalorganic precursors with fixed parameters. The *ω-2θ* XRD scans for several samples are shown in Fig. 3. The main diffraction peaks corresponding to GaN layers and InGaN QWs are clearly expressed. However, the satellite peaks in the XRD scans can hardly be clearly resolved. Instead, a shoulder in the range between 33.5° and 34° is observed. This is an indication of non-abrupt QW/barrier interfaces. As a result, the simulations of the XRD curves provided ambiguous values of In content in the QWs. Therefore, to estimate the In content in the QWs, optical characterization results were used as discussed below.

The estimation of In content from the position of the PL band is known to be complicated due to the presence of internal electric field [20] as well as the large density of localized states [21]. On the other hand, the DT technique has been shown to separate the field screening behavior from the band filling effects [22,23]. The typical DT spectra measured at different excitation intensities are shown in Fig. 4. At high excitation intensities, the DT spectra consist of a single band with a negative sign, indicating the dominant bleaching of absorption in the band gap vicinity. As the excitation is decreased, the DT spectra transform to the negative-positive-negative swing, which is characteristic of the screening of the internal electric field [22,23]. The positive peak in this case can be used to approximately estimate the excitonic resonance (marked by an arrow in Fig. 4) [23]. The excitonic resonances were estimated for all the samples under study (not shown here), and only a small shift in the resonance position in respect to that in sample S1 was detected (the largest shift was ~100 meV in sample S7). Meanwhile, the shift of the PL band (see Fig. 1) was considerably larger. The largest shift (in sample S7) was 730 meV and 420 meV at low and high excitation conditions, respectively.

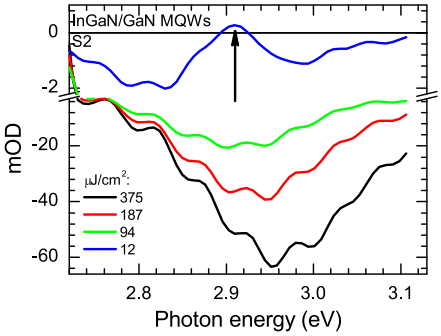

Fig. 4. DT spectra of sample S2 under different excitations (indicated) at time delay of 10 ps. Arrow shows the exciton resonance position.

The In content in the QWs was estimated from the resonance positions using the theoretical values of the built-in field. The resulting In content was approximately 11–12% in all the structures under study. The real internal field value might be reduced due to the strain-relieving SPSL buffer. Taking this reduction into account, the resulting In content values might increase up to 13–14%. Nevertheless, all the samples contain a very similar In content, while exhibiting a large red shift in PL peak position of up to 0.8 eV. This large shift between the spectral positions of DT and PL bands points out to extremely strong influence of carrier localization as the emission band shifts to longer wavelengths. The localizing potential arises due to the fluctuations in QW width and/or In content. The absorption occurs to the higher energy states (presumably, the extended states of the QW). Afterwards, the carriers relax to the low-energy localized states, where they recombine radiatively. The increase of the difference between DT and PL bands as the PL band redshifts in the samples grown at lower temperatures is related to the increasing strength of localization as well as increasing density of localized states. Meanwhile, the increasing PL band width points to the increasing energy distribution of the localized states.

To gain more data on the peculiarities of carrier recombination, we measured the PL spectra at different excitation intensities. As the excitation power density is increased, the PL bands shift to higher energies [see Fig. 1(b)]. Such excitation-induced blue shift is typically attributed to two effects: screening of the built-in electric field [24,25], and filling of deeper-lying localized states [25,26]. The value of the blue shift correlates well with the QW width: a larger QW width corresponds to a stronger blue shift of the PL band. This behavior is consistent with the field screening effect. We performed the numerical calculations of the expected band shift due to the screening by simultaneously solving Schrödinger and Poisson equations. While there is some uncertainty in indium content and internal electric field strength, the upper limit of the blue shift is equal to 115 meV and 250 meV in samples S1 and S7, respectively. Consequently, the rest of the observed blue shift (32 meV and 210 meV in samples S1 and S7, respectively) can be attributed to the filling of the localized states, in consistence with the increasing role of carrier localization.

Moreover, the detailed analysis of the PL spectra at increasing excitation intensity reveals the emergence of a second PL band peaked at 2.75–2.8 eV. This band can be clearly observed in the spectra of sample S7 (see Fig. 1), while it is not as clearly resolved in the samples with the main band at shorter wavelengths, since the overlap between the two PL bands is larger in those samples. The existence of similar PL bands has been usually attributed to phase separation [27,28]. Transitions from higher energy levels in the QWs have been suggested as an alternative explanation [29], however, the energy level calculations eliminate this interpretation for our case. The similarity in the

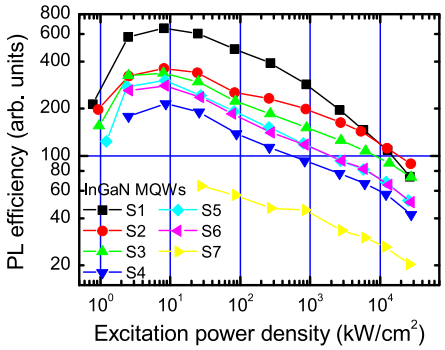

Fig. 5. Photoluminescence efficiency as a function of excitation power density for the InGaN samples under study.

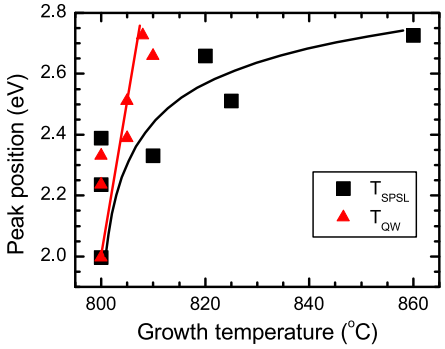

Fig. 6. Dependence of PL band peak position on growth temperatures for short-period superlattice (T_{SPSL}, squares) and quantum well (T_{QW}, triangles). Each pair of points (one square and one triangle) having the same peak position corresponds to one sample. Solid lines are guides for an eye.

spectral positions of the high-energy PL and DT bands leads to conclusion that the second PL band emerging at high excitation intensities is caused by band-to-band recombination of free carriers.

Fig. 5 presents the PL efficiency as a function of excitation power density for the InGaN/GaN MQWs under study. The PL efficiency was calculated as the ratio of spectrally-integrated PL intensity and excitation power density. Two features are worth of noting: the efficiencies of all the samples, though rather different in absolute value, (i) are peaked at approximately the same excitation power density, and (ii) this density is rather low. While the droop onset happens at approximately the same excitation in all the samples, the corresponding carrier densities differ due to different carrier lifetimes. The carrier lifetimes were estimated from the initial transients of TRPL and DT kinetics (not shown here) measured at low excitations. The lifetimes varied from 1 ns down to 100 ps in samples S1 and S7, respectively, which results in the efficiency droop onset densities from 2×10^{18} to 2×10^{17} cm^{-3}, respectively. Such values of carrier density at the efficiency droop onset rules out the Auger recombination as the dominant droop mechanism in the samples under study, since the Auger recombination is effective at the carrier densities above 10^{19} cm^{-3} [30,31]. Therefore, the carrier transfer/redistribution within the localized states related processes is the most probable main origin of the efficiency droop for InGaN emitting in the vicinity of the "green gap". This conclusion is in agreement with the dominant role of localized carriers in the PL observed by comparison of PL and DT spectra of the samples under study. A similar situation has been observed in blue QW structures [32].

The low value of the droop onset regardless of the PL band position or, consequently, of the density and energy distribution of the localized states looks similar to the behavior observed in AlGaN with strong carrier localization [33]. The efficiency droop in high-Al-content AlGaN materials was attributed to the enhancement of nonradiative recombination of localized excitons [34]. The link between the localized states and nonradiative recombination has also been suggested to explain the negative PL intensity-band width correlation in semi-polar InGaN MQWs, where the localized states have been associated with the partially relaxed regions having higher defect concentration [35]. Thus, the decrease in PL intensity (see Fig. 1) or efficiency (see Fig. 5) is consistent with a higher defect density reasonably expected in InGaN MQWs with strongly redshifted emission wavelengths. The higher density of nonradiative recombination centers, in turn, results in efficiency droop onset occurring at lower nonequilibrium carrier density.

Thus, the decrease in growth temperature for both QWs and SPSL results in a considerable red shift of the PL band peak position, as illustrated in Fig. 6, where the peak position at low excitations is plotted as a function of temperature for growing SPSL (T_{SPSL}) and QWs (T_{QW}) of the corresponding samples. The PL band peak position can be shifted down to the red region (~620 nm) by lowering T_{SPSL} and/or T_{QW}. As the temperatures are decreased down to 800 °C, a rather small shift of the effective band gap is achieved mainly by the increase in the QW width, while the In content in the QWs remains practically unchanged. The main contribution to the shift is caused by a strongly increasing tail in the energy distribution of localized states.

4. Conclusions

From the point of view of practical application, the lowering of the temperatures in the pulsed MOCVD growth of short-period superlattices in the buffer layer and active quantum wells results in a substantial red shift of emission band at low carrier densities but suffers from a considerable blue shift as the densities are increased. The decrease in the emission efficiency of the samples grown at lower temperatures might be acceptable, however, a low threshold for the droop onset as the carrier density is increased is a problem. The comparison of the data obtained by photoluminescence and differential transmittance techniques and supported by structural analysis and calculations of the built-in field evidences that the considerable red shift in the photoluminescence band position is caused by increasing influence of carrier localization rather than by increasing In content. The efficiency droop effect in the samples under study is caused mainly by nonradiative carrier recombination, which is enhanced by increasing density of nonradiative recombination centers in the increasingly disordered quantum wells. Since the carrier dynamics is predominantly determined by the growth-condition-dependent localization conditions, both the peak quantum efficiency and the efficiency droop onset might be improved by further optimization of technological growth conditions.

Acknowledgments

The research at Vilnius University was supported by the Lithuanian Research Council (Contract No. MIP-079/2015).

References

[1] M. Krames, O. Shchekin, R. Mueller-Mach, G.O. Mueller, L. Zhou, G. Harbers, M. Craford, J. Disp. Technol. 3 (2007) 160.
[2] Z. Gacevic, V.J. Gomez, N. Garcia Lepetit, P.E.D. Soto Rodriguez, A. Bengoechea, S. Fernandez-Garrido, R. Notzel, E. Calleja, J. Cryst. Growth 364 (2013) 123.
[3] A.G. Bhuiyan, A. Hashimoto, A. Yamamoto, J. Appl. Phys. 94 (2003) 2779.
[4] K. Hiramatsu, Y. Kawaguchi, M. Shimizu, N. Sawaki, T. Zheleva, R.F. Davis,

H. Tsuda, W. Taki, N. Kuwano, K. Oki, MRS Internet J. Nitride Semicond. Res. 2 (1997) 6.
[5] B. Wilsch, U. Jahn, B. Jenichen, J. Lahnemann, H. Grahn, H. Wang, H. Yang, Appl. Phys. Lett. 102 (2013) 052109.
[6] C. Bazioti, E. Papadomanolaki, Th Kehagias, T. Walther, J. Smalc-Koziorowska, E. Pavlidou, Ph Komninou, Th Karakostas, E. Iliopoulos, G.P. Dimitrakopulos, J. Appl. Phys. 118 (2015) 155301.
[7] Y. Chen, T. Takeuchi, H. Amano, I. Akasaki, N. Yamada, Y. Kaneko, S.Y. Wang, Appl. Phys. Lett. 72 (1998) 710.
[8] T.V. Cuong, J.Y. Park, M.S. Kumar, C.-H. Hong, E.K. Suh, M.S. Jeong, Jpn. J. Appl. Phys. 46 (2007) L372.
[9] N.H. Niu, H.B. Wang, J.P. Liu, N.X. Liu, Y.H. Xing, J. Han, J. Deng, G.D. Shen, J. Cryst. Growth 286 (2006) 209.
[10] S.J. Leem, Y.C. Shin, K.C. Kim, E.H. Kim, Y.M. Sung, Y. Moon, S.M. Hwang, T.G. Kim, J. Cryst. Growth 311 (2008) 103.
[11] S.P. Chang, C.H. Wang, C.H. Chiu, J.C. Li, Y.S. Lu, Z.Y. Li, H.C. Yang, H.C. Kuo, T.C. Lu, S.C. Wang, Appl. Phys. Lett. 97 (2010) 251114.
[12] W.V. Lundin, A.E. Nikolaeva, A.V. Sakharova, E.E. Zavarina, G.A. Valkovskiy, M.A. Yagovkina, S.O. Usov, N.V. Kryzhanovskaya, V.S. Sizov, P.N. Brunkov, A.L. Zakgeim, A.E. Cherniakov, N.A. Cherkashin, M.J. Hytch, E.V. Yakovlev, D.S. Bazarevskiy, M.M. Rozhavskaya, A.F. Tsatsulnikov, J. Crys. Growth 315 (2011) 267.
[13] T. Akasaka, H. Gotoh, T. Saito, T. Makimoto, Appl. Phys. Lett. 85 (2004) 3089.
[14] C. Jia, T. Yu, H. Lu, C. Zhong, Y. Sun, Y. Tong, G. Zhang, Opt. Express 21 (2013) 8444.
[15] R.M. Lin, Y.H. Lin, C.H. Chiang, M.J. Lai, Y.L. Chou, Y.C. Lu, S.Y. Kuo, B.R. Fang, M.C. Wu, Microelectron. Reliab. 50 (2010) 679.
[16] M. Moseley, B. Gunning, J. Greenlee, J. Lowder, G. Namkoong, W.A. Doolittle, J. Appl. Phys. 112 (2012) 014909.
[17] V. Woods, N. Dietz, Mater. Sci. Eng. B 127 (2006) 239.
[18] K. Nomeika, M. Dmukauskas, R. Aleksiejūnas, P. Ščajev, S. Miasojedovas, A. Kadys, S. Nargelas, K. Jarašiūnas, Lith. J. Phys. 55 (2015) 255.
[19] Y.-S. Lin, K.-J. Ma, C. Hsu, S.-W. Feng, Y.-C. Cheng, C.-C. Liao, C.C. Yang, C.-C. Chou, C.-M. Lee, J.-I. Chyi, Appl. Phys. Lett. 77 (2000) 2988.
[20] U.M.E. Christmas, A.D. Andreev, D.A. Faux, J. Appl. Phys. 98 (2005) 073522.
[21] S. Srinivasan, F. Bertram, A. Bell, F.A. Ponce, S. Tanaka, H. Omiya, Y. Nakagawa, Appl. Phys. Lett. 80 (2002) 550.
[22] A.N. Cartwright, D.S. McCallum, T.F. Boggess, A.L. Smirl, T.S. Moise, L.J. Guido, R.C. Barker, B.S. Wherrett, J. Appl. Phys. 73 (1993) 7767.
[23] F. Chen, W.D. Kirkey, M. Furis, M.C. Cheung, A.N. Cartwright, Solid State Commun. 125 (2003) 617.
[24] F. Della Sala, A. Di Carlo, P. Lugli, F. Bernardini, V. Fiorentini, R. Scholz, J.-M. Jancu, Appl. Phys. Lett. 74 (1999) 2002.
[25] K. Kazlauskas, G. Tamulaitis, J. Mickevičius, E. Kuokštis, A. Žukauskas, Y.-C. Cheng, H.-C. Wang, C.-F. Huang, C.C. Yang, J. Appl. Phys. 97 (2005) 013525.
[26] P.G. Eliseev, P. Perlin, J. Lee, M. Osinski, Appl. Phys. Lett. 71 (1997) 569.
[27] H. Sun, Z. Ji, H. Wang, H. Xiao, S. Qu, X. Xu, A. Jin, H. Yang, J. Appl. Phys. 114 (2013) 093508.
[28] Y.-L. Lai, C.-P. Liu, Y.-H. Lin, T.-H. Hsueh, R.-M. Lin, D.-Y. Lyu, Z.-X. Peng, T.-Y. Lin, Nanotechnology 17 (2006) 3734.
[29] A. Laubsch, W. Bergbauer, M. Sabathil, M. Strassburg, H. Lugauer, M. Peter, T. Meyer, G. Bruderl, J. Wagner, N. Linder, K. Streubel, B. Hahn, Phys. Status Solidi C 6 (2009) S885.
[30] G. Verzellesi, D. Saguatti, M. meneghini, F. Bertazzi, M. Goano, G. Meneghesso, E. Zanoni, J. Appl. Phys. 114 (2013) 071101.
[31] D. Schiavon, M. Binder, M. Peter, B. Galler, P. Drechsel, F. Scholz, Phys. Status Solidi B 250 (2013) 283.
[32] R. Aleksiejunas, K. Gelzinyte, S. Nargelas, K. Jarasiunas, M. Vengris, E.A. Arbour, D.P. Byrnes, R.A. Asif, S.M. Lee, G.D. Papasouliotis, Appl. Phys. Lett. 104 (2014) 022114.
[33] J. Mickevičius, J. Jurkevičius, A. Kadys, G. Tamulaitis, M. Shur, M. Shatalov, J. Yang, R. Gaska, AIP Adv. 6 (2016) 045212.
[34] J. Mickevičius, J. Jurkevičius, A. Kadys, G. Tamulaitis, M. Shur, M. Shatalov, J. Yang, R. Gaska, J. Phys. D: Appl. Phys. 48 (2015) 275105.
[35] M.D. Mensi, D.L. Becerra, R. Ivanov, S. Marcinkevičius, S. Nakamura, S.P. DenBaars, J.S. Speck, Opt. Mater. Express 6 (2016) 39.

5th publication / 5 publikacija

Impact of carrier localization and diffusion on photoluminescence in highly excited cyan and green InGaN LED structures

K. Nomeika, R. Aleksiejūnas, S. Miasojedovas, R. Tomašiūnas, K. Jarašiūnas, I. Pietzonka, M. Strassburg, H.-J. Lugauer

Journal of Luminescence **188** (2017) 301–306
DOI:10.1016/j.jlumin.2017.04.055

Journal of Luminescence 188 (2017) 301–306

Contents lists available at ScienceDirect

Journal of Luminescence

journal homepage: www.elsevier.com/locate/jlumin

Impact of carrier localization and diffusion on photoluminescence in highly excited cyan and green InGaN LED structures

K. Nomeika[a,*], R. Aleksiejūnas[a], S. Miasojedovas[a], R. Tomašiūnas[a], K. Jarašiūnas[a], I. Pietzonka[b], M. Strassburg[b], H.-J. Lugauer[b]

[a] Vilnius University, Institute of Applied Research, Saulėtekis av. 3, Vilnius, Lithuania
[b] OSRAM Opto Semiconductors GmbH, Leibnizstr. 4, 93055 Regensburg, Germany

ARTICLE INFO

Keywords:
InGaN
Green LED
PL redshift
Localized states
Carrier diffusion
Redistribution

ABSTRACT

Localization of charge carriers is of crucial importance in InGaN light emitting devices since it governs carrier transport and ensures high radiative efficiency. In this work, we observe the dynamics of carrier localization from an untypical redshift of photoluminescence spectra. We investigate two light emitting diode structures grown by MOCVD on c-plane sapphire and emitting at 500 nm (cyan) or 530 nm (green). For the study, we employ photoluminescence, differential transmission, and light induced transient gratings techniques. We observe non-monotonous dynamics of photoluminescence peak position: a blueshift at short delay times (< 10 ns) is later replaced by a redshift, which increases both with time and excitation. The redshift values as large as 30 meV in the cyan and 20 meV in the green structure were observed at 40 ns delay. We attribute this redshift to density-dependent and diffusion-driven carrier redistribution between the shallower and deeper localized states. The carrier delocalization with increasing density is confirmed by growing diffusivity of carriers with excitation. We also demonstrate a correlation between the growth of diffusion coefficient and the onset of efficiency droop.

1. Introduction

InGaN/GaN quantum structures are attractive for various lighting applications due to high internal quantum efficiency (IQE) reaching 90% for blue and 30% for green light emitting diodes (LEDs) [1]. High IQE values are obtained even in the heteroepitaxial structures despite the high density of threading dislocations exceeding 10^8–10^9 cm^{-2}. Localization of free carriers in the local potential minima is believed to be responsible for low nonradiative recombination rate at dislocations [2]. Quantum dot-like indium clusters were believed to be the main source of local potential minima [3], but later it has been shown that both random indium density fluctuations and monoatomic variations in quantum well thickness can result in carrier localization even at room temperature [4]. Recently, it was demonstrated that localization is much stronger for holes than electrons due to higher effective mass of the former [5–7].

Role of carrier localization becomes stronger with the increasing indium content since it is accompanied by a larger disorder in distribution of indium atoms [8]. On the other hand, higher indium content also results in stronger internal electric fields, higher strains, and larger defect densities. Stronger carrier localization can further separate the carriers from the defect states, but it also results in the decrease of radiative recombination coefficient [8,9] due to non-correlated potential fluctuations of valence and conduction bands and a smaller overlap of electron and hole wavefunctions [10,11]. Carrier localization can also alter the nonradiative recombination (SRH and Auger) rates [9,12]. An opposite process of carrier delocalization takes place at high temperatures and/or carrier densities, which increases carrier mobility and nonradiative recombination rate leading to the onset of efficiency droop at carrier densities that are lower than those required for Auger recombination [13–15].

In this paper, we study the impact of localization to carrier dynamics by analyzing the time and excitation-dependent spectra of photoluminescence and absorption, as well as diffusion coefficient. For this, we use several optical techniques: time-resolved and time-integrated photoluminescence (TRPL and TIPL), differential transmission (DT), and light induced transient gratings (LITG). Concerted application of PL and DT enables monitoring the electronic transitions in both the localized and extended states, while LITG provides a unique possibility to directly measure and separate the carrier lifetime and diffusivity. This allows for overcoming a certain limitation of SNOM and confocal microscopy, were only a product of carrier diffusion coefficient and

* Corresponding author.
E-mail address: kazimieras.nomeika@tmi.vu.lt (K. Nomeika).

http://dx.doi.org/10.1016/j.jlumin.2017.04.055
Received 25 March 2017; Received in revised form 24 April 2017; Accepted 25 April 2017
Available online 26 April 2017

carrier lifetime – carrier diffusion length – can be measured [16–18]. As a result, we reveal an untypical redshift in PL peak position, which increases with time and carrier density and cannot be related neither to band gap renormalization nor to electric field dynamics. Based on the analysis of DT and PL data, we attribute this shift to a slow relocalization of carriers from shallower to deeper potential minima. We show that carrier diffusivity increases with density due to delocalization and discuss the correlation between the growth of diffusivity and the onset of efficiency droop.

2. Samples and techniques

We investigate two complete InGaN/GaN multiple quantum well (MQW) LED structures, grown by metalorganic chemical vapor deposition on c-plane sapphire substrates. They emit light in the cyan and green spectral ranges with characteristic peak wavelengths of 500 nm and 530 nm (hereafter, the structures are referred to as "cyan" and "green", respectively). The samples consist of a standard sequence of LED epilayers: a buffer layer (unintentionally doped GaN), a moderately n-doped GaN:Si current spreading layer followed by a highly n-doped GaN:Si contact layer, an active layer consisting of a stack of five InGaN QWs with 3 nm well width (with an indium content of ~26% for cyan and ~30% for green emission), separated by GaN barriers, and a p-doped AlGaN:Mg electron blocking layer as well as a p-type GaN:Mg contact layer on top. Since the growth processes and layer structures of both samples are basically identical, we estimate that the In distributions are fairly similar, although the amplitude of variations might be a bit larger in the sample with higher In content [19].

TRPL, TIPL, DT, and LITG measurements were carried out using 250 fs duration pulses generated by a PHAROS (Light Conversion) laser (1030 nm, 30 kHz repetition rate) and spectrally tuned with an ORPHEUS (Light Conversion) optical parametric amplifier. Pump wavelength was set at 392 nm (DT, TIPL, LITG) or 405 nm (TRPL) to selectively excite the quantum wells. Pump energy fluence (further, we will be using a term "excitation") as high as 1 mJ/cm^2 per pulse could be achieved. A Hamamatsu C10627 streak camera along with an Acton SP2300 spectrometer was used for the measurements of TRPL spectra and kinetics. TIPL spectra were measured using a fiber spectrometer AvaSpec ULS 2048 (300 mm^{-1}).

To calibrate and compare the quantum efficiency in the structures, an integrating sphere and a three-measurement approach [20] were employed instead of a temperature-dependent PL method. The latter is based on an assumption that nonradiative recombination is thermally activated and vanishes at low temperatures. Recently, it has been shown that this assumption lacks a fundamental support [21]. To estimate the defect-related absorption coefficient at 392 nm in GaN buffer, the test samples were produced by removing the active LED structures by reactive ion etching. The measured absorption coefficient values in quantum wells and GaN buffer were equal to 8×10^4 cm^{-1} and 2×10^2 cm^{-1}, correspondingly. These values were used for estimation of photogenerated carrier density and quantum efficiency. We assume that light extraction coefficient is the same in both samples since they have the same structure.

White light continuum pulses within a 380–550 nm spectral range were created in a sapphire window and used as a probe in DT. Transmittance with and without pump ($T_p(\lambda, t)$ and $T_0(\lambda)$, correspondingly) at various probe delays and spectral positions was recorded using a Harpia system (Light Conversion) with a spectrograph with 300 lines/mm grating and a CCD camera. Differential transmittance is further presented in a scale of mOD as:

$$T(\lambda, t) = 1000\times\log\left(\frac{T_0(\lambda)}{T_p(\lambda, t)}\right). \quad (1)$$

In LITG measurements, the sample was excited by a spatially-modulated interference field of two coherent pump beams, which created a transient spatially modulated free carrier pattern

$$N(x) = N_0+\Delta N\left(1+\cos\left[\frac{2\pi x}{\Lambda}\right]\right) \quad (2)$$

with the grating spacing Λ [22]. For probing, the pulses at 1030 nm were used, since the sample is transparent for this wavelength. Diffraction efficiency $\eta(t)$ of a transient grating is given as

$$\frac{I_{diffracted}(t)}{I_{transmitted}(t)} = \eta(t)\propto\exp\left(\frac{-2t}{\tau_g}\right), \quad (3)$$

where the grating decay time τ_g consists of recombination and diffusion times τ_R and τ_D as

$$\frac{1}{\tau_g} = \frac{1}{\tau_R}+\frac{1}{\tau_D}, \quad (4)$$

where $\tau_D = \Lambda^2/4\pi D$. Since τ_D depends on Λ, the bipolar diffusion coefficient D can be determined by performing measurements with different induced grating periods. LITG technique has been successfully used previously for lifetime and diffusivity measurements in GaN and InGaN layers and structures [23–25].

All measurements were performed at room temperature.

3. Results and discussion

Fig. 1 shows the TIPL (top pictures) and DT (bottom pictures) spectra in the cyan (a) and green (b) QW samples recorded at various excitation levels. At low excitation (10 μJ/cm^2), the PL lines are centered at 2.53 eV (490 nm, cyan) and 2.36 eV (525 nm, green) and have full width at half maxima (FWHM) around 140 meV for both samples. The QE curves (see Fig. 4(b)) are typical for the optically pumped InGaN QWs [26], with the onset of efficiency droop at ~60–70 μJ/cm^2 (this corresponds to the carrier density of ~10^{19} cm^{-3}). The measured peak QE values reach 18 ± 3% in the cyan and 19 ± 3% in the green structures; we note that light extraction was not optimized in the structures. Since the PL linewidth is determined by the fluctuations of hole localization energy due to random alloy disorder [27] and a direct link was shown to exist between the disorder and luminosity of polar InGaN layers [28], the similar FWHM and QE of PL emission indicate similar structural quality of investigated structures, despite higher indium content in the green QWs. DT signal has a negative sign (bottom pictures in Fig. 1) indicating the absorption bleaching due to the state filling effect [29]. DT spectra are shifted towards the higher photon energies with respect to the PL peak by ~230 meV (cyan) and ~360 meV (green). Stokes shift is considerably larger in the green sample, which points out to stronger carrier localization in this structure [30].

Two trends are visible in TIPL spectra with increasing excitation: (i) the width of PL spectra increases and (ii) a redshift in PL peak position at low excitations is followed by a blueshift at high excitations; this is especially noticeable in the cyan sample. The PL line broadening with increasing carrier density has been attributed to gradual saturation of shallow localized states and the consequent population of both higher and lower energy states [31,32]. The behavior of PL line position, however, is untypical: in polar QWs, one expects a PL blueshift with excitation due to screening of the internal electrical field and state filling [33]. Only at very high carrier densities, a redshift of PL band due to band gap renormalization has been observed [34].

To investigate the temporal evolution of PL peak position, TRPL and DT spectra were recorded at various excitations. Fig. 2 displays the PL and DT peak positions for several delay times as a function of excitation in the cyan sample. It is seen from Fig. 2(a) that the PL redshift at high excitations evolves in time span of tens of nanoseconds. Thus, within first 5 ns only a blueshift in PL peak position is seen. A closer look into the early stage of spectral dynamics is provided by DT measurements with better time resolution (Fig. 2(b)). Only the blueshift of DT spectra

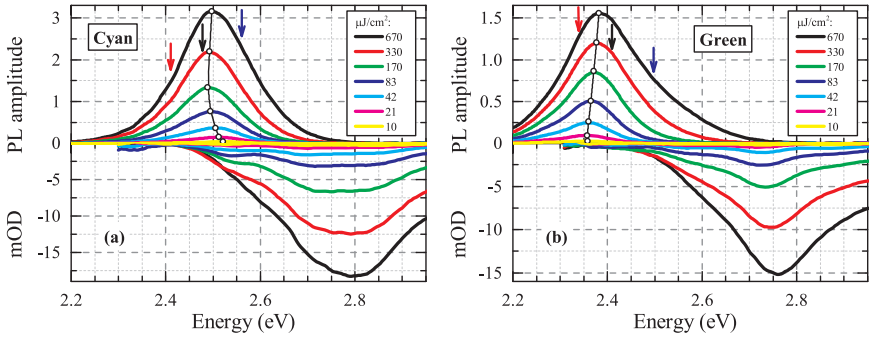

Fig. 1. Time integrated PL (top) and DT (bottom) spectra in the cyan (a) and green (b) QW structures at various excitations. The arrows indicate the spectral positions where PL decay times shown in Fig. 3 were measured. (For interpretation of the references to color in this figure legend, the reader is referred to the web version of this article).

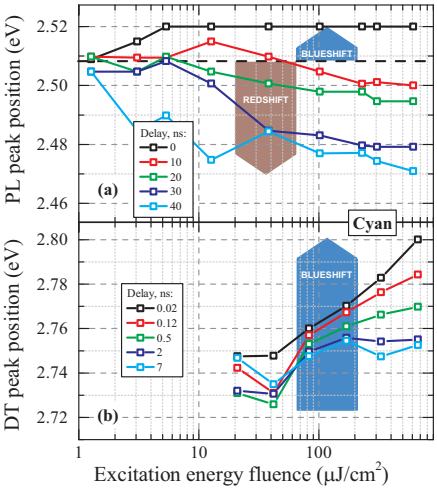

Fig. 2. Peak positions at various time delays as functions of excitation energy density obtained from (a) PL and (b) DT spectra.

is seen within 7 ns delay; but the difference between the DT peak position at high and low excitations constantly decreases with increasing delay (from ~50 meV at 20 ps delay to ~20 meV at 7 ns delay). By comparing the DT and PL spectra, we estimate that the redshift becomes dominant between 7 ns and 10 ns. At 40 ns, the PL peak in the cyan sample redshifts by 30 ± 4 meV from 2.5 eV to 2.47 eV. In the green sample the picture is qualitatively similar, but the shift is smaller reaching 20 ± 4 meV after 40 ns at the highest excitation (not shown).

In Fig. 3, we show the PL decay times at three different spectral positions as a function of excitation. Two excitation regions can be distinguished: low excitations below 10–20 μJ/cm^2, where the PL decay rate remains roughly the same at all wavelengths within the PL band, and high excitations, where the blue PL wing decays faster than the red one. In the low excitation range, the PL decay time in the cyan and green samples falls within 12–15 ns and 20–30 ns, correspondingly. It is interesting to note, however, that almost twofold difference in carrier lifetime does not result in substantial differences in peak QE values. This fact suggests that PL lifetime by itself is not a decisive indicator of LED emission efficiency, as it reveals the carrier dynamics in rather narrow spectral window with respect to DT [35].

Now we discuss possible origins of the PL redshift. Let us consider the band gap renormalization (BGR), screening of the electrical field, and carrier redistribution between the localized states as the possible causes of this redshift. BGR is a fast process appearing instantly after generation of free carriers. A shift of PL emission band due to BGR is usually presented as

$$E_G(n) = E_{G0} - \beta n^{1/3}; \quad (5)$$

here, n stands for carrier concentration and β is a fitting coefficient with the reported values in the range $(1.66-2)\times10^{-8}$ eV cm [33,34]. BGR should appear instantly after the excitation even at small delay times; redshift of PL position due to BGR must increase with excitation, as it was observed in $In_{0.2}Ga_{0.8}N$ QW by Sun et al. [34]. In contrast, the PL peak is blue shifted at small delays (see black curve in Fig. 2(a)) making BGR an unlikely reason behind the PL redshift at later times.

Similarly, a redshift of PL emission due to quantum confined Stark effect (QCSE) in QW with internal electric field can be expressed as

$$h\nu(n) = E_G(0) - edF(n); \quad (6)$$

here d is the QW thickness, e is elementary charge and $F(n)$ is the internal electric field strength

$$F(n) \approx F_0 - \frac{ned}{\varepsilon\varepsilon_0} \quad (7)$$

with maximum electric field strength F_0, electric constant ε_0 and static relative dielectric constant ε [33]. QCSE results in a rapid PL blueshift due to screening of electrical field by free carriers and a subsequent field recovery when carriers recombine; the spectral shift is proportional to free carrier density n. While this situation resembles that depicted in Fig. 2, one has also to bear in mind that the redshift due to recovery of internal field cannot exceed the initial blueshift, i.e. the PL peak position with increasing delay should approach that at small excitations. In the samples under study, the redshift at long delays and high excitations exceeds the initial blue shift considerably, thus indicating that screening and subsequent recovery of the internal electrical field cannot single handedly explain the PL spectral dynamics.

Hence, we attribute the observed redshift of PL emission at long delays to the redistribution of carriers from the initially occupied shallower localized states to deeper ones. This is feasible in a system with large potential inhomogeneities and many local potential minima that are considerably deeper than the thermal energy k_BT [36,37]. After the excitation, the nonequilibrium carriers are randomly distributed between these minima. At low densities, the quasi-Fermi energies of electrons and holes are low, thus carriers can get trapped in the shallower potential minima. Increasing excitation raises the quasi-Fermi levels increasing a probability for carriers to escape the shallower minima and reach the deeper ones. It was proposed that localization of

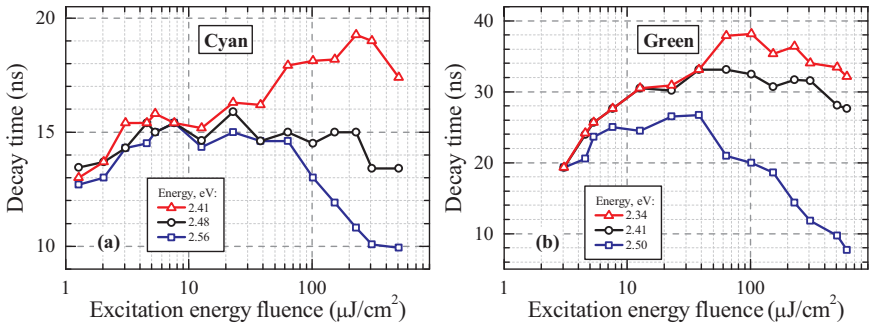

Fig. 3. PL decay time at different spectral positions (the blue wing, central area, and the red wing of a corresponding PL spectrum; the exact spectral positions are indicated by arrows in Fig. 1) as a function of excitation in cyan (a) and green (b) QW structures. (For interpretation of the references to color in this figure legend, the reader is referred to the web version of this article).

carriers into deeper states is slower than that into the shallower ones [32]. This model agrees with larger PL red shift at higher excitations and longer delay times, presented in Fig. 2. Similar arguments were used in explaining a tendency of the small red shift of PL spectra (few meV) with increasing excitation power observed by near-field photoluminescence in semipolar QWs [17]. Also, it is in line with the fact that at low excitations the PL decay time is the same for all states within the PL bands (Fig. 3). Usually, the PL decay time is constant in the red part of PL band for the localized states and then exponentially decreases with photon energy for the extended states [35,38]. In our case, the distribution of localized states must be very broad and emission from these states seems to govern the entire PL line at low excitations. It can be concluded that the deep localized states become saturated with increasing excitation resulting in transfer of carriers into the extended mobile states, which is reflected in the appearance of fast recombination component within the blue PL wing with recombination rate increasing with excitation (Fig. 3). Within this model, the smaller PL redshift and longer PL decay time (up to the excitation, where the extended states come into the play) in the green sample indicates relatively small disorder and smooth indium distribution.

To investigate the dependence of carrier mobility on excitation, the bipolar diffusion coefficient D (diffusivity) was measured using LITG technique; the obtained values are shown in Fig. 4(a) as a function of excitation. We note that D values were extracted within first nanosecond after the photoexcitation when the carrier density is close to the initial one. It is seen that (i) diffusivity non-monotonously increases with excitation and (ii) D values in the samples under study differ below 40 μJ/cm^2 but become very similar at higher excitations. Increase in D with excitation was observed previously in blue LED structure and was explained by the increasing ratio of carriers in the mobile extended states with respect to those in localized states; a change in the occupancy was proposed as a reason for increasing rate of nonradiative recombination with excitation [15]. The different recombination rates in cyan and green samples at low excitations can be therefore attributed to different diffusivity, which in highly excited nitrides is governed by the mobility of holes [39]. Indeed, at 10 μJ/cm^2 D is 0.44 ± 0.02 cm^2/s and 0.26 ± 0.07 cm^2/s in cyan and green structures and correlates well with the values of τ_{PL} 15 ± 0.3 ns and 25 ± 0.3 ns, correspondingly; i.e. an increase by 1.7 times in diffusivity results in the same drop in the lifetime. With increasing excitation, the extended mobile states become increasingly more populated, causing faster nonradiative recombination from these states. As it was discussed, this is also expressed as the increase in the recombination rate of the blue PL wing (Fig. 3). We note that droop threshold (60–70 μJ/cm^2) is very close to that when D becomes equal in both structures. To illustrate the possible role of carrier transport in the efficiency droop, in Fig. 4(b) we plot quantum efficiency (PL normalized to excitation, open symbols) and PL signal normalized to diffusion coefficient (closed symbols) as a function of excitation. It can be seen that both PL curves behave similarly above the droop threshold. This similarity suggests that the onset of efficiency droop in the given samples is related to the increasing mobility of holes with excitation due to their delocalization. This result agrees well with

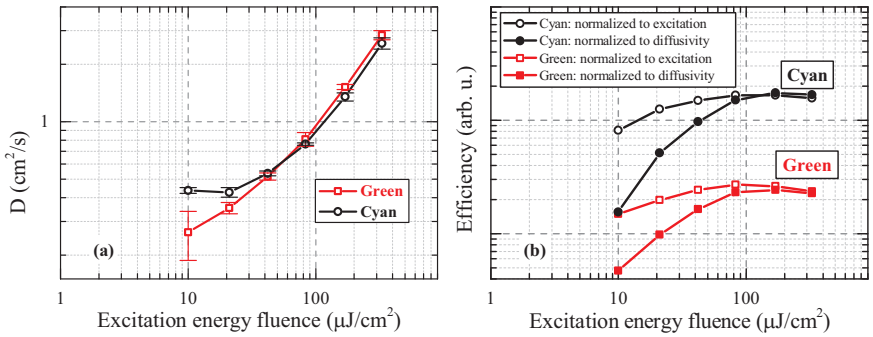

Fig. 4. (a) Diffusion coefficient in the cyan and green QW samples as a function of excitation energy fluence. (b) PL signal normalized either to excitation energy fluence (open symbols) or diffusion coefficient (filled symbols) in the cyan (red) and green (black) structures. The efficiency curves of cyan and green samples are arbitrarily shifted in respect to each other for the sake of visibility. (For interpretation of the references to color in this figure legend, the reader is referred to the web version of this article).

the numerical study by Dawson et al. [6] showing that while electrons are mostly delocalized at all densities, the holes remain localized both in-plane and cross-plane even at room temperature. With increasing excitation, a relative part of delocalized holes increases, which gives rise to higher rate of nonradiative recombination and efficiency losses. The delocalization is expected to be of significance up to densities of $\sim 10^{19}$ cm^{-3} when the majority of carriers should become delocalized. At higher densities, the e-e-h Auger recombination process was suggested to dominate the efficiency droop [40].

4. Conclusions

In summary, we investigated two complete LED structures emitting in cyan (500 nm) and green (530 nm) spectral ranges using several optical techniques. Both structures are shown to be of similar optical and structural quality, in spite of higher indium content in the green structure. We observed the dynamics of carrier redistribution between the localized states of various depths as an untypical redshift of PL peak emerging at long delays and increasing with excitation. We demonstrated that considerably different PL decay time did not result in different QE at higher carrier densities; therefore, it cannot be used as a reliable criteria for LED luminosity prognosis. The increase in carrier density resulted in faster carrier recombination in the high energy states and higher diffusivity, which in turn correlated with the onset of efficiency droop. This fact supports the claim that increasing diffusivity plays an important role in efficiency droop since the probability for carriers to reach non-radiative recombination centers increases with carrier mobility.

Acknowledgements

This work was supported by the project NEWLED (EC FP7 #318388).

References

[1] C. Weisbuch, M. Piccardo, L. Martinelli, J. Iveland, J. Peretti, J.S. Speck, The efficiency challenge of nitride light-emitting diodes for lighting, Phys. Status Solidi Appl. Mater. Sci. 212 (2015) 899–913, http://dx.doi.org/10.1002/pssa.201431868.

[2] S.F. Chichibu, H. Marchand, M.S. Minsky, S. Keller, P.T. Fini, J.P. Ibbetson, S.B. Fleischer, J.S. Speck, J.E. Bowers, E. Hu, U.K. Mishra, S.P. DenBaars, T. Deguchi, T. Sota, S. Nakamura, Emission mechanisms of bulk GaN and InGaN quantum wells prepared by lateral epitaxial overgrowth, Appl. Phys. Lett. 74 (1999) 1460, http://dx.doi.org/10.1063/1.123581.

[3] J.R. Jinschek, R. Erni, N.F. Gardner, A.Y. Kim, C. Kisielowski, Local indium segregation and bang gap variations in high efficiency green light emitting InGaN/GaN diodes, Solid State Commun. 137 (2006) 230–234, http://dx.doi.org/10.1016/j.ssc.2005.10.030.

[4] C.J. Humphreys, Does in form In-rich clusters in InGaN quantum wells? Philos. Mag. 87 (2007) 1971–1982, http://dx.doi.org/10.1080/14786430701342172.

[5] S. Schulz, D.P. Tanner, E.P. O'Reilly, M.A. Caro, T.L. Martin, P.A.J. Bagot, M.P. Moody, F. Tang, J.T. Griffiths, F. Oehler, M.J. Kappers, R.A. Oliver, C.J. Humphreys, D. Sutherland, M.J. Davies, P. Dawson, Structural, electronic, and optical properties of m -plane InGaN/GaN quantum wells: insights from experiment and atomistic theory, Phys. Rev. B – Condens. Matter Mater. Phys. 92 (2015) 235419, http://dx.doi.org/10.1103/PhysRevB.92.235419.

[6] P. Dawson, S. Schulz, R.A. Oliver, M.J. Kappers, C.J. Humphreys, The nature of carrier localisation in polar and nonpolar InGaN/GaN quantum wells, J. Appl. Phys. 119 (2016) 181505, http://dx.doi.org/10.1063/1.4948237.

[7] D.S.P. Tanner, M.A. Caro, E.P. O'Reilly, S. Schulz, Random alloy fluctuations and structural inhomogeneities in c-plane InxGa1 − xN quantum wells: theory of ground and excited electron and hole states, RSC Adv. 6 (2016) 64513–64530, http://dx.doi.org/10.1039/C6RA07540A.

[8] M. Auf Der Maur, A. Pecchia, G. Penazzi, W. Rodrigues, A. Di Carlo, Efficiency drop in green InGaN/GaN light emitting diodes: the role of random alloy fluctuations, Phys. Rev. Lett. 116 (2016) 1–5, http://dx.doi.org/10.1103/PhysRevLett.116.027401.

[9] F. Nippert, S.Y. Karpov, G. Callsen, B. Galler, T. Kure, C. Nenstiel, R. Markus, M. Straßburg, H. Lugauer, A. Hoffmann, F. Nippert, S.Y. Karpov, G. Callsen, B. Galler, T. Kure, Temperature-dependent recombination coefficients in InGaN light-emitting diodes: hole localization, Auger processes, and the green gap temperature-dependent recombination coefficients in InGaN light-emitting diodes: hole localization, Auger processes, Appl. Phys. Lett. 161103 (2016) 161103, http://dx.doi.org/10.1063/1.4965298.

[10] A. Morel, P. Lefebvre, S. Kalliakos, T. Taliercio, T. Bretagnon, B. Gil, Donor-acceptor-like behavior of electron-hole pair recombinations in low-dimensional (Ga,In)N/GaN systems, Phys. Rev. B. 68 (2003) 1–6, http://dx.doi.org/10.1103/PhysRevB.68.045331.

[11] T.J. Badcock, P. Dawson, M.J. Davies, M.J. Kappers, F.C.P. Massabuau, F. Oehler, R.A. Oliver, C.J. Humphreys, Low temperature carrier redistribution dynamics in InGaN/GaN quantum wells, J. Appl. Phys. 115 (2014) 113505, http://dx.doi.org/10.1063/1.4868628.

[12] S.Y. Karpov, Effect of localized states on internal quantum efficiency of III-nitride LEDs, Phys. Status Solidi – Rapid Res. Lett. 4 (2010) 320–322, http://dx.doi.org/10.1002/pssr.201004325.

[13] J. Hader, J.V. Moloney, S.W. Koch, Density-activated defect recombination as a possible explanation for the efficiency droop in GaN-based diodes density-activated defect recombination as a possible explanation for the efficiency droop in GaN-based diodes, Appl. Phys. Lett. 96 (2010) 221106, http://dx.doi.org/10.1063/1.3446889.

[14] G. Pozina, R. Ciechonski, Z. Bi, L. Samuelson, B. Monemar, Dislocation related droop in InGaN/GaN light emitting diodes investigated via cathodoluminescence, Appl. Phys. Lett. 107 (2015) 251106, http://dx.doi.org/10.1063/1.4938208.

[15] R. Aleksiejunas, K. Gelžinyte, S. Nargelas, K. Jarašiunas, M. Vengris, E.A. Armour, D.P. Byrnes, R.A. Arif, S.M. Lee, G.D. Papasouliotis, Diffusion-driven and excitation-dependent recombination rate in blue InGaN/GaN quantum well structures, Appl. Phys. Lett. 104 (2014) 22114, http://dx.doi.org/10.1063/1.4862026.

[16] A. Vertikov, I. Ozden, A.V. Nurmikko, Diffusion and relaxation of excess carriers in InGaN quantum wells in localized versus extended states, J. Appl. Phys. 86 (1999) 4697–4699, http://dx.doi.org/10.1063/1.371423.

[17] S. Marcinkevičius, K. Gelžinytė, Y. Zhao, S. Nakamura, S.P. DenBaars, J.S. Speck, Carrier redistribution between different potential sites in semipolar (202¯1) InGaN quantum wells studied by near-field photoluminescence, Appl. Phys. Lett. 105 (2014) 111108, http://dx.doi.org/10.1063/1.4896034.

[18] H. Solowan, J. Danhof, U.T. Schwarz, Direct observation of charge carrier diffusion and localization in an InGaN multi quantum well direct observation of charge carrier diffusion and localization in an InGaN multi quantum well, Jpn. J. Appl. Phys. 7 (2013) 4–9.

[19] S.-W. Feng, Y.-C. Cheng, Y.-Y. Chung, C.C. Yang, Y.-S. Lin, C. Hsu, K.-J. Ma, J.-I. Chyi, Impact of localized states on the recombination dynamics in InGaN/GaN quantum well structures, J. Appl. Phys. 92 (2002) 4441, http://dx.doi.org/10.1063/1.1506393.

[20] S. Leyre, E. Coutino-Gonzalez, J.J. Joos, J. Ryckaert, Y. Meuret, D. Poelman, P.F. Smet, G. Durinck, J. Hofkens, G. Deconinck, P. Hanselaer, Absolute determination of photoluminescence quantum efficiency using an integrating sphere setup, Rev. Sci. Instrum. 85 (2014) 123115, http://dx.doi.org/10.1063/1.4903852.

[21] E. Matioli, C. Weisbuch, Active region Part A. Internal quantum efficiency in LEDs, in: T.-Y. Seong, H. Jung, A. Hiroshi, M. Hadis (Eds.), III-Nitride Based Light Emitting Diodes Applications, Springer, 2013, pp. 121–153.

[22] A. Miller, Nonlinear optics in semiconductors. II. Semiconductors and semimetals, in: E. Garmire, A. Kost (Eds.), Nonlinear Optics in Semiconductors II. Semiconducors Semimetals, 292 Academic, New York, 1999, p. 287.

[23] R. Aleksiejunas, M. Sudžius, T. Malinauskas, J. Vaitkus, K. Jarašiunas, S. Sakai, Determination of free carrier bipolar diffusion coefficient and surface recombination velocity of undoped GaN epilayers, Appl. Phys. Lett. 83 (2003) 1157–1159, http://dx.doi.org/10.1063/1.1599036.

[24] K. Jarašiunas, R. Aleksiejunas, T. Malinauskas, M. Sudžius, S. Miasojedovas, S. Juršėnas, A. Žukauskas, R. Gaska, J. Zhang, M.S. Shur, J.W. Yang, E. Kuokštis, M.A. Khan, Carrier diffusion and recombination in highly excited InGaN/GaN heterostructures, Phys. Status Solidi Appl. Mater. Sci. 202 (2005) 820–823, http://dx.doi.org/10.1002/pssa.200461351.

[25] K. Jarašiunas, T. Malinauskas, R. Aleksiejunas, M. Sudžius, E. Frayssinet, B. Beaumont, J.P. Faurie, P. Gibart, Characterization of differently grown GaN epilayers by time-resolved four-wave mixing technique, Phys. Status Solidi Appl. Mater. Sci. 202 (2005) 566–571, http://dx.doi.org/10.1002/pssa.200460430.

[26] R. Aleksiejūnas, K. Nomeika, S. Miasojedovas, S. Nargelas, T. Malinauskas, K. Jarašiūnas, Ö. Tuna, M. Heuken, Carrier dynamics in blue and green emitting InGaN MQWs, Phys. Status Solidi 252 (2015) 977–982, http://dx.doi.org/10.1002/pssb.201451583.

[27] D. Watson-Parris, M.J. Godfrey, P. Dawson, R.A. Oliver, M.J. Galtrey, M.J. Kappers, C.J. Humphreys, Carrier localization mechanisms in InxGa1-xN/GaN quantum wells, Phys. Rev. B - Condens. Matter Mater. Phys. 83 (2011) 1–7, http://dx.doi.org/10.1103/PhysRevB.83.115321.

[28] H. Jeong, H.J. Jeong, H.M. Oh, C.-H. Hong, E.-K. Suh, G. Lerondel, M.S. Jeong, Carrier localization in In-rich InGaN/GaN multiple quantum wells for green light-emitting diodes, Sci. Rep. 5 (2015) 9373, http://dx.doi.org/10.1038/srep09373.

[29] F. Chen, M.C. Cheung, P.M. Sweeney, W.D. Kirkey, M. Furis, A.N. Cartwright, Ultrafast differential transmission spectroscopy of excitonic transitions in InGaN/GaN multiple quantum wells, J. Appl. Phys. 93 (2003) 4933–4935, http://dx.doi.org/10.1063/1.1559432.

[30] R.W. Martin, P.G. Middleton, K.P.O. Donnell, W. Van Der Stricht, Exciton localization and the Stokes' shift in InGaN epilayers, Appl. Phys. Lett. 74 (1999) 263, http://dx.doi.org/10.1063/1.123275.

[31] M.J. Davies, T.J. Badcock, P. Dawson, R.A. Oliver, M.J. Kappers, C.J. Humphreys, High excitation density recombination dynamics in InGaN/GaN quantum well structures in the droop regime, Phys. Status Solidi Curr. Top. Solid State Phys. 11 (2014) 694–697, http://dx.doi.org/10.1002/pssc.201300498.

[32] N.I. Bochkareva, Y.T. Rebane, Y.G. Shreter, Efficiency droop and incomplete carrier localization in InGaN/GaN quantum well light-emitting diodes, Appl. Phys. Lett. 103 (2013) 191101, http://dx.doi.org/10.1063/1.4828780.

[33] E. Kuokstis, J.W. Yang, G. Simin, M.A. Khan, R. Gaska, M.S. Shur, Two mechanisms of blueshift of edge emission in InGaN-based epilayers and multiple quantum wells, Appl. Phys. Lett. 80 (2002) 977–979, http://dx.doi.org/10.1063/1.1433164.
[34] G. Sun, G. Xu, Y.J. Ding, H. Zhao, N. Tansu, Investigation of fast and slow decays in InGaN/GaN quantum wells, Appl. Phys. Lett. 99 (2011) 10–13, http://dx.doi.org/10.1063/1.3627166.
[35] K. Jarašiunas, S. Nargelas, R. Aleksiejunas, S. Miasojedovas, M. Vengris, S. Okur, H. Morkoç, Ü. Özgür, C. Giesen, Ö. Tuna, M. Heuken, Spectral distribution of excitation-dependent recombination rate in an In0.13Ga0.87N epilayer, J. Appl. Phys. 113 (2013) 0–9, http://dx.doi.org/10.1063/1.4793637.
[36] Y. Cho, G.H. Gainer, A.J. Fischer, J.J. Song, S. Keller, U.K. Mishra, S.P. DenBaars, "S-shaped" temperature-dependent emission shift and carrier dynamics in InGaN/GaN multiple quantum wells, Appl. Phys. Lett 73 (1998) 1370–1372, http://dx.doi.org/10.1063/1.122164.
[37] Q. Li, S.J. Xu, M.H. Xie, S.Y. Tong, Origin of the "S-shaped" temperature dependence of luminescent peaks from semiconductors, J. Phys. Condens. Matter 17 (2005) 4853–4858, http://dx.doi.org/10.1088/0953-8984/17/30/011.
[38] S.F. Chichibu, T. Azuhata, T. Sota, T. Mukai, S. Nakamura, Localized quantum well excitons in InGaN single-quantum-well amber light-emitting diodes, J. Appl. Phys. 88 (2000) 5153, http://dx.doi.org/10.1063/1.1314906.
[39] R. Aleksiejunas, M. Sudžius, V. Gudelis, T. Malinauskas, K. Jarašiunas, Q. Fareed, R. Gaska, M.S. Shur, J. Zhang, J. Yang, E. Kuokštis, M.A. Khan, Carrier transport and recombination in InGaN/GaN heterostructures, studied by optical four-wave mixing technique, Phys. Status Solidi C Conf. 2690 (2003) 2686–2690, http://dx.doi.org/10.1002/pssc.200303261.
[40] M. Binder, A. Nirschl, R. Zeisel, T. Hager, H.J. Lugauer, M. Sabathil, D. Bougeard, J. Wagner, B. Galler, Identification of nnp and npp Auger recombination as significant contributor to the efficiency droop in (GaIn)N quantum wells by visualization of hot carriers in photoluminescence, Appl. Phys. Lett. 103 (2013), http://dx.doi.org/10.1063/1.4818761.

Vilniaus universiteto leidykla
Saulėtekio al. 9, LT-10222 Vilnius
El. p. info@leidykla.vu.lt,
www.leidykla.vu.lt
Tiražas 20 egz.